MORPHOMETRIC STUDY OF LONGITUDINAL RIDGES IN LONG RUNOUT LANDSLIDES ON MARS, EARTH, AND THE MOON.

Giulia Magnarini

A thesis submitted to University College London

for the degree of Doctor of Philosophy.

Department of Earth Sciences

January 2021

Declaration.

I confirm that the work presented in this thesis is my own. Where information has been derived from other sources, I confirm that this has been indicated in the thesis.

Giulia Magnarini

January 2020

Acknowledgments.

The journey to arrive to this point has been much longer than the four years of the actual doctorate. Therefore, firstly I would like to thank the people who have constantly been by my side. As banal as it sounds but so true, this could not have happened without the unconditional support of my fantastic parents and the patience of my partner.

I am immensely grateful to my supervisor Tom Mitchell, who supported me and cared for me for the past four year. He gave me freedom of action throughout my PhD. His trust, respect, and craziness have generated the confidence I needed.

I am thankful to my second supervisor Peter Grindrod, whose enthusiasm and geekiness are so contagious. He has also always given me support and full independence in my research and this has been empowering.

Every PhD student should have their own Tom and their own Pete.

I am thankful to my Liran Goren for the critical discussions on my work whenever revision and help was needed.

I am thankful to Apollo 17 astronaut geologist Harrison ‘Jack’ Schmitt for the discussions on the Light Mantle avalanche on the Moon. He went there! I am also incredibly thankful to him for bringing me on board of the NASA ANGSA programme to study a newly open sample of the Light Mantle avalanche and so allowing me to benefit of the long lasting legacy of the Apollo programme.

There is a long list of other people I want to thank. I have found so many friends-colleagues in the department. Following the desk order (so to be impartial): Gab, Mark, Ashley, Thomas, Will G., Isobel, Claire, Lucia, Michael, Giles, Becky P., Bobby, Almu, Pauline, Kate, Antoinette, Frans, Manu,

Catalina, Chris. Their daily support, the non-sense but profound conversations, the incredible fun we had in the department, at conferences, night outs, and trips have been so precious. There are also some members of staff I am thankful for the time we have shared: Nic, with all his knowledge, opinions, sense of humour, and eventually friendship; Juergen and Phil, for all their anecdotes and the good company sharing überklass drinks and food during field trips.

I would like to thank Jen, Louise, and Sarah J. for sharing some drinks together and being supportive; Joel, for helping me with martian datasets and digital elevation models, and teasing me with martian landforms; Enrica, for the chats and the support.

The PhD gave me opportunities to travel and meet people who then have become friends: Michele, Rodrigo, Erik, Simone, Elena, and Giulio, with whom I shared the scorching sun and the silent starry nights of the Atacama desert with; Kati and Martin, with whom I shared two wild weeks in Kyrgyzstan; Jacopo, who I met in Nantes and found again in Padua.

Final acknowledgment goes to the people who helped me during field work and laboratory experiments: John B., who accompanied me in Iquique; señor Alfredo of the Mina San Marco, who voluntarily escorted us through unknown sand dune fields; señor Bernardo and his dogs, who offered me shade at the shooting range in Iquique for two years; Tatiana and Manu, who welcomed me at the Universidad de Atacama in Copiapo, showed me some geological beauty around Caldera, and arranged me for a trip to the Parco National Nevado Tres Cruces; Stefano A., who patiently helped me with friction experiments at the INGV in Rome.

I loved every moment of my PhD.

“The force is with you, young Skywalker,
but you are not a jedi yet.”
- Darth Vader, The Empire Strikes Back -

“Never tell me the odds.”
- Han Solo, The Empire Strikes Back -

Abstract.

Long runout landslides are hypermobile landslides ubiquitous in our solar system. The exact mechanism(s) that have to be invoked in order to explain their high velocity and exceptional travel distances over nearly horizontal surfaces has yet to be successfully determined. In this thesis I focused on the distinctive longitudinal ridges that mark the surface of long runout landslide deposits in the attempt to link these morphological features and their related internal structures to the mechanisms involved during the emplacement of such catastrophic events.

I conducted a morphometric analysis of longitudinal ridges of three case studies: the Coprates Labes landslide in Valles Marineris on Mars; the El Magnifico landslide in Chile – on Earth; the Tsiolkovskiy crater landslide – on the Moon. For the first time in natural landslides, I found that the wavelength of the longitudinal ridges is consistently 2 to 3 times the thickness of the landslide deposit, in agreement with experimental work on rapid granular flows. The recurrence of the scaling relationship suggests a scale- and environment-independent mechanism. Therefore, I concluded that the existence of longitudinal ridges in long runout landslides cannot be used to infer the presence of specific lithologies forming the basal surface; nor environmental and climatic conditions at the time of landslide emplacement.

Based on the agreement between the results obtained from my morphometric analysis and the laboratory experiments on rapid granular flows, I proposed that longitudinal ridges in long runout landslides are imparted by high-speed granular flow convection mechanisms. In order to ground truth such hypothesis, I conducted field work at the terrestrial El Magnifico landslide and studied the internal structures of the deposit and their relationship with the longitudinal ridges. I concluded that evidence cannot rule out a convection-

style mechanism observed in laboratory experiments of granular flows but is also not equivocal in its support. I advanced an alternative hypothesis that longitudinal ridges may have formed by a mechanism that involves pattern-forming vibrations. Such proposed mechanism supports the existence of heterogeneous stress distribution and stress fluctuation within long runout landslide deposits, which are considered the hallmark of acoustic fluidization.

I suggested the use of the scaling relationship between the wavelength of longitudinal ridges and the thickness of the deposit as a tool to infer the thickness of landslide deposits where its calculation is not otherwise possible using typical methods in geomorphology. I applied this novel idea to the Light Mantle landslide, Taurus-Littrow valley, at the Apollo 17 landing site: by calculating the representative wavelength of the longitudinal ridges I derived the thickness of its deposit, as it could not be derived through interpolation.

I discussed the finding of my work within the context of the literature on frictional weakening in fault mechanics, on the similarity of weakening of shear zones in landslide and earthquake mechanics, and on the geomorphology of long runout landslide deposits. Following this, I defined a new framework under which the understanding of the formation mechanism of long runout landslides should be approached.

Finally, I identified four possible directions for future work: extending the morphometric analysis of longitudinal ridges in martian double layer ejecta; investigating the importance of the roughness of the substrate in the formation of longitudinal ridges; performing friction experiments to study weakening mechanisms in lunar rock analogues; using martian long runout landslide deposits as stratigraphic markers in order to constrain the timing of geological processes.

Impact Statement.

Landslides have high environmental and socioeconomic impact, which can include loss of life, destruction of infrastructure, damage to land and loss of natural resources. The assessment of risk linked to landslides is paramount to mitigate their potentially devastating impact on human activity. The risk posed by long runout landslides is difficult to evaluate, because the hypermobility that characterizes them is still not well understood. Therefore, being able to predict whether a slope collapse will generate a long runout landslide or not represents a major challenge and failure to predict these failures can have catastrophic consequences, as the 1963 Vajont landslide tragically demonstrated. In that occasion, despite interventions were taken to mitigate the well-known active slope deformations, a catastrophic slope failure occurred unexpectedly, causing the death of more than two thousands people.

The development of longitudinal ridges during the emplacement of long runout landslides is an overlooked process. The question of why and how these structures form is relevant to further the understanding of the mechanisms that are responsible for the hypermobility of long runout landslides and their behaviour that departs from classical friction theory.

For the first time in natural long runout landslides, this doctoral work provides evidence of the existence of a scaling relationship between the wavelength of longitudinal ridges and the thickness of the landslide. Such a scaling relationship has previously only been reported in laboratory experiments on rapid granular flows, and hence this work provides a novel link between theoretical models, and experimental and field observations. Therefore, the outcomes of this work will be of interest to a wide range of people who are

involved in the physics of rapid granular flows, in terrestrial and planetary geomorphology, and in modelling long runout landslides.

Contents.

List of acronyms and abbreviations.

A	Area of landslide deposits
CMOS	Complementary metal-oxide-semiconductor
CNES	Centre National d'Etudes Spatiales (French National Centre for Space Studies)
CRISM	Compact Reconnaissance Imaging Spectrometer for Mars
CTX	Context camera
DEM	Digital Elevation Model
DLE	Double Layer Ejecta
DTMRDR	Digital Terrain Map Reduced Data Record
ESA	European Space Agency
EVA	Extra Vehicular Activity
GCS	Geographical Coordinate System
GCP	Ground Control Point
GIS	Geographic Information System
H	Height drop (vertical drop)
$H_{c.g}$	Height drop calculated from the centre of gravity
HiRISE	High Resolution Imaging Science Experiment camera
HRSC	High Resolution Stereo Camera
IFOV	Instantaneous field of view
ISIS	Integrated Software for Imagers and Spectrometers
L	Length (horizontal runout)
$L_{c.g}$	Length calculated from the centre of gravity
LiDAR	Light Detection and Ranging
LOLA	Lunar Orbiter Laser Altimeter
LRO	Lunar Reconnaissance Orbiter

List of acronyms and abbreviations

LROC	Lunar Reconnaissance Orbiter Camera
MGS	Mars Global Surveyor
MOLA	Mars Orbiter Laser Altimeter
MRO	Mars Reconnaissance Orbiter
MSI	Multi-Spectral Instrument
NAC	Narrow Angle Camera
NASA	National Aeronautics and Space Administration
ODE	Orbital Data Explorer
PDS	Planetary Data System
PSD	Power Spectral Distribution
SAFC	Sample Analogue Facility Curation
SfM	Structure from Motion
SHIVA	Slow to High Velocity Apparatus
SNAP	Sentinel Application Platform
SRTM	Shuttle Radar Topography Mission
STS	Space Transportation System
T	Thickness of landslide deposits
TMC	Terrain Mapping Camera
UAV	Uncrewed Aerial Vehicle
USGS	United States Geological Survey
V	Volume of landslides deposits
V_f	Final volume of landslides deposits
V_i	Initial volume of landslides deposits
WAC	Wide Angle Camera
XRD	X-Ray Diffraction

Table of Figures.

Table of Tables.

1 Introduction.

1.1 Motivation.

Long runout landslides are a type of hypermobile mass-wasting processes that is widespread on planetary bodies in our Solar System. The debate on the formation mechanism of such landslides is on-going, as the proposed models fail to satisfactorily explain their ability to travel for up to tens of kilometres, moving on nearly horizontal surfaces with velocities that can exceed 100 km/h.

Comparative planetary geology studies are of fundamental importance in advancing the general knowledge about the planetary bodies in our Solar System and in providing key information to aid in the understanding of terrestrial processes that are still difficult to explain. The mechanics of long runout landslides is one of the unsolved issue that is benefiting from a comparative planetary geology approach. Importantly, further unlocking the understanding of the hypermobility of long runout landslides will help to mitigate the risks that they pose to infrastructures and human lives.

To date, many mechanisms have been proposed to explain the ability of long runout landslides to move unconfined over flat valley floor with high velocity for significant distances. Each proposed mechanism is able to account for several physical aspects or dynamic evidence of a single or few cases, but they nonetheless fail to provide a universal explanation for the apparent reduction of friction that characterizes this type of landslide.

The study of long runout landslides on planetary bodies raises several important questions:

a) to what extent is the role of fluids important for the emplacement of these catastrophic events?

b) to what extent does slope lithology and material present on valley floors play a role in facilitating the runout?

c) to what extent does the tectonic and structural context predispose slope failures to evolve into long runout landslides?

d) is there a universal explanation or instead different mechanisms that are able to produce the same end result?

Here on Earth, addressing these unanswered questions about the behaviour of long runout landslides will help in producing more specific hazard maps and in better constraining areas at risk. In addition, finding answers to some of these open issues could have important implications for advancing our knowledge of the geological, climatic, and environmental history of other planetary bodies. In particular, as space exploration programmes are intent on sending humans to explore the surface of the Moon and Mars, these answers will set background knowledge for risk mitigation of human settlements beyond Earth, no matter how far in the future they are.

1.2 Aims and objectives.

This thesis examines the formation mechanism of long runout landslides on planetary bodies, focusing on specific case studies from the Earth, Mars, and the Moon. The case studies presented in this thesis have distinct morphological features in common; longitudinal ridges that extend in the direction of movement of the landslide. By focusing on these morphological structures, I have attempted to link the morphology of landslide deposits to emplacement mechanisms involved during these catastrophic events.

Although the study of terrestrial, martian, and lunar long runout landslides serves to advance the knowledge of the individual planetary bodies, this work primarily emphasizes the geological surface process itself, capitalizing on a comparative planetary geology approach. On our planet we can conduct field work, make direct observations, and collect samples. On Mars, thanks to the current availability of high resolution satellite images and the magnificently preserved landforms, we can conduct detailed morphometric measurements

that are not so easy on our planet because of erosion. To date, the lunar long runout landslide in Taurus-Littrow Valley, landing site of the Apollo 17 mission, is the only landslide that has been studied by humans beyond Earth and of which samples have been collected and brought back to Earth.

1.3 Thesis structure.

Chapter 2 is a review of the literature on long runout landslides, a truly multidisciplinary area of research. This is a field that has advanced with the advent of high resolution imagery of the surface of other planetary bodies, since the late 2000's, which have shown the ubiquity of this type of landslide in our Solar System. The field of physics of rapid granular flows has provided an approach to approximate landslide behaviour at laboratory scale and, alongside it, the increase in computational power has also greatly contributed to the modelling of long runout landslides, providing insight on their potential behaviour. The need for a better understanding of the mechanisms leading to the reduction of friction has seen the long runout landslide research field reaching out into both experimental and theoretical rock mechanics, which has been similarly addressing the dramatic reduction of friction occurring along faults during seismic events using improved high-speed rotary apparatuses since the mid 2000's.

Chapter 3 describes the imagery datasets used in this work and the software used for image processing and data analysis.

Chapter 4, 5, and 6 present the four case studies of this work: the Coprates Labes landslide (Valles Marineris, Mars), the El Magnifico landslide (Chile, Earth), the Tsiolkovsky crater landslide (far side of the Moon), and the Apollo 17 avalanche (Taurus-Littrow Valley, the Moon). Although each of these chapters is designed as a stand-alone chapter, the order they are presented in this thesis reflects the order in which the studies have been conducted, therefore reflecting a progression in the level of analysis: the results and hypotheses presented for the case study of the martian landslide (Chapter 4) lay the background that inspired the work conducted for the landslide in Chile (Chapter 5) and the morphometric results presented for the landslide at the

lunar far side (Chapter 6) confirm some of the results and conclusions provided in the previous chapters; the work conducted for the landslide at the Apollo 17 landing site (Chapter 6) is based on assumptions reasonably rooted in the outcomes form the previous work as a whole.

Chapter 7 discusses the major findings of the case studies and their overall significance for the mechanisms of emplacement of long runout landslides; it also attempts to connect the dots between the conclusions from this work and from the past work from the different disciplines reviewed in Chapter 2, providing a new comprehensive framework within which the development of long runout landslides and their emplacement should be envisioned.

Chapter 8 provides a summary of the main conclusions; it also outlines planned future work as continuation of this research project, as well as ideas for new research projects inspired by the new questions that have arisen during this work.

1.4 Specification of the use of terminology.

The term '*landslide*' is a very general term used to describe both a general downslope movement of rock under the effect of gravity and the landform that results from such movement. However, the complexity and variety of landslide processes reflects the diversity of definitions used in the literature to describe more specifically a landslide.

In this thesis, I use the general term '*landslide*'. Interchangeably with the term '*landslide*', the terms '*mass-wasting*', '*slope failure*', and '*mass movement*' are used to refer to the process that generates a landslide. Occasionally, terms that refer to specific classification of a type of landslide are used and follow the original terms used in the literature. Here is the list of such terms, for which a brief description is given following the USGS Landslide Handbook [Highland and Bobrowsky, 2008]. Note that despite the use of different terms, all the landslides I refer to in this thesis are considered '*long runout landslides*', which definition is provided in Section 2.1 and Section 2.4.

- Slide: downslope movement of a rock mass occurring on surfaces of rupture or on relatively thin zones of intense shear strain.
- Rotational Slide: a landslide on which the surface of rupture is curved upward and the slide movement is more or less rotational about an axis that is parallel to the contour of the slope. The head of the displaced material may move almost vertically downward, and the upper surface of the displaced material may tilt backwards toward the scarp.
- Debris/Rock Avalanche: Large, extremely rapid, often open-slope flows formed when an unstable slope collapses and the resulting fragmented debris is rapidly transported away from the slope.
- Debris Flow: a form of rapid mass movement in which loose soil, rock and sometimes organic matter combine with water to form a slurry that flows downslope.

1.5 Published and submitted work.

- Part of Chapter 4 has been published as peer-reviewed article in Nature Communications as: Magnarini G., Mitchell T. M., Grindrod P. M., Goren L., Schmitt H. H. (2019), Longitudinal ridges imparted by high-speed granular flow mechanisms in martian landslides, Nature Communications 10, 4711, https://doi.org/10.1038/s41467-019-12734-0.
- Part of Chapter 5 has been submitted for peer-review in EPSL as: Magnarini, G., Mitchell, T.M., Grindrod, P.M., Goren, L., and Browning, J. – Implications of longitudinal ridges for the mechanics of ice-free long runout landslides.
- Part of Chapter 6 has been submitted for peer-review in JGR Planets as: Magnarini, G., Mitchell, T.M., Grindrod, P.M., Schmitt, H.H., and Petro, N.E. – Scaling relationship between the wavelength of longitudinal ridges and the thickness of long runout landslides on the Moon.

2 Literature review.

2.1 Overview.

Long runout landslides are a type of hypermobile mass-wasting processes that is widespread on planetary bodies in our Solar System. (Figure 2-1; Figure 2-2; Table 2-1; Appendix Table 1).

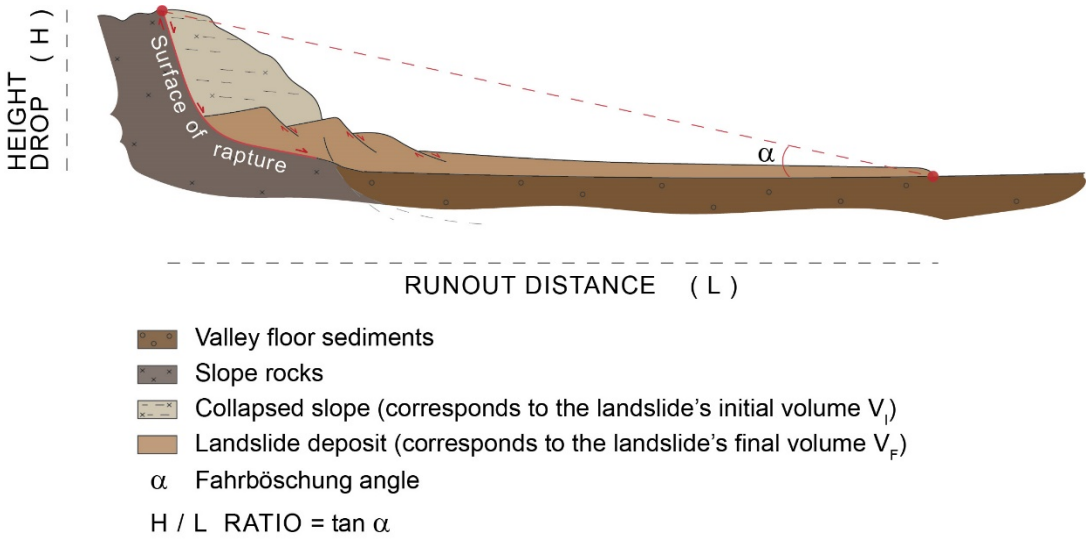

Figure 2-1 – Schematic representation of a long runout landslide. The runout distance (L) of long runout landslides is many times their height drop (H). The hypermobility of long runout landslides is expressed using the H/L ratio.

Long runout landslides are characterized by large volumes (> 10^6 m^3) and their mobility (i.e., the ability of moving away from the head scarp) increases with increasing volume. Moreover, long runout landslides are characterized by a number of distinct physical, kinematic, and geomorphological features. As such, mechanisms proposed to explain the behaviour of long runout landslides have to be consistent with, or at least not contradict, the presence

of these observed features. Some of the issues relevant to the discussion about the behaviour of long runout landslides on planetary bodies and the reduction of friction that takes place during their emplacement are related to the understanding of the influence of gravity, the effect of volume, the role of fluids, and the development of high velocities. These aspects are discussed in this chapter. The chapter is organized in three parts. The first part describes the physical and morphological characteristics of long runout landslides and includes an account of the early stages of research regarding long runout landslides, which provide detailed descriptions of events and from which the important, although debated, H/L ratio was suggested (Figure 2-1). The second part provides the description of the friction reduction mechanisms most relevant to the work conducted for this thesis. Finally, the third part of the chapter provides a summary of the contribution that different fields of research have been providing to the understanding of long runout landslides.

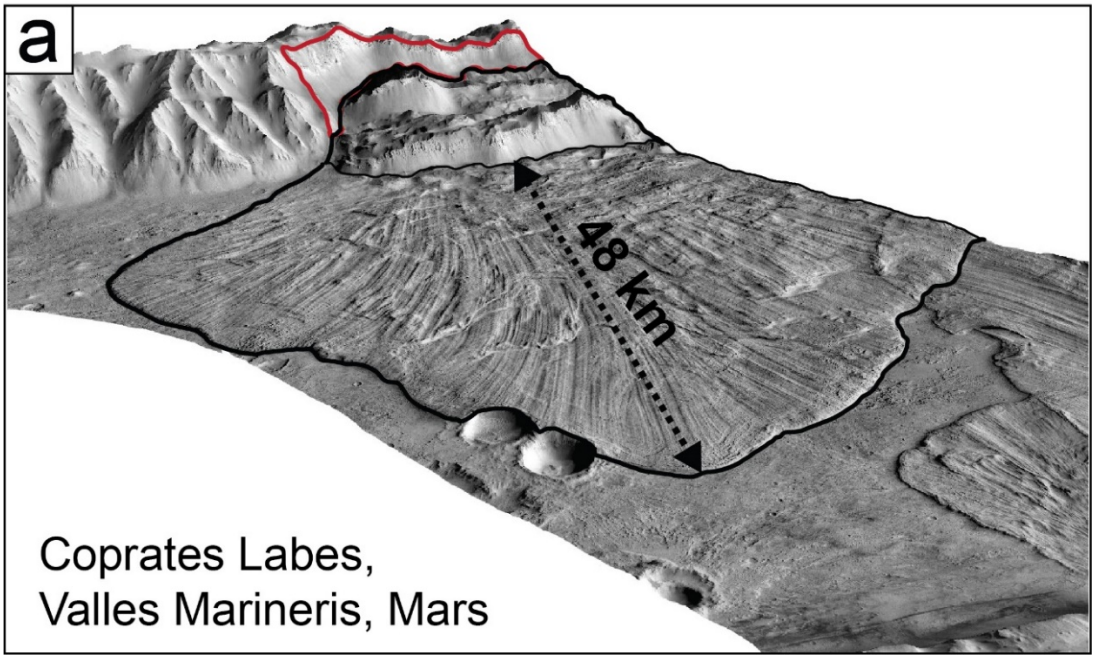

Figure 2-2 – Examples of long runout landslide (continue next pages). a) The Coprates Labes landslide in Valles Marineris, Mars. NEXT PAGE: b) The Tsiolkovskiy crater landslide at the far side of the Moon. c) The Saidmarreh landslide in the Zagros Mountains, Iran, Earth. d) Long runout landslides in the North Atacama region, Chile, Earth (the landslide in the centre is named El Magnifico). Black lines mark the landslide deposits; and red lines mark the failure scarps of the landslides.

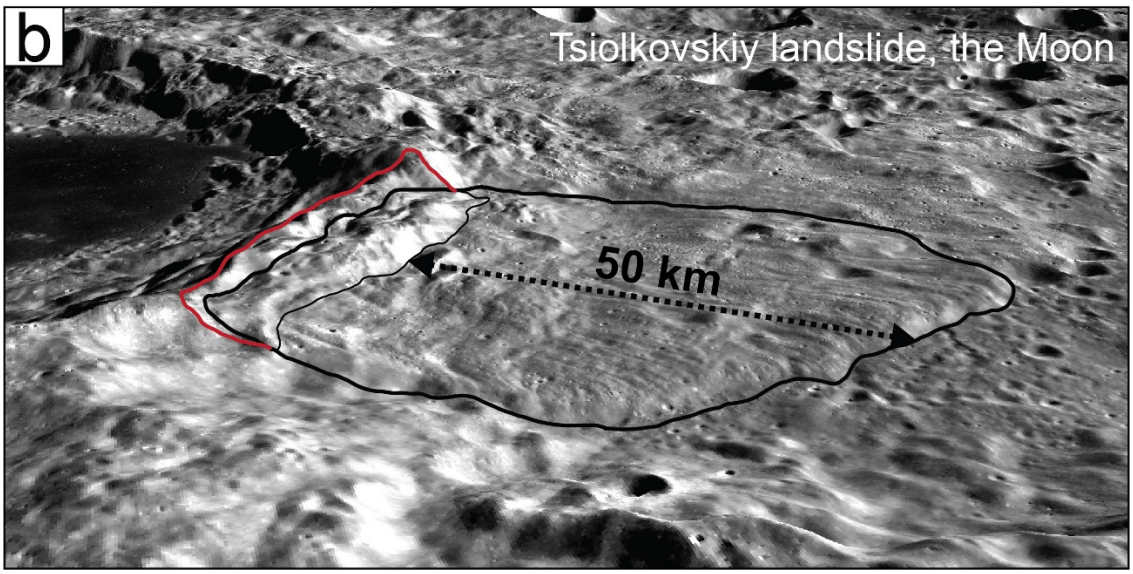
b
Tsiolkovskiy landslide, the Moon
50 km

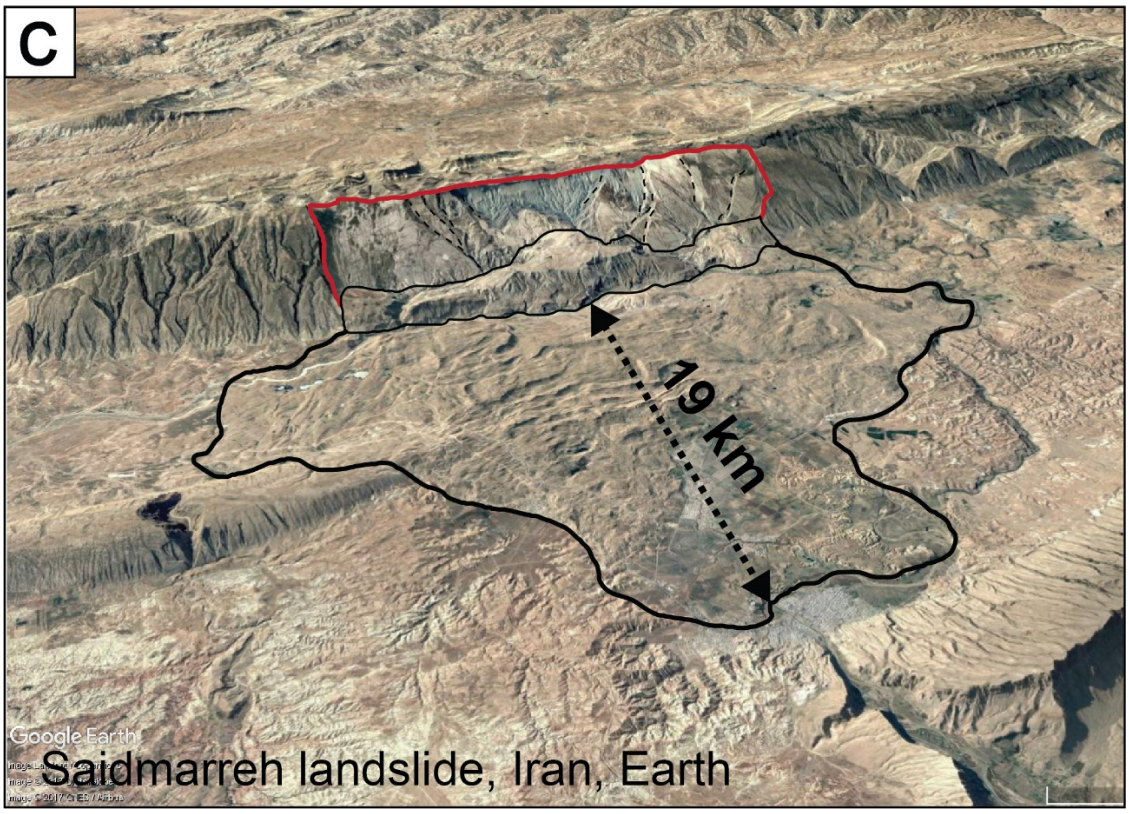
c
19 km
Google Earth
Saidmarreh landslide, Iran, Earth

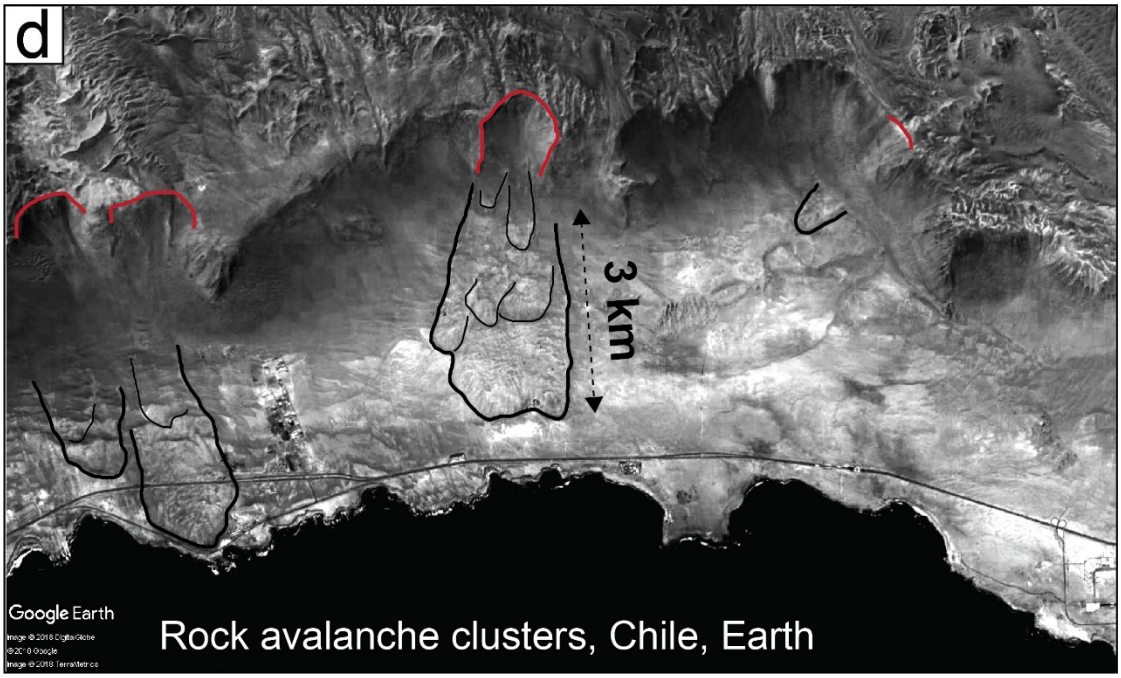

2.2 Early studies.

The first terrestrial report of a long runout landslide dates back to the end of the 19th century [Buss and Heim, 1881; Heim, 1882]. As reconstructed by the authors, the landslide of Elm, in the Swiss Alps, started as a rock fall and moved on a nearly flat valley floor for 2 km at very high velocity. As Heim concluded, “the rock apparently did not slide, it flowed!”. Compared to a torrential flood, the event, as many others described by Heim [1932], was later named *sturzstrom*, which literally translates as “fallstream” [Hsü, 1975]. However, it was clear that no water or mud was involved in the process but, instead, the interstitial medium between the colliding blocks of rock was dry dust. Heim spent his career gathering a series of empirical observations of historical and prehistorical rock avalanches, creating an informative database of measurement of landslides (e.g., fall height, runout, size, etc.). In order to compare the travel distance of sturzstroms, he made use of the *Fahrböschung angle*, which is the angle of the slope that connects the highest point from where the rock mass collapses and the furthest point where the mass stops (Figure 2-1). At a later time, the tangent of the Fahrböschung

angle was adopted as approximation of the apparent coefficient of friction of long runout landslides [Shreve, 1968a], which should be instead derived from the slope that connects the centre of gravity of the mass before and after the event [Legros, 2002]. For small landslides, the Coulomb friction model (Figure 2-3) holds true and so the coefficient of friction ($\tan\alpha = H_{c.g.}/L_{c.g} \sim 0.6$; c.g. stands for 'centre of gravity') and the tangent of the Fahrböschung angle ($\tan\alpha = H/L$; this is also called 'apparent coefficient of friction' because the runout distance, L, and the height drop, H, of the landslide are not calculated from the centre of gravity of the initial slope and the centre of gravity of the final deposit; see Figure 2-1) are approximately equal [Hsü, 1975]. However, it was noted by Heim that *sturzstrom* were characterized by a H/L ratio smaller than 0.6, implying a travel distance longer than the distance expected by the Coulomb friction model. Interestingly, a low H/L ratio (i.e., H/L < 0.6) is observed for landslides with volume > 10^6 m^3 [e.g., Mcewen, 1989; Legros, 2002]. It is from the initial work on the Blackhawk landslide, California, that first appears evidence for the lack of turbulence within such landslides during their emplacement [Shreve, 1968a; Johnson, 1978]. The observations of the so-called 'jigsaw-puzzle boulders' and the preservation of the original stratigraphy, will later be acknowledged to be a distinctive internal structure of long runout landslides (see Dufresne *et al.* [2016] for a review), inspired the idea that these catastrophic landslides does not flow but rather slide.

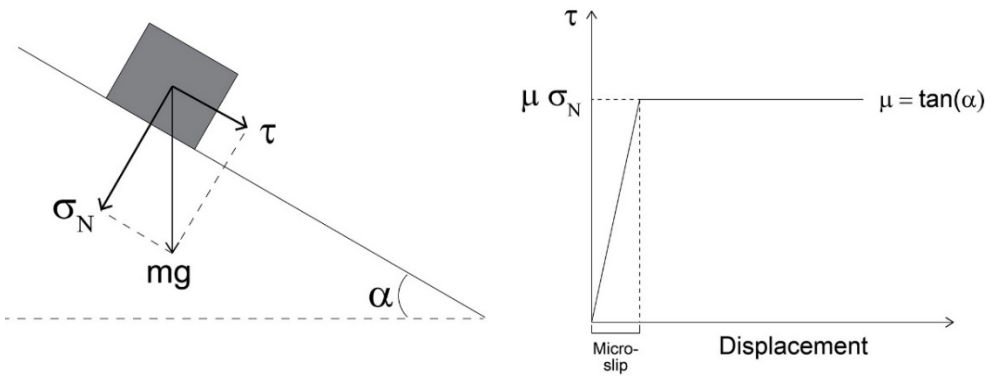

Figure 2-3 – Schematic representation of the classic Coulomb's friction law. The stability of a block resting on an inclined plane is determined by the balance between the normal component (σ_N, normal stress) and tangential component (τ, shear stress) of the gravitational force vector. When the block starts sliding, the ratio of these two forces is equal to the coefficient of friction ($\mu = \sigma_N / \tau = \tan\alpha$).

2.3 Recent planetary studies.

The discovery of long runout landslides on the Moon and on Mars in the late 1960's and 1970's, respectively, represents a turning point in the study of these landforms and the mechanisms that generate them. The presence of these long runout landslides on airless and, at least currently and at the surface, dry planetary bodies questioned the importance of fluids and the necessity of low friction basal surfaces, such as ice or clay-rich lithologies in long runout landslides. These points become focal points in the study of martian long runout landslides, because they have implications for the understanding of Mars' climate over time. Since the 1990's, but mainly since the 2010's, the expansion of data returned from space exploration has provided evidence for the ubiquity of long runout landslides throughout our Solar System. Examples include: Mercury [Brunetti *et al.*, 2015]; Venus [Malin, 1992]; Mars [e.g., Quantin *et al.*, 2004b]; asteroid Vesta [Krohn *et al.*, 2014]; dwarf planet Ceres [Schmidt *et al.*, 2017]; rocky moons such as the Moon [Kokelaar *et al.*, 2017] and Phobos [Shingareva and Kuzmin, 2001]; icy moons in the outer Solar System such as Callisto [Chuang and Greeley, 2000], Iapetus [Singer *et al.*, 2012] and Charon [Beddingfield *et al.*, 2019]. This has resulted in the creation of several inventories that compile a series of information about geometrical and physical aspects of long runout landslides, such as height drop, length of runout, volume, and area of the final deposit [e.g., Singer *et al.*, 2012; Lucas *et al.*, 2014; Crosta *et al.*, 2018b].

2.4 Characteristics of long runout landslides.

2.4.1 Mobility and its relationship with volume and gravity.

THE H/L/ RATIO | The physical meaningfulness of the H/L ratio has been questioned by Legros [2002], following a series of observations during laboratory experiments and simulations. Despite the H/L ratio being considered as physically meaningless [e.g., Legros, 2002], it is nevertheless the accepted discriminatory parameter that describes the efficiency of

landslide mobility, thus identifying long runout landslides (i.e., H/L << 0.6). The H/L ratio decreases with increasing volume of long runout landslides (Figure 2-4). The increase in mobility with increasing volume was a fact already known by Heim [1932] and a linear correlation between the two parameters was later showed by Scheidegger [1973] and Hsü [1975]. Mcewen [1989] showed for the first time that the mobility dependency on the volume holds true also for martian long runout landslides. Since then, a similar linear relationship has been confirmed for long runout landslides on other planetary bodies in the Solar System [Singer *et al.*, 2012; Lucas *et al.*, 2014; Chilton *et al.*, 2019].

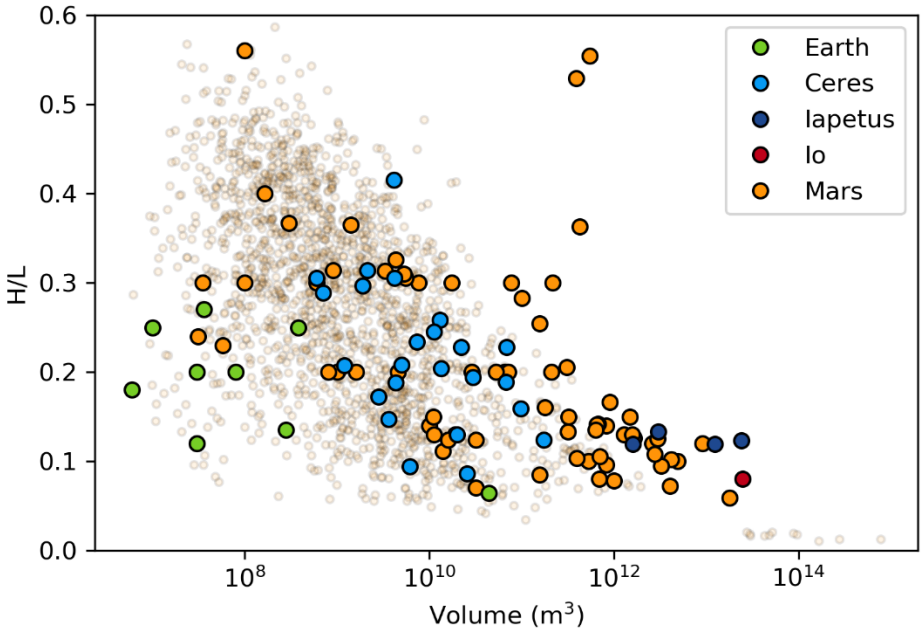

Figure 2-4 – The increase in mobility with increase of volume in long runout landslides in the Solar System. The plot shows the relationship between the mobility (expressed by the H/L ratio) and the volume of long runout landslides. For the Earth, I only included dry continental, but not volcanic, long runout landslides that I mention in my thesis; see Table 2-1 and Appendix Table 1 for references. Data for Cerean landslides are from Chilton *et al.* [2019]. Data for landslides on Iapetus are from Singer *et al.* [2012] and Lucas *et al.* [2014]. Data of landslides on Io are from Lucas *et al.* [2014]. For Mars, I selected landslides labelled 'rock avalanches' and 'rockslides' from the dataset of Crosta *et al.* [2018a] (applied transparency so as to make the plot readable), and landslides labelled 'structured deposit with debris apron' from Quantin *et al.* [2004a]; I also included data of martian landslides from Mcewen [1989], Brunetti *et al.* [2014] and Lucas *et al.* [2014]. Data entries are showed in Appendix Table 1.

Although in a plot H/L ratio versus volume there is a trend of decreasing H/L ratio with increasing volume, the large scatter of the points suggests that other

variables affect the mobility of landslides. Contrary to Hsü [1975] and Davies [1982], who showed that the height drop has secondary importance in the total runout distance, recent numerical simulations of landslides by Johnson and Campbell [2017] and Johnson and Sori [2020] reveal that landslide mobility is also dependent on fall height, in particular that landslides with lower fall heights tend to be more mobile.

The acceleration due to gravity is also expected to affect the mobility of long runout landslides, however its role has always been ambiguous. Mcewen [1989] notes that for long runout landslides of a given volume, terrestrial landslides are more mobile than their martian counterparts. However, it is difficult to explain the change in mobility on the two planets using classical friction models; in reducing the gravitational force, both the normal and shear component reduce proportionally (Figure 2-3), resulting in no overall change. Mcewen [1989] suggests that surface gravity would affect landslides with high yield strength meaning that higher gravity would reduce spreading, thus resulting in longer runout. Legros [2002] argues that this hypothesis contradicts the evidence for a volume-dependent process and that its prediction of the existence of a critical thickness, on which the runout depends, seems unlikely. However, interestingly, Melosh [1983] notes that “although the volume of known long runout landslides varies by several orders of magnitude, the final rock masses all appear to have roughly the same thickness”. It is Johnson and Sori [2020] that propose a link between surface gravity and acoustic energy in order to explain the difference in mobility of landslides on different planetary bodies. They explain that the resulting reduction of mobility with lower surface gravity is due to the fact that the increased timescale of landslides with lower surface gravity allows more time for acoustic energy to radiate away.

Interestingly, the acoustic fluidization mechanism is the only mechanism amongst those proposed to explain the hypermobility of long runout landslides that is able to provide an explanation to the reported effects of volume and gravity on the mobility of such landslides. However, the effect of the volume and gravity on the mobility of long runout landslides still remains

a debated issue, as the acoustic fluidization remains a mechanism that works well theoretically but for which field and experimental evidence is missing.

Table 2-1 – List of major terrestrial, martian and lunar long runout landslides and martian and lunar long runout landslides. The landslides are included in the mobility vs volume plot of Figure 2-4. Landslides in bold with asterisk are case studies of this thesis.

Planetary Body	H (km)	L (km)	H/L ratio	Volume (km^3)	Reference
Earth	1.22	9	0.135	0.28	The Blackhawk landslide [Shreve, 1968a]
	1.9	7.6	0.25	0.38	San Martinez Grande landslide [Bock, 1977]
	1.21	19	0.06	44	The Saidmarreh landslide [Harrison and Falcon, 1938; Roberts and Evans, 2013]
	0.18	1	0.18	0.006	The Oso landslide [Iverson *et al.*, 2015]
	0.6	2.4	0.25	0.01	The Elm landslide [Buss and Heim, 1881; Heim, 1882]
	0.75	2.7	0.27	0.036	The Frank landslide [Cruden and Hungr, 1986; Jones, 1993]
	0.8	**4**	**0.2**	**0.08**	**The El Magnifico landslide*** [Mather *et al.*, 2014; Crosta *et al.*, 2017]
	0.6	5	0.12	0.03	The Sherman glacier landslide [Marangunic and Bull, 1968]
	0.2	1.6	0.2	0.03	Sale Mountain landslide [Zhang *et al.*, 2002]
Moon	**3**	**72**	**0.04**	**3745**	**The Tsiolkovskiy crater landslide*** [Boyce *et al.*, 2020]
	2.2	**10**	**0.22**	**0.06**	**The Light Mantle avalanche*** (Apollo 17 landing site; [Schmitt *et al.*, 2017])
Mars	**4.6**	**63**	**0.07**	**505**	**The Coprates Labes landslide*** [Harrison and Grimm, 2003; Quantin *et al.*, 2004a; Lucas *et al.*, 2011]

2.4.2 High velocity.

Long runout landslides appear to be characterized by velocities of up to several tens of meters per second, both at the early stages of the catastrophic

slope failure [e.g., Hendron and Patton, 1987; Ibanez and Hatzor, 2018] and along the sub-horizontal sector of the runout [e.g., Goren *et al.*, 2010; Roberts and Evans, 2013; Mazzanti *et al.*, 2016; Magnarini *et al.*, 2019]. These velocities are considered extremely rapid for mass-wasting processes.

Velocity estimation of large landslides can be derived from accounts of eyewitnesses, as, for instance, in the case of the Elm landslide [Buss and Heim, 1881]. A common way to provide a minimum constraint of local velocity is using situations where slides run up on, or stop at, obstacles during their motion (Figure 2-5), assuming the complete conversion of the kinetic energy into potential energy, $v_{max} = \sqrt{2gh}$. This method has been used to infer the velocity of the Saidmarreh landslide, Iran [Roberts and Evans, 2013], the Blackhawk landslide, USA [Shreve, 1968a], the Sherman Glacier landslide, USA [Shreve, 1966], and the Heart Mountain landslide, USA [Goren *et al.*, 2010]. The run-up criterion including the influence of the coefficient of friction is instead adopted by Mazzanti *et al.* [2016] to infer the velocity of some martian landslides. In this case, the equation that assumes the complete conversion of the kinetic energy into potential energy appears as $v = \sqrt{2g\,[\mu L_{obstacle} + H_{obstacle}]}$, where $L_{obstacle}$ is the horizontal length of the obstacle and $H_{obstacle}$ is the height of the obstacle, both measured from the base to the summit. In addition, the authors also make use of the curvature of longitudinal furrows to estimate the velocity, which is based on a kinematic model that explains ridge bending effect as a consequence of diminished speed of the landslide. This method assumes a constant slope and a flat basal surface. Model simulations can also provide indication about emplacement velocity. However, as commented by Legros [2002], the value obtained is an overestimation as models usually adopt constant coefficient of friction.

Velocity estimation of long runout landslides has been also derived through energy balance considerations and model simulations of the mechanism proposed [Vardoulakis, 2002]. For instance, theoretical considerations and model simulations of the thermo-poro-elastic mechanism by Goren *et al.* [2010] (Figure 2-21) find a relation between velocity and temperature that is

expected because the process of shear heating depends on the sliding velocity. In doing so, the model predicts the maximum sliding velocity reached by the Heart Mountain landslide. The authors compared this value with the value obtained from the run-up criterion and found very good agreement.

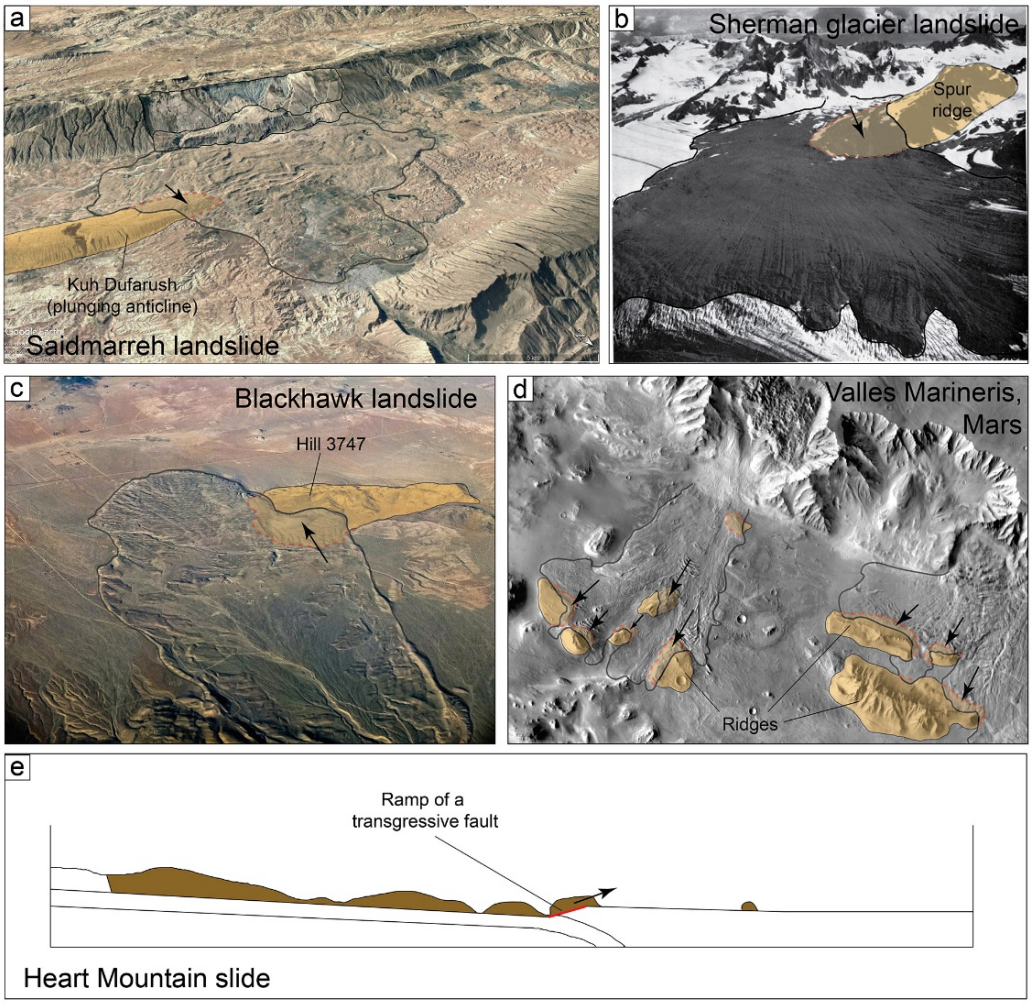

Figure 2-5 - Examples of long runout landslides that run up on, or stop at, obstacles during their motion. The run-up criterion is used to provide a minimum constraint of local velocity assuming the complete conversion of the kinetic energy into potential energy. Black arrows show locations where landslides have run over topographic obstacles. a) The Saidmarreh landslide, Iran; 21 km long; oblique view from Google Earth. b) The Sherman glacier landslide, Alaska; 5 km long; image credit: USGS. c) The Blackhawk landslide, southern California; 8km long; image credit: Lisa McShane Art. d) Landslides in Valles Marineris, Mars; about 70 km long; CTX images. e) Schematic illustration of a cross section of the Heart Mountain landslide, Wyoming; cross section is about 50 km long; modified after Goren *et al.* [2010].

Determining the velocity of long runout landslides relies on indirect methods, which are based on a number of assumptions and/or approximations.

Therefore the values obtained using such methods carry uncertainties, which are on the order of some tens of meters per second, yet they represent really important estimations for understanding the dynamics of long runout landslides.

2.4.3 Preservation of the original stratigraphy and the 'jigsaw' structure of rock masses.

Two distinct characteristics of the internal structure of long runout landslide deposits are: the preservation of the original stratigraphy (i.e., the lithology sequence of the slope prior failure, Figure 2-6) within the final deposit [e.g., Shreve, 1968a; Mcsaveney, 1978; Shaller, 1991; Dufresne *et al.*, 2016]; and the 'jigsaw' structure of deposited rock masses [Shreve, 1959; e.g., Dufresne *et al.*, 2016; Strom and Abdrakhmatov, 2018], that is shattered rock masses with little displacement of fragments (Figure 2-7), originating from high-speed impact of the collapsed slope.

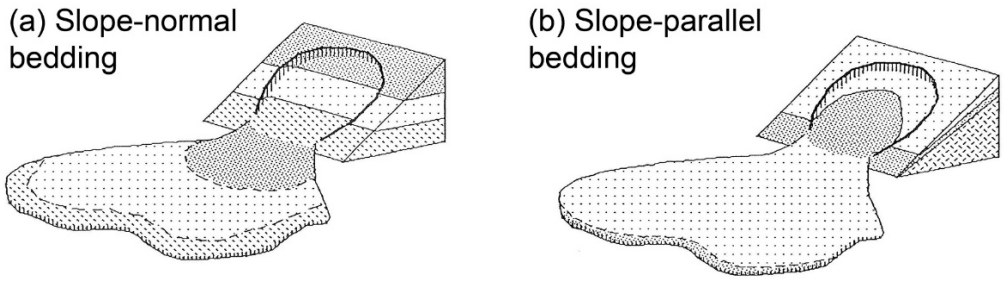

Figure 2-6 – Schematic representation of the preservation of the original stratigraphy in long runout landslide deposits. Modified after Shaller [1991].

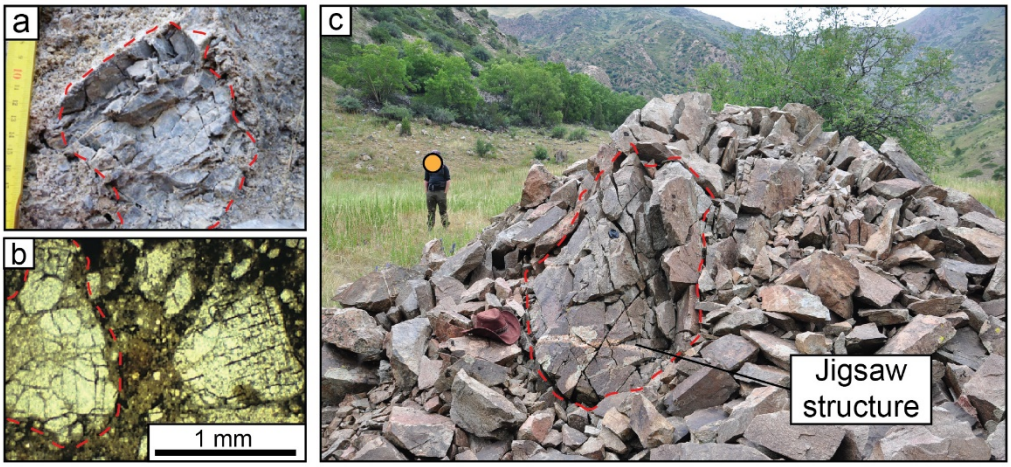

Figure 2-7 – Jigsaw structure. The jigsaw structure is observed in boulders and clasts that are appear shattered but which fragments are not displaced. a) Example of jigsaw-fractured clast in the Tschirgant rock avalanche, Austria (modified after Dufresne *et al.* [2016]). b) Example of a jigsaw-fractured quartz clast in the Dzongri rockslide, India (modified after Weidinger *et al.* [2014]). c) Example of jigsaw-fractured boulder at the Seit rock avalanche, Kyrgyzstan (hat and lens-cap for scale).

These observations provide constraints on the kinematics of long runout landslides, suggesting that the landslides moved with no turbulence and that there is no large-scale mixing of the debris during emplacement. However, views on the mode of motion are divisive, with some authors supporting the idea that the landslides move as a rigid plug atop an active shearing basal layer [e.g., Davies, 1982], whereas others support the idea that the entire sliding mass undergoes some degree of shear during the emplacement [e.g., Dufresne *et al.*, 2016].

Interestingly, landslide modelling by Campbell *et al.* [1995] and Johnson *et al.* [2016a] are able to reproduce the preservation of the initial stratigraphy in the final deposit (Figure 2-8) and show that the entire mass is shearing and it is not moving as a rigid block over a lubricant surface. Although the mechanism for the reduction of friction remained undetermined, Johnson *et al.* [2016a] show that their results are in agreement with the predictions of the acoustic fluidization hypothesis [Melosh, 1979].

The preservation of the original stratigraphy and the presence of 'jigsaw' boulders are considered an hallmark of terrestrial long runout landslide deposits and eventually any the mechanism proposed to explain the hypermobility of long runout landslides has to be able also to explain how

these characteristic internal structures are formed. Currently, in the literature there is no agreement on the way shear is distributed internally during the emplacement of long runout landslide, therefore the way the internal structures are generated and preserved is still an open question.

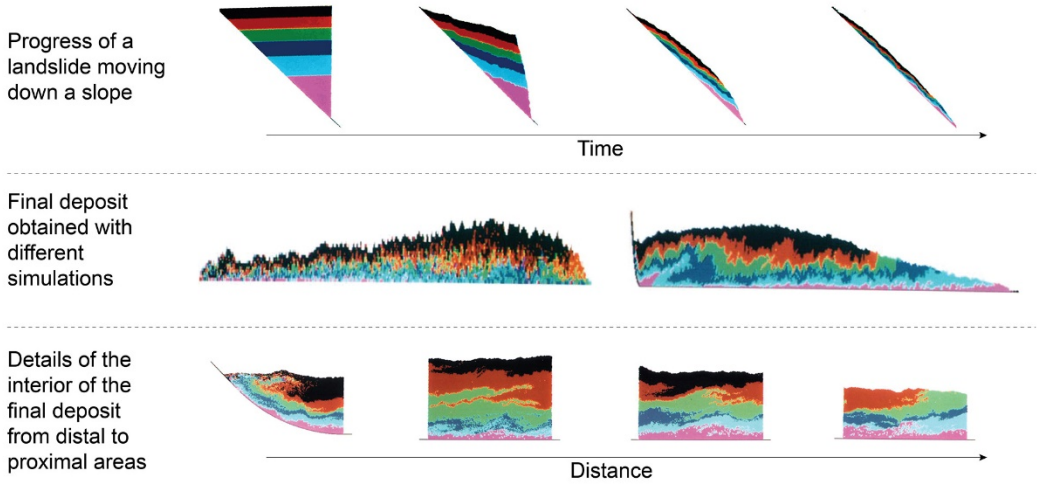

Figure 2-8 – Computer simulation of large landslides. Results of the computer simulations of long runout landslides run by Campbell *et al.* [1995]: the simulation describes the motion of a large number of disc-shaped particles; moreover, the simulation permits static assemblages of particles such as will be found at the start and stop of the landslide; it assumes volume conservation. Note the preservation of the initial strata in the final deposits. The preservation of the original slope stratigraphy in the final landslide deposit is reported in natural landslides and it is considered evidence of lack of turbulence and lack of large-scale mixing of the debris during emplacement.

2.4.4 Longitudinal ridges.

Long runout landslides exhibiting longitudinal ridges are widespread in the Solar System (Figure 2-9 to Figure 2-14).

Since the report of long runout landslides on Mars [Lucchitta, 1978a; 1979], well-preserved longitudinal ridges have been observed ubiquitously on the surface of martian deposits (Figure 2-9).

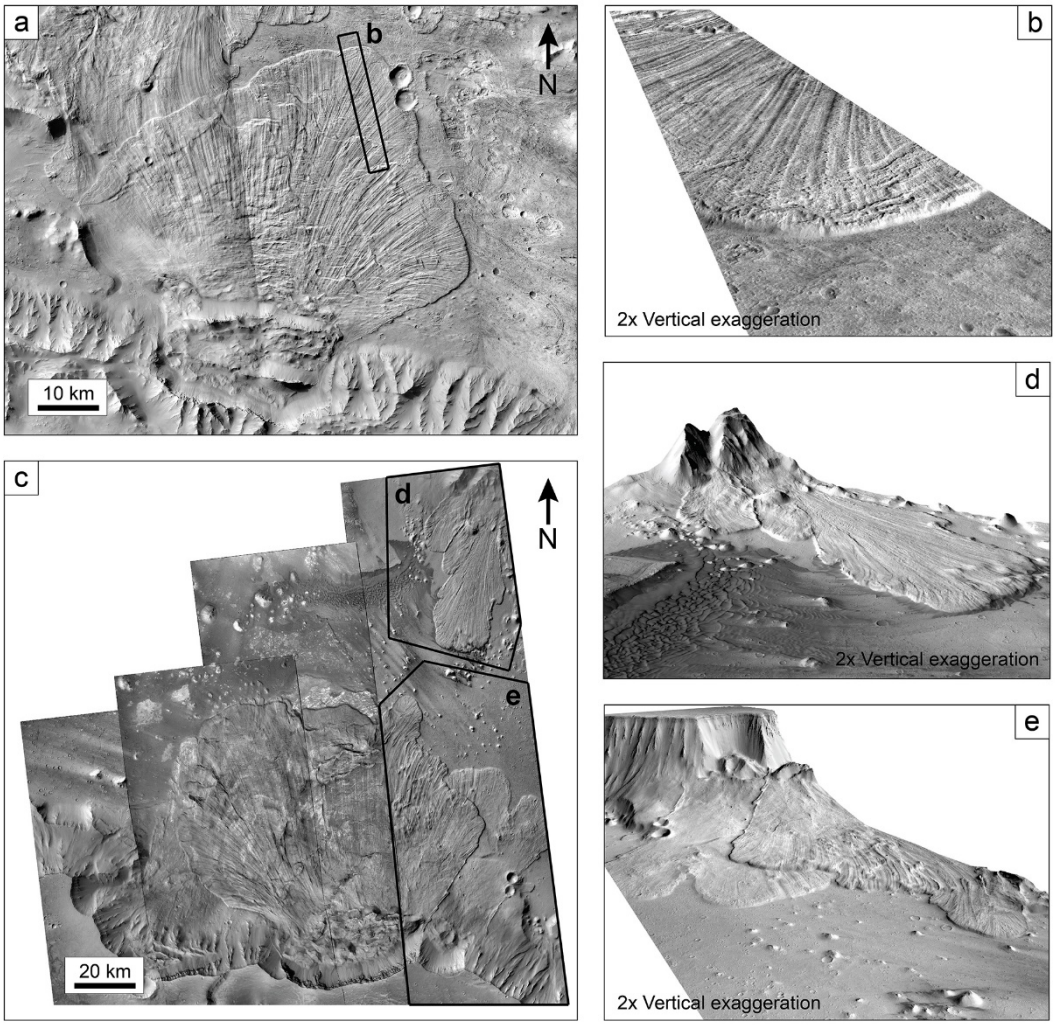

Figure 2-9 – Martian long runout landslides exhibiting well-preserved longitudinal ridges. a) Image mosaic of Coprates Labes landslide, in Coprates Chasma (11.76°S 67.73°W). c) Image mosaic of landslides in Ganges Chasma (8.41°S 44.64°W). Landslides in a) and c) appear in the very first publications concerning martian long runout landslides [Lucchitta, 1978a; 1979]. b) Oblique view of the terminal edge of the Coprates Labes landslide shows details of the longitudinal ridges (HiRISE orthoimage PSP_009763_1685 overlapping a DEM I made using HiRISE image pair PSP_009763_1685/PSP008906_1685). d) and e) are oblique views of some of the landslides in Ganges Chasma (CTX orthoimage P20_009037_1718 overlapping a DEM I made using CTX image pair P20_009037_1718/P20_008681_1722).

This type of ridge has been also mapped in long runout landslides on the dwarf planet Ceres ([Schmidt *et al.*, 2017]; Figure 2-10) and observed in the Tsiolkovsky crater landslide, on the far side of the Moon ([El-Baz, 1972]; Figure 2-11). Although less prominent than the previous examples, longitudinal ridges on the surface of the landslide at the Apollo 17 landing site are described by El-Baz [1972] and Schmitt *et al.* [2017] (Figure 2-12).

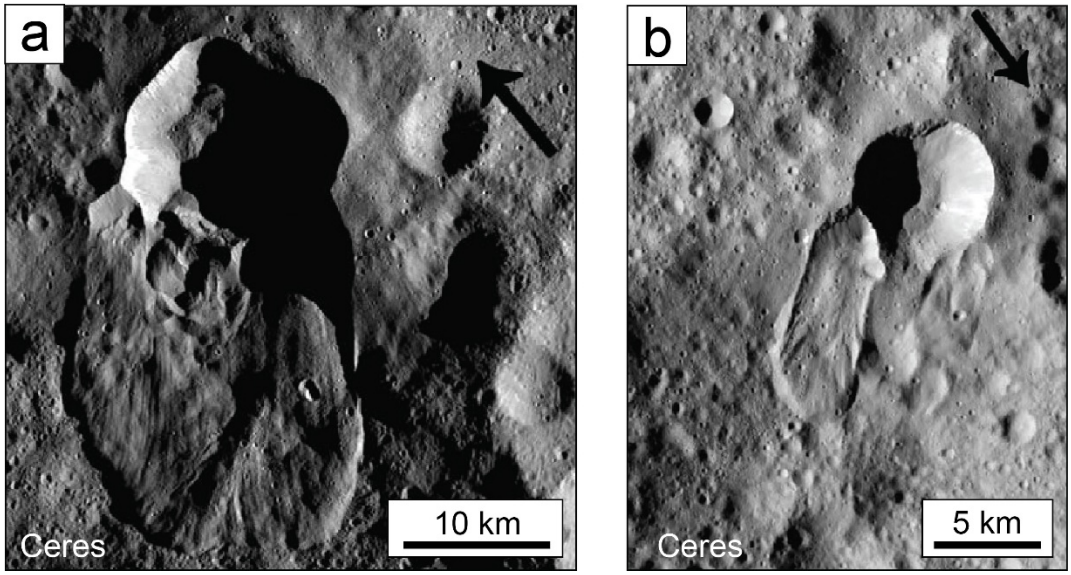

Figure 2-10 – Cerean long runout landslides exhibiting longitudinal ridges. a) and b) Long runout landslides on Ceres (modified after Schmidt *et al.* [2017]).

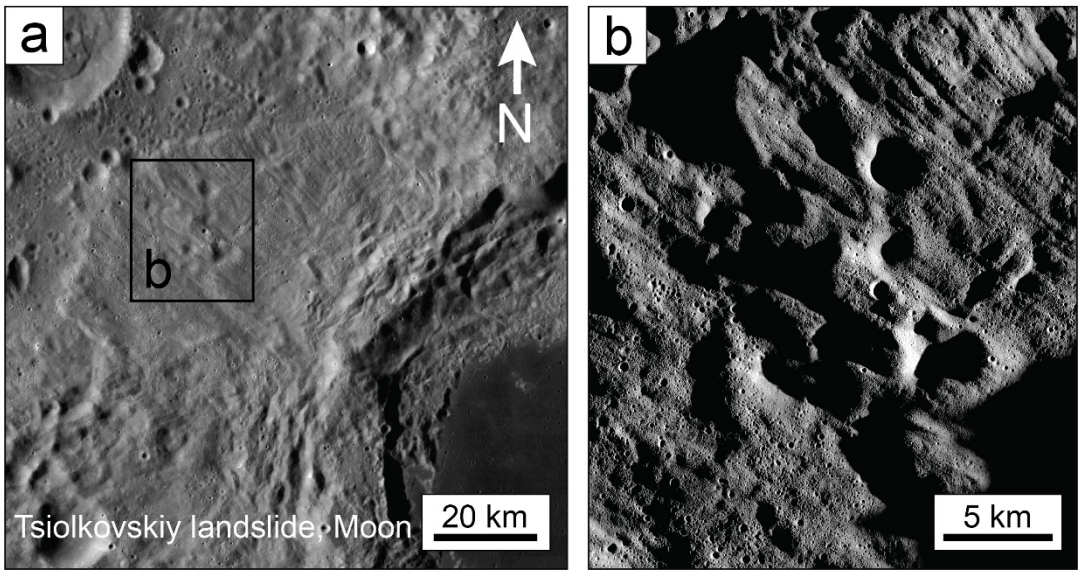

Figure 2-11 – Lunar long runout landslide exhibiting longitudinal ridges: the Tsiolkovskiy crater landslide. a) North sector of the Tsiolkovski crater landslide, on the far side of the Moon. b) Details of the surface of the Tsiolkovski crater landslide (courtesy of Joseph M. Boyce, University of Hawaii).

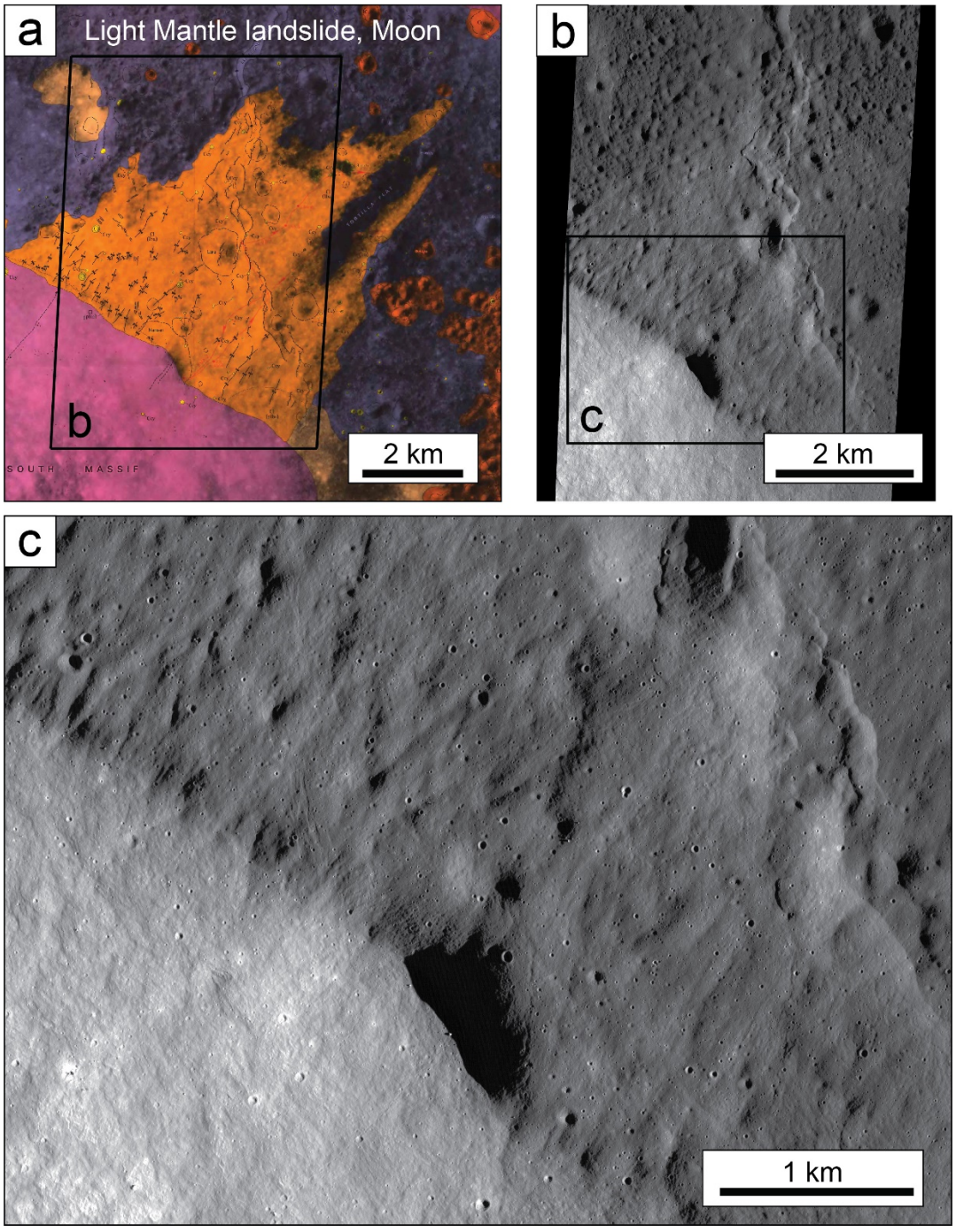

Figure 2-12 – Lunar long runout landslide exhibiting longitudinal ridges: the Light Mantle landslide. a) Detail of the USGS geological map of the Apollo 17 landing site [Wolfe *et al.*, 1981, Plate 2], in which longitudinal troughs (thus locating ridges in between them) are mapped as black lines with mirrored triangles in the centre. b) Low-sun LROC NAC image M1276388423R (courtesy of Noah Petro); longitudinal ridges are visible at the base of the South Massif (bright area in the lower part of the image). c) Close-up view of the base of the South Massif in the low-sun LROC NAC image in b).

In Singer *et al.* [2012], longitudinal ridges were not mapped in long runout landslides on Iapetus and Rhea. However, in two of the landslides on Iapetus (Figure 2-13a and b) and one landslide on Rhea (Figure 2-13c; [Singer *et al.*,

2012], especially, longitudinal ridges are shown in the images from the Cassini mission. The landslides were identified using Cassini mission images with a resolution of 450 m/px and 870 m/px. Such resolution may not be sufficient to unequivocally resolve longitudinal ridges, however illumination conditions may allow to infer they existence through casted shadows.

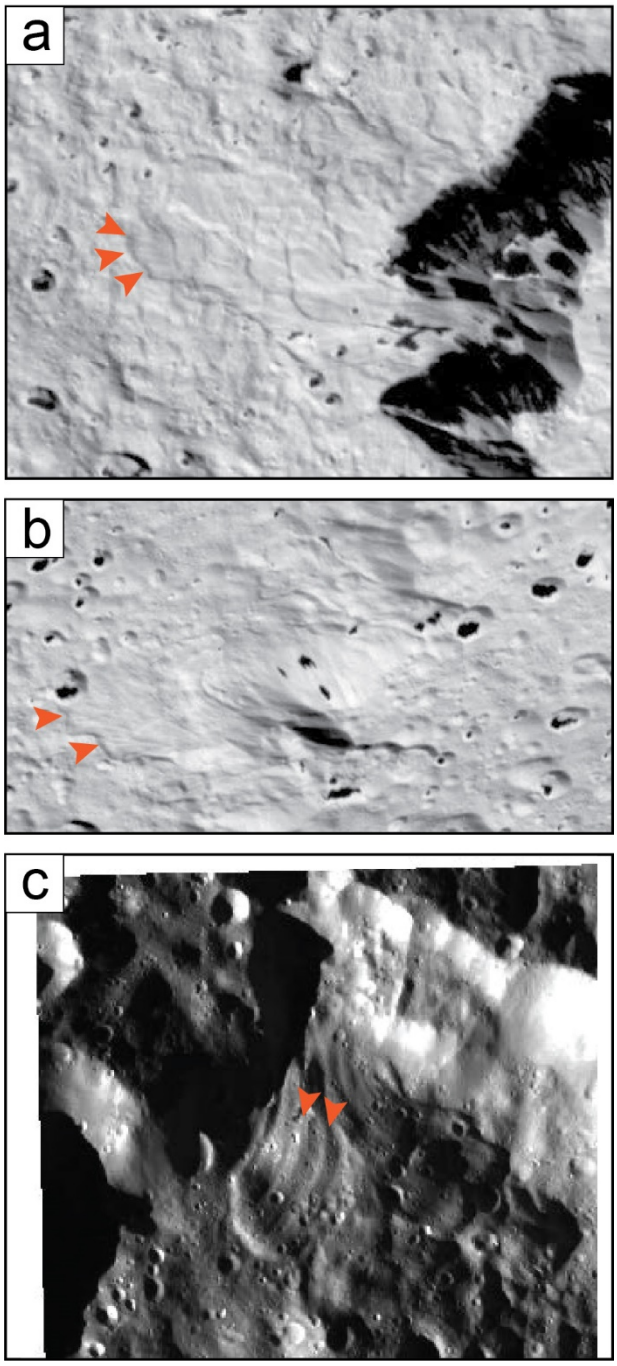

Figure 2-13 – Possible existence of longitudinal ridges in landslides on Iapetus and Rhea. a) and b) show long runout landslides on Iapetus. c) shows a long runout landslide on Rhea. Orange triangular arrowheads points at locations where I suggest that longitudinal ridges are visible exploiting illumination conditions that allow shadows to be casted. Images are extracted from Singer *et al.* [2012 and Supplementary Material]

Longitudinal ridges have not been identified in long runout landslides on Charon [Beddingfield *et al.*, 2019]. In this work, landslides were identified using the Long-Range Reconnaissance Imager (LORRI) on board the New Horizons mission. The images were captured with a resolution from 1 km/px to as good as 157 m/px. A lack of sufficient resolution may be the reason why no longitudinal ridges were neither mapped nor imaged.

On Earth, longitudinal ridges are commonly, but not exclusively, observed in landslides emplaced on glaciers. The most iconic example is the Sherman Glacier landslide ([Shreve, 1966; Marangunic and Bull, 1968]; Figure 2-14).

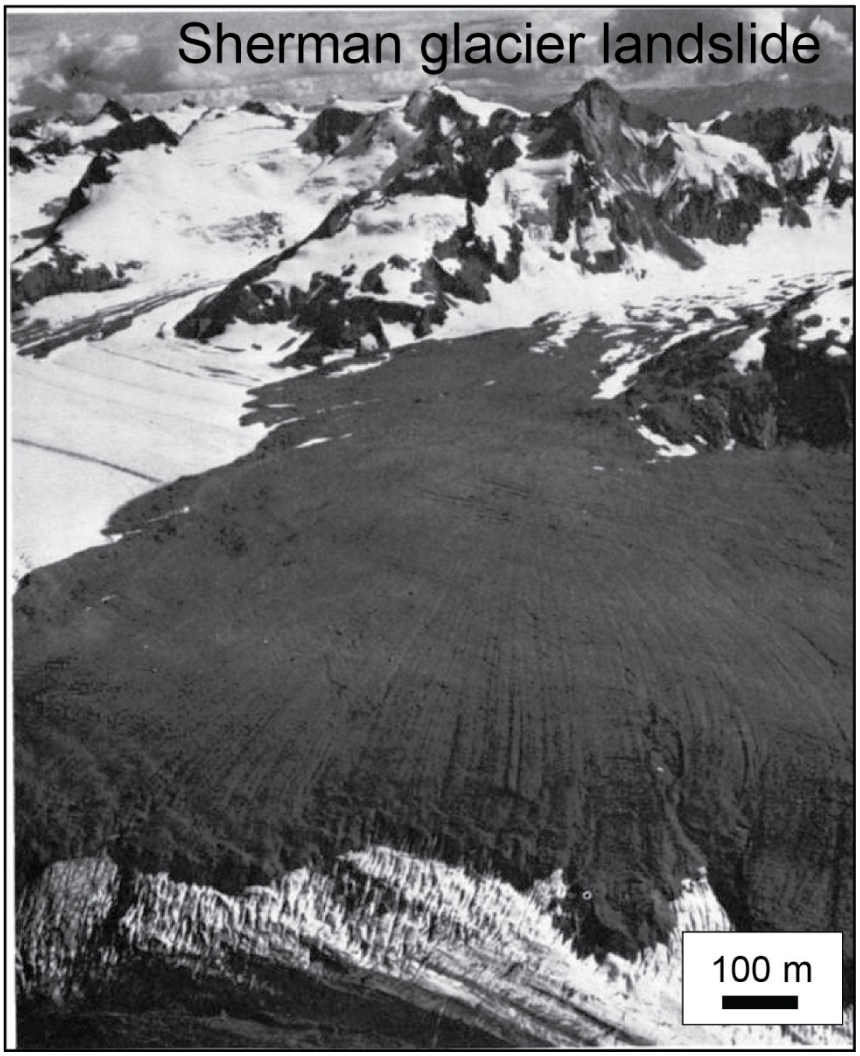

Figure 2-14 – Terrestrial long runout landslides emplaced on glaciers exhibiting longitudinal ridges: the Sherman glacier landslide, Alaska. The Sherman Glacier landslide, Alaska, USA (photo by USGS).

Given the similarity in morphology, the occurrence of longitudinal ridges in martian landslides was initially associated with the presence of an icy substrate at the time of landslide emplacement [Lucchitta, 1979; De Blasio, 2011]. Few papers to date have attempted to define a model for the formation of longitudinal ridges in long runout landslides. Based on laboratory experiments and field observations, Dufresne and Davies [2009] concluded that formation of longitudinal ridges is the result of the fragmentation of the flowing mass due to failure in extension caused by the material moving with high velocity accompanied by a modest lateral spreading (Figure 2-15). In addition to emplacement velocity and direction, they recognized the importance of the frictional behaviour of the material, the angularity and size variety of clasts, the emplacement geometry and flow cross section, and the influence of substrate on the flow dynamics.

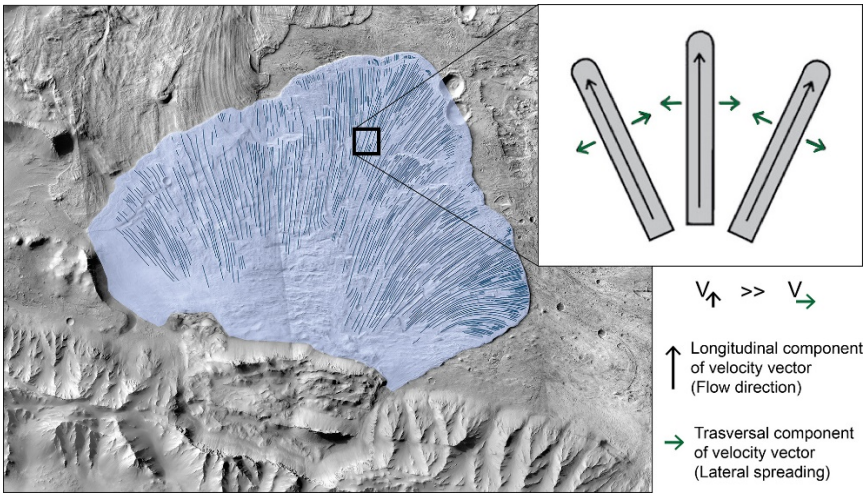

Figure 2-15 – The formation of longitudinal ridges according to Dufresne and Davies [2009]. The formation of longitudinal ridges is favoured when the longitudinal component of the landslide velocity vector is much larger than the transversal component of the velocity vector (top-right inset modified after Dufresne and Davies [2009]). The authors identify rock avalanches emplaced on glaciers, snow and ice avalanches, and volcanic debris avalanches as high-velocity events in which longitudinal ridges are most prominent. (The main figure shows the Coprates Labes landslide in Valles Marineris, Mars, with mapped deposit and longitudinal ridges as visual aid to identify velocity vector components).

However, field observations made by Dufresne and Davies [2009] include remnant structures nowadays covered by vegetation. The authors do not mention the possible effect of erosion on modifying the original morphology,

yet it should be an important aspect that cannot be ignored, especially in terrestrial cases, as this could lead to misinterpretation of the geomorphological record. Instead, De Blasio [2011] suggests that the formation of longitudinal ridges is the consequence of the tearing apart of the flowing mass by lateral spreading (Figure 2-16). They define that the condition necessary for ridge formation is the presence of soft terrains, such as ice, water, and/or evaporates, which can provide strong lubrication.

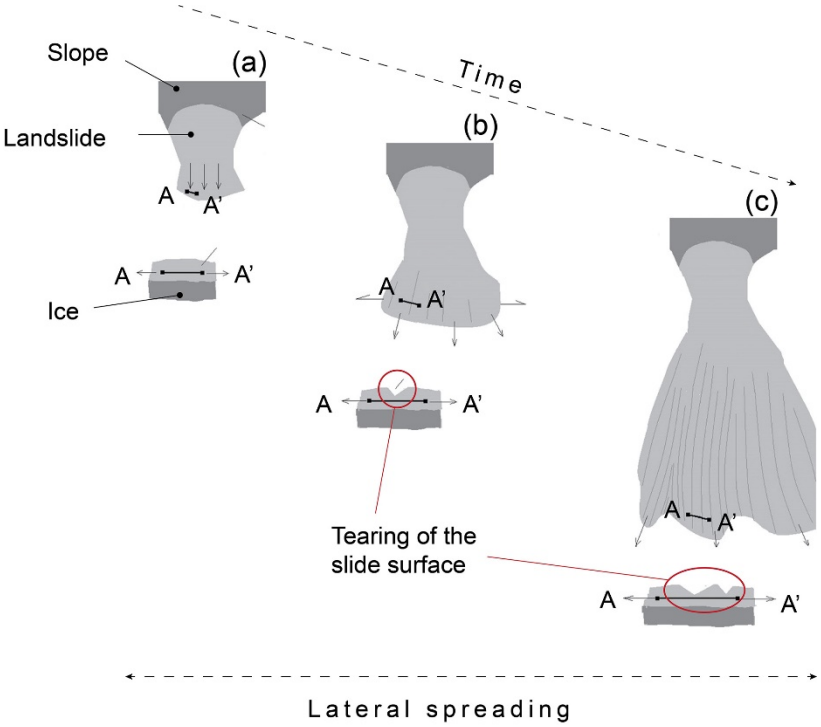

Figure 2-16 – The formation of longitudinal ridges according to De Blasio [2011]. Conceptual model for the formation of longitudinal ridges (modified after De Blasio [2011]). Troughs form as a result of the tearing apart of the slide that moves over a soft-material base.

However, there are terrestrial long runout landslides that were not emplaced on an icy surface, and still exhibit longitudinal ridges. Among these cases is the rock avalanche cluster El Magnifico, Chile ([Mather *et al.*, 2014; Crosta *et al.*, 2017]; Figure 2-17b), the Chaartash-3 (Kyrgyzstan, Central Asia; Figure 2-17d), and the Blackhawk landslide (California, USA; Figure 2-17c). It must be mentioned that the original topographies of the Blackhawk and Chaartash-3 landslides have been affected by alluvial deposition as well as by erosion,

resulting in current morphologies that do not necessarily accurately represent the original surfaces, therefore leaving uncertainties about their interpretation as primary features of the landslide deposits.

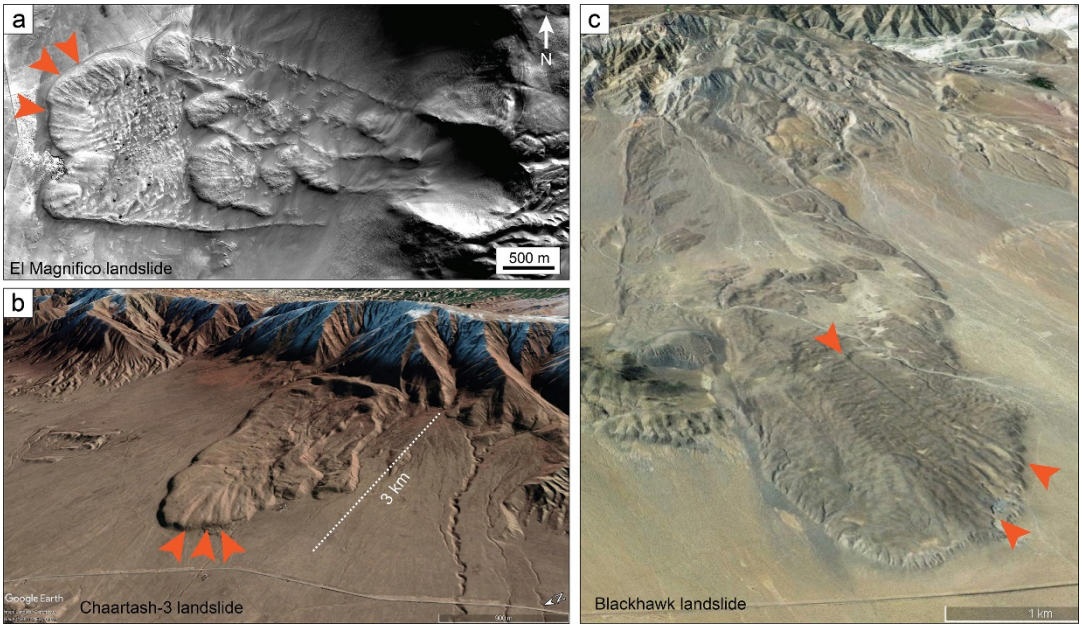

Figure 2-17 – Terrestrial long runout landslides not emplaced on glaciers and exhibiting longitudinal ridges. a) The El Magnifico landslide, Chile (© CNES, 2013, distribution Airbus Defence and Space). b) Chaartash-3 landslide, Kyrgizstan, (Google Earth image). c) The Blackhawk landslide, California, USA; the visible deposit is about 8 km long (Google Earth image).

In addition, the presence of extensive ice at the time the lunar landslide took place at the Tsiolkovsky crater can be excluded, further supporting the idea that the presence of ice is not a necessary condition for the development of longitudinal ridges [Boyce *et al.*, 2020]. Evidence of longitudinal ridges in long runout landslides that certainly have not emplaced on ice should motivate research on the formation mechanism of such structures, as the necessity of a basal icy surface is controversial.

In conclusion, longitudinal ridges are observed in long runout landslides on a number of rocky planetary bodies that have been imaged with sufficient resolution, suggesting the ubiquity of such morphological features in the Solar System. Despite longitudinal ridges are commonly reported in terrestrial long runout landslides emplaced on glaciers, they are not exclusive of a glacial

environment. Compared to martian long runout landslides, terrestrial landslides exhibiting longitudinal ridges may appear scarce. Such observation might suggest that longitudinal ridges are not an ubiquitous feature in terrestrial landslides. However, tens of landslides characterised by longitudinal ridges are easily identifiable in Iceland, where currently there is no ice (Figure 2-18). Such further observation suggests that indeed there is no reason to consider longitudinal ridges not common on Earth, rather their record is more easily lost on our planet.

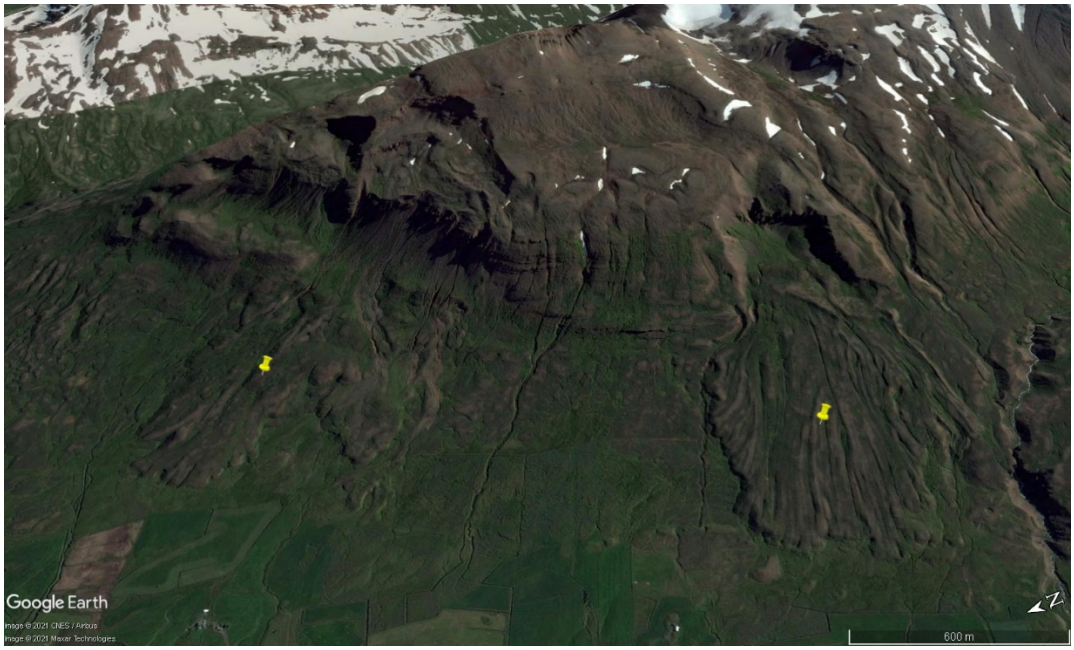

Figure 2-18 – Example of long runout landslide exhibiting longitudinal ridges in Iceland. Tens of landslides with longitudinal ridges are easily identifiable in north Iceland. This is an oblique view taken from Google Earth. Left landmark: 65°55'06'' N 18°30'52" W. Right landmark: 65°54'10"N 18°32'12" W.

2.5 The role of fluids and their origin.

Note to clarify the terminology used in this section. The term 'fluid' can refer to both a liquid or a gas phase. The term 'wet' is used to refer to the presence of liquid water within a sliding mass and it can refer to any degree of saturation of the sliding mass. The term 'dry' is used for landslides for which there is no evidence of the presence of a fluid. The term 'fluidization' refers to the process

that allows a landslide to have a dynamic fluid-like behaviour and does not refer to the agent that cause such behaviour. Therefore, the terms 'wet' and 'dry' are used to specify whether the fluidization is caused by water or by fine particles, respectively.

As the addition of an interstitial pressurized fluid reduces the effective coefficient of friction of a granular material by partly supporting grains, thus reducing the normal stress, $\tau = \mu(\sigma_N - p)$ (Figure 2-19; [Terzaghi, 1943]), many authors have suggested that interstitial fluids play a significant role in the emplacement of long runout landslides. However, cases such as the Elm landslide [Heim, 1882] and the Blackhawk landslide [Shreve, 1968a] show lack of evidence for the presence of fluids during emplacement. The importance of fluids in landslide mobility has been particularly questioned since the discovery of long runout landslides on the Moon [Howard, 1973] and on Mars [Lucchitta, 1978a; 1979; Mcewen, 1989]. This has led some authors to explore the possibility that landslides can travel as dry granular flows, without the need of any interstitial fluid [Hsü, 1975; Melosh, 1979; Davies, 1982; Davies and Mcsaveney, 2002; Collins and Melosh, 2003; Davies and Mcsaveney, 2009].

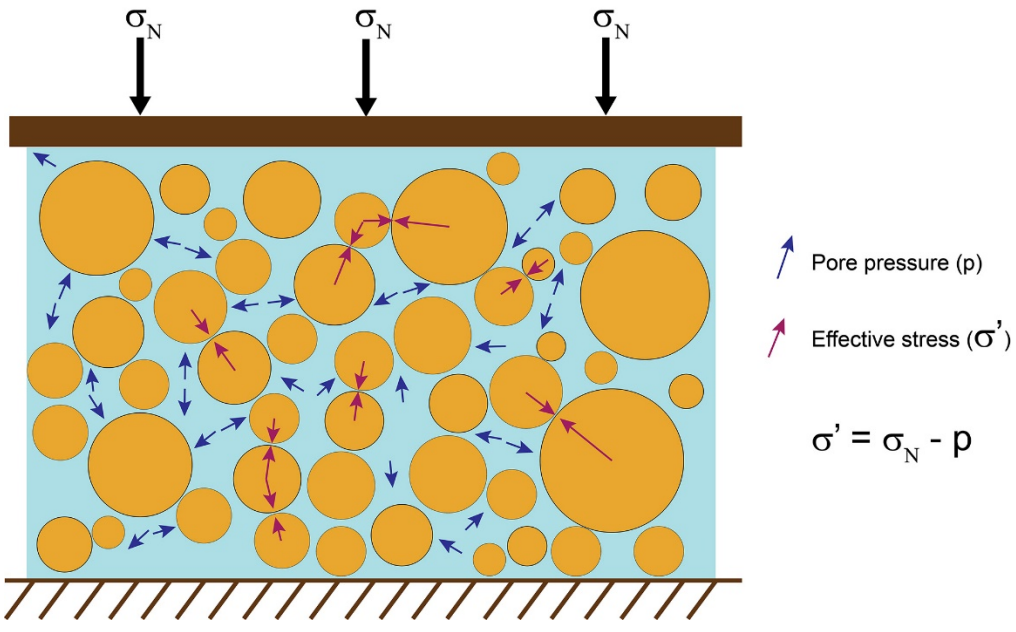

Figure 2-19 – Pore pressure reduces normal stress. Pressurized fluids decrease shear resistance by decreasing normal stress.

Water in liquid or vapour state is expected to be generated through the frictional heating that accompanies these catastrophic events. Frictional heating is expected to melt the ground ice present within the collapsing slope, allowing liquid water to enter the sliding mass. Frictional heating is also expected to affect the surface material over which the slides move. For instance, it would affect an icy surface by partially melting it and so generating a thin surface of pressurized water at the base of the slide, which would reduce the coefficient of friction [e.g., Singer *et al.*, 2012]. Moreover, frictional heating is expected to lead to dehydration of hydrated minerals [Brantut *et al.*, 2008; Brantut *et al.*, 2011a; Watkins *et al.*, 2015; 2020], so fluids can be produced in nominally 'dry' lithologies by the chemical dehydration of hydrous rocks, e.g. clays.

On Earth it is well known that long runout landslides can develop from both dry and wet rock sources. For instance, the ancient Marcus landslide [Douglass *et al.*, 2005] is an example of a landslide that quickly transformed into a debris flow. Similarly, the Carlson landslide, began as a dry rock avalanche and evolved into a large debris flow [Shaller, 1991]. Incorporation of saturated valley sediments or direct mixing with water from a river is likely to play a very important role in fluidization of landslides, as in the case of the gigantic Saidmarreh landslide in Iran [Harrison and Falcon, 1938; Watson and Wright, 1969; Roberts and Evans, 2013], the Hítardalur landslide in West Iceland [Helgason *et al.*, 2019], and the Oso landslide in the State of Washington, USA [Iverson *et al.*, 2015]. In contrast, some examples of large terrestrial landslides have been described as dry, such as the Elm landslide [Heim, 1882], the Blackhawk landslide [Shreve, 1968a; Shaller, 1991], the El Magnifico landslide [Mather *et al.*, 2014; Crosta *et al.*, 2017], and four rock avalanches in Sierra Aconquija, Argentina [Fauque and Strecker, 1988].

2.5.1 The role of water in landslides on Mars.

The debate regarding whether long runout landslides are emplaced dry or with support of a fluid has become central in martian geomorphological studies. Martian landslides are characterized by a long runout and lobate

debris aprons, features that are considered evidence of fluidization mechanisms, either by water or by dry fluidization. This dualism has seen authors taking sides based on different lines of evidence. For instance, according to Lucchitta [1978a; 1987], based on morphological comparison with terrestrial landslides, landslides in Valles Marineris involved a flow of motion of debris lubricated by water. On the contrary, Mcewen [1989] suggested a dry origin for landslides in Valles Marineris based on the similarity between the 'H/L ratio vs volume' trend of martian landslides and terrestrial dry rock avalanches. Instead, based on a combination of terrestrial field work evidence and image analysis, Shaller [1991] disagreed with both interpretations, suggesting that martian landslides most likely travelled in a moist state. As discussed by Legros [2002], "there must be a continuum of water saturation between hypothetical dry landslides and saturated debris flows". Pudasaini and Miller [2013] propose a parameter that represents the degree of fluidization, either wet or dry. The authors find that long runout landslides formed in different environments are characterized by different degrees of fluidization: fluidization is limited in extra-terrestrial events, significant in non-volcanic and volcanic events, and dominates submarine events. Despite the numerous studies published, the role of water in martian landslide dynamics is currently not unanimously agreed.

Water, as a lubricating and fluidization factor in mass-wasting systems, can have different origins. Terrestrial landslides can entrain water during the motion through entrainment of saturated valley floor sediment or water directly from rivers, or through entrainment and melting of snow, ice, and permafrost. On Earth, it is well known that precipitation increases the level of saturation of slopes, increasing their propensity to fail. However, lack of evidence of heavy rain falls in the history of Valles Marineris, on Mars, tends to exclude rain as origin for possible water content within the canyon walls. Alternatively, water is expected to be stored as both ground water and ground ice, which current climate models predict to exist at the depth at which slope failures occurred [Clifford *et al.*, 2010; Andrews-Hanna and Lewis, 2011]. Salese *et al.* [2019] provide evidence for the expected deep water table by studying water-related landforms within impact craters. Interestingly, Salese

et al. [2019] notes that landslides inside a number of craters at mid-latitudes become more plastic and display flow structures at a consistent elevation that the authors link to the existence of a stationary water level. The past existence of lacustrine environments has been demonstrated in Valles Marineris [e.g., Lucchitta, 2010; Davis *et al.*, 2018] and long runout landslides have been suggested to represent subaqueous, or partially so, landslides in Valles Marineris [De Blasio, 2011]. Past existence of ice in form of extensive glaciers is suggested at equatorial and low latitudes on Mars [Mège and Bourgeois, 2011; Gourronc *et al.*, 2014; Stucky De Quay, 2014]

Given the rising evidence for a complex evolution of the martian climatic history (i.e., although showing an undeniable global trend of transitioning from wet to hyperarid, it is expected that the martian climate had regional and local diversity [e.g., Kite *et al.*, 2011; Davis *et al.*, 2018; Sejourne *et al.*, 2019]) and given the latitudinal variability in sub-surface ice content (i.e., sub-surface ice increases moving towards the poles [e.g., Head *et al.*, 2003; Sejourne *et al.*, 2019]), martian landslides ought to be expected to reflect such diversity in terms of water content and the polarized debate ‘wet or dry’ should be considered anachronistic.

2.6 Factors and mechanisms to explain the behaviour of long runout landslides.

Although some studies adopt the hypothesis that there is a single mechanism for the formation of long runout landslides that applies to all situations, it is possible that instead different mechanisms operate in different circumstances. Under this perspective, no mechanism should be discarded until is able to reproduce field observations of at least one case. Indeed, such approach feels reasonable in the light of the fact that long runout landslides occur in disparate terrestrial environmental conditions (e.g., subaerial continental, subaerial volcanic, submarine, hyperarid climate, glacial environment) and disparate planetary bodies. Thus, long runout landslides

may not be attributable to a single and unique process. Moreover, it may be that more than one mechanism is involved during their emplacement.

Numerous mechanisms have been proposed to explain the high mobility of long runout landslides. They can be grouped in 4 main categories [Mckinnon, 2010]:

I. Mechanisms that invoke the physical consequences of volume.
II. Geomorphological controls on the runout path.
III. Mechanisms responsible for the reduction of internal friction.
IV. Mechanisms responsible for the reduction of basal friction.

Eventually, proposed mechanisms have to provide an adequate explanation of the characteristic features of long runout landslides, such as those discussed in Section 2.1.1.

Here, follow some of the mechanisms that are most relevant to this thesis. A more exhaustive list of the mechanisms proposed in the literature is provided at the end of this section (Table 2-2).

2.6.1 Physical consequences of volume.

As field data demonstrate that the mobility of long runout landslides increases with increasing volume, understanding whether this correlation derives from the effects of a volume-dependent mechanism or reflects a purely geometrical correlation has been the focus of several studies [e.g., Davies, 1982; Okura *et al.*, 2000; Lajeunesse *et al.*, 2006; Staron and Lajeunesse, 2009; Holsapple, 2013; Lucas *et al.*, 2014]. Davies and Mcsaveney [2002; 2012] argue that the process of mechanical fluidization satisfactorily explains the volume effects seen in long runout landslides, as the increase in areal dispersion of the debris is the result of its fragmentation. With the purpose to clarify the effects of rockfall volume on runout distance, Okura *et al.* [2000] carried out outdoor rockfall experiments using cubic blocks of granite and numerical simulations (Figure 2-20).

They show that, in a setting where blocks at the front accelerate more than the rear blocks, increasing the number of blocks increases the frequency of collisions between the blocks, resulting in the front-arranged blocks to be pushed further by an increase in acceleration. According to Lajeunesse *et al.* [2006], the increase of landslide mobility with volume is a simple consequence of volume conservation. However, their conclusions should be taken with caution as they are drawn from experimental granular column collapse that, as the same authors state, are not meant to capture the whole complexity of natural landslides. In fact, the experimental granular collapses performed exhibit several obvious differences, such as differences of several order of magnitude in volume and the type of material involved (i.e., dry monodisperse granular material is used to represent real landslide lithology and grain size involved).

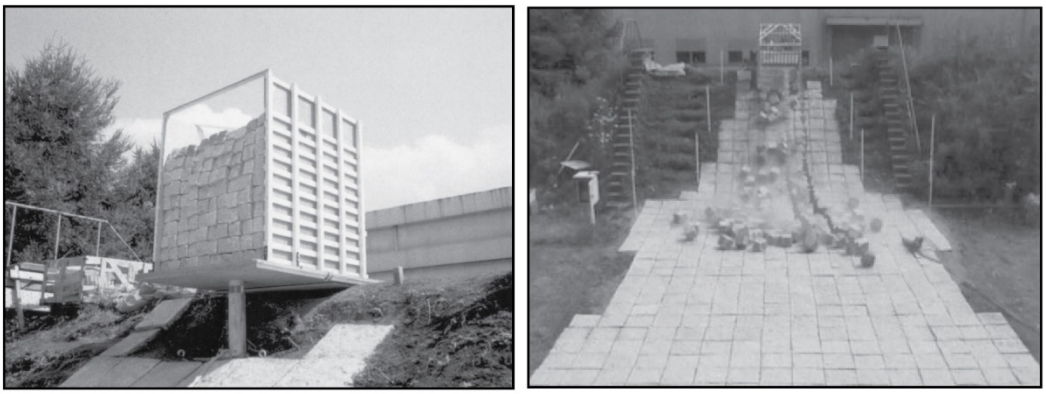

Figure 2-20 - Rockfall-inducing apparatus used to study the effect of volume on runout distance. From Okura *et al.* [2000].

Also Staron and Lajeunesse [2009] suggest that the correlation between the mobility of long runout landslides and volume does not contain any information about the dynamics of the flow, rather it is a purely geometrical correlation. In this case, their argument is suggested by the two power-laws derived from dimensional analysis of field data ($L \propto V^{1/3}$ and $L \propto A^{1/2}$). In their opinion, searching for a volume-dependent mechanism is not a well-posed problem.

However, in their simulated slides, Johnson and Campbell [2017] shows that the mobility increase with increasing volume when considering a rheology where shear stresses increase with increasing shear rate faster than normal stresses increase. The correlation between the mobility and the volume is also consistent with the predictions made by the mechanism of acoustic fluidization (see Section 2.4.4; [Melosh, 1979; Collins and Melosh, 2003; Johnson *et al.*, 2016a]. Also, Campbell *et al.* [1995] show that the coefficient of friction decreases monotonically with landslide volume, indicative that its reduction is due to some physical mechanism and not simply by spreading of the granular mass. Instead, Lucas *et al.* [2014] propose the novel idea that correlates the sliding velocity and the volume, interpreting the decrease of the friction coefficient with volume as a velocity-dependent frictional weakening process (see Section 2.5.3).

The increase of mobility with increased volume by entrainment of debris is critical to the dynamics of rock avalanches. Rock avalanches increase their volume by means of fragmentation [Hungr, 1981] and entrainment of valley floor material [Hutchinson and Bhandari, 1971]. Hungr and Evans [2004] illustrate the mechanism of material entrainment in several steps, which has different characteristics depending on relative quantities of rock and saturated material and the valley profile shape. The sequence of events suggested is: a rapidly moving landslide impacts relatively loose, saturated sediments on the valley floor at the base of the slope; following the impact, such saturated sediments liquefy, partially or completely, therefore loosing strength; part of the liquefied material is pushed forward and part of it is overridden by the landslide; as a consequence, the landslide moves over a cushion of liquefied soil. This allows the landslide to reach further distances that those predicted by a dry frictional model. According to [Hungr and Evans, 2004], the hypothesis of lubrication by entrainment of saturated soil can also explain the apparent increase of mobility with volume. The larger is the volume of a landslide the higher is its potential to excavate deeper into thicker alluvial saturated material at the base of the slope, whereas a smaller landslide would only be able to entrain coarser and dry sediments forming the top part of the slope and valley floor.

Watkins *et al.* [2015] also show the presence of clay minerals in material entrained in five long runout landslides in Valles Marineris, on Mars. Similarly to the sequence of events proposed by Hungr and Evans [2004], Watkins *et al.* [2015] propose that the alteration of Valles Marineris wall rock formed a talus constituted of clay minerals; subsequently, the emplacement of long runout landslides overrode and entrained the hydrated-silicate-bearing floor deposits, causing further loss of coherence, due to high shear strain. This allowed landslides to move over a low-friction clay-bearing surface that facilitated the long runout.

2.6.2 Geomorphological control.

Several studies have tried to assess the influence of scar geometry and topography on landslide dynamics and deposit morphology. Lucas and Mangeney [2007] perform a series of numerical simulations to investigate the effects of topography on the behaviour of landslides in Valles Marineris, Mars. The authors conclude that topographic effects cannot explain the high mobility of martian landslides, therefore a key contribution to landslide dynamics is expected from other physical and/or geological processes. Similarly, Lucas *et al.* [2011] show that the runout distance is little affected by the change in the geometry of the initial scar, which instead affects the overall geometry of the landslide deposit, assuming the absence of lateral and frontal confinement of the slide.

The scope of Lucas and Mangeney [2007] and Lucas *et al.* [2011] is primarily understanding the role of the scar geometry and the topography, so to provide a stronger calibration of the rheological parameters (e.g., friction coefficients and area of the deposit) involved in numerical modelling, which have been largely calibrated using runout distance. As remarked by Lucas *et al.* [2011] in their work on martian landslides, the geometry of the sliding surface is not trivial to assess because of the effect of erosion and insufficient availability of topographic data prior slope failure. This has major importance in the evaluation of the volume of the slope involved in the landslide, which is a fundamental input in numerical models.

2.6.3 Reduction of basal friction.

Mechanisms that cause a reduction of basal friction involve the presence of a thin (relative to the thickness of the flowing mass) lubricaning layer between the sliding mass and the surface over which the mass slides. The lubrication can be due to the presence of water [Abele, 1974; Sassa, 1988; Voight and Sousa, 1994; Hungr and Evans, 2004], ice [e.g., De Blasio, 2011; 2014], cushion of trapped air [Shreve, 1959; 1966; 1968b], gas over-pressuring [e.g., Habib, 1975; Goguel, 1978; Beutner and Gerbi, 2005; Aharonov and Anders, 2006; Goren *et al.*, 2010], frictionite [Erismann *et al.*, 1977; Erismann, 1979; De Blasio and Elverhøi, 2008], flash heating [Singer *et al.*, 2012], and increase in granular temperature [Campbell, 1989; Cleary and Campbell, 1993; Straub, 1996]. Each of these is discussed below.

ICE SURFACE | Ice is considered a lubricating surface in the cases of landslides emplaced on glaciers, as for the case of the Sherman Glacier landslide, Alaska, for which Erismann and Abele [2001] propose a reduced friction because of the effect of ice melting. Experiments on solid-to-ice friction demonstrate that it is affected by velocity-weakening mechanisms, that is friction decreases with increasing velocity. For instance, Persson [2000] shows that for a polished rock sliding over ice at temperatures below 0 degrees Celsius static friction coefficients are greater than dynamic friction coefficients, which means that a lower stress is required to move an object that is already moving. Similar behaviour is found by Tusima [2010] for curling rocks moving on icy surfaces. Departing from the rock-ice sliding interface, De Blasio [2014] suggests a 2-phase mechanical model for rock avalanches travelling on ice that involves the coating of the landslide basal debris by the ploughed ice, which then allows the sliding to occur between wet icy surfaces. Incorporation of snow and ice within the debris is observed in the 2016 Lamplugh supraglacial rock avalanche, Alaska, USA [Dufresne *et al.*, 2019]. Interestingly, Dufresne *et al.* [2019] identified two stages of the rock avalanche emplacement, in which the increasing incorporation of snow and ice saturated the debris leads to a change in the rock avalanche behaviour,

from strong interaction of the debris with the ground (manifested with a clear seismic signal) to a “passive sliding” of the rock avalanche debris on the glacier (manifested with an essentially aseismic signal).

AIR CUSHION MODEL | Shreve [1959] formulated the air-cushion model hypothesis to explain the dynamics and physical characteristics of the Blackhawk landslide, California, USA. According to this hypothesis, the high momentum that characterized voluminous landslides allows them to separate from the ground at the break in slope. The deflection off the ground causes the landslide to arch forward and downward and, in doing so, trapping a cushion of compressed air. The air cushion constitutes a low-friction layer over which the landslide moved. Following this work, he extended this hypothesis to explain the long runout of the Sherman Glacier landslide, Alaska, USA [Shreve, 1966]. However, the air-lubrication mechanism has been discarded as it was contradicted by the observation of long runout landslides on the Moon and Mars (although this point should not be discriminatory, as discussed earlier). More importantly, the model fails to describe the predicted particle grading by high gas pressure [Cruden and Hungr, 1986] and to provide direct evidence in support of the absence of air leakage from beneath the flow.

GAS OVERPRESSURING | Consequences of mechanical energy dissipation in heat at the base of the Vajont landslide, Italy, were discussed by Habib [1975], who proposed that the vaporization of pore water created a hovering cushion. However, simulations by Voight and Faust [1982] showed that high pore water pressure that leads to catastrophic acceleration of landslides can derive from heat generation without vaporization occurring. In such case, the mechanism proposed is a thermo-poro-elastic instability that occurs along thin fluid-saturated shear zone, in which the evolution of the sliding occurs as a feedback cycle between velocity, temperature, and pore pressure. The feedback cycle starts the temperature rise due to frictional heating; the temperature rise causes the pore pressure to increase, which reduces the

effective normal stress, thus friction. Such a thermal pressurization phase allows further acceleration, thus reaching further distances [Voight and Faust, 1982; Vardoulakis, 2000; Goren and Aharonov, 2007]. Goren and Aharonov [2007] showed the depth-dependence of such mechanism and so offering further support to the volume-runout distance relation observed in long runout landslides. Studies by Beutner and Gerbi [2005] and Goren *et al.* [2010] have proposed that a similar thermo-poro-elastic mechanism takes place during emplacement of catastrophic landslides that involve carbonate formations, such as the Eocene Heart Mountain landslide, USA. Frictional heating induces thermal decomposition of carbonates, whose reaction kinetics adds competing processes in such feedback mechanism (Figure 2-21).

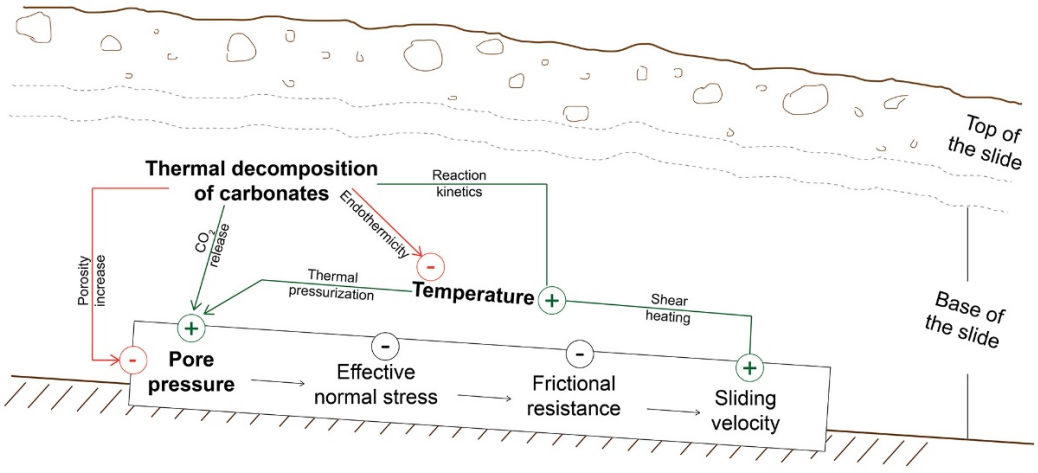

Figure 2-21– Schematic representation of the competing processes involved in the chemical-thermoporoelastic (CTPE) mechanism. CTPE mechanism is a feedback between shear heating, thermal pressurization and thermal decomposition of carbonates at the slide shear zone. Such a feedback arises when a porous, fluid-filled shear zone heats up because of frictional sliding. If the shear zone is confined, the generated heat leads to pore pressure rise, which in turn reduces frictional resistance to sliding, leading to acceleration. Temperatures at the shear zone quickly reach the decomposition temperature of carbonates (modified after Goren *et al.* [2010]).

Mitchell *et al.* [2015] present experimental evidence in support of the role of carbonate decomposition in the generation of the exceptional runout distance for the Heart Mountain landslide: extreme frictional heating associated with shear at the base of the landslide leads to thermal decomposition of carbonate and consequent release of CO_2 gas, which, combined with porosity

reduction due to grain crushing, generates overpressure, thus the reduction of effective stress. The existence of over-pressurization at the base of the Heart Mountain landslide is supported by the presence of huge injection veins originating from the basal section [e.g., Anders *et al.*, 2010; Craddock *et al.*, 2012]

FRICTIONITE | The hypothesis of lubrication by mechanism of melting rock was originally proposed by Preuss [1971], following the discovery of pumice in the deposit of the Kofels landslide, Austria. Through numerical analysis of heat generation, Erismann *et al.* [1977] demonstrated that the production of frictional melt is plausible and further discussion by Erismann [1979] provide additional support to the hypothesis of frictionite. In particular, their quantitative analysis points against laminar or turbulent flow as predominant mechanisms, rather it shows a tendency to concentrate the entire relative displacement within the bottom-most layers. This could explain observations of undisturbed stratigraphic order in landslide deposits. Moreover, as turbulence appears not to be a predominant mechanism, the bottom-most layers would be zones of high energy concentration and their thickness would be approximately proportional to the thickness of the sliding mass. Indeed, the sliding thickness appears to be an important parameter in the formation of frictionite. As discussed by Legros *et al.* [2000], most landslide deposits less than 100 m thick do not show basal frictionite. In fact, frictionite is found at the base of the 300 m thick central part of the Arequipa volcanic landslide deposit, Peru [Legros *et al.*, 2000], at the base of a rockslide at least 250 m thick in the Indian Himalayas [Weidinger and Korup, 2009] and below the several hundred meters thick Langtang landslide deposit [Masch *et al.*, 1985] and Kofel rockslide ([Erismann *et al.*, 1977]). Therefore, Legros *et al.* [2000] concludes that the thickness of the landslide deposits is an important variable in controlling the formation of frictionite at their base.

Several models imply that most of the energy is dissipated in a narrow basal zone [Shreve, 1968b; Erismann, 1979; Davies, 1982; Campbell, 1989]. On the contrary, Legros *et al.* [2000] conclude that energy is dissipated through

the whole moving mass, as their calculations show that basal melting only accounts for a small fraction of the total energy released during the event and supported by the fact that frictionite layers at the base of most landslide deposits are absent. Assuming frictionite has same formation process as pseudotachylyte generated in faults, the 1 cm thick frictionite of the Arequipa landslide would be generated by a basal friction over a length of few tens of meters, whereas the landslide's runout is 20 km. Legros *et al.* [2000] suggest that the dissipation of kinetic energy over a significant part of the landslide body could be explained by the presence of a turbulent flow, although in contradiction with the commonly reported preservation of the initial stratigraphy. However, from fault mechanics studies, it is known that the key factor in the onset of thermally-activated friction weakening mechanisms is the localization of shear stress to a narrow slip zone [e.g., Rice, 2006]. Such concept is also valid for long runout landslides. Spray [1997] envisioned intact rockslides as large displacement single-slip faults and proposed the term 'superfaults'. In this type of rockslide, the localization of slip allows the sliding body to remain coherent and allows the strain energy to be dissipated along the displacement surface(s) and to be converted into heat generating frictional melting (Figure 2-22).

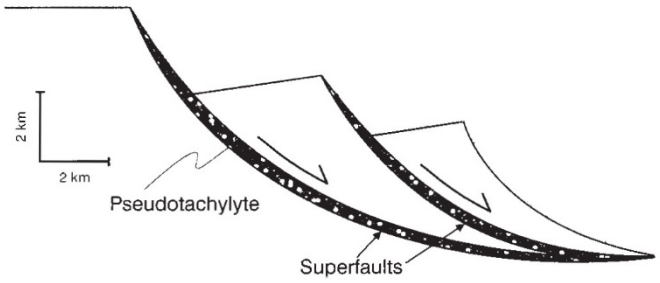

Figure 2-22 – Gravity-driven slope collapse as superfaults. This schematic representation shows the development of pseudotachylyte within superfaults, which are unconstrained faults capable of undergoing very large displacement during a single-slip event. Giant intact rockslides could be seen as a type of superfault (modified after Spray [1997]).

Despite energy budget calculations and models support the feasibility of the generation of molten rock due to fictional heating [e.g., De Blasio and Elverhøi, 2008], evidence for the presence of frictionite has been reported in

few terrestrial cases [Erismann *et al.*, 1977; Masch *et al.*, 1985; Legros *et al.*, 2000; Weidinger and Korup, 2009]. The rarity of pseudotachylytes at outcrop scale is also difficult to explain in the case of fault mechanics studies [e.g., Di Toro *et al.*, 2006; Kirkpatrick and Rowe, 2013; Rowe and Griffith, 2015; Fondriest *et al.*, 2019]. Understanding this apparent contradiction could come from the study of pseudotachylytes along fault zones, including experiments with granular media conducted at high shear rates and pressures. However, one should bear in mind that pseudotachylytes in long runout landslides are observed at single outcrops. Therefore, I consider the assumption questionable that pseudotachylytes extend for the entire length of the landslide deposit. The presence of pseudotachylyte could be just localized, representing the existence of transient and localized conditions for pseudotachylyte formation during the landslide emplacement. Such a scenario would explain the apparent rarity of pseudotachylytes in long runout landslides. On a final note, one should question the stage of the landslide emplacement at which the pseudotachylyte is formed; the fact that it is found at a distal area of the deposit, for instance, may not necessarily imply that it formed there; very early-stage formation of pseudotachylytes near the source region and their successive transport cannot be excluded.

FLASH HEATING | In earthquake studies, flash heating is a dynamic fault-weakening mechanism. When a sufficiently high slip rate is reached, the friction weakening results from intense and transient heating of microscopic asperity contacts that characterize localized slip planes. The abrupt increase in temperature results in instantaneous melting at the asperity contacts (Figure 2-23).

The melt lubricates the fault and causes the degradation of frictional strength [Rice, 1999; 2006; e.g., Goldsby and Tullis, 2011]. However, this mechanism remains highly localized at the asperity contacts so that, while melting droplets are formed at these locations, the average temperature of slip barely increases [e.g., Goldsby and Tullis, 2011]. Singer *et al.* [2012] have proposed a similar mechanism that could explain long runout of landslides on Iapetus,

suggesting that frictional heating may raise the temperatures so that the ice becomes slippery, although there is no experimental demonstration that such process would occur given Iapetus' surface conditions (very cold surface temperatures, <100°K, and in a vacuum).

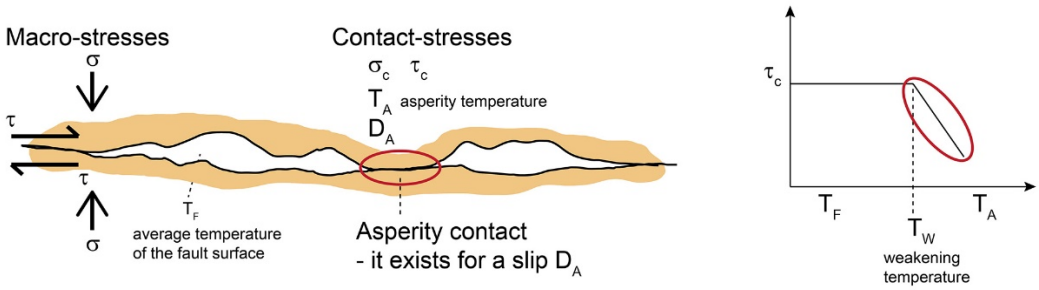

Figure 2-23 – Model for friction weakening by flash heating mechanism. The stage of the weakening depends on the slip rate. Below a critical sliding velocity the contact does not weaken but above it does. The slip length D_A corresponds to the asperity contact size (modified after Rice [2017]).

DISPERSIVE GRANULAR FLOW | Following computer simulation of gravity-driven two-dimensional granular flows, Campbell [1989] proposed a mechanism in which a dilute layer of highly agitated particles supports the mass that moves in bulk above. The formation of such low-density layer naturally occurs in rapid granular flows that move down inclined rough planes, as a by-product of the rapid flow itself [e.g, Forterre and Pouliquen, 2001]. Campbell [1989] shows that a similar low-density layer should form at the bottom of long runout landslides. The simulations show that the particles at the bottom of the slide collide with the surface over which they move and, in doing so, generate a dilative pressure that supports the entire mass. Surface roughness appears to be a crucial aspect in the generation of this supportive pressure [Cleary and Campbell, 1993], for it acts to convert the horizontal motion component of grains into a vertical motion component. Using the analogy with the molecular temperature in a gas, the random motion of grains is referred to as 'granular temperature' (Figure 2-24).

In fact, they are thought to play a similar role in governing the behaviour of their respective systems. Although a physical analogy exists between

thermodynamic temperature and granular temperature, a fundamental difference is in the fact that granular temperature is dissipated through collisions and so, to maintain the granular temperature, energy must be supplied from the kinetic energy of the landslide bulk.

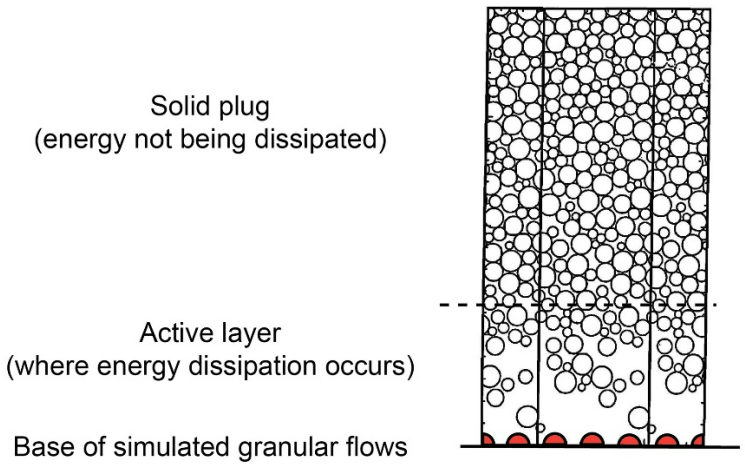

Figure 2-24 – Computer simulation of granular flows. Discrete particle computer simulations are used to test whether the low apparent coefficient of friction of long runout landslides can be explained in terms of simple granular mechanics. Red half circles represent the surface roughness of the model (Modified after Cleary and Campbell [1993]).

As noted by Cleary and Campbell [1993], “it appears that the substantial increases in runout distance cannot be attributed to any reduction in boundary friction but are produced entirely by the additional kinetic energy that is made available from the gravitational potential energy.”. Eventually, the landslide comes to a halt when all the energy is dissipated. This implies that the larger the mass the larger the initial kinetic energy, therefore providing a possible explanation of the volume effect on the apparent coefficient of friction. In addition, the active layer predicted to develop at the bottom of the sliding mass (i.e., the layer where the energy dissipation occurs) would be a small fraction (about 20%) of the entire thickness and the remaining volume would consist of a ‘solid plug’ with no shear between grains (i.e., energy is not being dissipated). This represents an important difference with other mechanical fluidization mechanisms, which instead assume that energy is dissipated

through the entire volume; and importantly this would allow the stratigraphy to be preserved, as is observed.

2.6.4 Reduction of internal friction.

ACOUSTIC FLUIDIZATION | Acoustic fluidization was proposed by Melosh [1979] as a new geological process able to provide a qualitatively correct description of observed natural phenomena during which classical frictional arguments appear not to hold, such as seismic faulting, crater slumping, and long runout landslides. Acoustic fluidization provides an adequate explanation to the observed increased mobility of large dry rock avalanches, by envisioning a system in which transient, sufficiently strong acoustic waves can momentarily relieve the static overburden pressure and regenerate themselves as the slide moves (Figure 2-25).

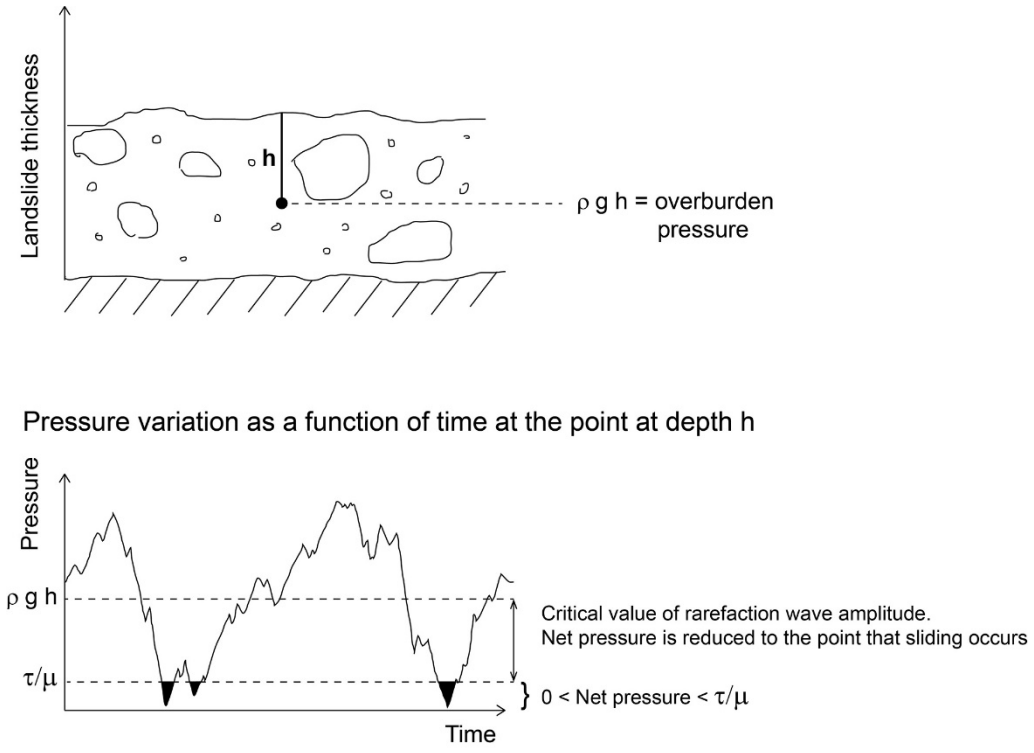

Figure 2-25 – Schematic diagram of the pressure variations predicted in the acoustic fluidization mechanism. The top figure shows part of a landslide deposit (in motion) and a selected point at depth h, at which the overburden pressure is ρgh. The lower figure shows the pressure variations as a function of time at the point at depth h. Pressure fluctuates randomly and at times the static overburden pressure can be momentarily relieved when the pressure falls between zero and τ/μ (Modified after Melosh [1979]).

As described by Melosh [1979; 1983], the acoustic waves must have shorter wavelengths compared to the thickness of the landslide, because longer wavelengths would not be trapped in a unit smaller than their length. This also implies that acoustic fluidization ceases when the landslide thickness becomes small enough so that the acoustic energy loss exceeds the energy gained from gravitational potential energy. As noted in Melosh [1983], although the volume of long runout landslides varies greatly, the final deposits appear to have roughly the same thickness. In fact, as discussed by Collins and Melosh [2003], there exists a critical thickness above which acoustic fluidization may enable self-sustained flow of the landslide also at low slope angles and below which the landslide would be controlled by 'standard mechanics' until termination. Intuitively, the greater the initial thickness, thus the greater the initial volume involved, the farther the landslide can travel before the critical thickness is reached, and thus coming to a halt. By extending and quantifying the acoustic fluidization model for the mechanics of large dry rock avalanches, Collins and Melosh [2003] demonstrate that acoustic fluidization can increase the mobility of long runout landslides and facilitate the self-sustaining motion of the landslide. Johnson *et al.* [2016a] implemented the soft particle code by Campbell *et al.* [1995] on modern workstations in the attempt to clarify the apparent reduction of friction in long runout landslides. Their results are in agreement with the prediction of acoustic fluidization theory. Moreover, they determine that vibrations associated with acoustic fluidization have a wavelength that is defined by the size of the rock fragments in the landslide, rather than the thickness of the flowing mass.

A major problem in the modelling of the acoustic fluidization process is the difficulty in constraining important model parameters, such as scattering diffusivity, dominant wavelength of the acoustic vibrations, and the dissipation quality factor. These difficulties emerge from the challenges that direct acoustic measurements pose as well as from the challenges to simulate large landslides at laboratory scale. For example, dissipation is size dependent and it may be so important for small systems that the energy level to induce acoustic fluidization in laboratory slides is never reached, thus explaining why

acoustic fluidization has never been observed at laboratory scale. Quantifying these parameters means quantifying the amount of acoustic energy present, which determines the rheology of the material. The uncertainties in constraining such parameters do not permit to determine whether acoustic fluidization is the major mechanism controlling the emplacement of long runout landslides because they make simulations and direct measurements of acoustic signal in long runout landslides difficult to compare.

MECHANICAL FLUIDIZATION | Mechanical fluidization involves collisions between the individual grains of a granular sliding mass. These collisions generate a high energy input to the rock avalanche, allow the sliding mass to dilate, and relieve the overburden pressure. Heim [1882] suggested that the internal motion of the debris consisted of numerous high-energy collisions between individual grains. Davies [1982] investigated the hypothesis that the spreading of rock avalanches by mechanical fluidization is caused by high basal shear rates as the landslides rapidly move. From this initial study, the mechanism named ‘dynamic rock fragmentation’ was developed [Davies and Mcsaveney, 2009; 2012]. The high shear rates that characterize the basal layer of a sliding mass cause rocks to break to form a granular flow. The breaking of rocks is the source of vibrations that change the resistance of the flow to shear. However, this mechanism has received strong opposition related to energy balance, pointing out that collisions consume energy and therefore this process cannot increase the runout [Melosh, 1983; Johnson *et al.*, 2016b]. However, Davies and Mcsaveney [2009] argue that, instead of consuming energy, the collisions between grains and the following fragmentation redistribute the energy in the granular flow as elastic strain energy, which is then radiated as acoustic emissions with frequency corresponding to the sizes of the grains that break.

Mechanical fluidization could be confused with the very similar acoustic fluidization. Both mechanisms predict that a landslide may be fluidized if the overburden pressure is relieved by random motions within the sliding mass. However, as stressed by Collins and Melosh [2003], the crucial difference is

that acoustic fluidization assumes that the random movement is not that of individual rock fragments, but of groups of fragments organized into waves. Moreover, collisions transfer energy and momentum from one grain to another with large energy loss. In acoustically fluidized landslides, the motion of adjacent grains is strongly correlated, collisions are rare and/or gentle with smaller energy loss, and the landslides still possess high degree of mobility. According to Davies and Mcsaveney [2016], the theory of dynamic fragmentation better explains the reduction of friction in long runout landslides than the acoustic fluidization theory. However, Johnson *et al.* [2016b] suggest that dynamic fragmentation cannot be considered an alternative to acoustic fluidization but rather acoustic fluidization with an alternative acoustic energy source.

Table 2-2- List of mechanisms proposed to explain the reduction of friction and high mobility of long runout landslides.

Mechanism Category	Group/Medium	Mechanism	Reference
Reduction of basal friction			
	Air	Air layer beneath the slide	[Shreve, 1966; 1968b; a]
		Existence of an additional aerodynamic lift - in addition to mechanism of Kent (1966)	[Krumdieck, 1984]
	Water	Lubrication by undrained loading of saturated substrates	[Abele, 1974; Sassa, 1988; Hungr and Evans, 2004]
		Shear of a wet basal zone	[Voight and Sousa, 1994]
	Ice	Lubricant layer of ice	[Dufresne and Davies, 2009; De Blasio, 2011; 2014]
	Molten Rock	Lubricant layer of molten basal rock produced by frictional heat.	[Erismann *et al.*, 1977; Erismann, 1979] [De Blasio and Elverhøi, 2008]
	Gas-overpressuring	Vaporization of water at the base of slide by frictional heating produces increase of pore pressure	[Goguel, 1978] [Habib, 1975]
		Pore-water pressure increase via frictional heating (no vaporization)	[Voight and Faust, 1982; Vardoulakis, 2000; 2002]
	Chemical-Thermo-poro-elastic mechanical coupling	Overpressuring from generation of CO_2 gas caused by thermal decomposition of the basal carbonates	[Beutner and Gerbi, 2005; Aharonov and Anders, 2006; Goren and Aharonov, 2007; Anders *et al.*, 2010]
	Dispersive grain flow	Layer of highly agitating particles beneath the densely packed main body reduces the frictional forces between the slide and the ground.	[Campbell, 1989; Cleary and Campbell, 1993]
Reduction of internal friction			
	Fluidization by air	Fluidization by interaction of particles and entrapped air	[Kent, 1966]

		that escape upward through the sliding body	
	Fluidization by volcanic gases	High mobility is induced by hot fluids of the depressurized magmatic-hydrothermal system	[Voight *et al.*, 1983]
	Mechanical fluidization (by interaction of particles)	The myriad of highly energetic collisions among individual grains tend to maintain the original kinetic energy of the fall.	[Heim, 1932]
	Mechanical fluidization (by interaction of particles)	Material self-fluidized by dispersive stresses	[Hsü, 1975; 1978]
	Mechanical fluidization (by interaction of particles)	Dynamic rock fragmentation	[Davies, 1982; Davies and Mcsaveney, 2002; 2009]
	Earthquake fluidization	Due to vibrational energy imparted by the earthquake which caused the original fall, the debris mass became dilated and fluidised	[Mcsaveney, 1978]
	Acoustic fluidization	Acoustic waves can momentarily relieve the static overburden pressure, allowing sliding.	[Melosh, 1979; 1983; Collins and Melosh, 2003]

Volume change			
	Mass changes	Loss	[Gassen and Cruden, 1989]
	Mass changes	Entrainment of saturated valley sediments	[Hungr and Evans, 2004]

2.7 Multi-disciplinary approach to the study of long runout landslides.

Many different approaches have been used to contribute to understanding of mechanisms that allow for the apparent reduction of friction of long runout landslides and the development of their characteristic structures and morphologies. In an attempt to support competing hypotheses and models, studies have focused on terrestrial field work, planetary geomorphology studies [e.g., Lucchitta, 1979; 1987; Quantin *et al.*, 2004a], planetary comparative studies [e.g., Shaller, 1991], laboratory experiments using granular material [e.g., Lajeunesse *et al.*, 2006; Roche *et al.*, 2011], and analogue [e.g., Shea and Van Wyk De Vries, 2008] and numerical modelling [e.g., Harrison and Grimm, 2003; Lucas *et al.*, 2014].

In addition, useful contributions have been provided from research areas not strictly related to long runout landslides, such the physics of granular flows and fault mechanics. The research on granular flows has stimulated applications for the description and prediction of long runout landslides behaviour [e.g., Campbell, 1989; Cleary and Campbell, 1993; Campbell *et al.*, 1995; Johnson *et al.*, 2016a]. Although this approach successfully describes the local rheology and predicts some flow configurations, its application to more complex media, such as long runout landslides, remains an open question. Interesting analogies can be drawn from the field of fault mechanics. Indeed, faults and long runout landslides share dramatic drops in the coefficient of friction [e.g., Di Toro *et al.*, 2011; Viesca and Rice, 2012; Germanovich *et al.*, 2016; Ibanez and Hatzor, 2018]. In this respect, well established theoretical and experimental knowledge of weakening processes during earthquakes can be extended to the study of the formation mechanism of long runout landslides [Lucas *et al.*, 2014].

Here follows a description of the contribution to the understanding of long runout landslides by the fields of planetary remote sensing, the modelling of long runout landslides as granular flows, and fault mechanics friction experiments. These are the main areas that has influenced much of the work and discussion of this thesis.

2.7.1 Planetary remote sensing.

The study of long runout landslides is very reliant on direct field observations and sample analysis. Early work [Heim, 1882; e.g., Harrison and Falcon, 1938; Sharpe, 1938] provides precise accounts and details of landslide case studies that are still relevant to current discussions. The accessibility of terrestrial landslide sites also allows us to directly study the lithology involved, the macro-structures of deposits, and to collect rock samples, from which information at microscopic scale can be obtained [e.g., Mitchell *et al.*, 2015]. Absolute dating of ancient landslide deposits can be attempted [e.g., Roberts and Evans, 2013; Crosta *et al.*, 2017].

The study of extra-terrestrial long runout landslides cannot count on these methods yet, but instead relies on remote sensing techniques, which not only involve the visible wavelengths of the electromagnetic spectrum but also near and thermal infrared [Watkins *et al.*, 2015; 2020]. One of the advantages of studying long runout landslides on planetary bodies other than Earth lies in the preservation of the morphological record, as a consequence of reduced erosion rates and reduced geological activity compared to the Earth. On our planet, atmospheric weathering, erosion, and sedimentation can act at fast rates, quickly modifying the morphology of landforms; also, plate tectonics obliterate the geomorphological record of long runout landslide deposits, which may be preserved within the stratigraphic record [e.g., Sobiesiak *et al.*, 2018].

The preservation of the geomorphological record of long runout landslides on planetary bodies beyond Earth presents two main advantages. First of all, it allows the determination of the scale of the extent of the occurrence of long runout landslides in our Solar System. The ubiquity of long runout landslides appears clearly, thanks to missions to the terrestrial planets (Mercury [Brunetti *et al.*, 2015]; Venus [Malin, 1992]; Mars [e.g., Lucchitta, 1979; Quantin *et al.*, 2004b]), asteroids (Vesta [Krohn *et al.*, 2014]) and dwarf planets (Ceres [Schmidt *et al.*, 2017]), rocky moons (the Moon [e.g., El-Baz, 1972; Kokelaar *et al.*, 2017], Phobos ([Shingareva and Kuzmin, 2001]) and icy moons in the outer Solar System (Callisto [Chuang and Greeley, 2000];

Iapetus [Singer *et al.*, 2012]; Charon [Beddingfield *et al.*, 2019]). In addition, in the past two decades, the availability of high resolution global coverage of the surface of Mars - thanks to the superb Mars Reconnaissance Orbiter mission – has allowed the identification of martian mass-movements on a global scale and the creation of large inventories [Legros, 2002; Quantin *et al.*, 2004b; Crosta *et al.*, 2013; Brunetti *et al.*, 2014], of which the latest published counts 3,118 deposits greater than 0.1 km^2 across the whole planet [Crosta *et al.*, 2018b]. Secondly, on Mars and on the Moon, for which repetitive high-resolution imaging of the surface allows the generation of high-resolution digital elevation models, detailed morphometric analysis can be conducted on landforms that are almost pristine (Figure 2-26).

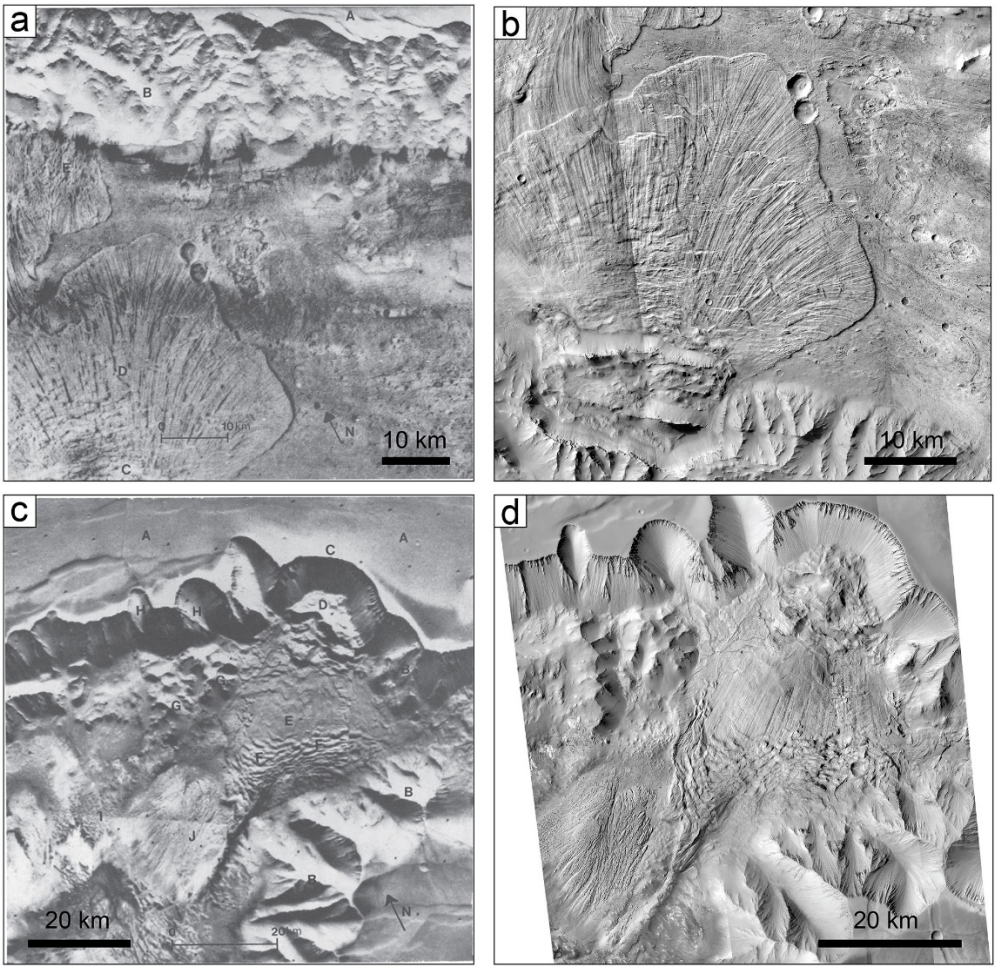

Figure 2-26 – Improvement in martian imagery resolution. Comparison between Viking (a, c) and Mars Reconnaissance Orbiter (b, d) missions to Mars. a) and b) Coprates Labes landslide in Coprates Chasma, Valles Marineris. c) and d) Landslide in Tithonium Chasma, Valles Marineris.

This has resulted in the creation of several inventories that compile a series of information about geometrical and physical aspects of long runout landslides, such as height drop, length of runout, volume, area of the final deposit, as well as the morphometry of distinctive structures, such as longitudinal ridges. Database of this sort are useful to create a comprehensive quantitative description of landslides that represent the starting point for kinematic investigations and mechanical modelling [e.g., Harrison and Grimm, 2003; Mckinnon, 2010; Pudasaini and Miller, 2013; Lucas *et al.*, 2014].

2.7.2 Modelling long runout landslides as granular flows.

Models of granular flow motion can be applied to the study of long runout landslides [e.g., Campbell, 1989; Cleary and Campbell, 1993; Straub, 1996; 1997]. Simple granular mechanics has been adopted in an attempt to describe the frictional behaviour of long runout landslides. In these works, the landslide motion is simulated using a column of particles with periodic boundaries, in which particles collide and their interactions are modelled. These simulations represent infinite landslides that are assumed to have started with a uniform velocity. Therefore, results do not provide any indication about the initial motion of the landslide nor about how it comes to a halt, but provide insights about the internal mechanics. Despite the existence of these not entirely negligible limits due to the simplification of the system, these discrete numerical simulations have been able to reproduce realistic characteristics of the landslides with a minimum number of assumptions on the flow rheology [Forterre and Pouliquen, 2011].

With the recent increase in computational power, simulations of an entire landslide can be run. Using a soft particle code, that is a model that assumes finite elastic properties, Campbell *et al.* [1995] modelled long runout landslides as granular flows. Importantly, this work offers a view of the way long runout landslides move that differs from the idea of a nearly solid block riding atop a low frictional basal layer proposed by Campbell [1989]: during motion, the simulated slides are completely shearing (i.e., shearing is not just

limited to a basal layer) and the apparent coefficient of friction is a function of the shear rate. Without including fluids nor thermal effects, this model is able to reproduce some of the characteristic aspects of long runout landslides, such as the preservation of the initial stratigraphy and the reduction of apparent friction with increasing landslide volume. The behaviour observed during these simulations supports mechanisms such as acoustic fluidization [Melosh, 1979] and self-lubrication [Campbell, 1989]. Further extension of this work by Johnson *et al.* [2016a] shows that the sliding occurs when the overburden pressure is relieved, in agreement with the predictions of the acoustic fluidization.

Laboratory experiments and simulations on rapid granular flows also provide important insights about the formation of characteristic features of long runout landslides, such as longitudinal ridges observed on the surface of their deposits. Although it is a common idea that the formation of such morphologies is linked to the presence of an icy surface, works on mechanical instabilities within rapid granular flows can yield new understanding of mechanical processes taking place during the emplacement of long runout landslides. The formation patterns generated by flow instabilities has been investigated by Forterre and Pouliquen [2001], who report the instability that spontaneously generates longitudinal vortices in rapid granular flows moving on a rough surface for the first time. As further confirmed by Borzsonyi *et al.* [2009], flow density plays an important role in the instability. Forterre and Pouliquen [2001] describe a mechanism that is based on the concept of granular temperature [Campbell, 1989; 1990] and on density profile inversion. In such a mechanism, the rough basal surface induces strong shear at the bottom of the flow that agitates the grains, causing an increase in the granular temperature and a consequent decrease in density; as a consequence, the top part of the flow is denser then the bottom part and the flow becomes mechanically unstable under gravity. The mechanical instability leads to the inversion of the density profile that, coupled with the high-speed downslope movement of the flow, generates convective longitudinal vortices. As discussed by Forterre and Pouliquen [2001], although reversed density profiles were observed in numerical simulations by Campbell [1989] and

Cleary and Campbell [1993], flow instabilities could not have been observed as the numerical simulations were two-dimensional, whereas pattern formation is three-dimensional. In fact Johnson *et al.* [2016a] endorse the need for three-dimensional computer simulations, as they provide insights on the importance of the three-dimensional effects of the mechanisms proposed to be involved in the emplacement of long runout landslides.

2.7.3 Friction experiments and modelling as inspired by earthquake studies.

A dramatic reduction of the coefficient of friction occurs in both long runout landslides and faults characterized by high slip rates (i.e., > 0.1 ms^{-1}). Laboratory friction experiments at slow slip rates show that slipping zones are characterized by friction coefficients in the range between 0.6 and 0.85 (Byerlee friction law [Byerlee, 1978]), according to which the magnitude of kinetic friction is independent of the velocity of slip. However, friction experiments at fast slip rates show a significant decrease in friction, termed fault lubrication [e.g., Di Toro *et al.*, 2011 and references within] (Figure 2-27).

A series of dynamic-weakening mechanisms, which are thermal in nature, have been identified to explain fault lubrication: gelification [Goldsby and Tullis, 2002; Di Toro *et al.*, 2004], thermal pressurization of pore fluids [Sibson, 1973; Rice, 2006], flash heating [Goldsby and Tullis, 2002; Rice, 2006], and frictional melt [Sibson, 1975; Di Toro *et al.*, 2006]. Experimental results demonstrate that the friction drop at seismic slip rates takes place independent of rock type and weakening mechanisms applied [e.g., Goldsby and Tullis, 2002; Di Toro *et al.*, 2004; Brantut *et al.*, 2008; Brantut *et al.*, 2011b; Di Toro *et al.*, 2011]. Inspired by fault mechanics studies, friction experiments have been used to study the friction-displacement-velocity relationship along basal surfaces of long runout landslides. High-speed rotary shear experiments have been conducted to better constrain physical and chemical processes that take place at the conditions of landslide emplacement [e.g., Mitchell *et al.*, 2015; Hu *et al.*, 2018; Ibanez and Hatzor, 2018].

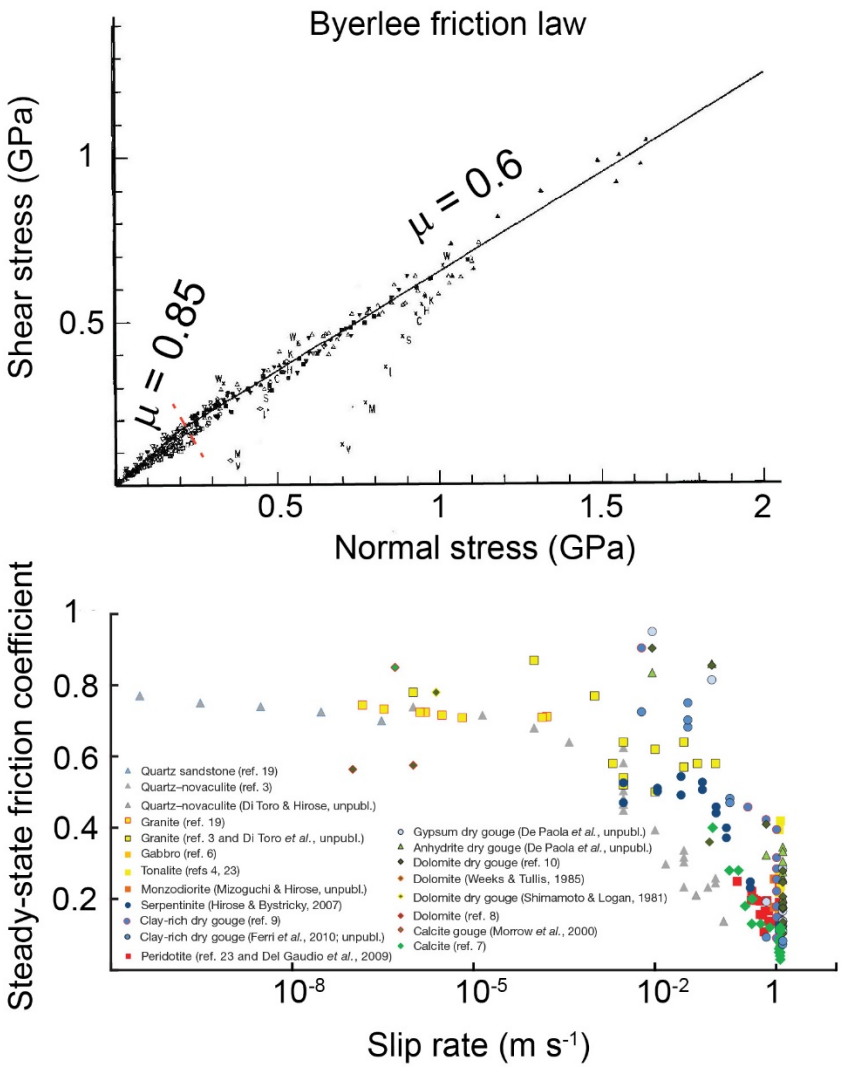

Figure 2-27 – Reduction of the coefficient of friction from slow to high slip rates found in laboratory experiments. Left panel shows the empirical relationship between shear stress and normal stress found by Byerlee [1978] (Modified after Byerlee [1978]). Right panel shows the reduction of the coefficient of friction with increased slip rates; in particular a sharp decrease occurs when seismic slip rates (~ 1 m s^{-1}) are reached (Modified after Di Toro *et al.* [2011]).

The similarity of processes in long runout landslides and high-slip-rate seismic faulting has been proposed in the light of the role of frictional heating as heat source that generates a series of physical and chemical reactions responsible for their behaviour [e.g., Voight and Faust, 1982; Vardoulakis, 2000; Goren and Aharonov, 2007]. Weakening mechanisms that have been suggested taking place during long runout landslides are gas overpressurisation [e.g., Goren *et al.*, 2010; Pinyol and Alonso, 2010; Mitchell *et al.*, 2015; Ibanez and Hatzor, 2018], melt production [e.g., Erismann, 1979;

Legros *et al.*, 2000], flash heating [Singer *et al.*, 2012; Beddingfield *et al.*, 2019] (see Section 2.4.3).

The tragic 1963 Vajont landslide, Italy (Figure 2-28), is an example of the potential of long runout landslides to develop extremely high velocities along their surface of detachment, already in the early stage of the emplacement.

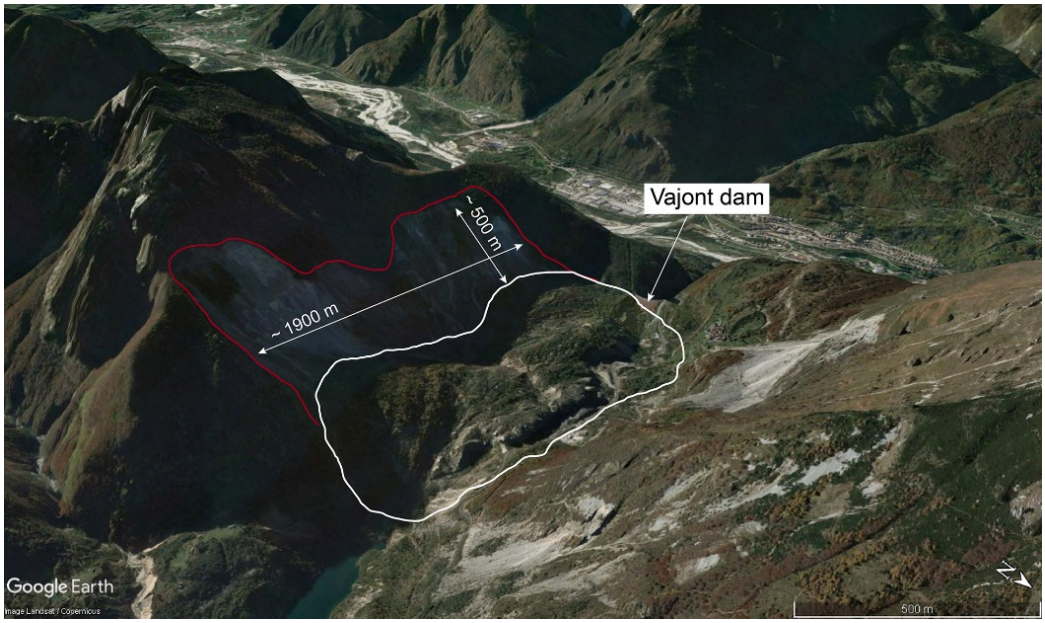

Figure 2-28 – The Vajont landslide. Geomechanical studies have showed that slope failure occurred along a deep localized surface and that the sliding mass has reached high velocities already few tens of second after the initiation. In order to explain the acceleration of the slide, a friction weakening mechanism that involves increase of pore pressure within the basal section of the slide is favoured. Red line marks the scarp area; white line marks the landslide deposit (view taken from Google Earth).

Dynamic analysis of the Vajont slide is not able to explain how the high velocity is reached along a basal plane characterized by a friction angle of 12° [Ibanez and Hatzor, 2018], but it indicates that internal rock strength degradation and friction degradation in the rock mass and joints and boundaries are contributing factors to the initial rapid acceleration [Hendron and Patton, 1987; Alonso and Pinyol, 2010; Ibanez and Hatzor, 2018]. The peak velocity of 90 km/h was reach after only 37 s of sliding [Ibanez and Hatzor, 2018]. Development of frictional heat at the sliding surface is the most favourable mechanism to explain the loss of basal strength, as the temperature increase would generate excess pore pressure [Voight and

Faust, 1982; Hendron and Patton, 1987; Vardoulakis, 2002; Pinyol and Alonso, 2010].

This is the case where the slip occurs on a localized shear surface, whose strength weakens with increasing slip. These type of surface ruptures can be conceptualised as ‘superfaults’, that is a special type of fault characterized by displacements larger than 100 m occurring during a single-slip event at seismogenic velocity [Spray, 1997].

Low coefficient of friction in faults and long runout landslides appears to derive from velocity-dependent processes. Lucas *et al.* [2014] propose an empirical velocity-weakening friction law applicable to landslides observed in the Solar System that is found to be surprisingly similar to a friction law derived for weakening by flash heating operating during earthquakes. Yet, analyses are not able to determine the physical origin of frictional weakening in landslides.

3 Data and methods.

The work that has led to the writing of this thesis is based on remote sensing techniques.

This chapter includes: a) the description of the cameras used to both carry out observations and to obtain the different imagery datasets (i.e., digital elevation models and orthoimages), together with a description of the satellite missions they are/were aboard; b) the description of the processing methods applied to martian and lunar images; c) the description of the photogrammetry techniques used to generate digital elevation models and orthoimages; d) the description of the software and tools used to analyse topographic data obtained. The actual satellite images (i.e., their ID number) used to generate digital elevation models and orthoimages are given in Chapter 4 for the martian case study, in Chapter 5 for the terrestrial case study, and in Chapter 6 for the lunar case studies.

3.1 Remote sensing data acquisition.

Remote sensing allows the study of objects at distance, therefore making it the inevitable choice for the study of long runout landslides on Mars and on the Moon. State-of-the-art satellite imagery is used to generate digital elevation models (DEMs) and orthoimages of the martian and lunar surfaces. Such data are also greatly helpful in the study of large areas and targets on Earth, as they allow us to obtain additional, and different information to that possible from the ground only. For this reason, high resolution imagery from terrestrial satellites is used in this thesis to generate the same type of topographic products for the study of a long runout landslide in Chile. In

addition, drone mapping based on images acquired with drones, is used to integrate satellite imagery with more detailed field observations of the landslide deposit.

Table 3-1 is provided to summarize the characteristics of the instruments used to acquire remote sensing data used in this study. This allows a quick comparison of the resolution between the different datasets (see also Figure 3-1, Figure 3-2, and Figure 3-3).

Table 3-1 - List of cameras and instruments on board satellite missions used for this work.

	Camera/ Instrument	Type of instrument	Resolution	Mission	Operational
Mars					
	Mars Orbiter Laser Altimeter (MOLA)	Laser	Along track ~300 m	NASA Mars Global Surveyor	1999 - 2001
	High Resolution Stereo Camera (HRSC)	Optical	10-100 m	ESA Mars Express	2003 -
	Context camera (CTX)	Optical	6 m	NASA Mars Reconnaissance Orbiter	2006 -
	High Resolution Imaging Science Experiment (HiRISE)	Optical	0.25-0.5 m	NASA Mars Reconnaissance Orbiter	2006 -
Moon					
	Lunar Orbiter Laser Altimeter (LOLA)	Laser	Along track spacing ~56 m	Lunar Reconnaissance Orbiter	2009 -
	Lunar Reconnaissance Orbiter Camera (LROC)	Optical	0.5 m -NAC 100 m -WAC	Lunar Reconnaissance Orbiter	2009 -
Earth					
	Multi-Spectral Instrument (MSI)	Spectral Imager	10-60 m	ESA Sentinel 2	2015 -
	High Resolution Camera	Optical	0.5 m	CNES/Airbus Pleiades	2011 -

3.1.1 Martian remote sensing datasets.

The first images showing typical landslide topography on the surface of Mars came from the Mariner 9 mission, in 1971 [Sharp, 1973b]. It is with the 1975 Viking 1 Orbiter mission that the extraordinary character of the gigantic martian long runout landslides and their ubiquity in Valles Marineris was revealed [Blasius *et al.*, 1977; Lucchitta, 1978b; a; 1979]. More accurate and precise topographic data and products came with instruments on board the 1996 NASA Mars Global Surveyor (MGS) mission – the Mars Orbiter Laser Altimeter (MOLA) and the Mars Orbiter Camera (MOC) – and the 2003 ESA Mars Express mission – the High Resolution Stereo Camera (HRSC). However, a milestone in the study of martian geomorphology is represented by the 2005 NASA Mars Reconnaissance Orbiter (MRO) mission. The spacecraft has two high-resolution cameras on board, the Context Camera (CTX) and the High Resolution Imaging Science Experiment (HiRISE) camera, which make possible the study from orbit of the martian surface in unprecedented detail (Figure 3-1).

Here follows a brief description of the instruments from which the martian datasets used for this study were obtained. The martian imagery and the MOLA-derived and the HRSC-derived topographic datasets have been freely downloaded from the NASA Planetary Data System – Mars Orbital Data Explorer (PDS – Mars ODE https://ode.rsl.wustl.edu/mars/). The CTX-derived and the HiRISE-derived digital elevation models were produced for this thesis and I provide a description of the software and method in section 3.2.2 and section 3.2.3.

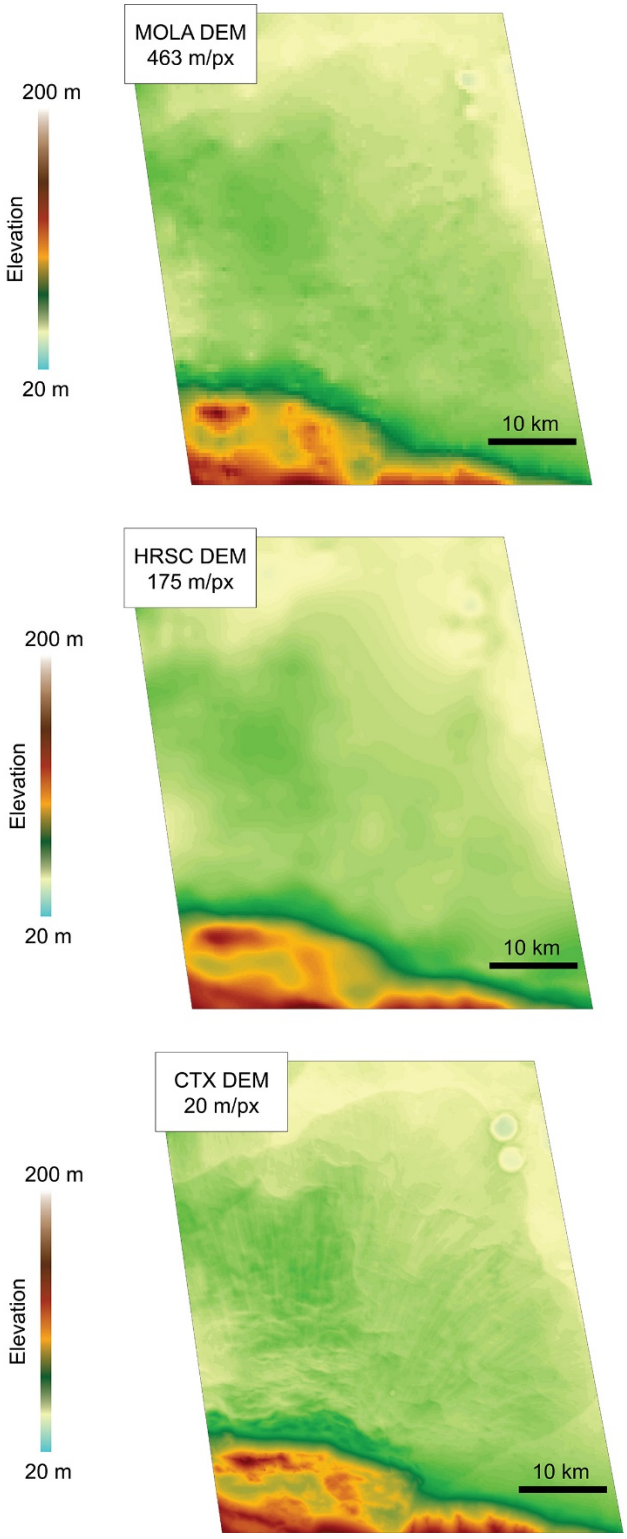

Figure 3-1 – Comparison of resolution of different martian elevation datasets. The area taken for reference covers part of the Coprates Labes landslide that is the case study in Chapter 4. Note how state-of-the-art CTX-derived digital elevation models are able to better resolve small scale features, such as craters, the landslide edge and longitudinal ridges on the landslide deposit.

3.1.1.1 MOLA.

The Mars Orbiter Laser Altimeter (MOLA) [Zuber *et al.*, 1992] is on board the NASA Mars Global Surveyor and it operated from 1999 to 2001. The instrument transmitted laser pulses (1.064 μm wavelength, 10 Hz frequancy) and measured their round-trip time of flight between the spacecraft and the martian surface to determine the range. The laser pulses create footprints along a track with a diameter of about 120 m every 300 m and a vertical accuracy of about 1 m. Interpolation of the altimetry data obtained from these optical pulses (gridded MOLA data) provides a global topographic map of Mars with a horizontal resolution of 128 pixel/degree, which corresponds to about 463 m/px at the martian equator, and a total elevation uncertainty of about ± 3 m [Smith *et al.*, 2001].

Prior to MOLA data, the martian datum (areoid) was defined as the surface with constant atmospheric pressure 6.1 mbar (pressure of the triple point of water). The MOLA data led to a new convention of the martian datum, which is now defined as the equipotential surface whose average value at the equator is equal to the mean radius of the planet [Smith *et al.*, 2001].

This instrument has fundamentally improved the accuracy of the martian surface topography, leading to some of the most critical discoveries that contributed to advance the geological and geophysical understanding of Mars. Since 2003 (i.e., since the Mars Express HRSC camera), MOLA is being used as the absolute vertical reference frame for all topographic datasets.

3.1.1.2 HRSC camera.

The High Resolution Stereo Camera (HRSC) is on board the ESA Mars Express, launched in 2003 and still operational at the time of writing. The HRSC instrument is a stereo colour (Blue, 440 nm; Green, 540 nm; Red, 750 nm; Near-Infrared, 955 nm) pushbroom instrument [Neukum *et al.*, 2004]. HRSC images have a resolution ranging from 10 to 100 m/pixel from, from which digital elevation models are produced at a resolution ranging from 25 to 200 m/pixel. The unique capability of the HRSC is to acquire near-

simultaneous along-track stereo imagery, thus avoiding time-dependent variations of the observational conditions [Neukum *et al.*, 2004; Jaumann *et al.*, 2007].

For this project, one of the available HRSC Digital Terrain Map Reduced Data Record (DTMRDR; product H0515_0000; resolution 175 m/px) has been used to compensate for the lack of good quality CTX-derived digital elevation models.

3.1.1.3 CTX camera.

The ConTeXt (CTX) camera is an instrument on board the ongoing NASA Mars Reconnaissance Orbiter mission. The camera provides grayscale images (in the 500nm to 800nm visible wavelength band) with a 6 m/px resolution and a variable footprint that is approximately 30x200 km [Malin *et al.*, 2007]. It is designed to provide large spatial context for HiRISE images and it represents a near global dataset with greater resolution than provided by HRSC. Although CTX does not provide stereo images, repeat coverage of the martian surface with different observation angles allows the generation of digital elevation models. CTX imagery represents principal dataset of the part of this work dedicated to martian long runout landslides. I used 4 CTX image pairs to produce 4 digital elevation models that were used in this thesis. I provide the full list of the CTX images in Table 4-1.

3.1.1.4 HiRISE camera.

The High Resolution Imaging Science Experiment (HiRISE) camera is one of the instruments on board the ongoing NASA Mars Reconnaissance Orbiter mission. The camera provides images with a 25-50 cm/px resolution collected in three colour bands (Blue-Green: 400 to 600 nm; Red: 500 to 850 nm; Near Infrared: 800 to 1000 nm; colour images are produced in the central portion of the field of view) and a variable footprint that is approximately 5x25 km [Mcewen *et al.*, 2007]. Although HiRISE is not a stereo camera, stereo acquisitions can be achieved of specific target with the aim to produce digital elevation models by taking images on different orbits with different

observation angles. Unfortunately, the martian long runout landslides which are the subject of part of this work lack complete coverage by HiRISE stereo images.

3.1.2 Lunar remote sensing dataset.

The first images of a lunar long runout landslide at the far-side Tsiolkovsky Crater were provided by the NASA 1967 Lunar Orbiter 3 mission [Guest and Murray, 1969] and followed by the images taken during the 1971 Apollo 15 mission [El-Baz, 1972; Wu *et al.*, 1972]. Apollo 17 pre-mission geological maps derived from orbital-science photography of previous missions led to the identification of an avalanche deposit in the Taurus-Littrow Valley [Scott *et al.*, 1972]. The NASA 2009 Lunar Reconnaissance Orbiter mission (still ongoing at the time of writing) has been providing high resolution images of the lunar surface, with the primary intent of obtaining measurements of the Moon that will enable future lunar human exploration. Amongst the missions goals are the identification and certification of the landing sites of the Apollo missions, the creation of a global morphology base map, and the characterization of regolith properties. In addition to orbital imagery, photographs taken from the lunar surface by Apollo 17 astronauts represent another invaluable dataset exploited in this thesis.

Here follows a brief description of the instruments from which the lunar datasets used for this study were obtained. The lunar imagery, the LROC WAC-derived, and the LROC NAC-derived topographic datasets have been freely downloaded from the NASA Planetary Data System – Lunar Orbital Data Explorer (PDS – Lunar ODE https://ode.rsl.wustl.edu/moon/). Some LROC NAC-derived digital elevation models were produced for this thesis and I provide a description of the software and method in section 3.2.2 and section 3.2.3.

3.1.2.1 LOLA.

The Lunar Orbiter Laser Altimeter (LOLA) is one of the instruments on board LRO. It provides a precise global lunar topographic model and geodetic grid that serves as the foundation for lunar remote sensing data and mapping. Similarly to the instrument MOLA on board the MRO mission to Mars, the instrument transmits laser pulses. However, LOLA is a multi-beam laser altimeter, whereby laser pulses are split into five beams, allowing greater spatial accuracy, and the measurements are obtained at higher frequency (28 Hz) along track [Smith *et al.*, 2010]. This sampling strategy produces five parallel profiles along the track, which are 10-12 m apart and with an along track spacing of ~56 m.

3.1.2.2 LROC cameras.

The Lunar Reconnaissance Orbiter Camera (LROC) is a system of three cameras on board LRO. The pair of narrow-angle pushbroom imaging cameras (NACs) provide panchromatic images with 0.5 m/px resolution over a 10 km swath (each image has a swath of 5 km); the single wide-angle camera (WAC) provides images in seven colour bands with 100 m/px resolution over a 60 km swath [Robinson *et al.*, 2010]. LROC acquires images of lunar regions considered as being of particular scientific interest from multiple angles on different orbits, to allow the generation of high resolution topographic maps (Figure 3-2). LROC imagery represents principal dataset of the part of this work dedicated to lunar long runout landslides.

I used 4 LROC NAC stereo-image pairs to produce 4 digital elevation models that were used in this thesis. I provide the full list of the NAC LROC images in Table 6-1.

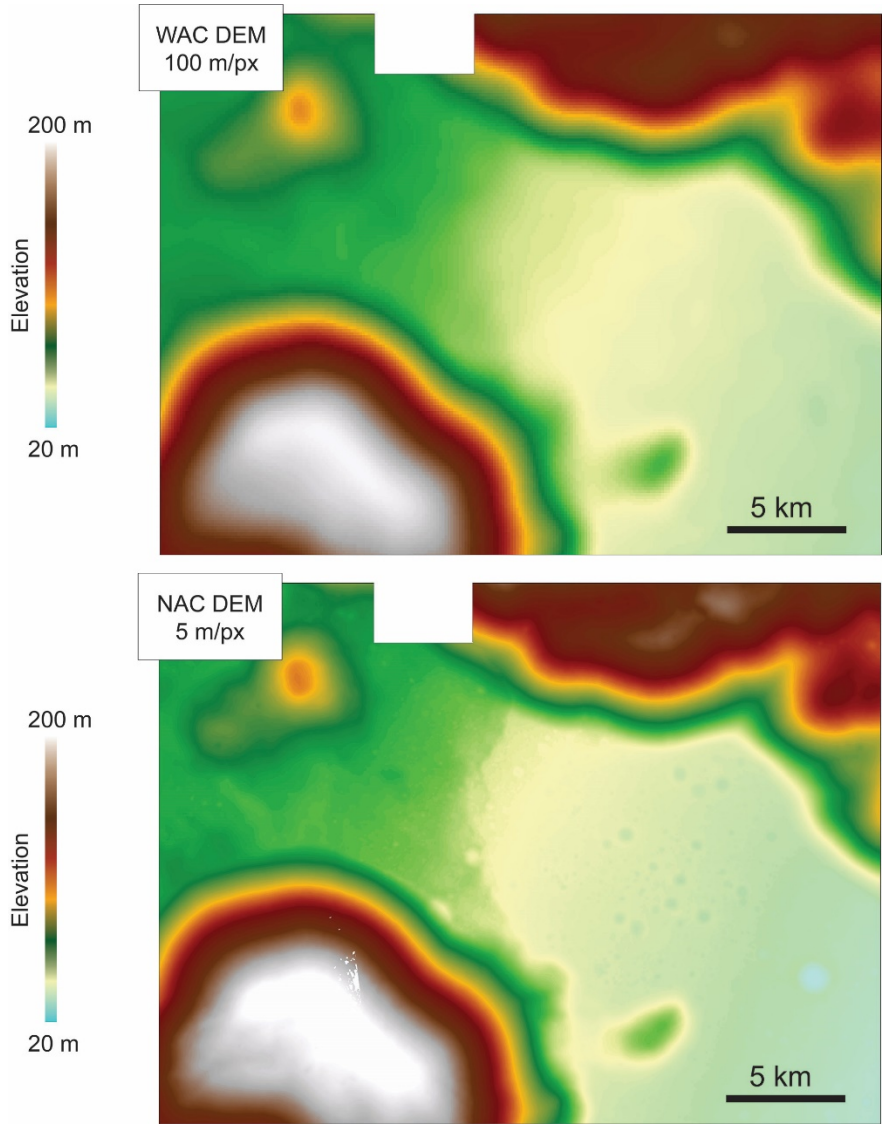

Figure 3-2 – Comparison of resolution between the two LROC cameras, Wide Angle camera (WAC) and Narrow Angle camera (NAC). The area taken for reference covers the Taurus-Littrow valley, site to the Apollo 17 landing. Note how the resolution of the LROC NAC-derived digital elevation models allow better resolution of surface features.

3.1.2.3 Lunar surface photographs, videos, and communication resource.

There exist a number of web repositories for the records of the lunar surface operations conducted by the astronauts of the Apollo missions. Of interest for this project are documents from the Apollo 17 mission, as the surface crew explored the Taurus-Littrow Valley, where the deposit of a long runout landslide was known to be present. The transcript of all recorded conversations between the astronauts and Houston, digital versions of all the

photographs taken by the astronauts during the mission, video recordings, maps, equipment drawings, voice tracks, commentary useful for this project have been obtained from the Apollo Lunar Surface Journal [Apollo Lunar Surface Journal].

3.1.3 Terrestrial satellite imagery datasets.

The gathering of information about the physical system of our planet is one of the objectives of 'Earth observation', whose function is to monitor and assess the status and changes of the Earth's natural environments from space. The first civilian satellite to be launched with the sole purpose of studying and monitoring our planet was the US Landsat 1 in 1972. The mission was a legacy from the Apollo missions, as well as the previous Mercury and Gemini missions, which inspired terrestrial terrain data acquisition from space. The Landsat 1 mission collected hundreds of thousands of photos that covered three quarters of the surface of the Earth, providing "a new window on our planet" [Williams Jr and Carter, 1976].

For this project, datasets from two European Earth observation programmes, Copernicus and Pleiades, are used to provide regional topography information of the area of study in the Northern Atacama region.

Here follows a brief description of the instruments from which the terrestrial datasets used for this study were obtained. Figure 3-3 shows the comparison of the resolution of different terrestrial elevation datasets.

3.1.3.1 Sentinel 2 satellite.

This Earth observation mission is part of the EU Copernicus Programme. The Sentinel 2 mission consists of two identical polar-orbiting satellites, Sentinel-2A and Sentinel-2B, equipped with a multispectral instrument (13 bands) and placed the same sun-synchronous orbit, phased at 180° to each other [European Space Agency, 2012]. Sentinel-2A was launched in 2015, followed by Sentinel-2B in 2017. They are able to acquire images at a resolution that

varies from 10 m to 60 m and to provide a global coverage of the Earth's surface every 5 days.

Three different types of product are generated by the mission. All data acquired are systematically processed to Top-of-Atmosphere reflectance Level-1C, which is derived from Level-1A and Level-1B products that are not made available to users. The Level-1C products are radiometrically and geometrically corrected (including orthorectification and spatial registration). From the Top-of-Atmosphere reflectance Level-1C products Bottom-of-Atmosphere reflectance Level-2A products are derived using Sen2Cor processor (discussed in Section 3.2.1).

The Sentinel 2 multispectral images were used in this project to obtain high resolution regional maps of the area in northern Chile where the landslide object of the terrestrial chapter is located. Sentinel 2 images are free to download from the USGS Earth Explorer website (https://earthexplorer.usgs.gov/).

3.1.3.2 Pleiades satellites.

The Pleiades programme was developed by the French space agency CNES and Airbus. Pleiades is an optical observation system that consists of two identical satellites, Pleiades-HR 1A and Pleiades-HR 1B, launched in 2011 and 2012 respectively, that provide very high-resolution images (50 cm) with a 20 km swath. The satellites operate in a sun-synchronous orbit, phased at 180° to each other [Eo Portal]. The along-track stereo image acquisition allows us to use the Pleaides dataset to generate high resolution digital elevation models (2 m/px; see Figure 3-3 for a comparison between resolutions of different terrestrial elevation datasets used in this thesis). For this project, Pleiades images were requested so to obtain high resolution imagery of the Chilean long runout landslide object of the terrestrial chapter, from which topographic information of the area has been extracted. The Pleiades images used for this work have CNES copyright and are distributed by the Airbus Defence and Space.

3.1.3.3 SRTM.

The Shuttle Radar Topography Mission (https://doi.org/10.5066/F7PR7TFT) consists of a radar system that flew on board the Space Shuttle Endeavour during the STS-99 mission in February 2000. The system consists of two radar antennas and applied a technique called Interferometric Synthetic-Aperture Radar to acquire topographic data.

For this project the 10 tiles of the SRTM 3 Arc-Second Global data product (90 m/px resolution; see Figure 3-3 for a comparison between resolutions of different terrestrial elevation datasets used in this thesis) have been used to obtain regional topographic information of the area in Chile that extends from Antofagasta to Iquique. SRTM data is free to download from the USGS Earth Explorer website (https://earthexplorer.usgs.gov/).

3.1.4 Drone mapping.

The use of Uncrewed Aerial Vehicles (UAVs) has been rapidly expanding in the geology community, as it represents a more affordable and more flexible alternative to traditional aerial and satellite imagery acquisition. It allows the acquisition of high-resolution images of study targets that can be used to obtain digital elevation models from Structure from Motion (SfM) techniques (e.g., James and Robson [2012]; Lucieer *et al.* [2014]; James *et al.* [2017]; see Figure 3-3 for a comparison between resolutions of different terrestrial elevation datasets used in this thesis). It also represents an effective assistive tool during field work, as it can be used to closely observe areas which are unsafe to reach or to survey potential areas of interest and assessing them in almost real time. A DJI Phantom 3 Pro drone and a DJI Phantom 4 drone were used for the 2018 and 2019 field campaign, respectively. The camera on board both models has a 1/2.3” CMOS sensor and lens with format equivalent to 35 mm, f/2.8. The Phantom 4 has 4K video recording mode. Phantom 3 Pro and Phantom 4 were flown using DJI GO app for iPhone. The free app Pix4D Capture was used to assist with drone flight route planning and automatic photo acquisition settings.

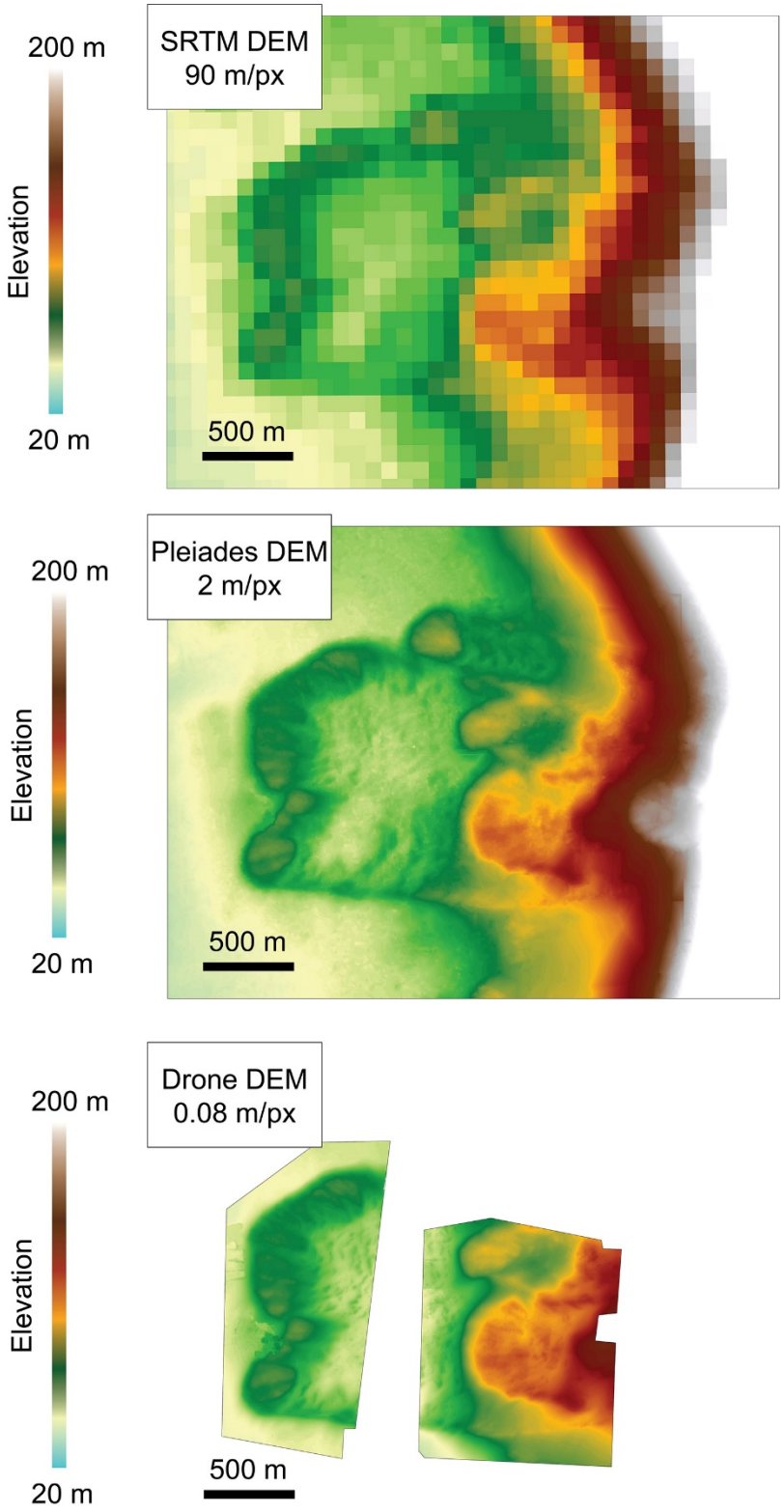

Figure 3-3 - Comparison of resolution of different terrestrial elevation datasets. The area taken for reference covers the deposit of the El Magnifico landslide, Chile, that is the case study in Chapter 5. Note the improvement in resolution of satellite-derived digital elevation model. Drone-derived digital elevation models allow to resolve the morphology of the landslide deposit even further.

3.2 Software and techniques.

3.2.1 SNAP.

The Sentinel Application Software (SNAP) is a free platform for all Sentinel Toolboxes. For this work, the SNAP application has been used to perform atmospheric correction of the Sentinel 2 images, by using the *Sen2Cor* package [Main-Knorn *et al.*, 2017] that can be freely downloaded from https://step.esa.int/main/third-party-plugins-2/sen2cor/. Band 1 (coastal aerosol) and band 9 (water vapour) have been removed and the remaining 10 bands have been resampled to 10 m. The new image product is exported as GeoTiff to be used in ArcGIS environment.

3.2.2 Planetary Data Processing and Integrated Software for Imagers and Spectrometers (ISIS).

The Integrated Software for Imagers and Spectrometers (ISIS) is a specialized processing software package developed by the USGS for NASA [Torson and Becker, 1997]. Its key feature is the ability to place many types of data from a variety of missions and instruments in the correct cartographic location.

For this project, ISIS 3 [Anderson *et al.*, 2004] has been used to process raw images from CTX, HiRISE, and LROC cameras prior and after image processing with SOCET SET (section 3.2.3). The pre-processing includes the extraction of navigation and other ancillary information using the SPICE kernels (i.e., SPICE is an information system built to assist NASA scientists in planning and interpreting scientific observations from space-born instruments; kernels are the data files containing the information; SPICE Concept (nasa.gov)) and radiometrically calibrates the images, preparing them for ingestion into SOCET SET. Product files obtained with SOCET SET (i.e., orthorectified images and DEMs) are processed again via ISIS3 to convert from planetocentric to planetographic coordinates, and converted into cube files that have been used in ArcGIS.

3.2.3 SOCET Set.

SOCET SET is a commercial software package for stereo photogrammetry sold by BAE Systems (note, SOCET SET has been enhanced and superceded by SOCET GXP; however planetary data cannot yet be processed in this new version; https://www.geospatialexploitationproducts.com/content/socet-gxp/). It uses stereo images as input data to generate digital elevation models and orthoimages as output data. Image pairs can be used for stereophotogrammetry as long as they satisfy two key requirements: they overlap (ideally at least 60%) and their emission angles differ by more than 5°. SOCET SET performs a series of steps through which the position of the two cameras are precisely calculated using a number of ground control points along with the vertical ground control information from MOLA gridded data and track points (triangulation based on epipolar geometry); images are then rectified; a digital elevation model is produced by extracting the individual pixel elevations from the images at a specific resolution; finally, the orthoimages are created.

For the creation of digital elevation models and orthoimages used in the martian and lunar chapters of this project, the USGS photogrammetry tutorial guidebook (https://astrogeology.usgs.gov/search/map/Docs/Photogrammetry/TUTORIALS_JUNE2009), which follows well-validated stereo method [Kirk *et al.*, 2008], has been used. Vertical precision is provided in the respective chapters. In order to generate digital elevation model and orthoimages of the terrestrial landslide studied in this work SOCET GXP has been used applying standard methods [e.g., Walker and Pietrzak, 2015].

3.2.4 Agisoft Photoscan (Metashape).

Agisoft Photoscan is a stand-alone software product that performs photogrammetry processing of digital images, both aerial and close-range photography, and generates 3D spatial data (https://www.agisoft.com/pdf/metashape_1_6_en.pdf - at the time of writing it

has become Agisoft Metashape). The software provides an automated processing system, consisting of a series of tasks: camera alignment, building dense point cloud, building mesh, generating texture, generating digital elevation model, and generating orthoimage.

For this project Agisoft Photoscan has been used to generate digital elevation models and orthoimages from images acquired with drone of the landslide in the north Chile. Vertical ground control information has been obtained from the Pleiades-images-derived digital elevation model. This was decided so to have comparable topographic datasets, as the accuracy and precision of the onboard drone GPS are of low quality for the purposes of this work. The details of ground control points selection and the comparison between Pleiades and onboard drone GPS-derived elevation data are provided in Chapter 5, where the work on the terrestrial case study is described (see section 5.2.1, Figure 5-5, and Figure 5-7).

3.2.5 ArcGIS and Python.

The digital elevation models and orthoimages generated from the different imagery datasets have been imported in the ESRI geographic information system ArcGIS, the primary tool for geomorphological mapping and analysis for this project. ArcGIS has a geoprocessing toolbox that allows to perform fundamental GIS operations. ArcGIS uses Python, a programming language. The use of Python for ArcGIS is a powerful tool that allows users to customize the functionalities found in the ArcGIS Toolbox.

3.2.5.1 Python custom scripts.

For this project, Python has been used in ArcGIS to make steps of the mapping and processing automated and more efficient. More importantly, this implementation allows to carry out analysis consistently throughout all the case studies, limiting the introduction of errors and bias by the user (Figure 3-4, Figure 3-5). Custom scripts have been written to: 1) mark the intersection of mapped longitudinal ridges with transverse profiles traced to conduct

morphometric analysis; 2) calculate the average thickness of landslide deposits and the average spacing between longitudinal ridges in correspondence of transverse profiles traced for conduction the morphometric analysis; 3) plot data (see Appendix IV).

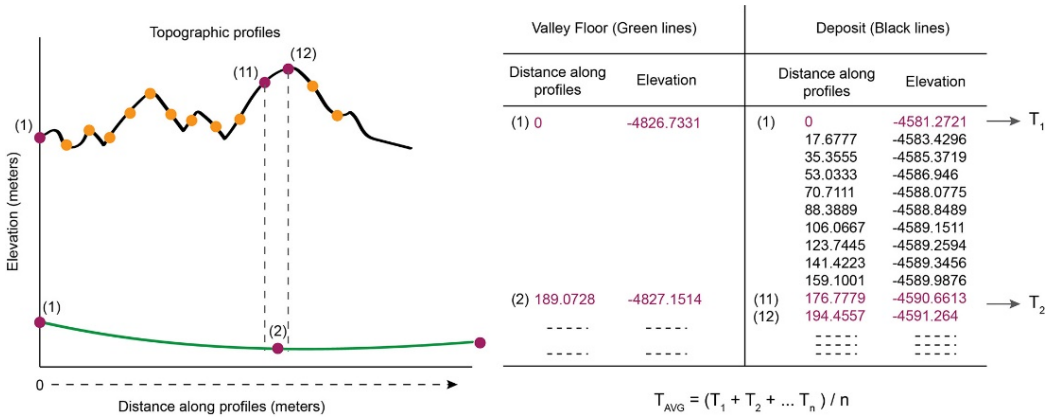

Figure 3-4 – Visualization of the method used to calculate the average thickness of landslide deposit along transverse topographic profiles. The surface deposit and the reconstructed valley floor have different spatial resolution, so that surface deposit topographic profiles have more points than reconstructed valley floor profiles, therefore preventing a direct correlation and thickness assessment point by point. Elevations are calculated in correspondence of every point of the reconstructed valley floor profile. For each point of a reconstructed valley floor profile, if its distance matches the distance of a point along the surface deposit profile (in the example is point (1), as both their distance is 0), the thickness is calculated by subtracting the two elevation values (e.g., T_1); if not, I consider the points of the surface deposit profile, whose distance is the closest (closest before, point (11), and closest after, point(12)) to the distance of the point of the reconstructed valley floor profile; the elevation of the two closest points is averaged and the elevation of the valley floor is subtracted to this averaged elevation (e.g., T_2). The final thickness of the deposit along a topographic profile (T_{AVG}) is then obtained by averaging all the thickness values obtained in correspondence of every point of the reconstructed valley floor profile. This procedure is automated with a custom Python script.

3.2.5.2 Geomorphological mapping.

The mapping of the long runout landslides chosen as case studies for this project has been done in ArcMap. Their deposits and, where possible, their source areas have been digitised using polygons features. Morphological features that are related to the landslides, such as longitudinal ridges, and other structures that are evident on the surface of their deposits, such as lineations and scarps, have been digitised as polyline features using CTX images (Figure 3-5).

Longitudinal ridges of long runout landslides are the main morphological features that have been studied in this project. As such, it is important to define what is considered a longitudinal ridge in this work and how it is identified:

- A longitudinal ridge is a long, elevated area that is delimited by its horizontal continuity in the direction of the flow (i.e., away from the headscarp);
- A longitudinal ridge can extend for almost the entire length of the landslide deposit;
- A longitudinal ridge is mapped as it appears as a continuous morphological feature from a top-view observation of the landslide deposit;
- A longitudinal ridge is mapped as a continuous line that is placed within the highest elevated area between two troughs (the line theoretically happens to be at the midpoint between adjacent the two lowest areas, as in an idealised periodic wave).

The distance between the two adjacent ridges is called ‘spacing’ in this work and the average spacing between ridges along a transversal profile is used as a proxy of the ‘wavelength’ of the ridges.

For the case study of the Coprates Labes landslide on Mars, other morphological features have been mapped on the surface of the deposit, which have been named ‘lineation’ and ‘scarp’ in this work. A lineation is a linear feature superposed to a longitudinal ridge; a lineation appears on a limb of the longitudinal ridge; it is oriented with an angle relative to the direction of the longitudinal ridge, with the forward termination (relative to the direction of movement of the landslide) pointing at the highest, central sector of the ridge, and the rear termination pointing at the adjacent trough; and it is roughly s-shaped. A scarp is a linear feature along which sections of the landslide deposit are displaced vertically, with the downstream section being lower; along a scarp a longitudinal ridge is vertically displaced but, from top-view, it maintains its continuity.

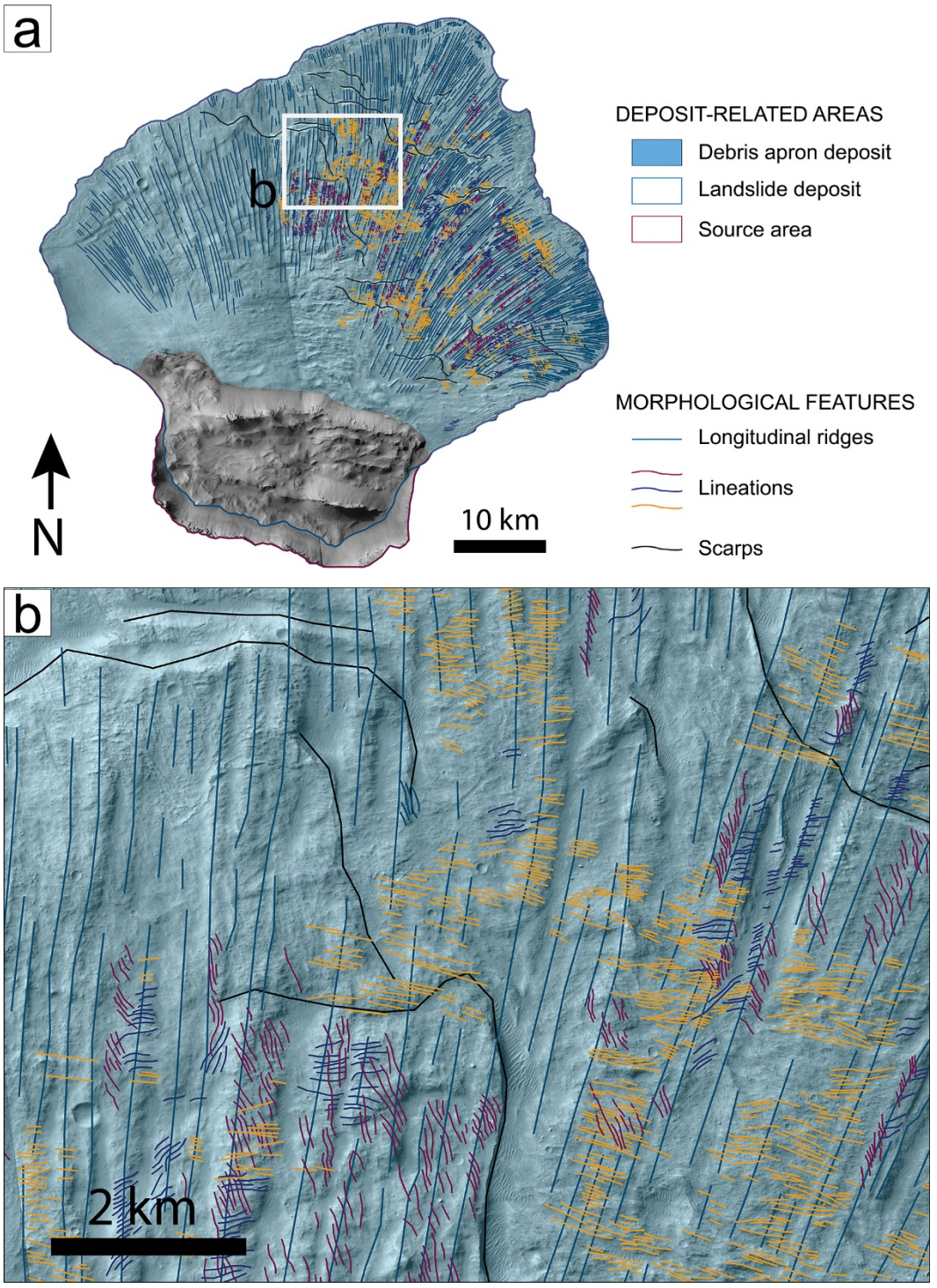

Figure 3-5 – Geomorphological mapping and Python automation. a) Example of geomorphological features mapped in ArcGIS. The different colours used to identify lineations represent different sets of orientations.

3.2.5.3 Volume calculation.

In this thesis, the volume has been calculated only for the Coprates Labes landslide on Mars. Therefore, here follows a description of various methods used in the literature to calculate the volume of martian landslide.

The volume of the mass that formed the slope prior to failure is referred to as the 'initial volume' (V_i) of a landslide. The volume of the landslide deposit generated during the mass-wasting event is referred to as 'final volume' (V_f) of a landslide. As discussed in Chapter 2.1.1 and Chapter 2.2.1, it is important to distinguish between the two types of volumes; the difference can reveal the existence of entrainment of valley sediment within the sliding mass.

The ideal way to calculate both initial and final volume of a landslide is studying the differences in high resolution topography of the slope and of the valley floor prior to and after failure. A number of terrestrial satellites allow regular and frequent coverage of the Earth surface with resolution down to tens of centimetres per pixel (e.g., the Pleiades satellite constellation). LiDAR airborne and ground data collection is an effective way to obtain high resolution topography data before and after mass-wasting events [e.g., Conway *et al.*, 2010; Conway *et al.*, 2015]. In recent years, the use of drones has reduced the cost of topographic surveying, while being able to provide digital elevation models with a couple of centimetres of resolution per pixel [e.g., James and Robson, 2012; Lucieer *et al.*, 2014; Slatcher *et al.*, 2015]. The combination of these different data sources is a powerful tool in landslide monitoring and volume estimations.

The surface of Mars and of the Moon has been being photographed regularly over recent decades thanks to NASA missions such as MRO and LRO. The relatively frequent coverage of the same areas of the martian surface has been providing evidence of active surface processes, amongst them gully formation [e.g., Dundas *et al.*, 2015; Jouannic *et al.*, 2019] and ice landsliding ([Becerra *et al.*, 2020]; Figure 3-6). However, currently high-resolution topography data prior to a long runout landslide event is not available. Therefore, volume calculation of martian and lunar landslides relies on

approximations of the slope and valley topography before the event. For this reason, in this work, the term ‘volume estimation’ will be used.

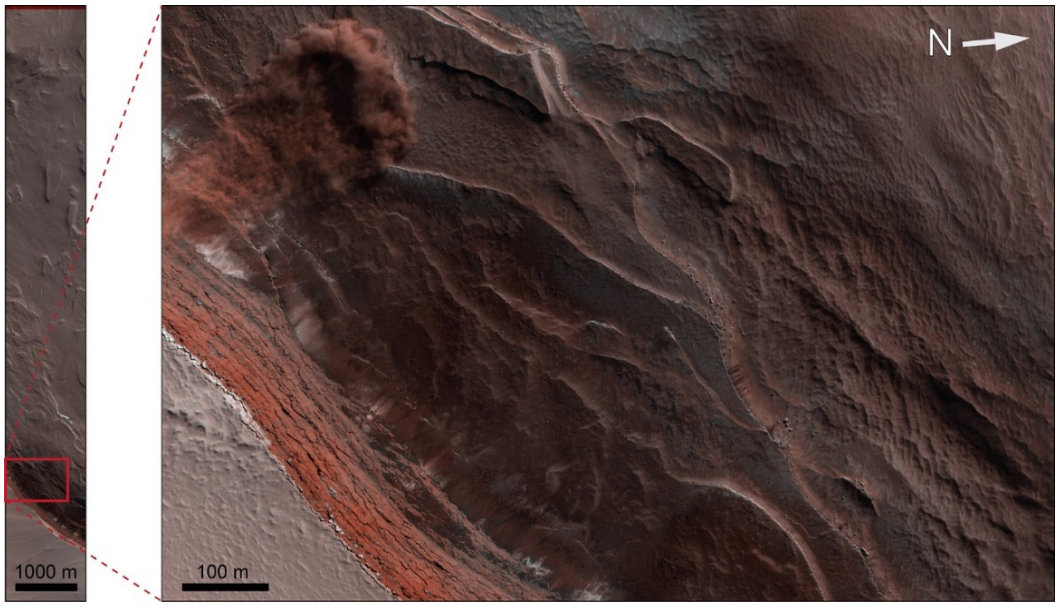

Figure 3-6 – Martian landslide live. This HiRISE image captured a number of landslides in the happening along a cliff of the martian North Pole. The cliff is about 500 m height and maybe of layered deposits. The landslides are caused by the sun warming the ice present within the layered deposits, causing the part of the rocky cliff to break loose. These mass wasting events generate a cloud. This HiRISE image was acquired 29th May 2019**;** https://www.uahirise.org/ESP_060176_2640. As these events did not produced well-defined deposit, they may correspond to rockfalls or avalanches.

In the literature, different methods have been used to obtain volume of long runout landslides on Mars, as follows:

1) in Mcewen [1989] (Figure 3-7), for large landslides with well-defined scarps, volume is computed as:

$$V = Z * A + 0.5\,W * Z^2\,(tan[90 - \theta_1] - tan[90 - \theta_2])\,,$$

where Z is the height drop, A is the estimated scarp area, W is the width of the scarp, θ_1 is the estimated pre-landslide slope, and θ_2 is the post-landslide slope.

2) in Mcewen [1989], for the smallest landslides, based on the assumption that small landslide deposit do not change as much as large ones, volume is calculated as:

$$V = A_{(landslide\ deposit)} * h_{(flow\ front)}$$

3) in Harrison and Grimm [2003] (Figure 3-8), the initial volume is estimated from the approximate measurements of the slope elevation H, inferred from surrounding topography of the canyon floor and canyon wall, approximate measurements of the scar width W, scar slope α_1, and a typical nearby wall slope α_2.

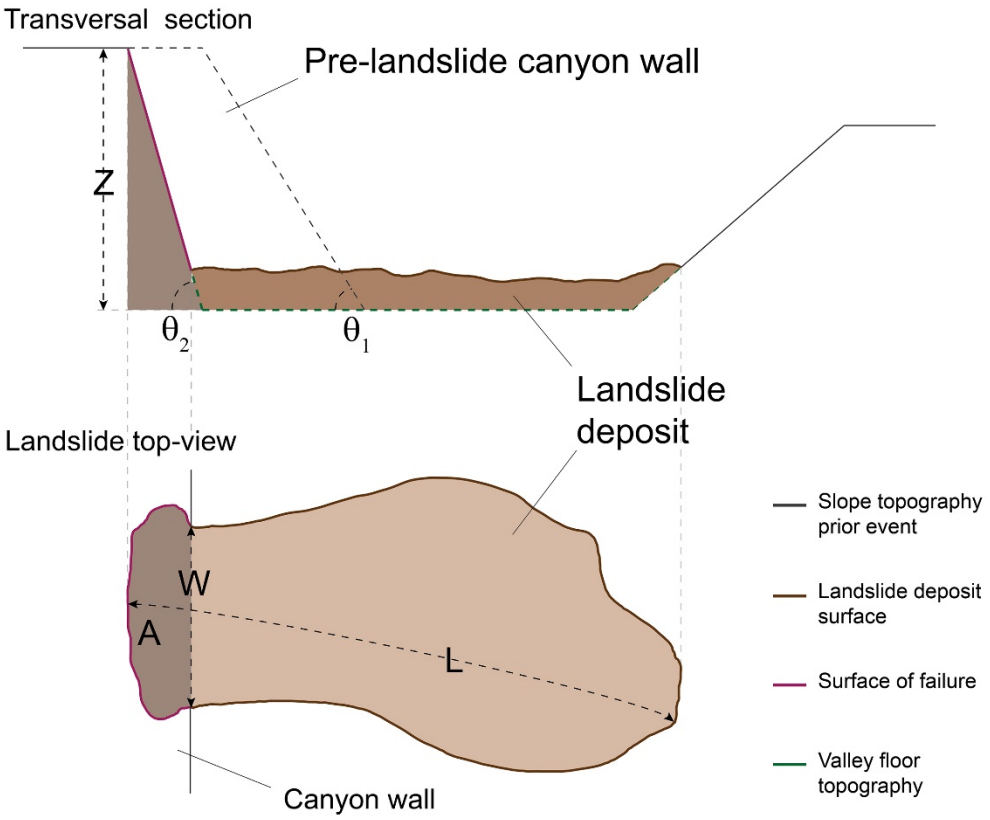

Figure 3-7 – Volume calculation after Mcewen [1989].

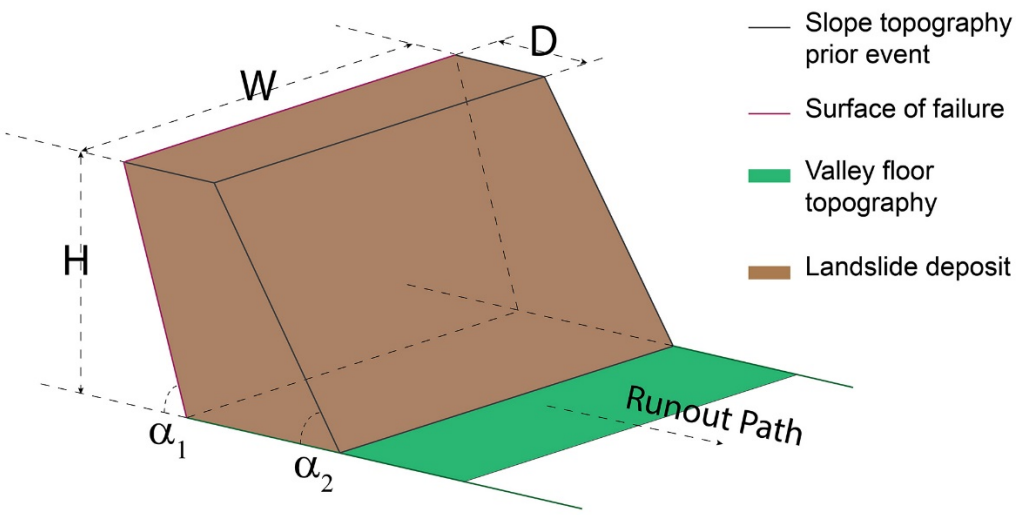

Figure 3-8 – Volume calculation after Harrison and Grimm [2003].

4) In Quantin *et al.* [2004a], initial and final volumes are assessed by using the MOLA DEM of the landslide deposit and the DEM of the reconstructed pre-landslide topography. The reconstruction of the topography prior to the event is done by linear interpolation between two reference topographic profiles on each side of the landslide across wall slopes not affected by slides.

In this project, the volume of the martian long runout landslide case study, Coprates Labes, has been estimated following the method used in Quantin *et al.* [2004a], that is digital elevation model of the current topography and digital elevation models obtained from reconstructing the slope topography and the basal surface covered by the landslide deposit. Compared to Quantin *et al.* [2004a], for this work, higher resolution topographic data was available from the NASA MRO mission. In Chapter 4, the result of the volume estimation is presented and compared to other values found in the literature.

4 Case study I – Mars: the Coprates Labes landslide, Valles Marineris.

Part of the work conducted in this chapter has been published as peer-reviewed article and it can be found in the appendix and at the following reference:

"*Magnarini, G., Mitchell, T.M., Grindrod, P., Goren, L., and Schmitt, H. (2019). Longitudinal ridges imparted by high-speed granular flow mechanisms in Martian landslides. Nat. Commun. 10, 4711. https://doi.org/10.1038/s41467-019-12734-0*".

4.1 Introduction.

The first images of landslides on Mars came from the NASA Mariner 9 mission [Sharp, 1973a]. However, it is with the Viking missions programme that their extraordinary morphologies were revealed and their importance as geological process in the shaping of Valles Marineris was grasped [Blasius *et al.*, 1977; Lucchitta, 1979]. The geomorphological similarity of martian and terrestrial landslides has sparked long lasting discussions on the importance of water in the emplacement of long runout landslides and, more generally, the necessity of fluids has been widely questioned (as discussed in Chapter 2.1.2). It is reasonable to consider that the high mobility that long runout landslides have in common and their morphological similarities are a result of a similar mechanism of emplacement. However, the geomorphological issue of 'equifinality' (i.e., similar landforms originate from different processes) is a major challenge in the interpretation of martian landforms, as in situ data are

limited to robotic exploration at few localized sites, and must be taken into consideration when linking morphology to processes [e.g., Balme *et al.*, 2011]. It follows also that interpretations based on morphological analysis may be biased due to morphological similarity [Johnson and Campbell, 2017].

Longitudinal ridges are ubiquitous on the surface of long runout landslides on Mars. On Earth, such features are commonly found in landslides emplaced on glaciers, amongst which is the iconic Sherman Glacier landslide [Marangunic, 1968]. Consequently, their morphological similarity to those observed in martian long runout landslides has been used as an analogy to infer the presence of an icy substrate at the time of landslide emplacement on Mars [Dufresne and Davies, 2009; De Blasio, 2011] (see Chapter 2.1.1/'Longitudinal ridges'). It has been proposed that the presence of ice on the surface reduces the frictional coefficient, permitting either the splitting of the deposit as a consequence of either lateral spreading [De Blasio, 2011] or the dominant role of inertia over lateral spreading forces [Dufresne and Davies, 2009], leading to the formation of ridges and troughs perpendicular to the spreading direction. The presence of ice is also suggested to explain the development of longitudinal grooves in martian double layered ejecta craters [Weiss and Head, 2013] which also show morphological similarity to the longitudinal ridges associated with landslides, although other mechanisms are not excluded [Boyce and Mouginis-Mark, 2006; Quintana and Schultz, 2014]. However, longitudinal ridges have been observed also in landslides on the Moon [Guest and Murray, 1969; Boyce *et al.*, 2016; Schmitt *et al.*, 2017], which is considered to have been free of extensive ice (glacier-like) throughout its geological history.

However, Borzsonyi *et al.* [2009] suggested the possibility that longitudinal ridges and furrows of large planetary rock avalanches may be related to fluid-like instabilities forming convection cells that result in longitudinal 'stripes' parallel to the flow direction. This was based on previous experimental and theoretical work [Forterre and Pouliquen, 2001; 2002] demonstrating turbulent flow processes that are well known to occur in fluid mechanics. The experimental work and stability analysis on rapid granular flows conducted by Forterre and Pouliquen [2001; 2002] showed for the first time the

spontaneous formation of longitudinal vortices that manifest as superficial longitudinal ridges and furrows, whose initiation depends on the velocity of the flow, roughness of the basal surface, and the consequent strong shear at the base of the flow. Importantly, Forterre and Pouliquen [2001] demonstrated a clear morphological scaling relationship in that the wavelength of the ridges scales with the thickness of the flow by a factor of ~2-3 and that the ridge pattern drifts in the transverse direction. Further experiments and numerical modelling by Borzsonyi *et al.* [2009] confirmed that the longitudinal pattern naturally arises from mechanical instabilities within rapid granular flows. While demonstrated experimentally, such scaling relationships have yet to be demonstrated in any planetary landslide.

Inspired by the results of the experimental and numerical modelling work on rapid granular flows, I decided to investigate whether the same scaling relationship between the wavelength of the ridges and the thickness of the deposit occur at field scale in long runout landslides. For this purpose, I chose a well-preserved martian long runout landslide, the Coprates Labes landslide (67.75 W° – 11.80° S), in Coprates Chasma, Valles Marineris (Figure 4-1), and conducted detailed morphometric analysis and morphological observations of its deposit.

Measuring from the head scarp to the toe, the landslide has an extension (L) of about 63 km long and a height drop (H) of almost 5 km, therefore characterized by an H/L ratio of about 0.08 (Figure 4-1d). The surface of failure scar is 28 km wide (measured parallel to the Coprates Montes ridge) and about 12 km long (measured perpendicular to the ridge). The surface morphology of the deposit consists of a very proximal zone characterized by rotational blocks that most entirely covers the lower part of the surface of failure and an unconfined outer zone with a fan-shaped lobe marked by longitudinal ridges. The fan-shaped lobe lies entirely on the Valles Marineris floor and it reaches 63 km away from the scarp at its furthest extent.

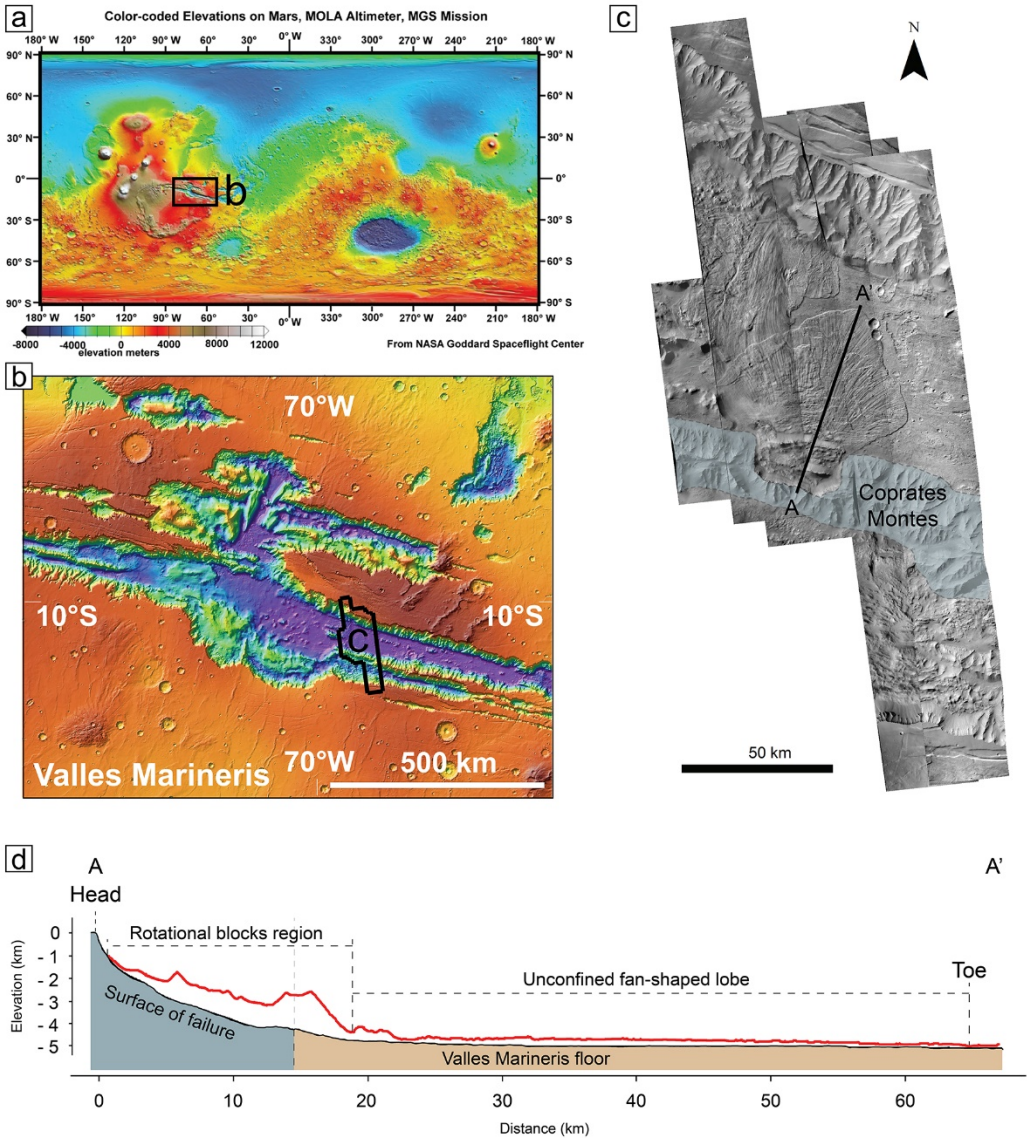

Figure 4-1 – Regional context of the Coprates Labes landslide. a) Topographic map of Mars; the black box shows the location of Valles Marineris. b) Topographic map of Valles Marineris; the black polygon shows the footprints of the CTX image mosaic that captures the Coprates Labes landslide. c) CTX image mosaic that shows the Coprates Labes landslide and the Coprates Montes (identified in light blue). d) Topographic profile of the landslide deposit (red line) along the section A-A'; features and regions of the landslide deposit are marked; the topographic surfaces are extracted using the CTX-derived digital elevation models and the reconstructed surfaces shown in Figure 4-4.

4.2 Data and methods.

This section describes the datasets and methods used to obtain the results for this case study. It also describes how the errors related to dimensional and volumetric measurements were quantified.

4.2.1 Photogrammetry.

Morphological mapping of the Coprates Labes landslide was conducted using the NASA Mars Reconnaissance Orbiter (MRO) Context (CTX) camera (6 m/px; Malin *et al.* [2007]) and HiRISE camera (25 cm/px; Mcewen *et al.* [2007]). I made use of the USGS Integrated Software for Imagers and Spectrometers (ISIS) package [Kirk *et al.*, 2008] to pre-process CTX stereo-pair images. The processed CTX images were imported in SOCET SET commercial suite from BAE Systems to obtain digital elevation models (DEMs) and ortho-rectified images using well-validated previous methods [Kirk *et al.*, 2008]. These image products were post-processed with ISIS to create final images that could be used in ArcGIS (see Section 3.2.2, 3.2.3, 3.2.4).

Despite the global coverage of Mars by CTX images, I was not able to find acceptable CTX stereo-pair images to make a DEM of the entire landslide deposit. I used 4 CTX stereo-pair images (Table 4-1) which left a discontinuity in the DEM of the landslide (Figure 4-2a).

***Table 4-1* - List of CTX image pairs used to make DEMs.** Vertical precision is estimated using the method of Okubo [2010] (IFOV = Instant Field of View).

Image Pairs (ID number)	Pixel size (m)	Incidence angle (°)	Phase angle (°)	Emission angle (°)	IFOV (m)	Vertical Precision (m)
B21_017688_1685_XN_11S067W	5.24	60.49	63.02	3.61	5.66	2.35
B22_018321_1685_XN_11S068W	6.06	62.54	47.41	22.17		
P20_008906_1685_XN_11S067W	5.28	61.93	57.0	19.47	5.56	2.24
P22_009763_1690_XN_11S067W	5.82	60.58	76.01	26.4		
P19_008616_1689_XI_11S068W	5.28	60.41	58.16	15.83	5.45	3.18
P21_009051_1688_XN_11S068W	5.61	60.79	72.57	18.89		
P16_007113_1678_XN_12S067W	5.25	45.61	49.76	8.6	5.29	13.08
F20_043784_1677_XI_12S067W	5.32	58.72	452.86	4.62		

Nevertheless, the DEM coverage available allowed me to conduct a detailed morphometric analysis of the central and eastern part of the landslide deposit. The DEM obtained from the High Resolution Stereo Camera (HRSC; H0515_0000) on board the ESA Mars Express was integrated to the CTX-derived DEMs in order to calculate the volume of the landslide deposit (Figure 4-2b).

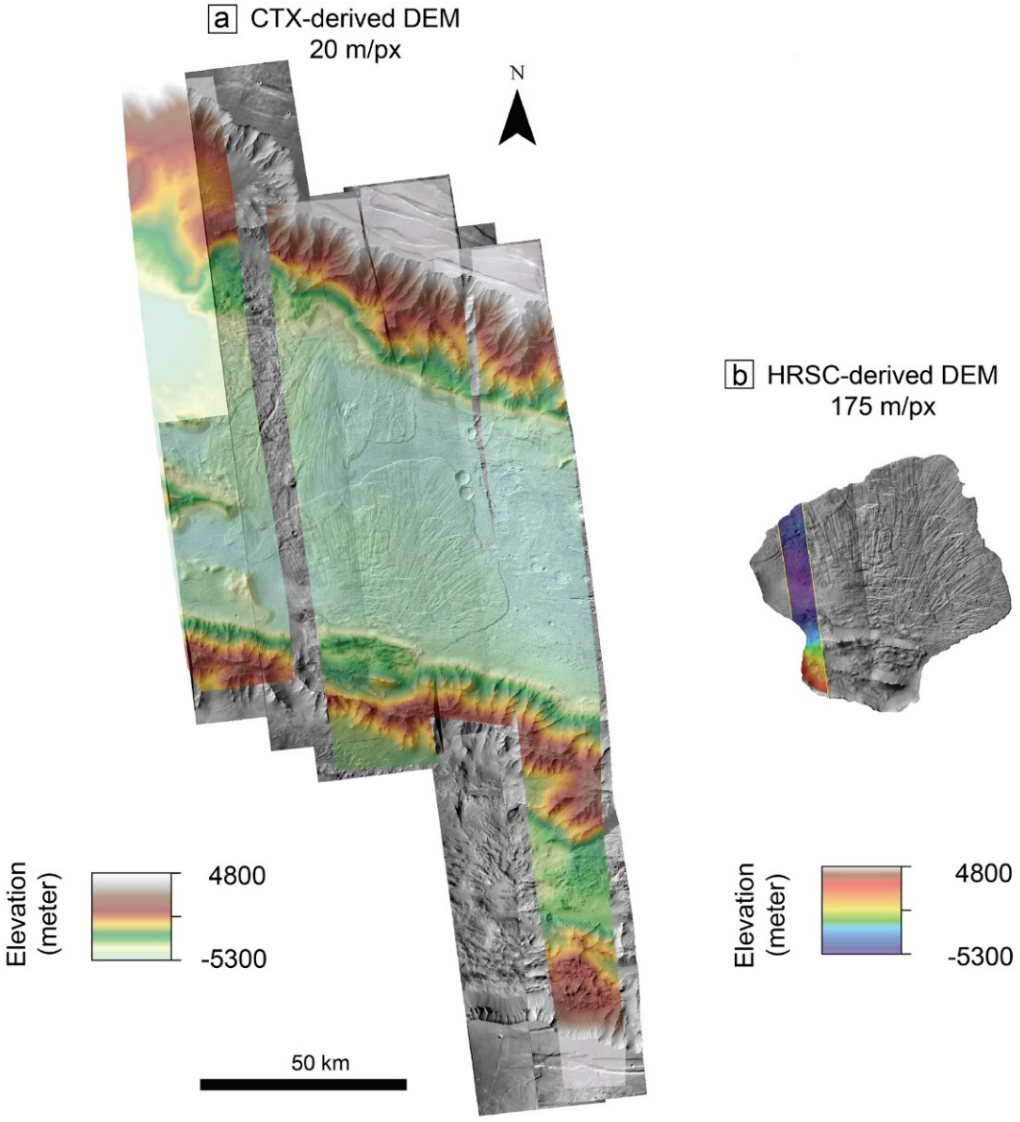

Figure 4-2 – Digital elevation models coverage of the Coprates Labes landslide. a) CTX-derived DEM of the area of study. The DEM coverage of the landslide deposit is not continuous. b) Mars Express HRSC-derived DEM used to obtained topographic data of the landslide deposit not covered by the CTX-derived DEM.

4.2.2 Morphological characterization.

The morphological mapping, morphometric analysis, and volume calculation were carried out in ArcGIS. Features and units of the landslide were digitized using polyline and polygon shapefiles (Figure 4-3). Central to this case study was the mapping of longitudinal ridges, which were digitized as polylines along their crest. A longitudinal ridge is determined by its horizontal continuity in the direction of the slide and its presence as morphological feature is unmistakable from a top-view observation of the landslide deposit (Figure 4-3a).

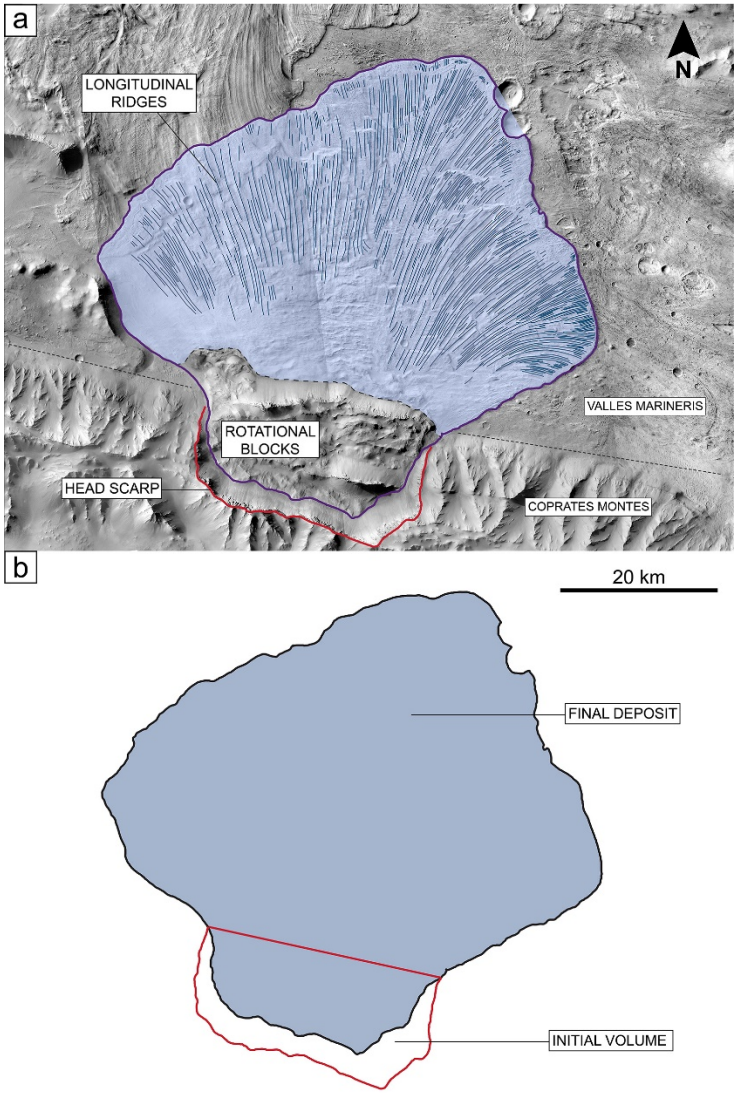

Figure 4-3 – Morphological mapping of the Coprates Labes landslide. a) Geomorphological features and units of the Coprates Labes landslide: the red line shows the head scarp of the landslide; the purple line shows the contour of the final deposit of the landslide; the black dashed line separates the rotational blocks that characterize the most proximal region of the landslide deposit from the region of the landslide deposit that lies entirely on the floor of Valles Marineris and is marked by longitudinal ridges (navy blue lines).

A number of operations involved in the morphometric analysis and the calculation of the thickness of the deposit were executed using a number of Python scripts that I wrote in order to automate otherwise repetitive and time-consuming calculations (see Appendix IV-Script n°1).

4.2.3 Deposit volume, deposit thickness and error estimation.

Volume calculation and thickness estimation of a landslide deposit require the reconstruction of the surface of the valley floor underneath the current deposit (Figure 4-4a and c), the initial topography of the slope (i.e., the slope topography prior the collapse; Figure 4-4a and d) and the surface along which the failure occurred (which is partially covered by the very proximal part of the deposit constituted of rotational blocks; Figure 4-4b and e). These newly created surfaces only approximate the real original topography and, therefore, the final estimations of the volumes and thickness carry uncertainties.

In order to recreate these surfaces I interpolated the topographic contours of the current topography around the landslide, as this is the method commonly used in the literature [Harrison and Grimm, 2003; Quantin *et al.*, 2004a; Conway and Balme, 2014]. For reconstructing the initial slope topography, I simply traced straight lines interpolating topographic contours of the head scarp (Figure 4-4d). For reconstructing the surface of failure, I manually traced the interpolating lines so that they closely follow the shape of the head scarp at the highest part and progressively straighten while getting closer to lowest part, assuming the last contour horizontal (Figure 4-4e); this configuration results in a concave-up shape of the surface of failure, similar to the spoon-shape surface reconstruction in Lucas *et al.* [2011]. For reconstructing the valley floor underneath the landslide deposit, I had to take into consideration the presence of the overridden terminal edge of a landslide that developed from the opposite cliff; moreover, by then simply tracing straight contour lines, the west part of the reconstructed surface would have appeared above the current landslide topography, hence impossible (Figure 4-4c; Figure 4-5).

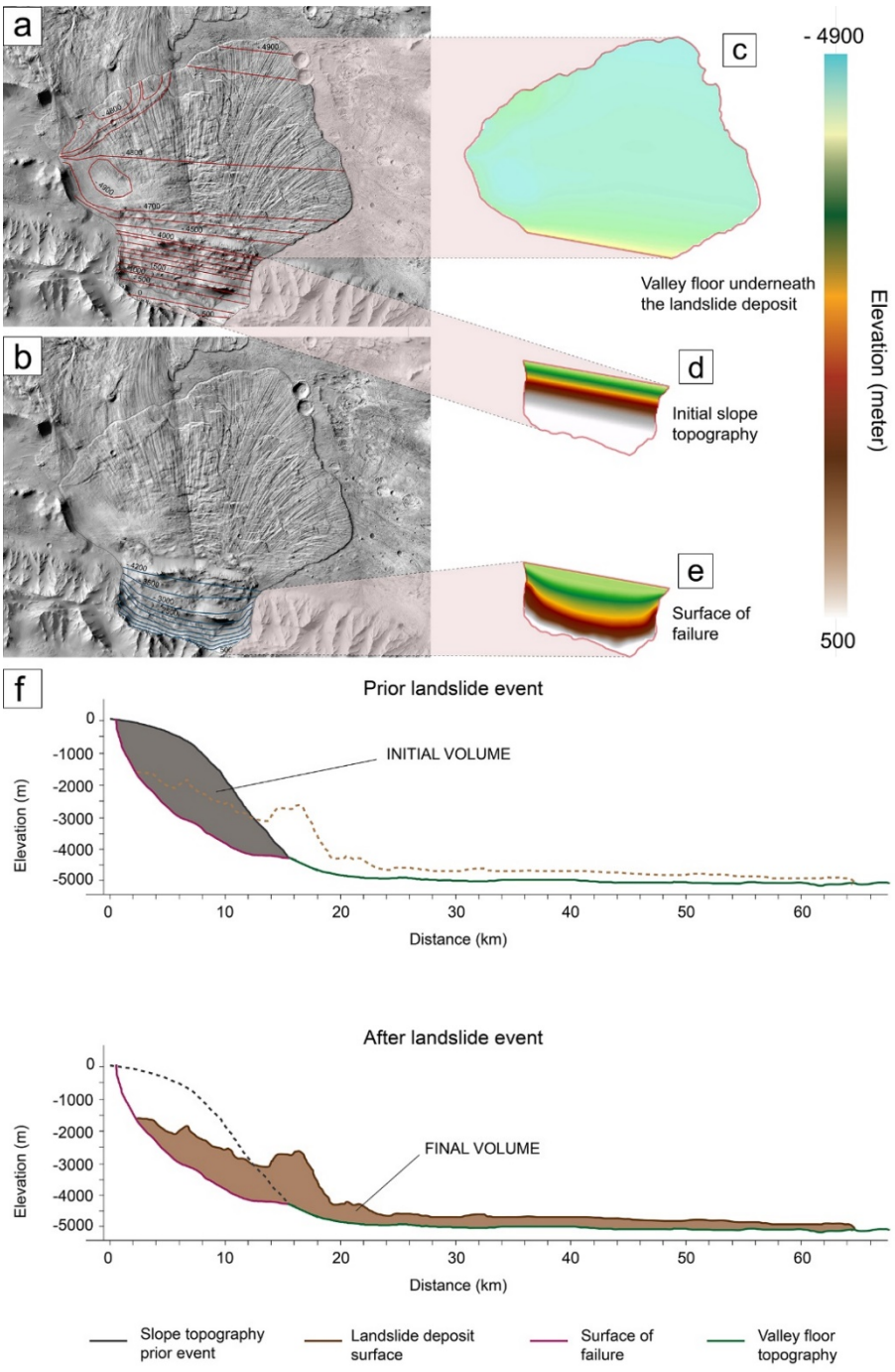

Figure 4-4 – Reconstruction of topographic surfaces at the Coprates Labes landslides. a) Estimated topographic contours of the topography prior the landslide event, which include the valley floor topography that is now underneath the landslide deposit and the initial slope topography; these contours were derived by manual interpolation of the topographic surfaces around the landslide. b) Topographic contours of the surface of failure, which is now partially covered by rotational blocks that form the very proximal region of the final deposit. c) and d) DEMs of the valley underneath the landslide deposit and of the initial slope, respectively, obtained from the contour lines in a). e) DEM of the surface of failure obtained from the contour lines in b). f) Longitudinal profiles of the landslide deposit showing the current and reconstructed topographies, which are used to calculate initial and final volume and the thickness of the deposit. These reconstructed surfaces are also used to produce the longitudinal topographic profile in Figure 4-1d.

In order to prevent such impossible scenario, a first order of plausibility of the reconstructed valley floor was provided by using the ArcGIS tool called 'CutFill': the tool subtracts two given raster surfaces and provides a colour-coded map where blue corresponds to a positive difference and red corresponds to a negative difference (Figure 4-5). Using this method, I realized that there must be a depression below the west side of the landslide deposit, which has a minimum elevation of -4900 m. It is not possible to determine the origin of such depressed area and it could be a crater as well as any other irregularities such as those observed to the north-east part of the deposit.

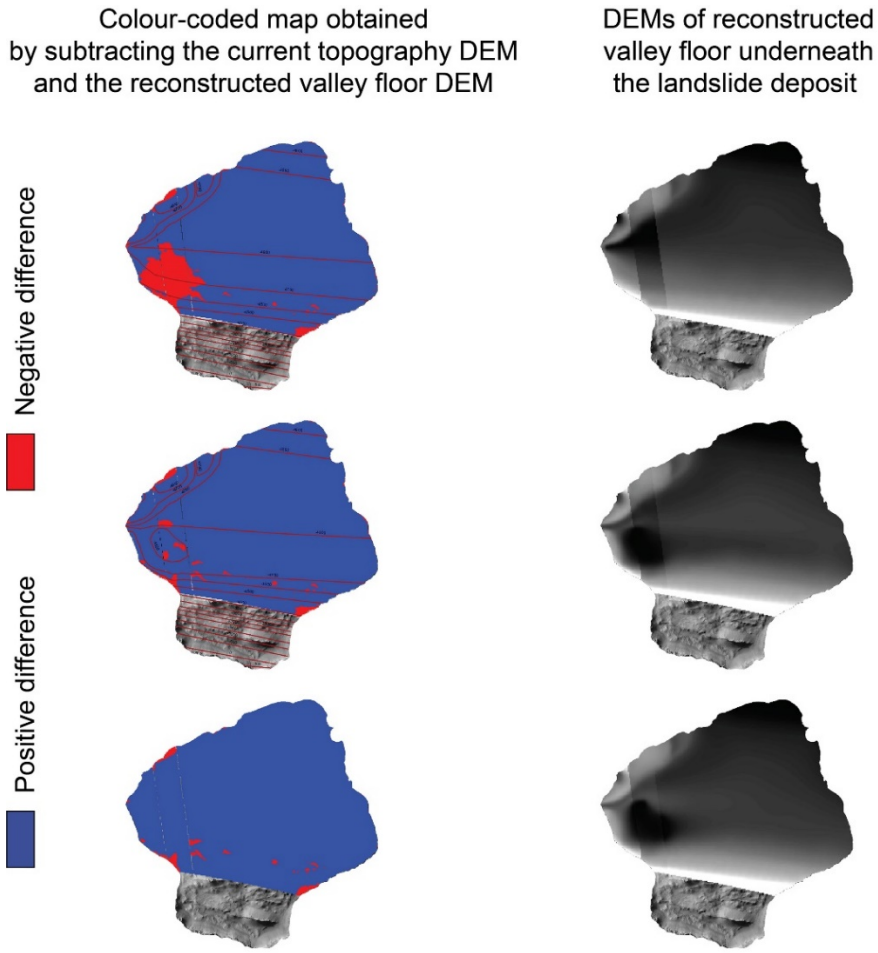

Figure 4-5 – Attempts to reconstruct the valley floor underneath the landslide deposit. The column to the left shows the results using the ArcGIS tool 'CutFill'. The column to the right shows the DEM of the reconstructed valley floor underneath the landslide deposit. In order to avoid the impossible situation where the reconstructed basal surface appears above the current topography (red areas in the left column), I adjusted the contour lines until a satisfactory result was obtained. However, the final reconstructed basal surface (bottom row; Figure 4-4a) can only be an approximation of the real underlying surface.

Beside the uncertainties derived from the reconstruction of the topography, other uncertainties are introduced in the thickness estimation because the CTX-derived DEM (landslide deposit topography) and the newly built DEM representing the valley floor (bottom surface of the landslide) have different resolution. This implies that the number of elevation points available for these surfaces is different, therefore preventing a direct correlation and thickness assessment point by point. I overcame this aspect by taking elevation points of the valley floor and the correspondent closest elevation points (one before and one after) of the landslide deposit. I then averaged the elevation between these two points and calculated the thickness. The thickness values obtained per each point of the valley floor were finally averaged. In order to automate these steps, I wrote a custom Python script (see Appendix IV-Script n°1).

Measuring the actual thickness of landslide deposit is an issue that other papers have raised as related to the landslide volume calculation [Mcewen, 1989; Harrison and Grimm, 2003; Quantin *et al.*, 2004a]. However, none of these works provide a quantitative error estimation. Given the importance of the thickness parameter to the principal conclusion of the paper, providing error estimation is of great significance in this case study. As such, I now explain the methods I used. First of all, I traced profiles transversal and longitudinal to the valley floor, adjacent to the central and east areas of study (Figure 4-5a). This set of transects (yellow lines), in the specific their linear fits (burgundy lines), is compared to a mirror set of transects traced in correspondence of the landslide deposit (blue lines) so as to: 1) assess the plausibility of the overall elevations of the reconstructed bottom surface, and 2) provide an error estimation of the average thickness calculation.

1) As the floor of Valley Marineris gently dips towards east, the higher elevation of the blue lines 1 and 2 are plausible (Figure 4-5b). However, I was also expecting a random natural roughness of the valley floor at various scales so that also blue lines 3 and 4 appear plausible, as their maximum offset is ~ 80 m (blue line 3), which is within a reasonable magnitude of topographic variation (Figure 4-5b).

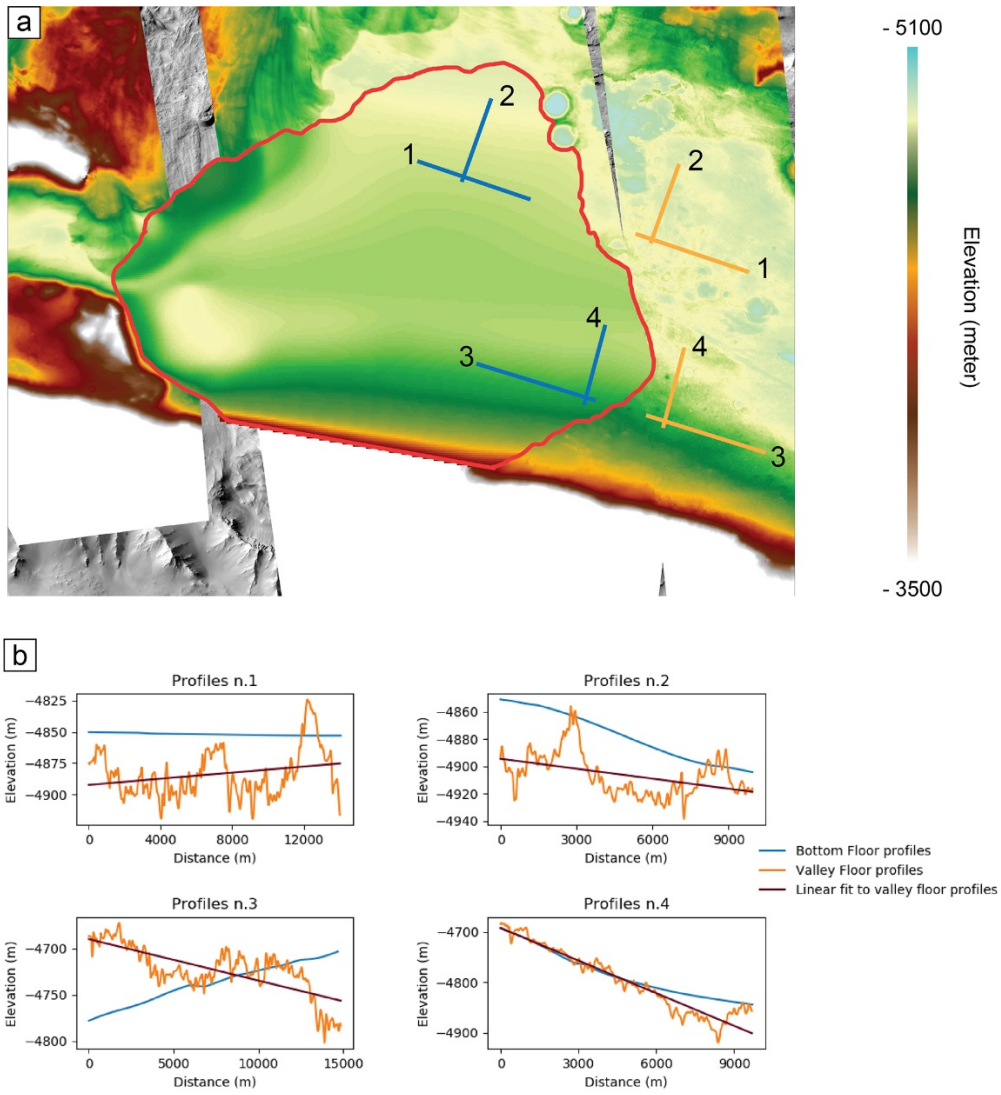

Figure 4-6 – Comparison of reconstructed valley floor topography and actual valley floor topography. a) Reconstructed DEM of the valley floor underneath the landslide deposit (marked with the red line) as inferred by interpolation of the CTX-derived DEM contour lines adjacent the deposit; using same colour-code convention provides a first order of comparison of the elevation data of the two digital elevation models. b) Plots show the comparison of mirror transects, the blue (reconstructed valley floor topography) and yellow (real valley floor topography) lines numbered from 1 to 4 in a); burgundy lines represent the linear fits of the real topography (yellow lines).

2) I decided to express the error as standard deviation of the elevation points of the topographic profiles on the actual valley floor. To do so, I used the topographic that I traced in the valley floor, adjacent to the central and east areas of study (yellow lines). As the topographic profiles that I traced for the morphometric analysis are parallel to neither transversal nor longitudinal

direction, I determined the final error taking into account the propagation of error along these two axes (Equation 1).

The propagation of error is obtained by combining standard deviation for yellow lines 1 and 2 to obtain the error in the central area of study (Table 4-2) and yellow lines 3 and 4 for the error in the east area of study (Table 4-2). The errors are represented as bars in Figure 4-9.

$$\sigma_k = \sqrt{\sigma_i^2 + \sigma_j^2} \quad (\textit{Equation 1})$$

Table 4-2 – Error estimation of the reconstructed surface underneath the Coprates Labes landslide. Standard deviation of the topographic elevation measurements along each set of transects and propagation of error, as derived from *Equation 1*, to evaluate errors on the deposit thickness calculation for the central area of study (c) and the east area of study (d).

Profiles	Standard deviation σ	Propagation of error σ_k
Yellow line 1	18.98 m (σ_i)	24.61 m (Central study area)
Yellow line 2	15.67 m (σ_j)	
Yellow line 3	25.86 m (σ_i)	67.9 m (East study area)
Yellow line4	62.78 m (σ_j)	

4.3 Results.

The results section consists of three parts: the morphometric analysis of longitudinal ridges, observations related to ridge development and kinematic features, and volume calculation.

4.3.1 Ridges morphometry with distance and with deposit thickness.

In ArcGIS, I identified longitudinal ridges on the surface of landslide deposit and traced them as polylines along the crest. I decided to conduct detailed morphometric analysis within the central and east parts of the landslide deposit (Figure 4-6).

This is because these regions are entirely covered by the high-resolution CTX-derived DEMs that I made and the longitudinal ridges are best

preserved. I traced two sets of topographic profiles transversal to the inferred flow direction to study how the ridges evolve with distance from the head scarp (Figure 4-7, Figure 4-8).

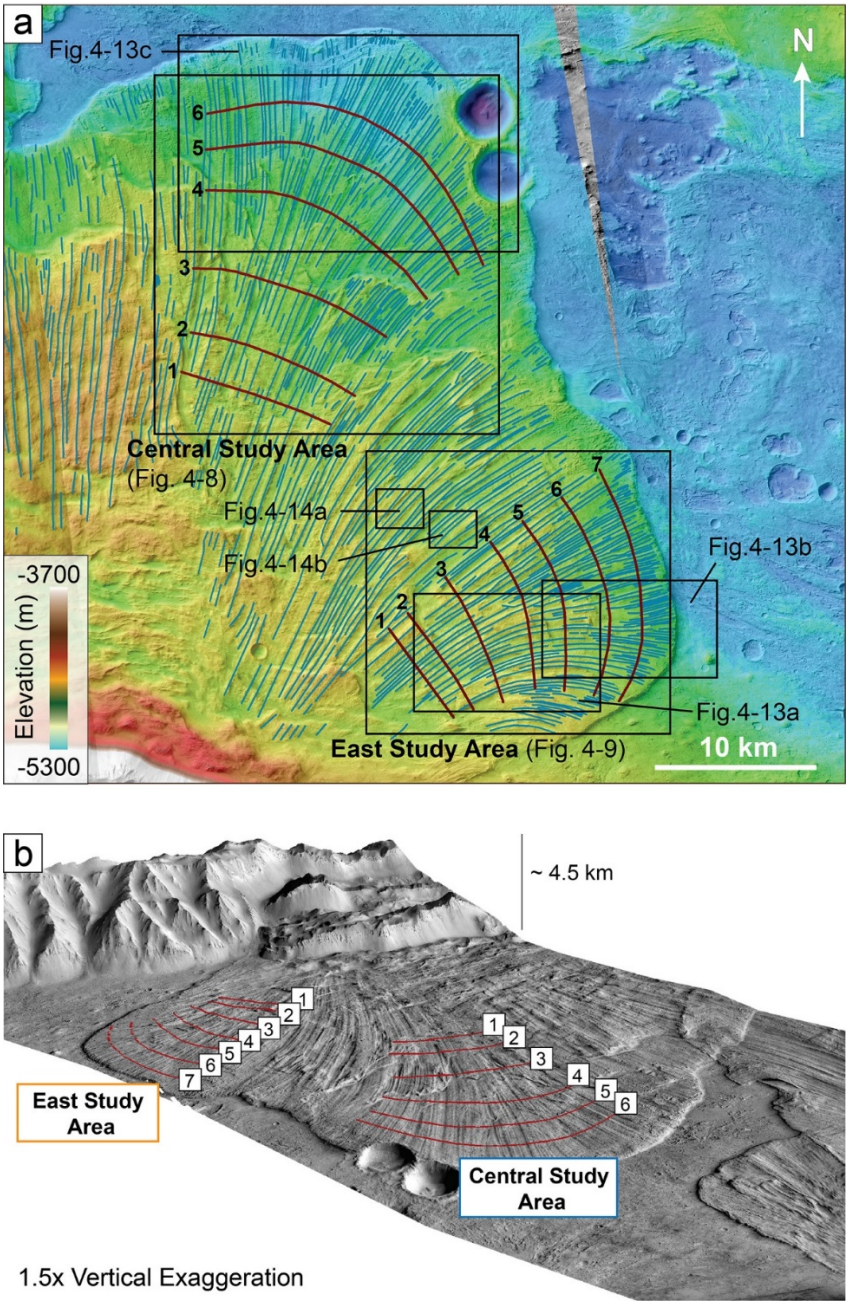

Figure 4-7 – Areas of detailed morphological study of the Coprates Labes landslide. a) Colour-keyed CTX stereo-derived DEMs overlaying a CTX-image mosaic; longitudinal ridges mapped in blue; topographic profiles are marked in burgundy lines and are numbered from proximal to distal edge of the landslide deposit (following the inferred flow direction). b) Oblique view of the same study areas with topographic profiles marked in red and numbered as in a); this image is created by overlaying CTX-derived orthoimages above the CTX-derived DEM (see Table 4-1 for the list of CTX images used).

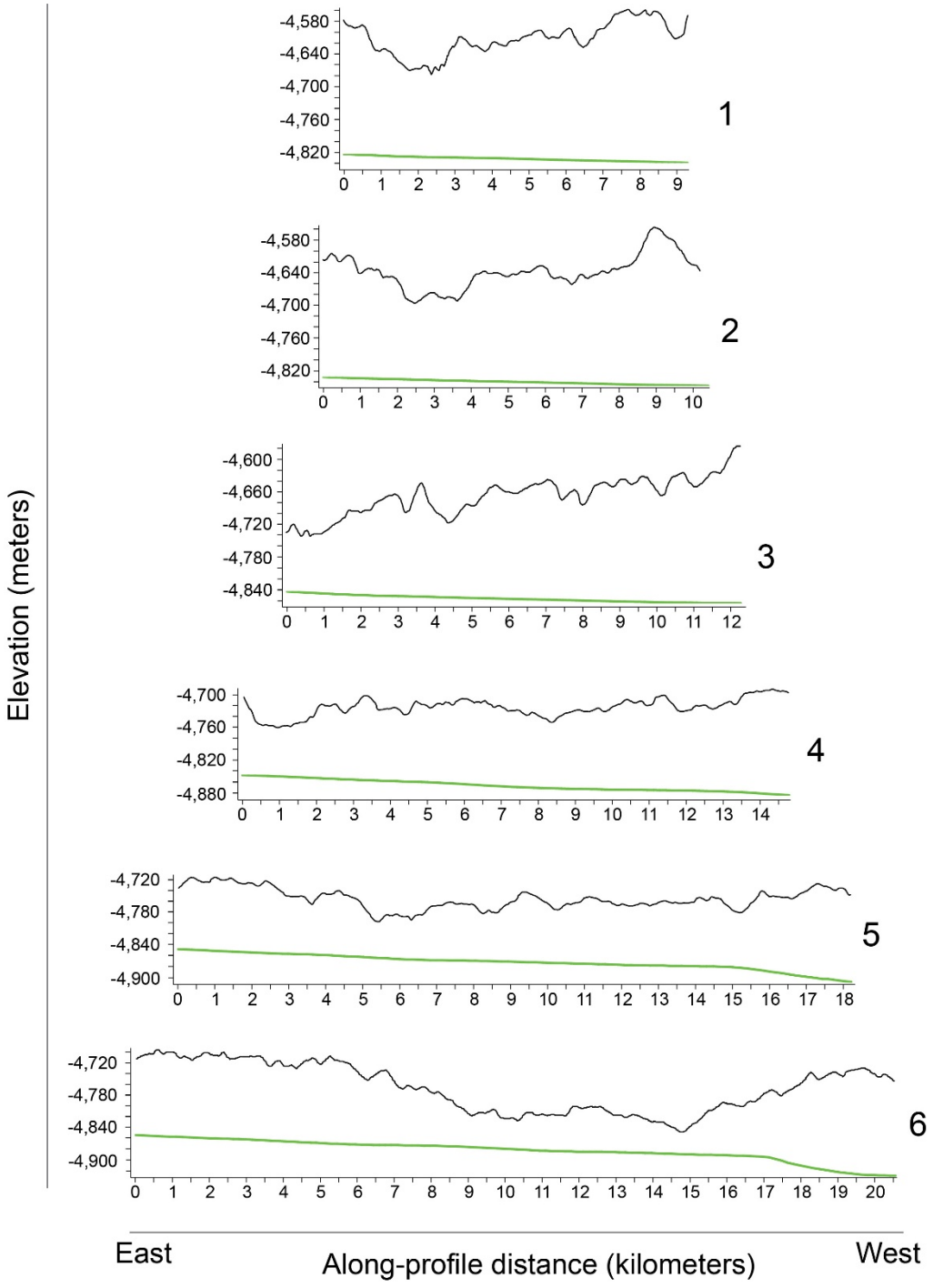

Figure 4-8 – Topographic profiles of the Coprates Labes landslide deposit in the central area of study. Black lines are the topographic profiles of the landslide deposit and the green lines are the topographic profiles of the base of the landslide deposit (derived from the reconstructed valley floor topography); profiles are numbered from 1 to 6, following the numbering used in Figure 4-6, where 1 is the most proximal profile and 6 is the most distal profile. The profiles were traced so that the most external ridges (at the left and the right ends of the profiles) were the same in each profile. Note how the length of the profiles increases with distance from the headscarp (i.e., from 1 to 6), suggesting that the ridges are becoming more spread out. The plots also show that the thickness of the landslide deposit decreases with the distance.

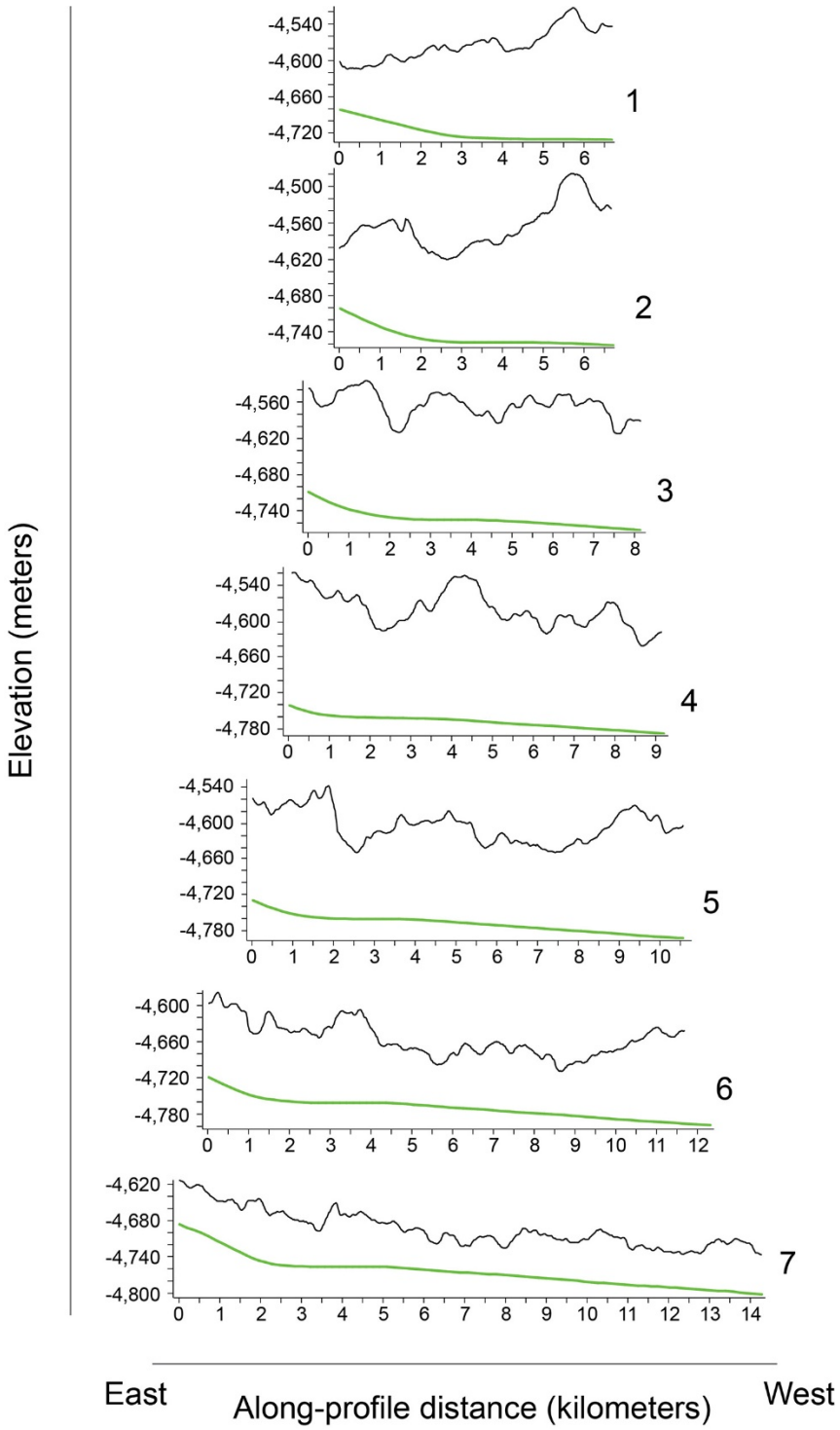

Figure 4-9 – Topographic profiles of the Coprates Labes landslide deposit in the east area of study. Black lines are the topographic profiles of the landslide deposit and the green lines are the topographic profiles of the base of the landslide deposit (derived from the reconstructed valley floor topography); profiles are numbered from 1 to 7, following the same numbering used in Figure 4-6, where 1 is the most proximal profile and 7 is the most distal profile. The profiles were traced so that the most external ridges (at the left and the right ends of the profiles) were the same for each profile. Note how the length of the profiles increases with the distance (i.e., from 1 to 7), suggesting that the ridges are becoming more spread out. The plots also show that the thickness of the landslide deposit decreases with the distance from the head scarp.

For every profile, the most external ridges (at the left and the right ends of the profiles) were the same ones, in order to have comparability of variables between profiles, such as the number of ridges and their spatial density. I measured the spacing between the ridges using ArcGIS Ruler tool. Within both areas of study, from the proximal to distal edge, longitudinal ridges diverge while their number increases and their amplitude and wavelength decreases (Table 4-3, Table 4-4, Figure 4-9a).

The results suggest a scaling relationship between the wavelength of the ridges (ridge spacing, S) and the average thickness of the landslide deposit (T). I compared the S/T ratio obtained from the morphometric analysis with the results obtained by Forterre and Pouliquen [2001]. The values of the S/T ratio obtained in the central area (blue points in Figure 4-9b) are in agreement with the value of ~ 2-3 found by Forterre and Pouliquen [2002]. In the east area (orange points Figure 4-9b), profile P3, P4, and P5 show S/T ratio below 2, which is a consequence of a localised increase in the deposit thickness (Table 4-4). However, if I considered their error bars, their values could fall in the grey area that represents the experimentally predicted range for the scaling relationship.

Table 4-3 – Results of the morphometric analysis in the central area of study of the Coprates Labes landslide. The thickness error estimation is 24.61 m; it is given in Table 4-2 and represented as error bar in Figure 4-10b. The spacing error corresponds to one standard deviation of the ridge spacing distribution.

Central Study Area

Profile	N. of ridges	Density of ridges (m^{-1})	Profile Length (m)	(S) Average Ridge Spacing (m)	(T) Average Deposit Thickness (m)	S/T
1	15	1.6	9283	607 ± 157	222 ± 25	2.73 ± 0.20
2	18	1.7	10409	562 ± 165	205 ± 25	2.74 ± 0.32
3	26	2.1	12225	465 ± 166	182 ± 25	2.55 ± 0.38
4	40	2.6	15134	368 ± 112	143 ± 25	2.56 ± 0.35
5	51	2.8	18105	353 ± 111	118 ± 25	2.99 ± 0.38
6	63	3	20809	329 ± 94	114 ± 25	2.87 ± 0.36

Table 4-4 – Results of the morphometric analysis in the east area of study of the Coprates Labes landslide. The thickness error estimation is 24.61 m; it is given in Table 4-2 and represented as error bar in Figure 4-10b. The spacing error corresponds to one standard deviation of the ridge spacing distribution.

East Study Area

Profile	N. of ridges	Density of ridges (m^{-1})	Profile Length (m)	(S) Average Ridge Spacing (m)	(T) Average Deposit Thickness (m)	S/T
1	16	2.5	6449	413 ± 152	170 ± 68	2.43 ± 0.54
2	17	2.5	6862	400 ± 117	185 ± 68	2.17 ± 0.32
3	23	2.8	8110	352 ± 95	192 ± 68	1.83 ± 0.30
4	33	3.6	9146	277 ± 135	193 ± 68	1.44 ± 0.50
5	39	3.7	10575	272 ± 109	169 ± 68	1.61 ± 0.43
6	49	3.9	12409	253 ± 84	110 ± 68	2.30 ± 0.40
7	82	5.7	14339	176 ± 48	73 ± 68	2.41 ± 0.44

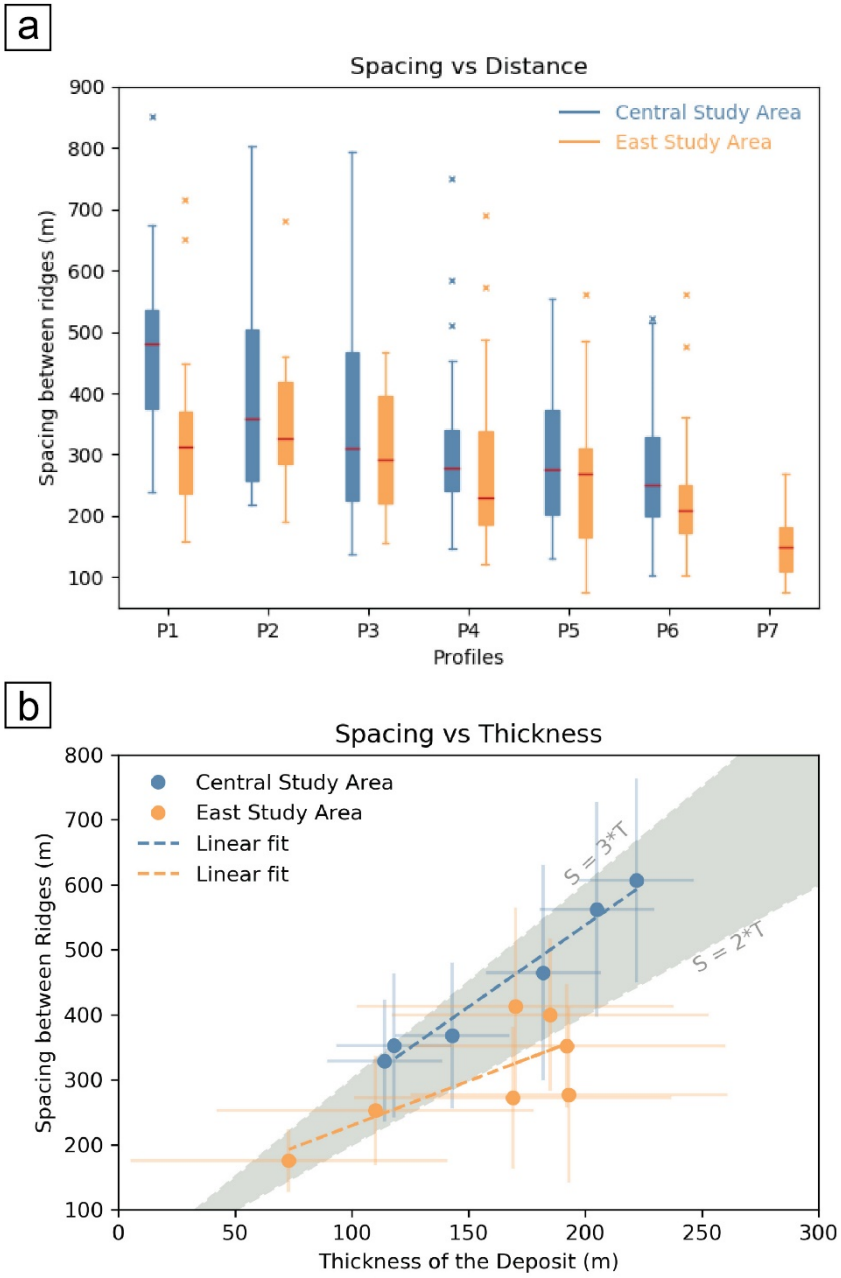

Figure 4-10 **– Variation of the spacing between longitudinal ridges with increasing distance from the head scarp and with thickness of the deposit at the Coprates Labes landslide.** a) The plot shows how the spacing between longitudinal ridges varies with distance (from the proximal to distal areas of the deposit); boxes represent the interquartile range, red segments within boxes indicates the median and the extent of the 'whiskers' show the locations of the maximum and minimum, symbols 'x' represent outlier values above three times interquartile range. b) The plot shows the relationship between the spacing of the ridges and the thickness of the deposit; the grey band shows the experimentally predicted range for the scaling relationship between the ridge-spacing and the thickness of the deposit (error bars represent the error values provided in Table 4-3 and Table 4-4).

4.3.1.1 Comments on the method used to identify a typical wavelength of longitudinal ridges.

In this work I used the average (mean) spacing between ridges along profiles as representative of the typical wavelength of the ridges. As the identification of the ridges and the calculation of their average spacing was done with manual and automated methods, the objectiveness of the measurement may be argued. Firstly, I made a hillshade raster of the CTX-derived DEM of the Coprates Labes landslide to verifying that the ridges are actually resolved by the DEM (FIGURE XX).

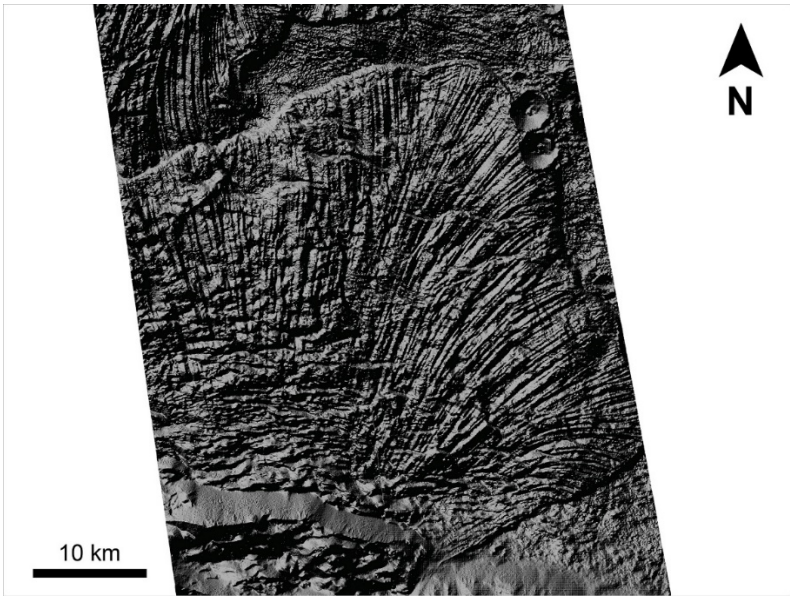

Figure 4-11 – Hillshade of the CTX-derived DEM of the Coprates Labes landslide. The longitudinal ridges are visible in the hillshade raster of the CTX-derived DEM of the landslide deposit. This means that the DEM is able to resolve the longitudinal ridges.

As the longitudinal ridges are visible in the hillshade raster, I decided to apply the Fourier analysis, as it provides a more systematic method identifying a typical wavelength. I ran a Fourier analysis for each profile and this is shown in Figure 4-10 and Figure 4-11.

However, this method did not provide a typical wavelength in the outcome. Nevertheless, I am convinced that this does not undermine the results of the morphometric analysis that I conducted for the following reasons:

a) A geomorphological signal usually carries noise that derives from other superficial features and weathering processes, masking the target feature and making its distinction non-trivial by automatic means; in this case study, this hundreds-million-years old martian long runout landslide has been subject to impact cratering, wind erosion, mega ripples formation in topographic lows, and so on, which inevitably add significant noise to the topographic signal.

b) I am not expecting that these field-scale morphological features would have a signal as clear as obtained at laboratory-scale under controlled experimental conditions, for instance, the roughness; Forterre and Pouliquen [2001] glued one layer of particles onto a glass plate that covered about 70% of the surface; given the diameter of the particles, 0.25 mm, and the thickness of the flow, ~ 2-2.5 mm, the artificial roughness represents a small fraction of the flow thickness; in the field-scale martian slide, I expect topographic oscillations that range from few meters to 60-80 m (Figure 4-5b), which, given that the slide thickness decreases from ~ 400-500 m in proximal areas to about 60-70 m at the terminal edge, represent a larger fraction compared to the laboratory case; therefore, these topographic variations are expected to have some degree of influence on the surface of the slide and so also can interfere with a ‘perfect’ pattern.

c) Finally, and probably more importantly, ridges diverge with the distance and at some point new ridges appear in between the diverging ones (see section 4.3.2; Figure 4-12); therefore, I do not expect to obtain a typical wavelength, as these are, during the motion, changing and transforming features, although able to produce an unmistakable pattern.

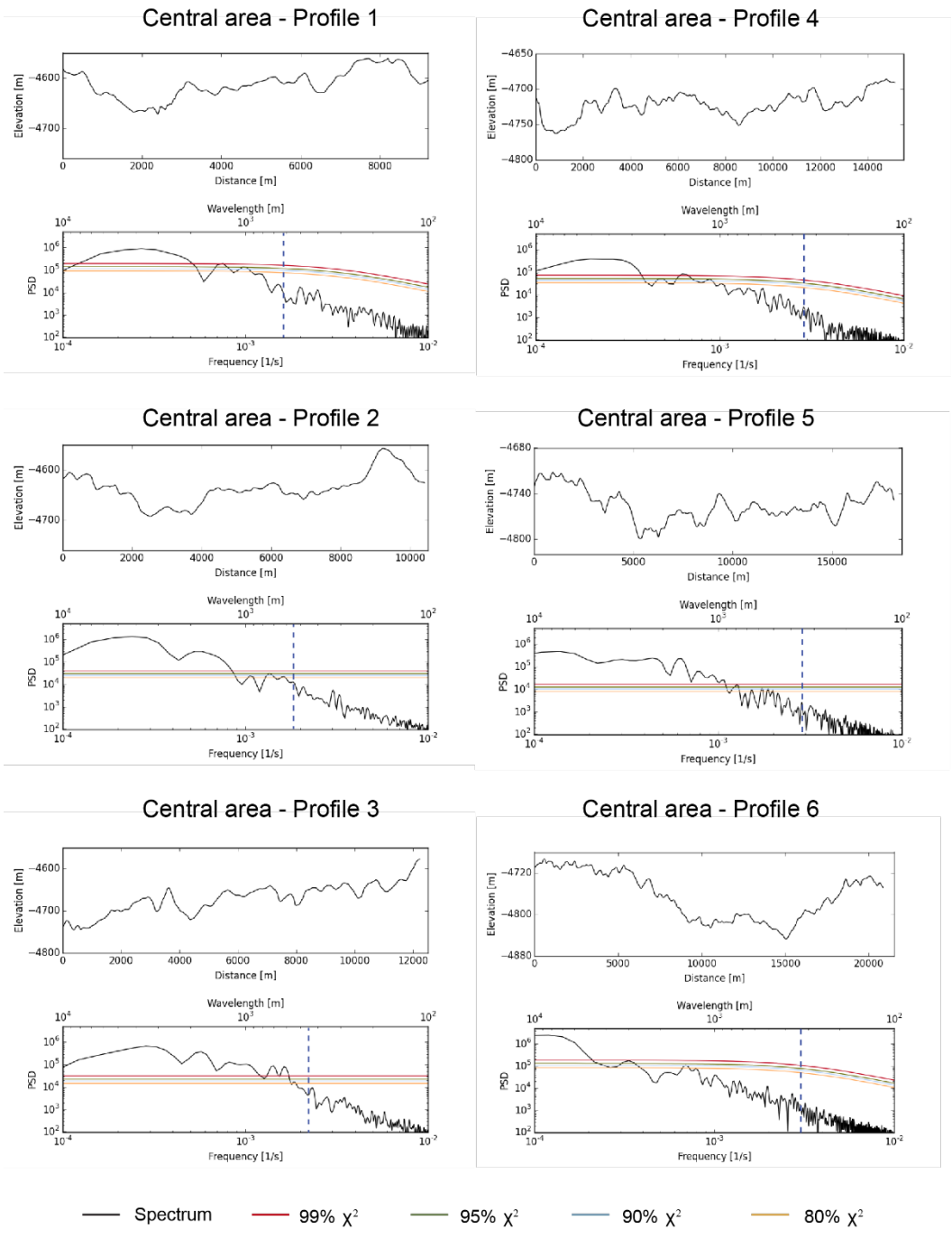

Figure 4-12 – Results of the Fourier analysis for the central area of study at the Coprates Labes landslide. The upper plot of each panel shows the topography of the landslide deposit and the lower plot of each panel shows the power spectral distribution (PSD) of the topographic signal; the dashed vertical lines in the PSD plots represent the average value of the spacing between ridges obtained from the morphometric analysis conducted at each profile.

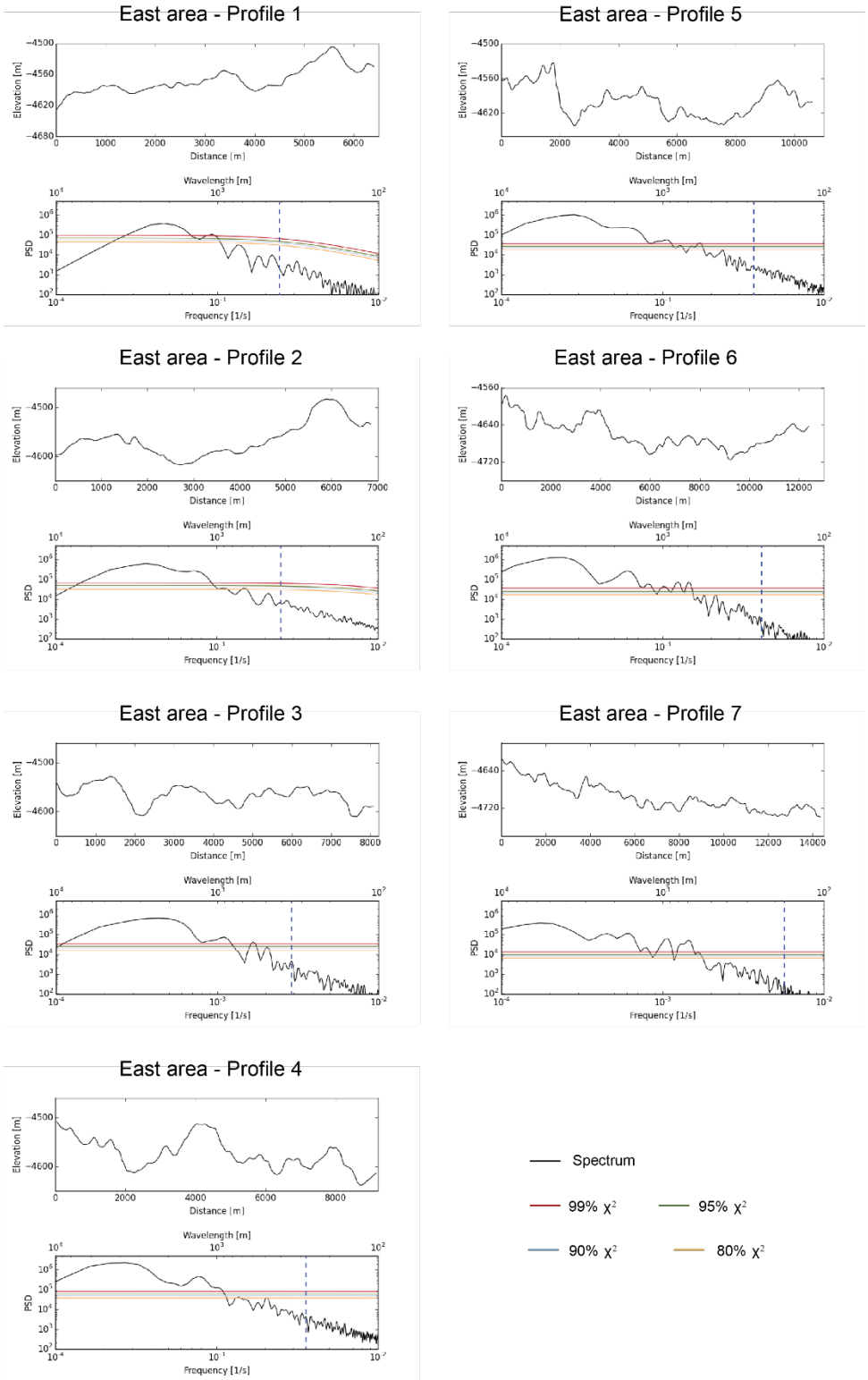

Figure 4-13 - Results of the Fourier analysis for the east area of study at the Coprates Labes landslide. The upper plot of each panel shows the topography of the landslide deposit and the lower plot of each panel shows the power spectral distribution (PSD) of the topographic signal; the dashed vertical lines in the PSD plots represent the average value of the spacing between ridges obtained from the morphometric analysis conducted at each profile.

4.3.2 Ridge behaviour and kinematic indicator features.

I observed that new ridges appeared between diverging ridges (Figure 4-12), confirming that the number of ridges increases with distance, as found from the morphometric analysis (Table 4-3, Table 4-4). This is also consistent with the observation of Forterre and Pouliquen [2001; 2002] of transversal drifting of the helicoidal cells (i.e., the vortexes within the flow that form following a mechanical instability and are responsible for the generation of the longitudinal pattern of ridge and trough) accompanied by annihilation and creation of ridges. S-shaped en-echelon features superposed on the longitudinal ridges were identified and interpreted as kinematic indicators on the Coprates Labes landslide (Figure 4-13).

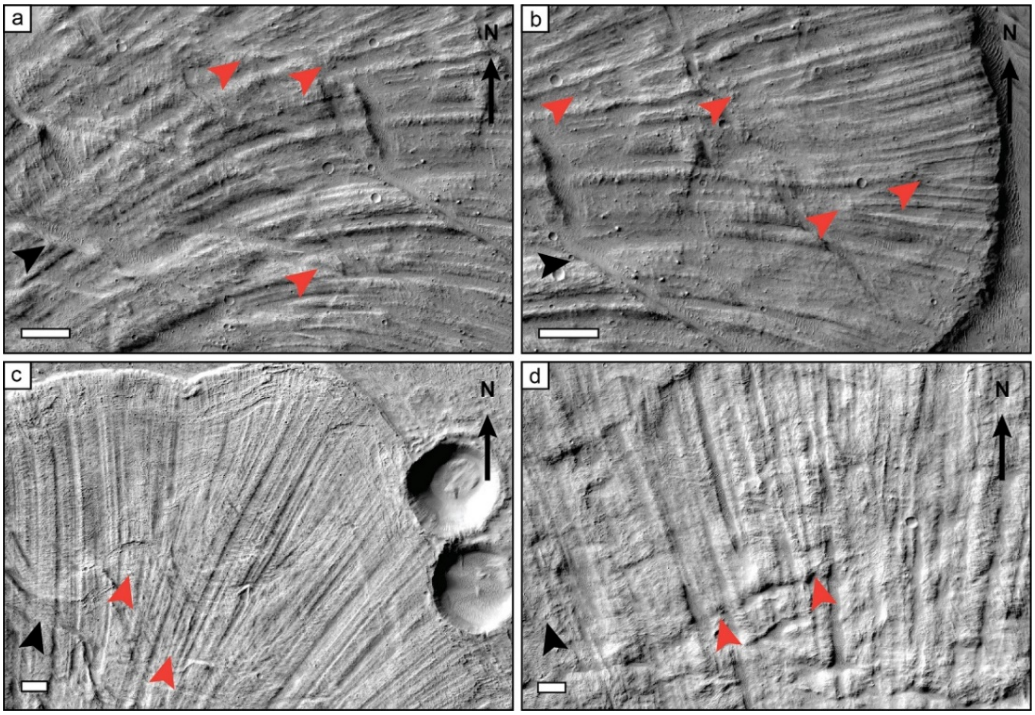

Figure 4-14 – Behaviour of longitudinal ridges at the Coprates Labes landslide. The close-up images show the appearance of new, smaller ridges between diverging ridges, as indicated by red arrowheads; these may represent field scale versions of laboratory observations made by Forterre and Pouliquen [2001], who reported a non-linear evolution of the surface of granular flows in the laboratory, including transversal drift and creation of longitudinal streaks. Locations of images a), b), and c) are shown in Figure 4-6a; location of d) to the west of Figure 4-6a. Black arrowheads indicate the inferred flow direction. The scale bars are all 1 km long.

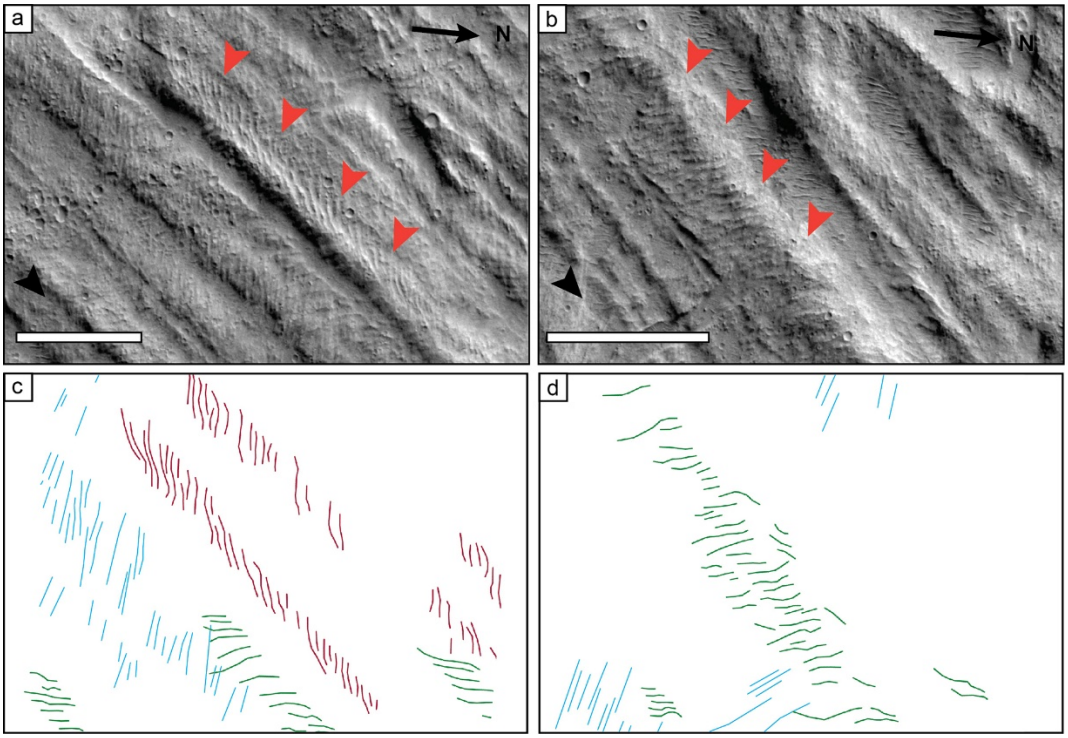

Figure 4-15 – Kinematic indicators at the Coprates Labes landslide. a) and b) Close-up images showing s-shaped en-echelon features superposed on the longitudinal ridges; these features may be kinematic indicators, which could suggest a velocity gradient between ridges and furrows. c) and d) are digitised versions of the en-echelon features observed on ridges in a) and b), respectively; red and green colours represent s-shaped features oriented roughly east-west and north-south, respectively; cyan colour represents other linear features that are not considered in this study. Black arrowheads indicate the inferred flow direction. Scale bar is 1 km.

Laboratory experiments have shown the existence of a velocity gradient between ridges and furrows: for very rapid flows (dilute regime), furrows move faster than ridges [Forterre and Pouliquen, 2001; Borzsonyi *et al.*, 2009], whereas for less rapid flows (dense regime), the ridges are the faster-flowing region [Borzsonyi *et al.*, 2009]. In both regimes, the faster-flowing regions are denser (i.e., their solid fraction is greater than in the slower-flowing features). As a consequence, when the flow ceases, an inversion of topography is expected in the dilute regime. Here, the ridges, being less dense, are expected to deflate and sink. The ridges become furrows, and the fast-flowing dense furrows become ridges. The en-echelon features that are shown in Figure 4-13 (a and b) oriented towards faster-flowing ridges are therefore consistent with both the dense regime and with the dilute regime after topography inversion (Figure 4-14).

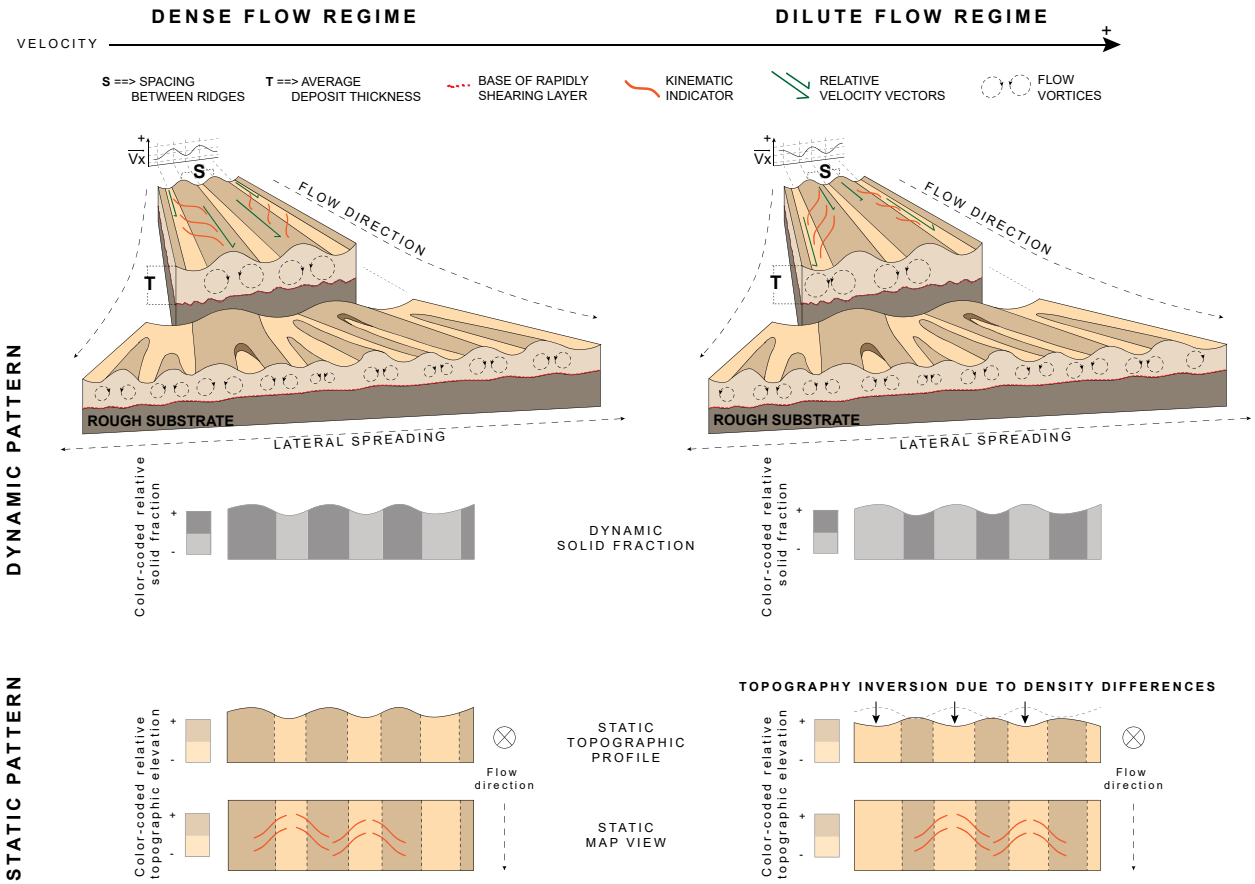

Figure 4-16 – Flow structure models for the Coprates Labes landslide. Illustration of the two possible flow structure scenarios as inferred from the orientation of the en-echelon features observed superposing longitudinal ridges and interpreted as evidence of a velocity gradient between ridges and furrows. The current static pattern that we observe matches two dynamic patterns, a dense regime flow structure and a dilute flow regime structure followed by inversion of the topography as the flow stops and the ridges deflate.

4.3.3 Volume calculation.

The CTX-derived DEMs do not entirely cover the landslide deposit and the landslide scar area (Figure 4-2a), because of a lack of suitable image pairs. I made use of the DEM derived from the HRSC camera to cover the areas for which it was not possible to obtain good quality topographic data from CTX-derived DEM. Datasets were transformed so to have consistent coordinate system and projection. The Mars geographic coordinate system IAU2000:49900 (Mars2000, planetocentric latitudes, positive East longitudes) was adopted and a sinusoidal projection (central meridian: 292.0) was chosen, as this projection represents areas accurately.

In order to calculate the initial volume (i.e., the volume of the slope that collapsed) and the final deposit (i.e., the volume of the deposit that came to rest on the valley floor), I made use of the reconstructed surfaces described in Section 4.2.3 (Figure 4-4). A series of polygons were digitized in ArcGIS so to identify the area of the failure surface (polygon 1 in Figure 4-15), which also corresponds to area of the initial slope, and the area of the final deposit, which was further subdivided so to distinguish areas covered by CTX-derived DEMs (polygons 3, 4, and 6 in Figure 4-15) from the areas covered by the HRSC-derived DEM (polygons 2 and 5 in Figure 4-15).

Volumes were calculated for the area under each polygon using the ArcGIS tool ‘CutFill’ (this tool calculates the volume by subtracting two given digital elevation models): at polygon 1, I calculated the initial volume using the reconstructed initial slope topography and the reconstructed surface of failure topography; at polygons 2, 3, 4, 5, 6 volumes were calculated separately using CTX-derived or HRSC-derived topography accordingly, and the reconstructed topography underneath the deposit; these latter volumes were finally summed up to obtain the value of the final volume of the landslide deposit. The results are shown in Table 4-5:

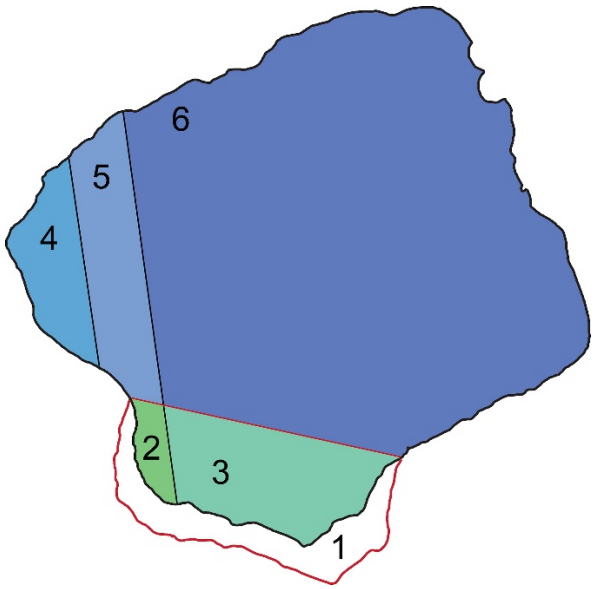

Figure 4-17 – Subdivision of the Coprates Landslide in polygons for the purpose of volume calculation the landslide. Polygon 1 (in red) represents the surface area occupied by the initial volume; polygons 2, 3, 4, 5, 6 make up the surface area of the final deposit; polygons 2, 3 represent the surface area of the final deposit that lies upon the surface of failure of the landslide (polygon 2 is covered by the HRSC-derived DEM, whereas polygon 3 is covered by the CTX-derived DEM); polygon 4, 5, 6 represent the surface of the final deposit that lies entirely on the valley floor (polygon 5 is covered by the HRSC-derived DEM, whereas polygons 4, 6 are covered by the CTX-derived DEM).

Table 4-5 – Results of volume calculation of the Coprates Labes landslide.

Initial Volume (km^3)	**Final Volume (km^3)**				
Polygon 1	Polygon 2	Polygon 3	Polygon 4	Polygon 5	Polygon 6
505	17	202	8	16	366
505			**609**		

Volume increase ~ 20%

The volume of the Coprates Labes landslide has also been calculated by Harrison and Grimm [2003], Quantin *et al.* [2004a] and [Lucas *et al.*, 2011]. I compare my results with these previous estimates in Table 4-6:

Table 4-6 – Comparison of volume of the Coprates Labes landslide obtained in different works. The table compares the volume of the Coprates Labes landslide obtained in this study with volumes obtained in previous studies.

Work	Method	Data	Initial Volume (km^3)	Final Volume (km^3)
Harrison and Grimm [2003]	Separate recreation of original slope surface, failure surface, and valley floor surface.	MOLA DEM + Viking images	460	
Quantin *et al.* [2004a]		MOLA DEM + Viking, THEMIS, and MOC images	500	346.52
This work		HRSC DEM + CTX stereo-derived DEMs + CTX images	**505**	**609**
[Lucas *et al.*, 2011]	Reconstruction of surface below deposit using ISIS digitizing package, initial slope that include spur-and-gully morphology of adjacent slopes, and shape of the surface of failure (spoon-seated and scar-seated)	MOLA DEM + HRSC-derived DEMs + HRSC images + THEMIS IR images	Spoon-seated	
			395	540
			Deep-seated	
			585	730

4.4 Discussion.

A self-lubrication mechanism for long runout landslides has been proposed by Campbell [1989] suggesting that a dilute layer of highly agitated particles at the bottom of the flow can explain the apparent low coefficient of friction in long runout landslides and that such a layer should form naturally in rapid granular flows. As the formation of longitudinal vortices also seems to be a natural development of rapid granular flows that involves a low-density layer at the bottom of the flow [Forterre and Pouliquen, 2001; 2002; Borzsonyi *et al.*, 2009], it is not unreasonable to suggest that longitudinal ridges and furrows are inevitable features that originate from a mechanical instability once certain threshold conditions within a flow moving over a rough surface are passed.

The mechanism responsible for the formation of longitudinal vortices proposed by Forterre and Pouliquen [2001] relies on the inversion of the

density profile, with denser granular packing closer to the top of the landslide, and on a continuous energy supply to the system, in the form of shear forces, so as to maintain the collisional regime and, therefore, to prevent the granular temperature decaying rapidly due to the inelastic nature of particle collision [Campbell, 1989]. The instability derives from the inversion of density profile, due to an increase of granular temperature [Campbell and Brennen, 1985; Campbell, 1990] at the base of the flow by collision and shear between particles and the rough substrate. Such particle interactions may well contribute to acoustic fluidization [Melosh, 1979] processes within the landslide that would lead to the dynamic reduction of viscosity and explain the long runout distance. Several other dynamic weakening mechanisms have also been proposed to explain long runouts, such as flash heating [Singer *et al.*, 2012], frictional melting [Masch *et al.*, 1985], and thermal decomposition [Voight and Faust, 1982; Vardoulakis, 2002; Goren *et al.*, 2010; Mitchell *et al.*, 2015] (and subsequent thermal pressurization). Such mechanisms rely on the generation of heat at the base of the landslide, which would contribute to the energy supply at the base of the system.

From the results of the morphometric analysis of longitudinal ridges that I conducted for this case study of a martian landslide, a scaling relationship between the wavelength of longitudinal ridges and the thickness of the landslide apparent in ice-free experiments, is observed. Moreover, scaling analysis of the martian landslide studied here indicates that its emplacement velocity could have been as high as tens to hundreds of m/s [Magnarini *et al.*, 2019]. It follows that longitudinal ridges that characterise long runout terrestrial and planetary landslides may be the expression of an instability that emerges within the flowing mass once a velocity threshold is surpassed, as observed in laboratory experiments on rapid granular flows [Forterre and Pouliquen, 2001]. Although not ruling out the presence of ice and other mineralogical facies as a key factor, the results suggest that the origin of longitudinal ridges does not necessarily depend on the presence of an icy substrate.

4.5 Conclusions.

The results and observations from this case study represent the first field evidence for the spontaneous development of longitudinal ridges in ice-free rapid granular flows observed in experimental and numerical studies. Also, they support the existence of a convincing fundamental process responsible for the origin of such morphologies, challenging the existing analogies to terrestrial landslides on ice that have been proposed to explain the widespread occurrence of this landslide surface feature throughout the Solar System. If indeed the scaling relationships that were identified in this case study indicate that Coprates Labes landslide developed longitudinal ridges through an instability that emerges from the physics of fast-flowing dry grains, then these morphological features should be expected throughout the Solar System, regardless of the availability of other lubrication mechanism, such as ice layers.

5 Case study II – Earth: the El Magnifico landslide, Chile.

Part of this chapter has been submitted for peer-review as: "*Magnarini, G., Mitchell, T.M., Grindrod, P., Goren, L., and Browning, J. - Wavelength of longitudinal ridges scales with thickness of terrestrial long runout landslides: The El Magnifico rock avalanche, Chile*."

5.1 Introduction.

The morphological features and internal structures of long runout landslides can be used as a way to characterize the mechanics of emplacement [e.g., Weidinger *et al.*, 2014; Dufresne *et al.*, 2016]. This is particularly useful for analysing planetary landslides, where data is derived only from remote sensing techniques. Many efforts have been made to describe the morphology and the internal fabric of long runout landslide deposits [e.g., Legros *et al.*, 2000; Shea and Van Wyk De Vries, 2008; Dufresne and Davies, 2009; Paguican *et al.*, 2014], in the attempt to clarify the relationship between their development and the mechanisms that take place during such catastrophic events. Unfortunately, on Earth, the partial, if not total, loss of the detailed geomorphological record of long runout landslide deposits due to tectonics, weathering, vegetation cover, and human activity undermines the characterization and interpretation of the residual landforms and, therefore, can hinder the understanding of the processes. To overcome this problem, we can study similar landforms on other planetary surfaces where limited erosion and surface processes compared to Earth better preserve the

morphological record. For instance, thanks to the latest high resolution imagery from orbital missions to Mars, detailed morphometric measurements of landslide deposits can be conducted [e.g., Mazzanti *et al.*, 2016; Magnarini *et al.*, 2019] and mineralogical signatures of the basal sliding surface can be detected [Watkins *et al.*, 2015]. On the other hand, contrary to planetary studies, terrestrial studies allow direct multiscale observations of landslides that can provide detail of how the internal structures relate to the surface morphology. Some of the best terrestrial cases of unconfined long runout landslides accompanied by detailed fieldwork observations of their deposit morphologies, internal structures, and, where possible, structural setting at the scarp are the Seymarreh landslide, Zagros Mountains, Iran [e.g., Harrison and Falcon, 1938; Roberts and Evans, 2013], the Blackhawk landslide, South California, USA [Shreve, 1959], the Frank slide, British Columbia, Canada [Cruden and Hungr, 1986; Charriere *et al.*, 2016], the Sherman Glacier landslide [Shreve, 1966], and the Heart Mountain landslide, Wyoming, USA [Beutner and Gerbi, 2005; Mitchell *et al.*, 2015].

One key morphological feature that is commonly documented in long runout landslides across the Solar System is distinctive longitudinal ridges that run parallel to the flow direction [e.g., Howard, 1973; Lucchitta, 1979; Schmidt *et al.*, 2017; Boyce *et al.*, 2020]. The presence of these longitudinal ridges has often been associated with the presence of basal ice [Dufresne and Davies, 2009; De Blasio, 2011]. However, longitudinal ridges are also observed in landslides whose emplacement is not associated with basal ice, such as the El Magnifico rock avalanche cluster, in the north region of the Atacama Desert, Chile [Mather *et al.*, 2014; Crosta *et al.*, 2017]. Results from the morphometric analysis of a martian long runout landslide (Chapter 4) show the existence of a scaling relationship between the wavelength of the ridges and the thickness of the landslide deposit, in agreement with ice-free laboratory experiments and simulations on instability patterns in rapid granular flows performed by Forterre and Pouliquen [2001] and Borzsonyi *et al.* [2009]. This supports the possibility that longitudinal ridges may develop from an instability that emerges from the physics of fast-flowing granular flows, without the need for the presence of basal ice.

In order to ground truth the model of longitudinal ridge formation proposed in Chapter 4, I present here the case study of the unconfined El Magnifico rock avalanche cluster, located on the coastal plain of the north part of the Atacama Desert, Chile, where I conducted two field campaigns in February 2018 and February 2019 (Figure 5-1a-c).

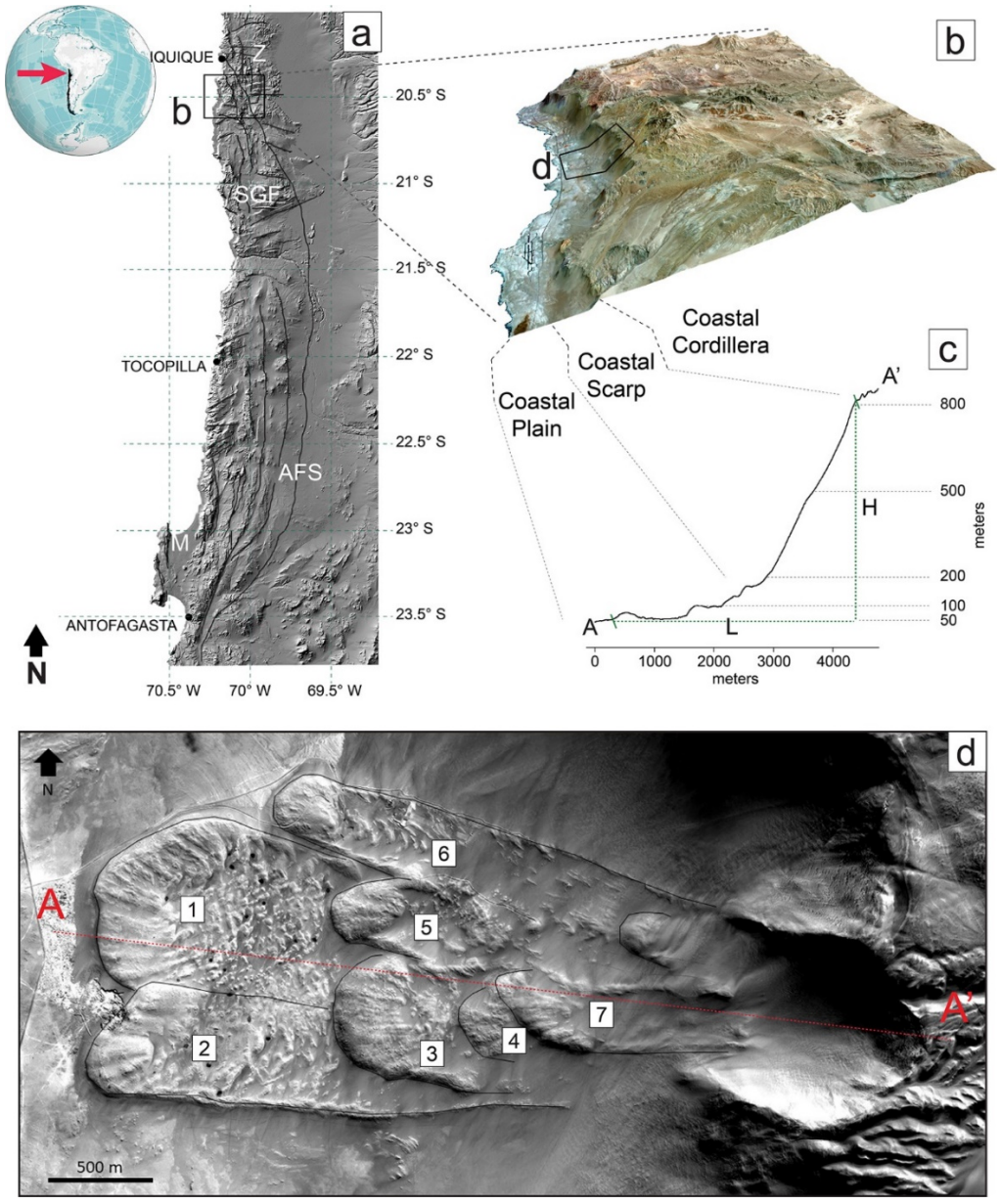

Figure 5-1 – Regional context of the El Magnifico landslide. a) Shaded relief map of northern Chile obtained from the SRTM Global_3 (90m) DEM; black lines represent major faults; AFS = Atacama Fault System, M = Mejillones, and SGF = Salar Grande Fault. b) Oblique view of the Sentinel multispectral image (Bands R5, G2, B1) overlying the SRTM DEM; black dots demark major cities; inset shows the location of the region on a global representation centred on South America, where Chile is marked in black. c) Profile where the topographic position of the physiographic units from b) are indicated. d) Pleiades orthoimage for the region of study of the El Magnifico landslide cluster; numbers represent

the lobes that form the cluster, as given by Mather *et al.* [2014]; Red dotted line shows the location of the topographic profile shown in c).

The El Magnifico cluster is made up of 7 lobes, each of them exhibiting diverging longitudinal ridges at their terminal part. The hyperarid climate of the Atacama Desert, its reduced erosion rate and weathering, and absence of vegetation, have improved the preservation of the landslide deposit and its morphological features for the past 60 kyr. This site offers unique conditions for conducting detail morphological observations and morphometric analysis, extending the initial work of Mather *et al.* [2014] and Crosta *et al.* [2017], which mainly focused on the wider tectonic and climatic significance at the regional scale of coastal giant landslides and on the origin and triggering mechanisms of such events under a regional hazard and risk assessment framework.

5.1.1 Area of study.

The El Magnifico rock avalanche cluster was first reported in detail by Mather *et al.* [2014]. It represents an exemplary well-preserved terrestrial unconfined long runout landslide, that comprises 7 lobes (Figure 5-1d). In this study, we will refer to individual lobes following the numbering system 1-7 established by Mather *et al.* [2014]. The subdivision was made from remote sensing and field mapping, where 1 represents the first lobe to be emplaced and 7 the last lobe to be emplaced. Using ^{14}C dating of organic material stratigraphically related to the rock avalanche deposit, ^{36}Cl cosmogenic nuclide, and optical stimulated luminescence, Crosta *et al.* [2017] have dated the rock avalanche cluster to 60 $\pm$ 10 kya. Unfortunately, dating uncertainties do not permit attribution of the time interval between the single events that generated the lobes.

The landslide cluster is located about 25 km south of Iquique, and originated from the collapse of a portion of the Coastal Cordillera scarp and the deposit lie on the coastal plain comprised of Pleistocene marine terrace deposits (Figure 5-1a-c). In this area of the Coastal Cordillera, the Jurassic and Cretaceous formations are intruded by andesitic and granodioritic plutons [Novoa, 1970], which are cut by normal faults that follow a N-S trend, E-W-

striking reverse faults, and WNW and NNW-striking dextral strike-slip faults [Allmendinger and González, 2010]. In particular, the cliff that was affected by the slope failure that generated the El Magnifico landslide is characterized by a sequence of layered sedimentary rocks, sandstones and pervasively foliated black to red to yellow siltstones and marls with localized thin levels of gypsum, overlain by conglomerates, through angular unconformity relationship (Figure 5-2; Figure 5-3).

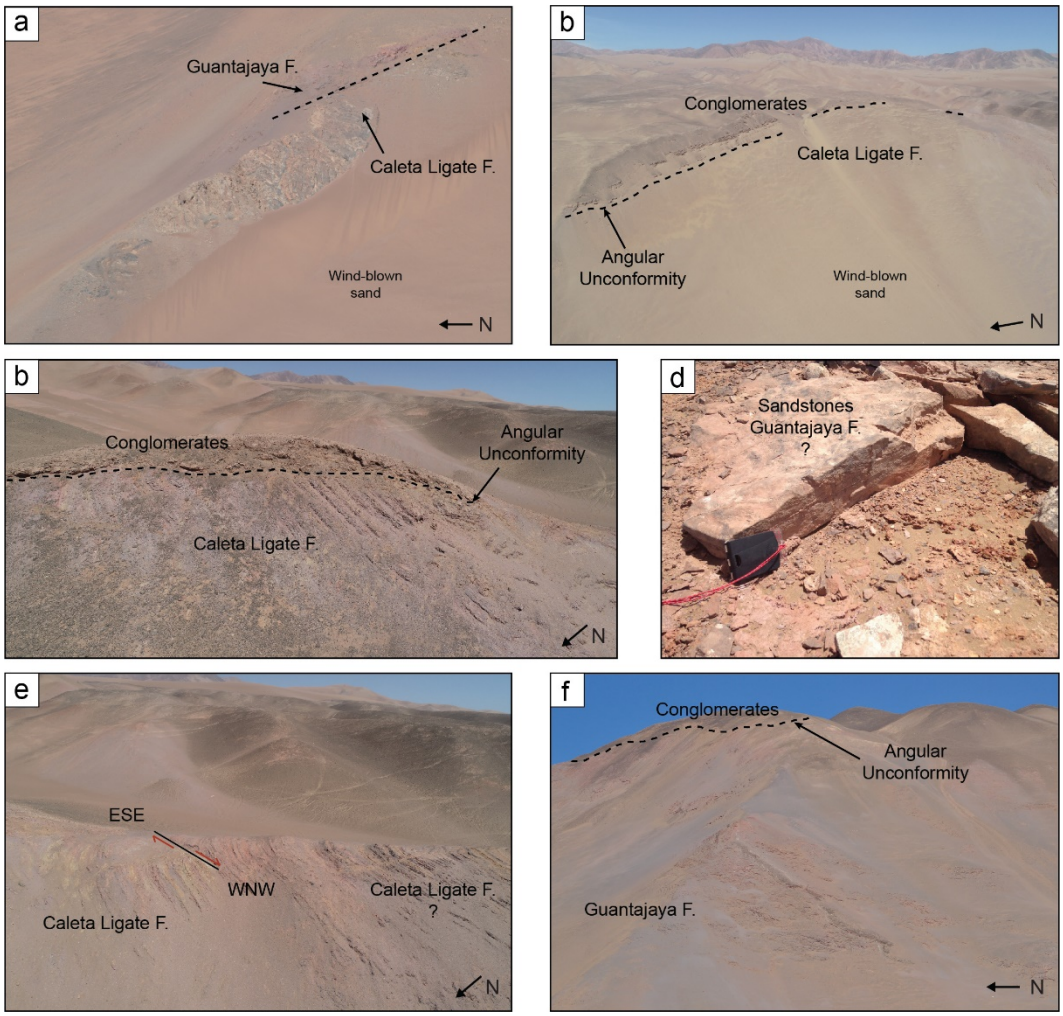

Figure 5-2 - Outcrops at the scarp of the El Magnifico landslide. Annotated drone photos of some of the outcrops along the head scarp of the landslide. These observations are mapped in Figure 5-3a and used to create the cross-section in Figure 5-3b.

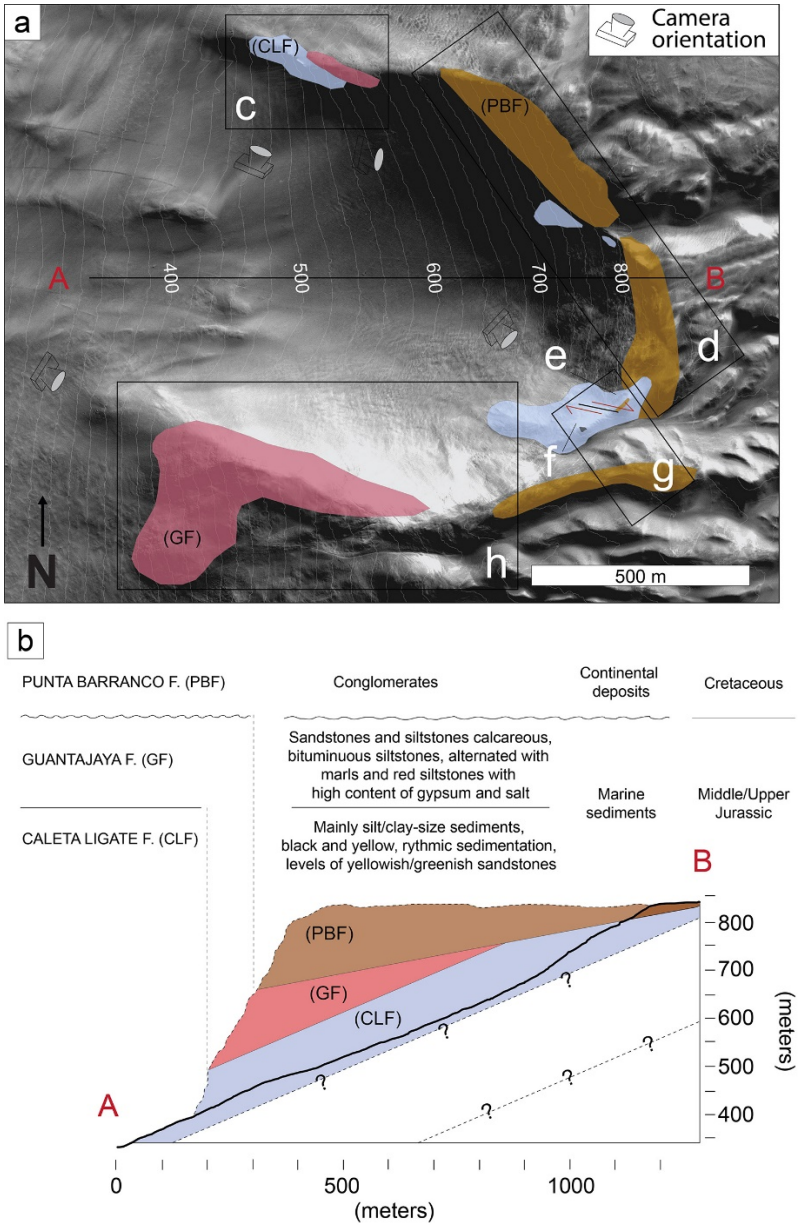

Figure 5-3 – Geological map at the scarp of the El Magnifico landslide. a) Locations at which the lithologies outcrop are shown (coloured patches that follow the classification given in b). The geological section (b) is made from matching our observations with the formations described and other information provided (such as expected formation thickness) in the Chilean geological map [Novoa, 1970]; the reconstructed slope topography is inferred from surrounding coastal scarp topography and it represents a plausible but not accurate topography.

Unfortunately, large areas of the coastal scarp, including the scarp of the El Magnifico landslide, are covered by wind-blown sands, limiting the locations at which outcrops are available. This is also true for locations on the coastal plain, where aeolian deposits locally shroud the landslide deposit, impeding observation of the contact between the deposit and the coastal plain surface.

As shown by the long profile A-A' in Figure 5-1c, the landslide scarp is at an elevation (H) of about 830 m. The horizontal runout (L), measured from the highest point of the scarp to the lowest point of the deposit, is about 4 km (Figure 5-1c). This results in a H/L ratio of about 0.2. The lobes that form the rock avalanche cluster have a terminal bulging morphology and a depressed central area (Figure 5-4a).

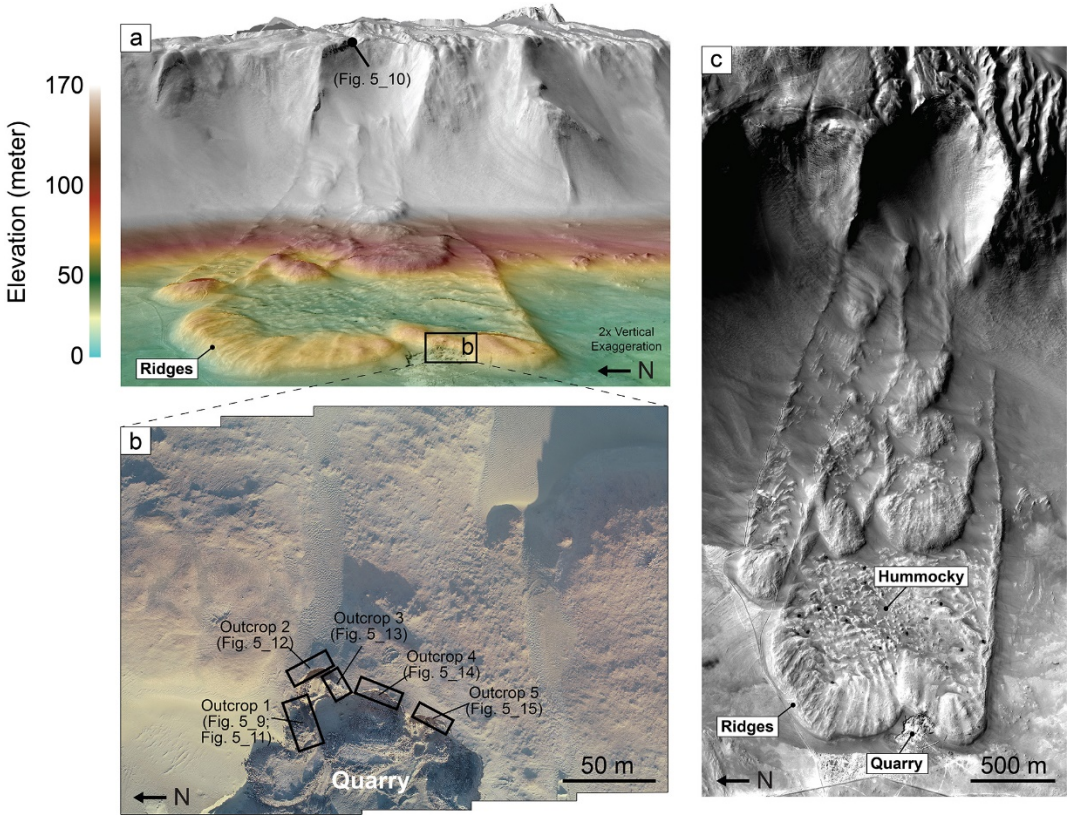

Figure 5-4 – Area of study of the El Magnifico landslide. a) Oblique view of the landslide, where digital elevation model is obtained from Pleiades satellite images and overlain by a Pleiades orthoimage. b) nadir-view of the quarry showing the locations of the outcrops discussed in the chapter. c) Annotated nadir view of the orthorectified image obtained from Pleiades satellite images.

Besides having distinctive elevations, these two parts also show distinctive morphologies: the higher-elevation rims exhibit longitudinal ridges, which extend for about 50 to 400 m, whereas lower-elevation central areas exhibit hummocky features (Figure 5-4c). The depressed-hummocky central areas are bordered by lateral levees, which at times are double-ridged.

5.2 Data and methods.

This section describes the datasets and methods used to obtain the results for this case study. It also describe how errors linked to measurements were assessed.

5.2.1 Satellite and drone photogrammetry mapping.

I used Pleiades Satellite stereo-images (©CNES, 2013, distribution Airbus Defence and Space) to generate high-resolution Digital Elevation Model (DEM; 2 m/px resolution) and orthorectified images (orthoimages) (Table 5-2) of the area that entirely covers the landslide deposit and its source area, and the adjacent coastal plane surface, using commercial photogrammetry software SOCET GXP from BAE Systems. These image products have been used to reconstruct the surface underneath the landslide deposit by manually interpolating between topographic contours (5 meters contour interval) of the coastal plane directly adjacent the landslide deposit, as previously done by other studies [e.g., Quantin *et al.*, 2004a; Conway and Balme, 2014; Magnarini *et al.*, 2019]. This reconstructed surface is used to calculate the thickness of the deposit.

With the use of drones (DJI Phantom Pro series), I collected nadir images of the area of the deposit that includes lobes 1, 2, 3, 5 and the central area, and the part of the head scarp (manual flight) (Figure 5-5). The landslide deposit areas were covered using planned flight missions created with the 'Pix4D Capture' app (flight details are provided in Table 5-1; Figure 5-5b,c). The head scarp area was covered in manual flight mode. From this image dataset I made high resolution DEMs and orthoimages of the area that cover lobes 1, 2, and 3 using commercial photogrammetry software Agisoft Photoscan (dark blue and light blue polygons in Figure 5-5; Figure 5-6). These products have been used for morphometric analysis of the longitudinal ridges that appear in the terminal part of the lobes (Figure 5-9). DEMs of the central area of the landslide deposit and of the scarp were also generated. However, as they are not of interest for conducting the morphometric analysis of longitudinal ridges, they are included in the Appendix Figure 1.

Table 5-1 – Details of planned drone flight paths.

Flight plan area (2019)	N° images	Altitude	Camera Angle	Frontal Overlap	Lateral overlap
Distal Lobes (Figure 5-5b)	290	150 m	90°	65%	65%
Proximal Lobes (Figure 5-5c)	134	250 m	90°	65%	65%

Table 5-2 – List of imagery datasets generated with photogrammetry software and used for the morphological analysis of the El magnifico landslide.

Locality	Data Source	Data Products		Software
		DEM	Orthoimage	
Context Area (Figure 5-5a)	Pleiades Satellites	2 m/px	B+W: 0.5 m/px Colour: 2 m/px	BAE Systems SOCET GXP
Distal Lobes (Figure 5-6)	Drone (2019)	8.22 cm/px	4.11 cm/px	Agisoft Photoscan
Proximal Lobes (Figure 5-6)	Drone (2019)	12.4 cm/px	6.19 cm/px	Agisoft Photoscan

I selected several points on the ground that could be identified on both a Pleiades-derived orthoimage and on drone-derived orthoimages (Figure 5-5a). The identification of these communal points was made it straightforward by the presence of a golf court on top of the landslide deposit, which provided unmistakable markers such as tee box, out of bound lines, putting green (in this location darker sand is used), and holes. Additional markers were provided by concrete posts and digs derived from the past quarry activity. Markers should be selected so to have an homogeneous distribution. This was possible for the Distal Lobes area, whereas for the Proximal Lobes not many marker where available on the ground and not well spread.

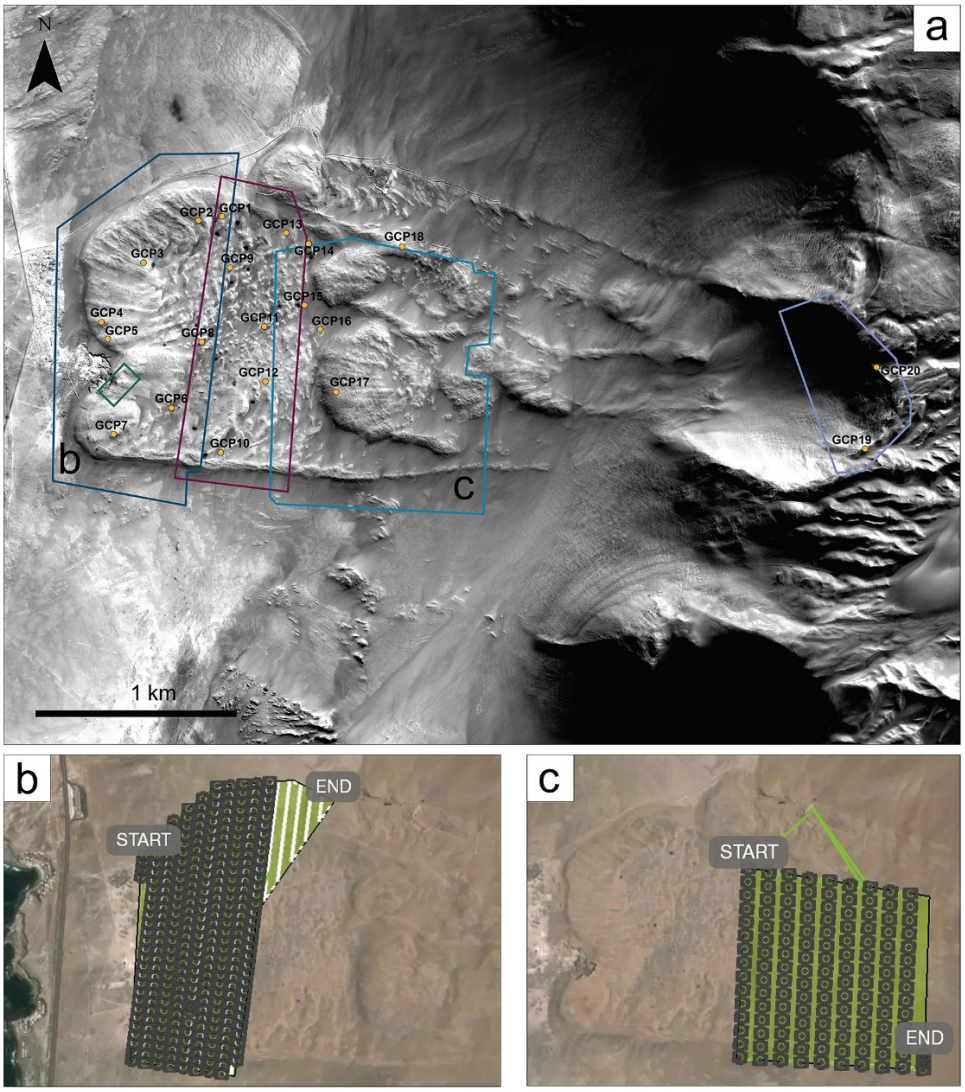

Figure 5-5 – Location of the ground control points used to calibrate drone-derived digital elevation models of the El Magnifico landslide and planned flight missions. a) Orthorectified image derived from Pleiades satellite images. The locations of GCPs is marked on the image with yellow dots. The coloured polygons outline the drone-derived digital elevation models. Dark blue and light blue polygons show the outlines of DEMs of the distal and proximal lobes, respectively, used to conduct the morphometric analysis of longitudinal ridges; magenta and violet polygons show the outlines of DEMs of the central area of the landslide deposit and part of the head scarp, respectively; b) and c) Flight path and camera positions planned using the 'Pix4D Capture' app to cover the distal lobes and proximal lobes areas, respectively.

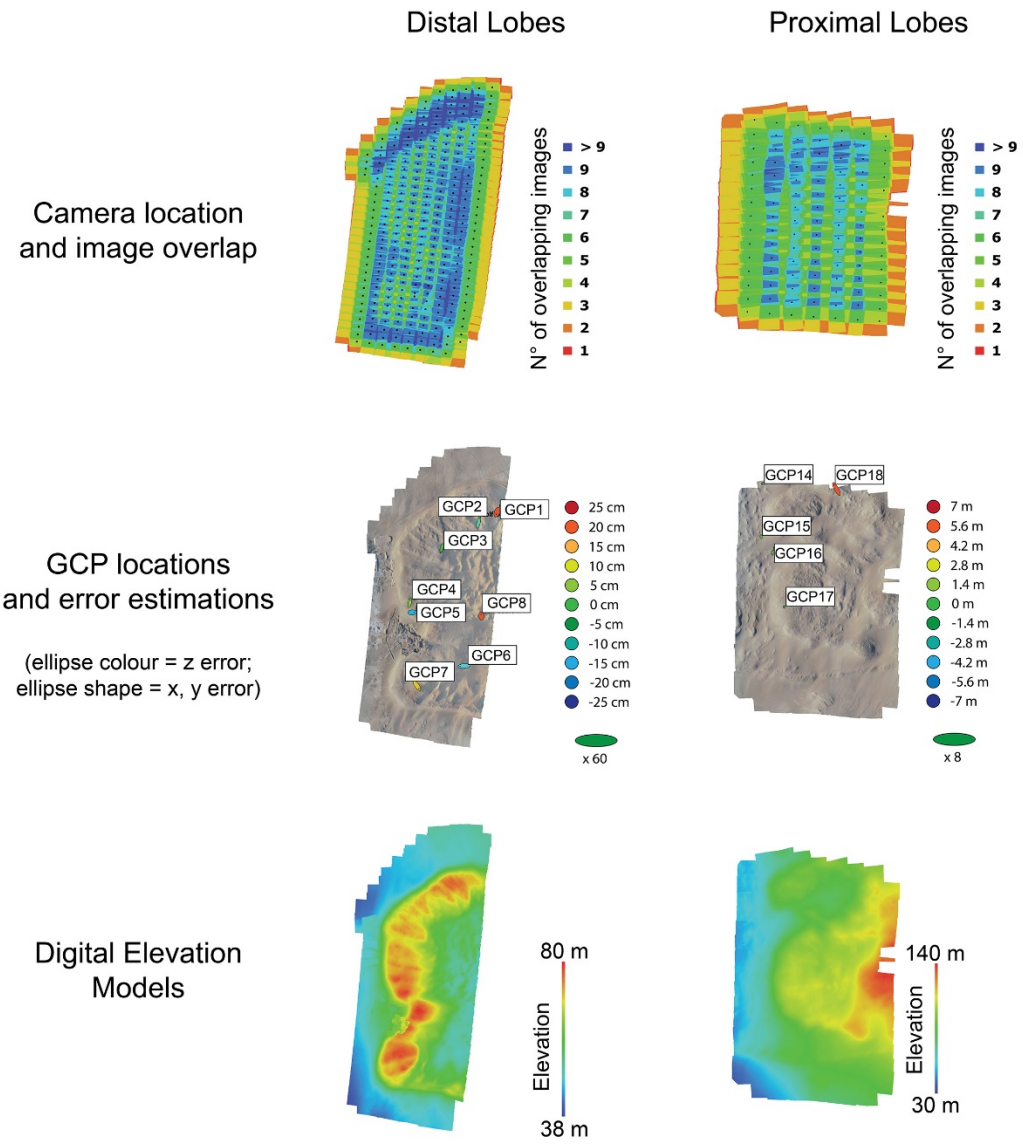

Figure 5-6 – Agisoft Photoscan data report of the digital elevation models and orthoimages derived from drone imagery obtained during the campaign in 2019. The figures show the camera locations and image overlap, the Ground Control Point (GCP) locations and error estimations provided by the software, and the resulting digital elevation models produced for the distal lobes area and the proximal lobe area.

Given that the Pleiades-derived orthoimage has a resolution of 0.5 m/px, the expected uncertainty of the marker localizations is about 1-2 pixels, thus about 1 m. The coordinates and elevation of these markers were obtained from the Pleiades-derived digital elevation model (Appendix Table 2). Such markers were used as ground control points (GCPs) to control the drone-derived digital elevation models. This approach provided consistency between Pleiades-derived and drone-derived datasets and avoided

introducing further error into our landslide deposit thickness calculation (Figure 5-7). In order to obtain good image alignment and thus good digital elevation model result, the GCPs should be homogeneously distributed. Therefore, the digital elevation model made for the Proximal Lobes could suffer from poor image alignment due to not homogeneous distribution of GCPs.

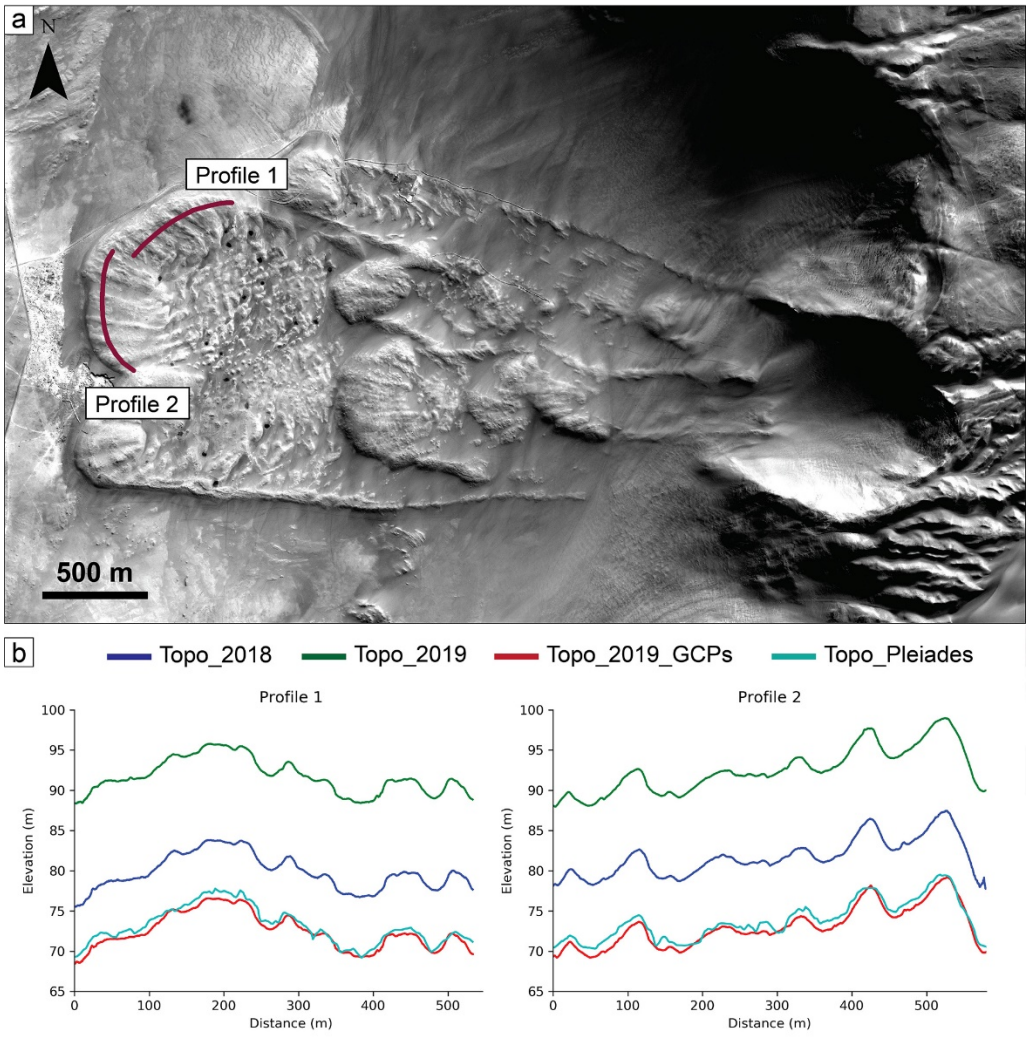

Figure 5-7 – Comparison of different digital elevation models of the El Magnifiico landslide. a) orthorectified image deived from Pleiades staellites images. It shows the location of two topographic profiles along which the topography of the landslide deposit is extracted from 4 different datasets, as shown in b). b) The dark blue lines corresponds to topography obtained from the drone-derived digital elevation model after 2018 campaign; the green lines corresponds to topography obtained from the drone-derived digital elevation model after 2019 campaign; the red lines correspond to the topography obtained from the georeferenced 2019 campaign DEM using terrain markers (GCPs in Figure 5-5) easily identifiable on Pleiades-derived orthoimages; the light blue lines correspond to the topography obtained from Pleiades stereo-image-derived digital elevation model. This figure highlights the importance of consistency when different datasets are used: all the topographic profiles show good agreement in terms of relative topography, however they have discrepancies in absolute elevation.

5.2.2 Ridge morphometry and their relationship to the thickness of the deposit.

In this section, I follow the approach used for the morphometric analysis conducted for the Coprates Labes landslide on Mars (Chapter 4). I identified longitudinal ridges using satellite-derived and drone-derived orthoimages: a longitudinal ridge is determined by its horizontal continuity in the direction of the slide and its presence as morphological feature is unmistakable from a top-view observation of the landslide deposit. In ArcGIS, I mapped longitudinal ridges tracing a line corresponding to what I interpreted to be the crest of the ridges from the orthoimages (Figure 5-9). From the topographic profiles in Figure 5-9c, the location of few ridges does not correspond to a topographic high. This may be due to local topography variation, such as through infill with wind-blown sand, for instance.

In order to estimate the thickness of the landslide deposit, I reconstructed the landslide basal surface. In order to recreate this surface, I manually interpolated the topographic contours of the current topography adjacent the landslide (Figure 5-8a). This surface was used to estimate the thickness of Lobe 1 and 2. As Lobe 3 lies on top of Lobe 1 and 2, I also reconstructed such basal surface (Figure 5-8b). These newly created surfaces only approximate the real original topography and, therefore, the final estimations of the volumes and thickness carry uncertainties, which will be commented in section 5.2.3.

I conducted the morphometric analysis at lobes 1, 2, and 3, where the ridge morphologies are most prominent, by tracing one transverse profile at each of the lobes (Figure 5-9a). For each profile, I measured the distance between the ridges and obtained an average spacing, which was considered representative of the wavelength of the ridges (S in Table 5-4). Using drone-derived topography and interpolation-derived basal surface, I also calculated the average thickness of the deposit corresponding to each profile (T in Table 5-4, Figure 5-9c), following the method used for the martian landslide case study (Chapter 4). For each profile, I calculated the ratio between the average

spacing between the ridges and the average thickness of the landslide deposit (S/T ratio in Table 5-4).

5.2.3 Deposit thickness error estimation.

I traced three sets of perpendicular profiles within the landslide deposit (blue profiles), so that they would coincide with the transversal and longitudinal component of the arc-shaped profiles used for the morphometric analysis of the longitudinal ridges Figure 5-8.

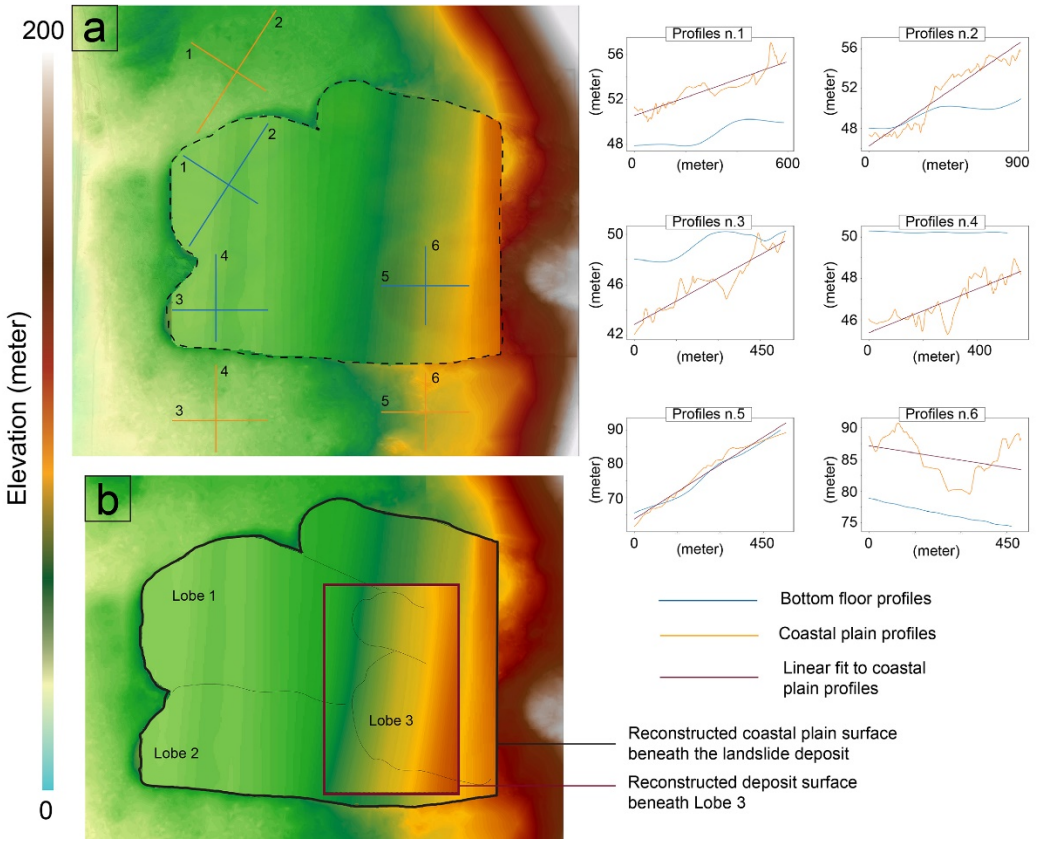

Figure 5-8 – Validation of the reconstructed surface underneath the El Magnifico landslide deposit. (a) shows the position of the sets of profiles adjacent to the landslide deposit (yellow lines) and within the landslide deposit area (blue lines); within the landslide deposit area (dotted black line) it is shown the reconstructed DEM of the valley floor underneath the landslide deposit as inferred by interpolation of the Pleiades DEM contour lines adjacent the deposit; the sets of profiles are used to generate the plots to the right-hand side of the figure, which show the comparison of the mirror transects (blue and yellow lines 1-6). (b) shows the reconstructed DEM of the coastal plain surface underneath the landslide deposit as inferred by interpolation of the Pleiades DEM contour lines adjacent the deposit (area within black solid line) and the reconstructed DEM of the deposit surface covered by Lobe 3.

The transects (blue lines) are compared to a mirror set of transects traced adjacent to the landslide edge (yellow lines), so to: 1) assess the plausibility of the overall elevations of the reconstructed bottom surface, and 2) to provide an error estimation of the average thickness that I provide in the morphometric analysis.

As done in Chapter 4, the error in the thickness calculation is expressed as standard deviation of the topographic elevation measurements along each transects adjacent to the landslide deposit (yellow transects). As the topographic profiles at Lobe 1, 2, and 3 are parallel to neither transversal nor longitudinal direction, the final error is obtained from the propagation of error along these two axes, using the equation $\sigma_k = \sqrt{\sigma_i^2 + \sigma_j^2}$. This equation combines standard deviation for yellow lines 1 and 2 to obtain the error for Lobe 1; yellow lines 3 and 4 to obtain the error for Lobe 2; and yellow lines 5 and 6 to obtain the error for Lobe 3. The errors reported in Table 5-3 are represented as error bars in Figure 5-9b.

Table 5-3 - Error estimation of the reconstructed coastal plain surface underneath the landslide deposit.

Sets of Profiles	Standard Deviation σ	Propagation of error σ_k
Yellow line 1	1.51 (σ_i)	3.48 (Lobe 1)
Yellow line 2	3.13 (σ_j)	
Yellow line 3	2.04 (σ_i)	2.27 (Lobe 2)
Yellow line 4	1.01 (σ_j)	
Yellow line 5	8.3 (σ_i)	8.61 (Lobe 3)
Yellow line 6	3.3 (σ_j)	

5.3 Results.

The results section consists of three parts: morphometric analysis of the longitudinal ridges, detailed description of the deposit internal structures observed at five outcrops, and interpretation of the internal structures.

5.3.1 Morphometric analysis.

Figure 5-9b shows the S/T ratio values found at the three profiles. Lobe 2 and Lobe 3 have S/T ratio values of 2.32 and 3, respectively, falling within the range of the scaling relationship between the two parameters found in laboratory experiments on rapid granular flows, which is represented as the grey area in Figure 5-9b. Instead, Lobe 1 has S/T ratio value of 1.54, falling outside the range of the scaling relationship.

Table 5-4 – Results of the morphometric analysis of longitudinal ridges at the El Magnifico landslide. The error of the thickness value is derived by combining standard deviation of the elevation variation of the set of profile (yellow lines) adjacent to the area of each profile used for the morphometric analysis: yellow profiles 1 and 2 for Lobe 1; yellow profiles 3 and 4 for Lobe 2; yellow profiles 5 and 6 for Lobe 3 (see Figure 5-8). The spacing error corresponds to one standard deviation of the ridge spacing distribution.

	Profile Length (m)	Number of Ridges	S (m)	T (m)	S/T ratio
Profile Lobe 1	1155	31	36.76 ± 20.28	23.8 ± 3.5	1.54 ± 0.57
Profile Lobe 2	642	11	56.22 ± 19.63	24.3 ± 2.3	2.32 ± 0.36
Profile Lobe 3	628	12	50.27 ± 18.30	16.7 ± 8.6	3.00 ± 0.63

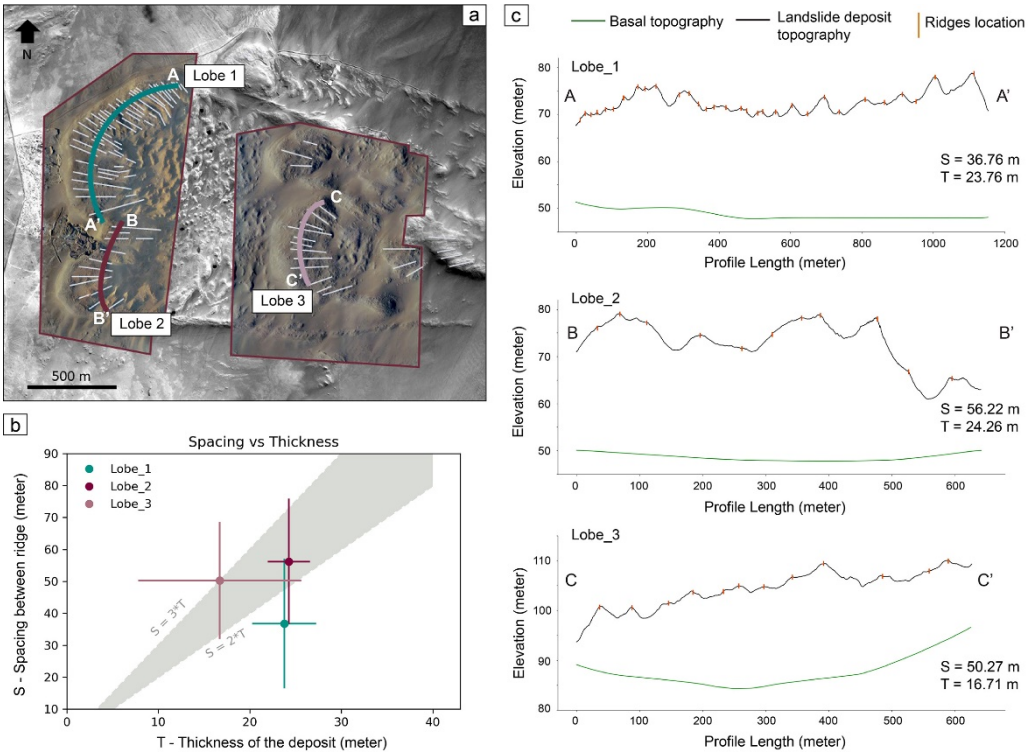

Figure 5-9 - Morphometric analysis of the longitudinal ridges of the El Magnifico landslide. a) Drone-derived coloured orthoimages within red polygons superposed on satellite-derived black and white orthoimage; white lines represent the location of the crest of the ridges; transversal profiles along which morphometric analysis and deposit thickness calculation are performed for Lobe 1, 2, and 3 are marked as green, red and pink lines, respectively; b) plot showing the relationship between the spacing of the ridges and the thickness of the deposit at Lobe 1, 2, and 3; the grey area represent the range of the scaling relationship found in laboratory experiments on rapid granular flows; the error of the thickness value is derived by combining standard deviation of the elevation variation of the set of profile adjacent to the area of each profile used for the morphometric analysis (see Figure 5-8); the error bars for the ridge spacing correspond to one standard deviation of the spacing provided in Table 5-4; c) transversal profiles at Lobe 1, 2, and 3: black lines represent the topographic surface of the deposit extracted from drone-derived digital elevation models; green lines represent the basal surface of the landslide deposit, as inferred by interpolation of topographic contours of the coastal plane; orange marks represent the location of the crests of the longitudinal ridges.

5.3.2 Outcrop description.

The presence of a quarry has exposed a series of outcrops at the terminal part of lobe 2 (Figure 5-4b). Mather *et al.* [2014] and Crosta *et al.* [2017] have exploited the excavation activity of the quarry to observe some internal structures of the landslide deposit. These two works described a ~130m-long and ~20m-high outcrop (see Fig. 6a in Mather *et al.* [2014] and Fig. 7 in Crosta *et al.* [2017]). This outcrop likely represents a transversal section of the landslide deposit and shows a wavy green-yellow-red coloured middle-

lower part. According to Mather *et al.* [2014], the yellow-red layer represents a shear surface which marks the contact between Lobe 1 and 2. However, I do not think this is the case, given the location of the quarry relative to the contact between the two lobes seen from a top-view image (Figure 5-4c). Unfortunately, at the time of the first campaign in 2018, the outcrop had been removed, as the activity of the quarry continued until 2015. Although the quarry was filled with debris, leaving only the top 6-10 m of the landslide deposit uncovered, a ~150m-long uninterrupted section made by excavations with different orientations was available, providing both longitudinal and transverse segments of the deposit. This allowed me to have a 3D view of the internal structures of the upper part of the deposit.

Starting from the northernmost section of the quarry and then moving south along the section, I divided the observations into five locations along the continuous wall. Outcrops 1 and 3 represent longitudinal views of the deposit, whereas outcrops 2, 4, and 5 represent transversal views (Figure 5-10 to Figure 5-16). The section of excavation that includes outcrops 3, 4, and 5 also happens to intersect a longitudinal ridge, hence making these outcrops key sites for interpretation of the internal structure of such morphological features.

OUTCROP 1

At outcrop 1 (Figure 5-10a), two main layers are visible, which are separated by a well-defined contact. The upper layer is brown in colour, matrix-supported, with sub-rounded clasts a few centimetres in size. The source lithology is likely the conglomerates observed at the scarp (Punta Barranco Formation), although a decrease in the maximum clast size is seemingly present (Figure 5-11). However, within this brown layer, linear patches of grey clasts appear widespread (Figure 5-10b). The grey clasts are larger than the clasts in the brown part and they appear imbricated in places.

The lower layer is a breccia mainly grey in colour, with a lens that appears red, yellow, and greenish in colour (Figure 5-10c). A closer look reveals that clasts similar in size and shape to those of the breccia are within the coloured lens and that they are cemented (Figure 5-12a). This lens dips towards the

inner part of the deposit with an angle of about 40°, has a wavy aspect, and separates the grey breccia into two distinct parts. The upper part is comprised of large (8 to 50 cm) angular to sub-rounded clasts, with the largest clasts found close to the contact with the conglomerate-derived layer above and, at one location, forming an injection structure within the above layer. Clasts are closely packed, generally displaying preferential orientation that mirrors the lens dip. The part below the lens is made of much smaller clasts (maximum size about 10 cm), yet still displaying a tight configuration and, at times, preferentially oriented as the lens and the upper part. The source lithology is likely to be a fine-grained sandstone from the Guantajaya Formation.

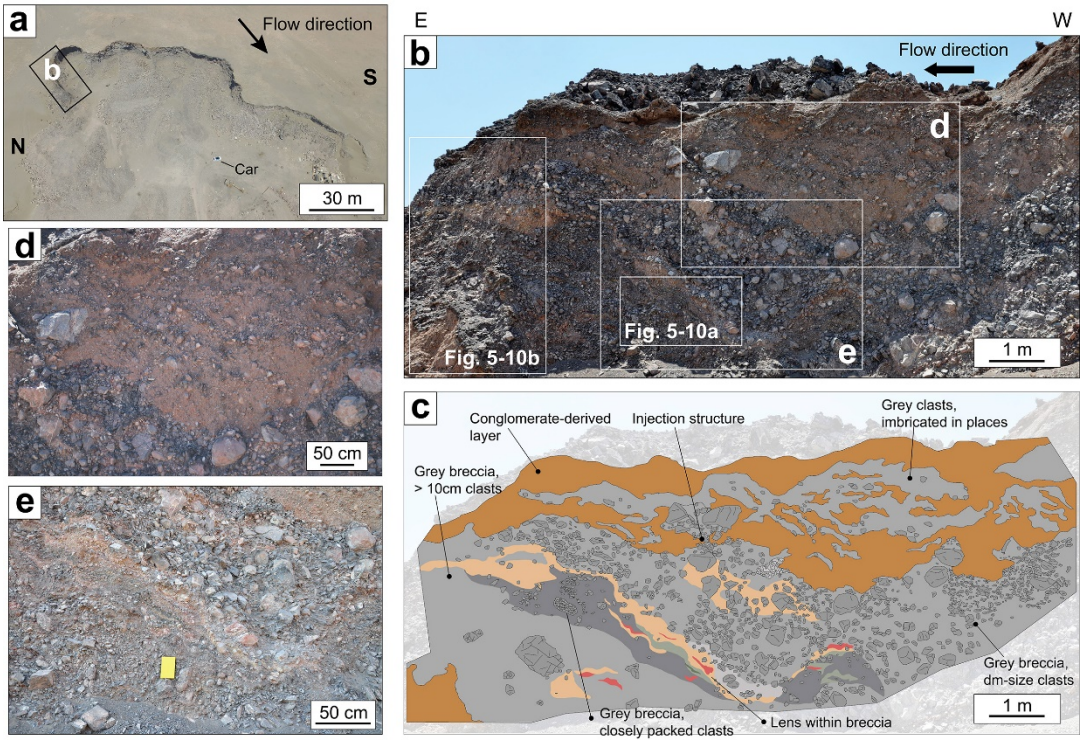

Figure 5-10 – Outcrop 1 at El Magnifico landslide quarry. a) Top-view of the quarry showing the location of outcrop 1; b) Photomosaic of a field-view of the outcrop; c) schematic representation of the lithologies and structures observed: two main layers are recognizable: a top layer brown in colour, matrix-supported and a bottom layer grey in colour, clast-supported breccia, with larger clasts in the upper part, within which a red-yellow-green lens appear; d) close view of the well-defined contact between the conglomerate-derived upper layer and the grey breccia; note the presence close to the contact of sub-rounded clasts about 40 cm in size; to the left, clasts of the breccia inject into the conglomerate-derived upper layer; e) a coloured-lens separates the dm-size clasts of the upper breccia from the > 10-cm-size clasts of the lower breccia.

Figure 5-11 – Conglomerates of the Punta Barranco Formation. This is likely the source lithology of the upper layer brown in colour, matrix-supported, with sub-rounded clasts a few centimetres in size observed at Outcrop 1.

Within the grey breccia layer, conglomerates-derived parts appear in two locations. In particular, conglomerates appear again at the lower left of the outcrop with a neat contact with the breccia (Figure 5-12b). Here, conglomerates show more, and larger, clasts compared to the one overlapping the grey breccia. Around the left corner of the outcrop, we could follow this lower layer of conglomerates for a few meters, before being covered by quarry debris. However, from this limited transversal perspective, it looked like the grey breccia layer lies in between two layers of conglomerates, which might be connected (Figure 5-12b).

The greenish-yellow-red lens that we observe at this outcrop is somehow reminiscent of the wavy greenish-yellow-red surface described in Mather *et al.* [2014] and Crosta *et al.* [2017]. I think that it is plausible that both observations are the expression of the same structures at different locations and with different perspectives (note that our outcrop is a longitudinal section, whereas the previous works showed a transversal section).

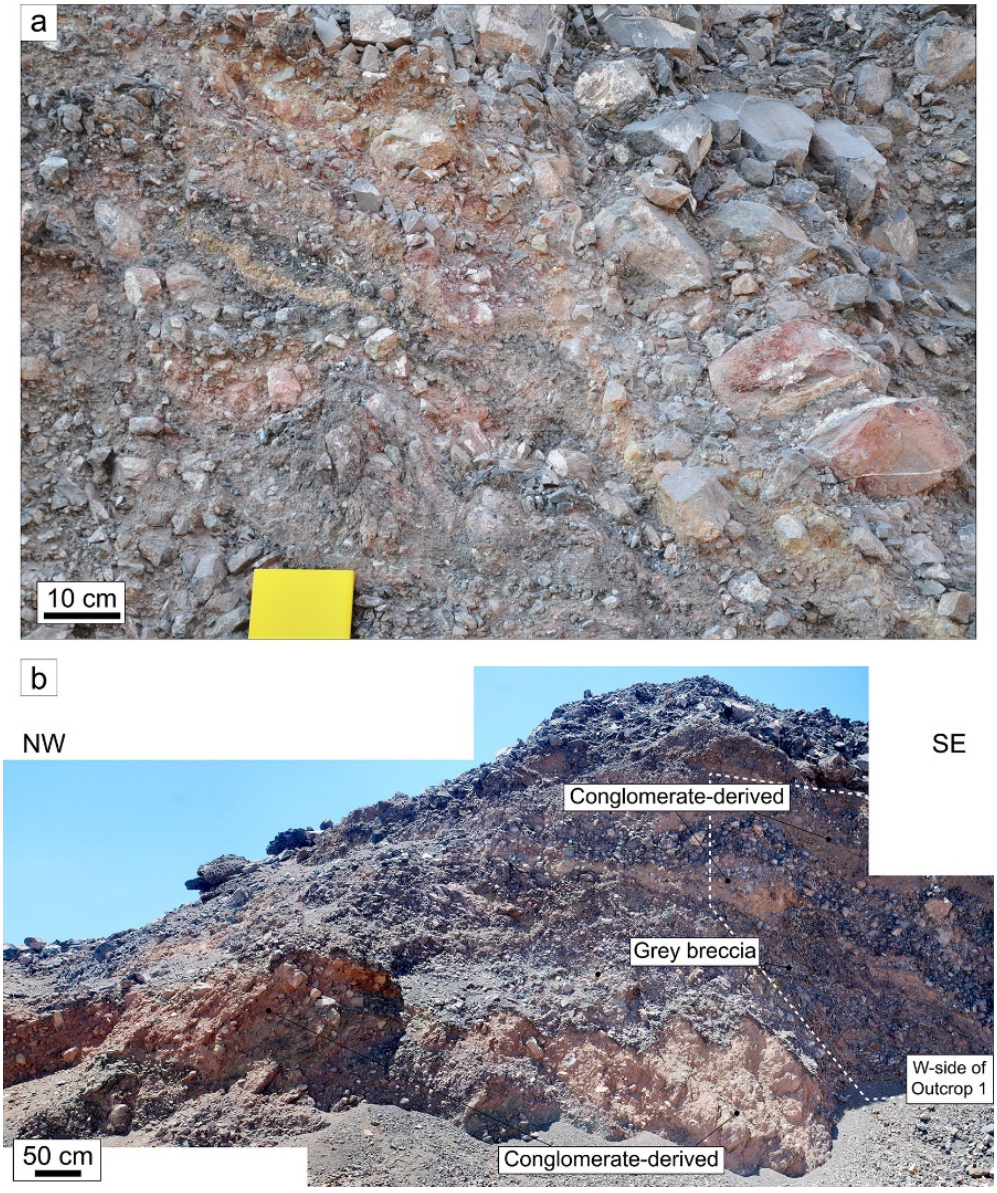

Figure 5-12 – Extended observations of outcrop 1 at El Magnifico landslide quarry. a) Close-up view of the coloured lens within the grey breccia observed at Outcrop 1. b) Observations near Outcrop 1 reveal the presence a conglomerate-derived layer also occurring below the grey breccia. It seems that the preservation of the stratigraphic order within rock avalanche deposits often mentioned in the literature does not occur for this case study (other evidence of this is also found at other locations). However, the different lithologies do not mix chaotically, rather they appear interfingered.

OUTCROP 2.

At outcrop 2 (Figure 5-13a), a transversal section of the landslide deposit, we observe the same grey breccia seen at Outcrop 1 both underlying and

laterally bounding the conglomerates-derived part also described at Outcrop 1.

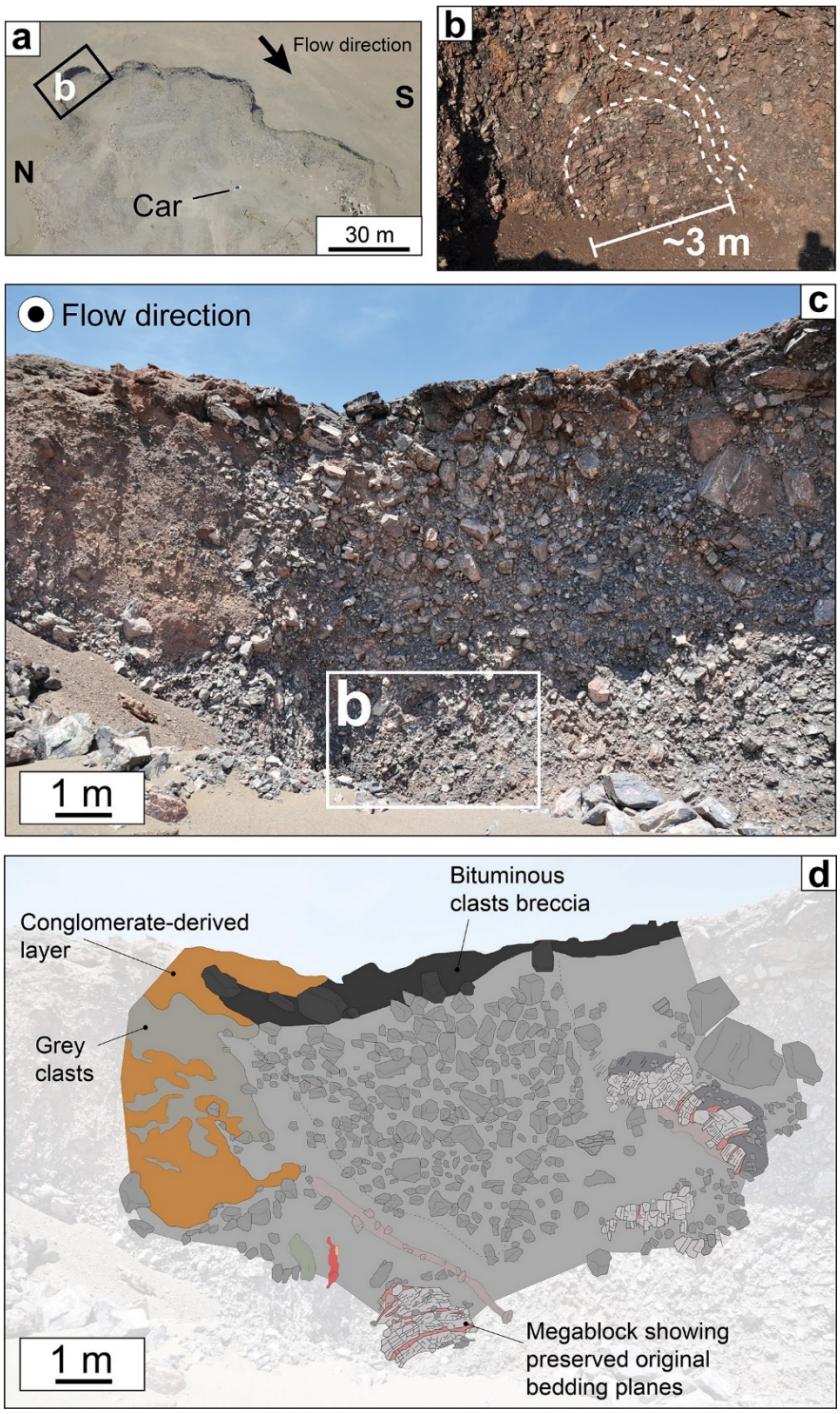

Figure 5-13 - Outcrop 2 at El Magnifico landslide quarry. a) Top-view of the quarry showing the location of the outcrop 2; b) Field photo of the outcrop, in which a lateral transition from the brown in colour, matrix-supported layer to the grey in colour, clast-supported breccia is visible; c) close view of a 3x3 meter block, within the grey breccia, that exhibits well-preserved original bedding planes; on its right side, a red/pink coloured band made of finer grained clasts is present; d) schematic representation of the outcrop 2 that highlights the structures observed: to the left, the contact between the conglomerate-derived layer and the grey breccia; at the bottom and to the right, blocks that show preserved original bedding planes are present within the grey breccia; in the centre, there is a roughly v-shaped area characterized by angular blocks densely packed with an apparent inverse grading.

Adjacent to the lateral contact between the two different lithologies, and within the grey breccia, we recognize a roughly v-shaped zone, about 6 m wide and 6 m deep, filled with dm-sized angular blocks, densely packed and seemingly inverse graded. Below this pocket-like structure, a 3x3 m sub-rounded block is observed, exhibiting well-preserved original bedding planes, spaced 5 to 15 cm apart (Figure 5-13b). The block is made of the same grey lithology that forms the grey breccia that surrounds it and shows several continuous red layers parallel to the bedding planes. A finer grained band with a slight red/pink hue is present between the block and the v-shaped zone (Figure 5-13b). On the right-hand side of these structures, the outcrop has a more typical breccia fabric, comprised mostly of closely packed angular blocks. Careful observations reveal several locations at which blocks show remnant bedding planes, yet tilted from the horizontal plane. The grey breccia is capped with a ~1 m thick breccia made of dm-size bituminous clasts (the source lithology is likely to be salt-rich bituminous siltstone of the Guantayaja Formation).

OUTCROP 3.

Outcrop 3 (Figure 5-14) is a longitudinal section of the deposit. A 6 m long and 5 m thick block showing well-preserved original bedding planes appears within the grey breccia, which is mainly composed of dm-size angular clasts. The bedding planes dip towards the inner part of the deposit with an angle of about 42°, a dip similar to the coloured lens at Outcrop 1.

From bottom to top, the beds forming the block decrease in thickness, from about 50 cm to few centimetres. The reduction in thickness seems to be related to the thrusting of the upper part that generates a wedge, which closes towards the top-right of the image. Within the wedge, we observe red layers parallel to the thinned beds (Figure 5-14), similar to the ones that I observed in the sub-rounded block at Outcrop 2. Similar red layers are seen within the breccia in locations where preserved original bedding are somehow recognizable, although not as part of a distinctive block.

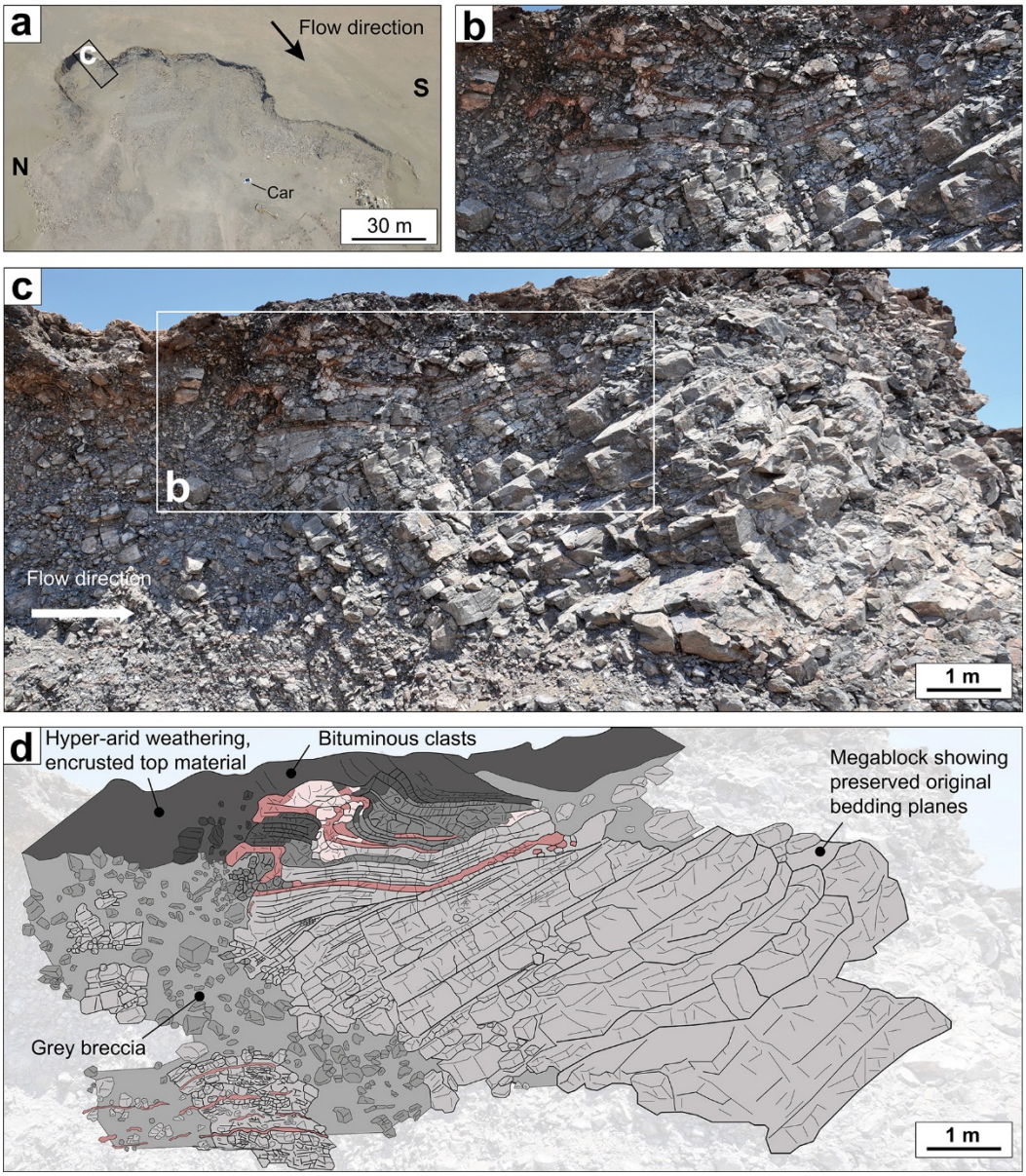

Figure 5-14 – Outcrop 3 at El Magnifico landslide quarry. a) Top-view of the quarry showing the location of the outcrop 3. b) close view of thrust structure that is found on the upper part of the megablock; the original beds of the block decrease in height from left to right, forming a wedge; the thrusted and folded part of the megablock is made of bituminous sandstones. c) Field photomosaic of the outcrop 3. d) schematic and annotated representation of the structures observed at the outcrop 3.

OUTCROP 4

Outcrop 4 (Figure 5-15) is again a transversal section of the deposit. At this location, a zone about 8 m wide and 7 m high is characterized by the presence of clear layering corresponding to original bedding planes. This zone, which resembles the blocks with original bedding planes seen at Outcrops 2 and 3, emerges within a breccia-type deposit. The preserved bedding planes have

a sub-horizontal apparent attitude. At the upper and left part of this block, planes have dm-spacing. Instead, at the right-hand side, planes are much closer to each other, only a few centimetres apart, and at times display more advanced comminution.

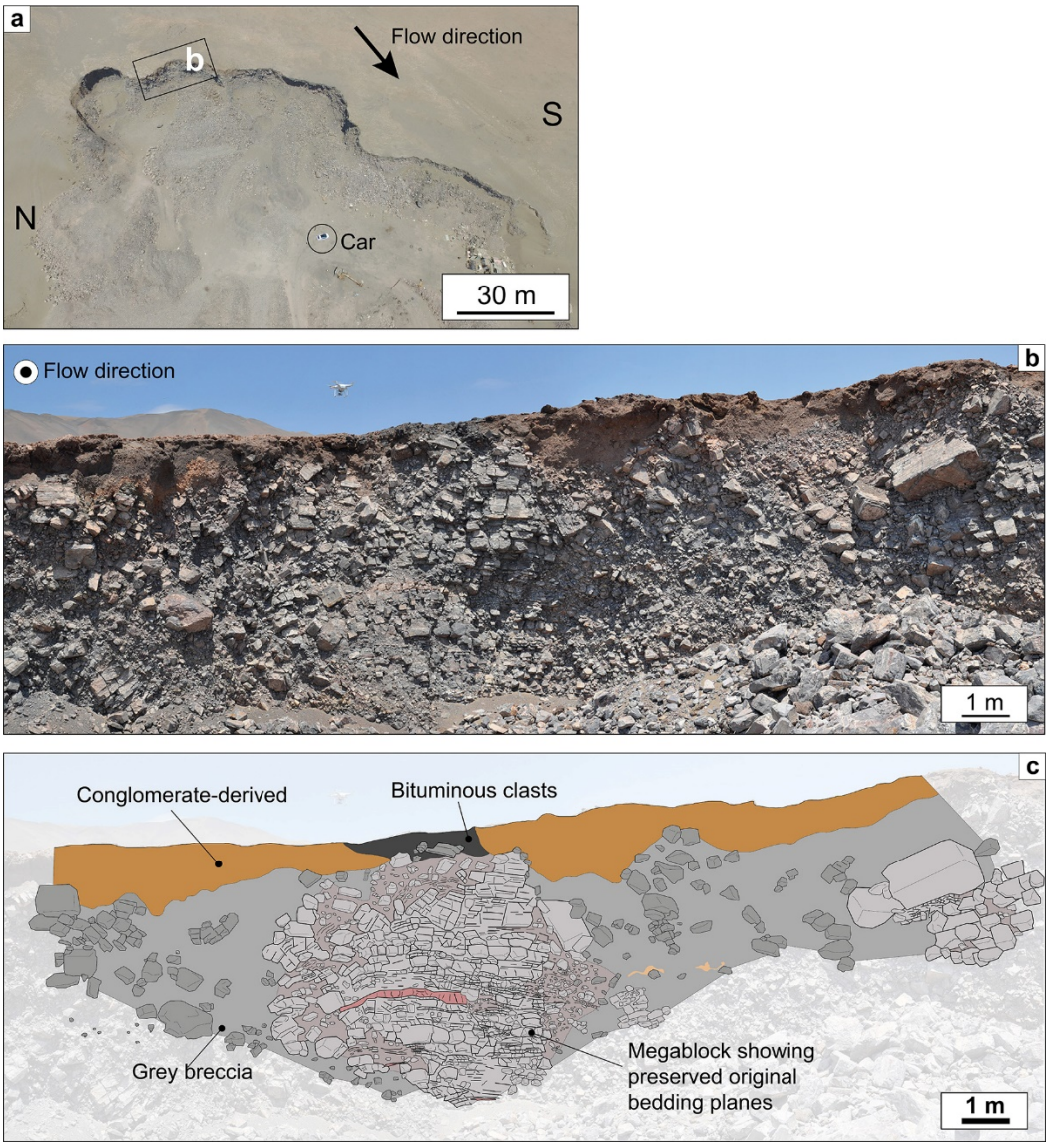

Figure 5-15 – Outcrop 4 at El Magnifico landslide quarry. a) Top-view of the quarry showing the location of the outcrop 4. b) Field photomosaic of the outcrop 4. c) schematic representation of the structures observed at outcrop 4: at the centre, a megablock about 8 m wide exhibiting well-preserved original bedding plane appears within the breccia; the megablock is capped by dm-size clasts of bituminous sandstones; the breccia is capped by a conglomerate-derived layer that does not exceed 1 m in thickness.

OUTCROP 5.

Outcrop 5 (Figure 5-16a) is another transversal section of the landslide deposit.

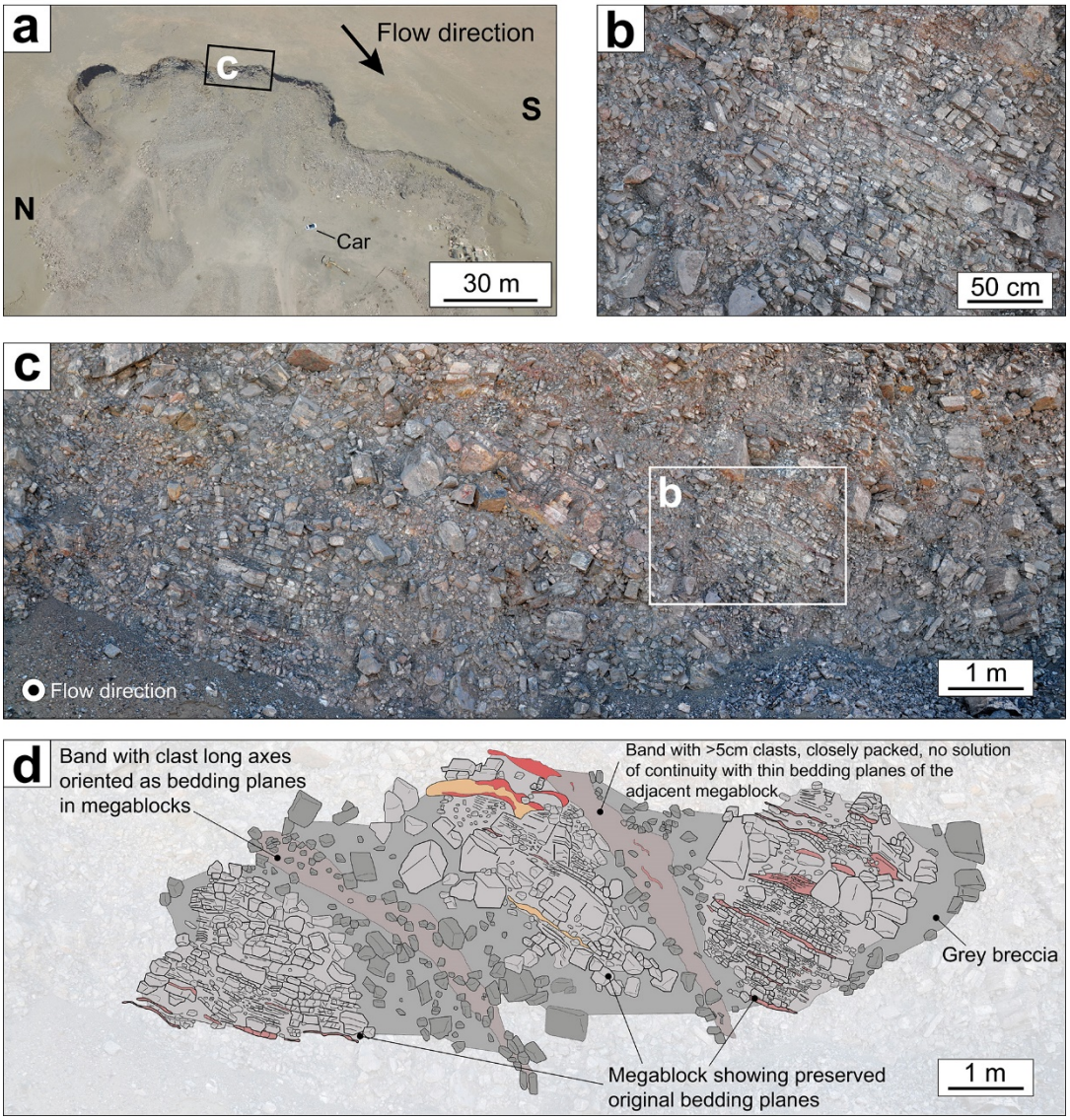

Figure 5-16 - Outcrop 5 at El Magnifico landslide quarry. a) Top-view of the quarry showing the location of the outcrop 4; b) close view of a section of the outcrop; c) Field photomosaic of the outcrop; d) schematic representation of the structures observed at outcrop 5; three areas that exhibit preserved original bedding planes alternate with bands made of smaller clasts oriented as the bedding planes; the band between the middle and right megablock is made of smaller clasts (>5 cm) with same orientation as the other described structures; at times, these clasts show some degree of continuity with the bedding planes of the megablock on the right; the continuity and the high degree of comminution recall a cataclastic aspect.

Here, we distinguish three zones that exhibit original bedding planes (an example is shown in Figure 5-16b). As observed at other outcrops, the preserved beds have varying thickness and several red layers parallel to the bedding planes are present. The bedding planes in all three zones have the same attitude, 40/38SE. These three zones are separated by two bands. The left band (Figure 5-16c and d) is made of clasts with sizes in the range of 5-40 cm. The clasts appear to have the long axis oriented following the direction of the bedding planes described earlier. The right band has the same orientation as the other structures so far described but it is made of smaller clasts, closely packed, which at times give the impression that there is continuity with the progressively thinner original bedding planes.

5.4 Discussion.

5.4.1 Interpretation of the internal structure of the landslide deposit.

The presence of a disused quarry at a far end of Lobe 2 provides a number of outcrops which show the internal structure of the landslide deposit. This is the only location at which outcrops of the landslide deposit are available, therefore the observations are limited to structures at the terminal part of the slide, which may have been affected, if not produced, at the time the landslide came to a halt. Unfortunately, another limitation comes from the fact that the disused quarry is now partially filled with debris produced by the excavation, leaving only the top 6-10 meters of the deposit visible, hence not allowing the observation of the entire deposit section, as was possible in the past (see Fig. 6a in Mather *et al.* [2014] and Fig. 7 in Crosta *et al.* [2017]). These limitations prevent an exhaustive reconstruction of the sedimentology of the El Magnifico landslide deposit (e.g., as done for other case studies by Weidinger *et al.* [2014]; Dufresne *et al.* [2016]), nevertheless I was able to make several interesting new observations:

1) At Outcrop 1 and 2, I see a well-defined contact between two different lithologies (conglomerates and breccia), which do not intermix. The contact

between these lithologies occurs sub-horizontally (see Figure 5-10) and sub-vertically (see Figure 5-13). Moreover, at Outcrop 1, we see the top lithology (i.e., conglomerates) appearing at places within the underlying breccia with distinct contact, suggesting an interfingering relationship from a transverse view point (Figure 5-12). These observations are in line with previous works which indicate a lack of chaotic mixing between the different original slope forming materials during emplacement [e.g., Shreve, 1968a; Dufresne *et al.*, 2016 and reference within]. The preservation of the source stratigraphy is often reported in the literature and the fact that we observe conglomerates at the top at Outcrop 1 (which is the lithology at the top of the stratigraphic sequence at the scarp , Figure 5-3) may suggest that this is also the case for the El Magnifico landslide. However, the lateral contact between the conglomerates and the breccia seen at Outcrop 2, and the seemingly interfingering relationship between the two lithologies suggest a more complex level of interaction during emplacement of the landslide. Moreover, although the conglomerates are the lithological unit at the top of the stratigraphic sequence at the head scarp of the El Magnifico landslide, they do not always correspond to the top unit within the landslide deposit, as visible by comparison of Outcrop 1 (Figure 5-10) and Outcrops 2 and 3 (Figure 5-13 and Figure 5-14, respectively). Interestingly, at Outcrop 4 (Figure 5-15), conglomerates reappear at the top of the deposit, with variable thickness that does not go beyond a metre or so. However, their occurrence seems to happen adjacent to bituminous clasts that cap the megablock. The contact between the bituminous clasts and the megablock does not seem to occur abruptly, rather as a transition. This is also observed at Outcrop 3 (Figure 5-14), with the grey breccia and the megablock transitioning to a bituminous colour.

These observations do not support the notion of a carapace made of angular clasts riding atop a shearing body, which some have used to represent typical rock avalanche and rockslide facies and features [Weidinger *et al.*, 2014; Dufresne *et al.*, 2016]. Similarly, these observations do not fit with the idea that long runout landslides move as a solid block with shearing restricted to the basal region, as some lubrication hypotheses propose [Shreve, 1968a].

This view has been challenged by Campbell *et al.* [1995], who showed, using 2D computer simulations, that long runout landslides are characterized by distributed shearing (see Figure 2-8). In fact, we note similarity between some of the observed types of contacts and structures at the El Magnifico landslide, and in the computer simulations by Campbell *et al.* [1995], such as interfingering relationships between the strata (see Plate 3 in Campbell *et al.* [1995] and Figure 5-12 of this chapter). As affirmed by Johnson *et al.* [2016a], three-dimensional computer simulations would be highly desirable; in addition to providing a further level of comparison for field-based observations, they would also provide insights on the importance of the three-dimensional effects of the mechanisms proposed for the formation of longitudinal ridges in long runout landslides.

2) I report the presence of several-meters-sized blocks that show preserved original bedding planes (from now on we refer to them as 'megablocks', following the use in Dufresne *et al.* [2016]). These structures exhibit different degrees of deformation, such as bed thickness reduction and fracturing normal to bedding planes, yet blocks maintain a coherent aspect, that is shattered fragments or sub-blocks do not show displacement relative to each other. The presence of such megablocks at the distal part of the landslide deposit throws doubt on the idea of progressive facies maturation with distance that apparently occurs in some cases [Dufresne *et al.*, 2016]. The megablocks reported in this study are reminiscent of the 'jigsaw puzzle effect' described by Shreve [1968a]. Moreover, their presence within a breccia may result from heterogeneous stress distribution within the sliding mass and through the entire runout, allowing the preservation of a large portion of the original slope-forming material.

Large fluctuation of stresses are reported in computer simulations by Campbell *et al.* [1995] and Johnson *et al.* [2016a], and they are considered the hallmark of the acoustic fluidization hypothesis [Melosh, 1979]. The presence of megablocks that preserve original bedding planes so far from the slide scarp can be plausibly associated with the existence of stress fluctuation within the sliding mass. In this regards, we also recall the wavy surface observed in the long transversal outcrop in Mather *et al.* [2014] and Crosta *et*

al. [2017] and suggest that it may be the expression of some sort of vibrational mode operating within the slide.

5.4.2 Relationship between morphological features and internal structures.

The present excavation created by the mining activity at the quarry provides a laterally continuous window of the landslide internal structures. Part of this section intersects a ridge and it offers an opportunity to interpret the internal structures of the deposit in relation to the ridge. In particular, I wanted to check whether the convection-style motion for longitudinal ridge formation proposed in Chapter 4 for the Coprates Labes landslides on Mars is supported by evidence provided through the anatomy of the internal structures in the El Magnifico landslide deposit.

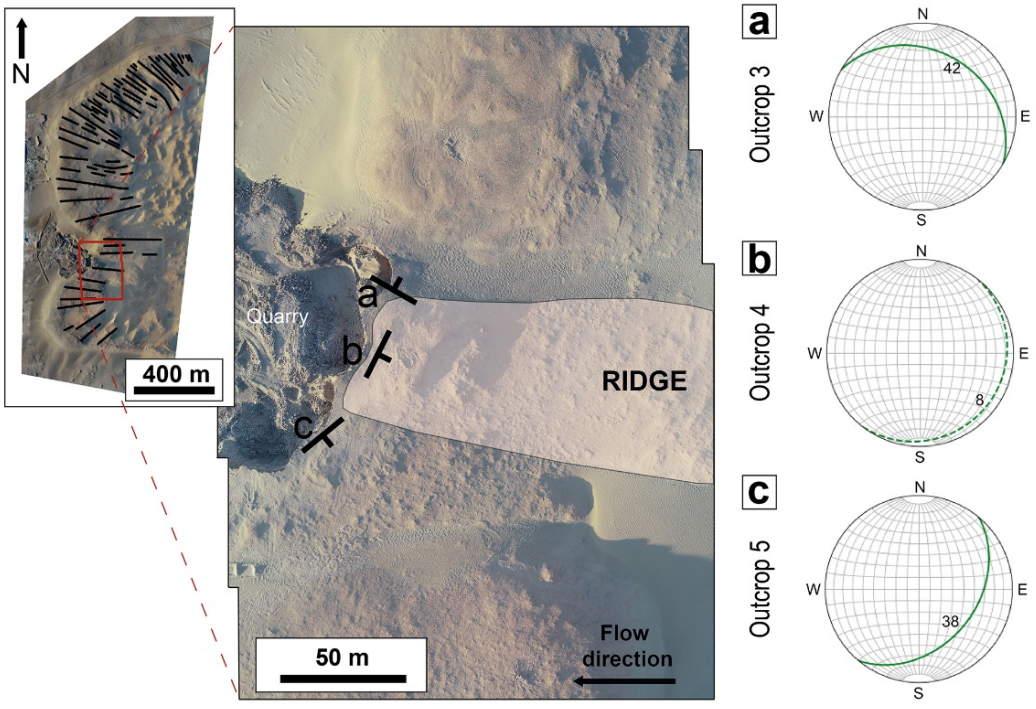

Figure 5-17 – El Magnifico attitude of Internal structures. Orthoimage of the terminal part of the landslide cluster and close-up top-down photomosaic of the quarry; the location of the ridge is represented by the light-coloured area; the orientation of the structures observed at outcrops 3, 4 and 5, are shown in the stereonets a), b), and c), respectively.

The outcrops of interest are 3, 4, and 5. The attitudes of the bedding planes preserved in the megablocks that we measured in these outcrops suggest that they are oriented according to their position relative to the ridge (Figure 5-17). The megablock at Outcrop 4, located in the central part of the ridge, gently dips inwards (i.e., towards the centre of the deposit, ~ 8°ESE), with a strike perpendicular to the ridge extension. Whereas the megablocks at Outcrop 3 and 5, located at the limbs of the ridge, dip outwards of the ridge structure, 120/42NE and 40/38SE, respectively.

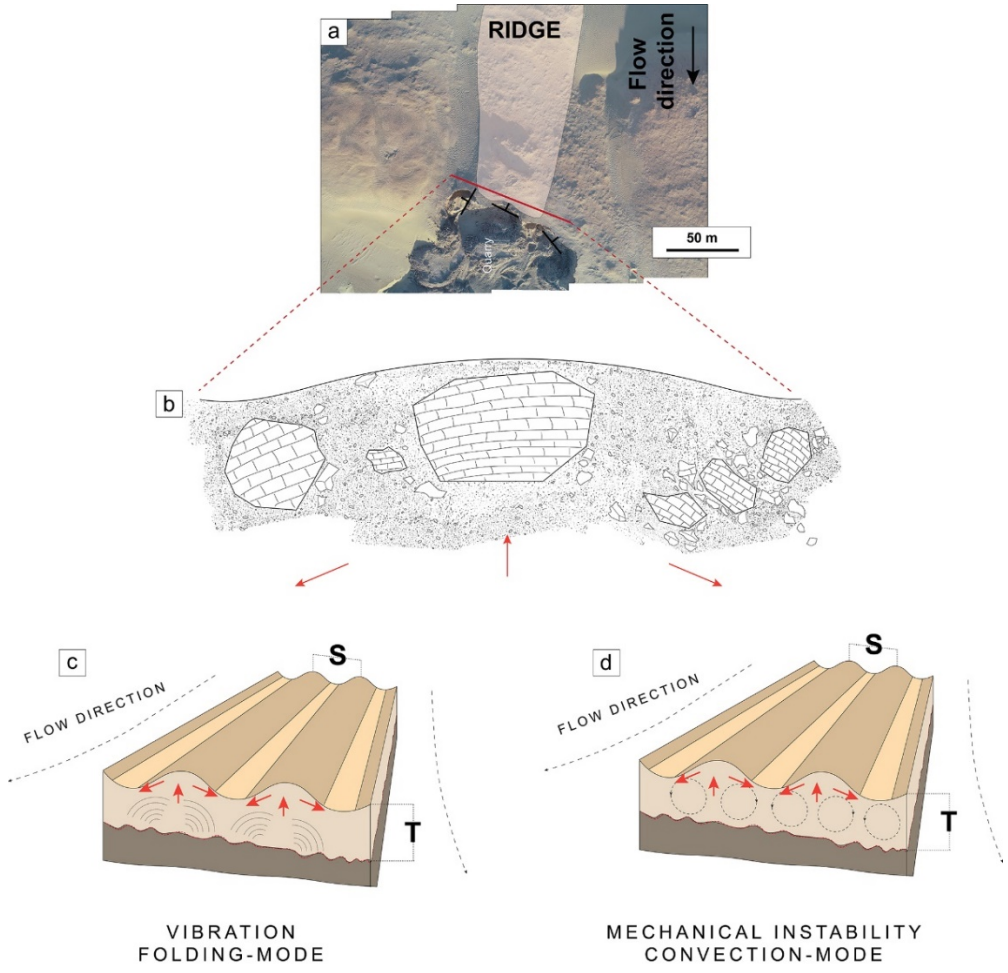

Figure 5-18 – Conceptualized models of longitudinal pattern-forming mechanisms at El Magnifico landslide. a) Top-view photomosaic of the ridge cut by the quarry where internal structures of the landslide deposit were observed; red line corresponds to the profile at which the internal structures observed are schematically represented in b). b) Schematic representation of the megablocks that show the preservation of original bedding planes as seen at the quarry relative to the presence of the ridge; the red arrows represent the direction of the internal deformation. c) Model of longitudinal ridge formation from internal folding of the sliding mass due to the existence of pattern-forming vibrations. d) Model of longitudinal ridge formation from convection-cells within the sliding mass due to the rise of a mechanical instability. In c) and d) red arrows show the expected displacement of entrained megablocks in these models.

The observed organization of the internal structures (i.e., original bedding planes preserved in the megablocks) apparently influenced by the presence of a surficial ridge is not necessarily evidence for a convective-style motion. Dipping of the megablocks away from the centre of the ridge, could also be generated by a folding-like modality that may derive from vibration propagation within the sliding mass (Figure 5-18). To confirm or refute these tentative interpretations, further work needs to be done, as these sections are the only outcrops available of the entire landslide and represent just a single highly local snapshot during its emplacement.

5.4.3 Implications for emplacement mechanism.

The ambiguity of the interpretation of the internal structures raises the question of whether the mechanical instability responsible for the formation of longitudinal ridges observed at laboratory scale in rapid granular flows actually occurs at the field scale in long runout landslides.

The antiform-like arrangement of the megablocks may plausibly represent a single frame of either a convective mechanism or a folding mechanism. However, the fact that chaotic mixing of the debris is not observed (i.e., at Outcrop 1, the upper conglomerate-derived layer and the lower grey breccia are separated by a neat contact) suggests that a convective mechanism did not take place during the emplacement of the El Magnifico landslide. If a different style of motion had indeed operated in the El Magnifico landslide, the recurrence of the same scaling relationship, between the wavelength of the ridges and the thickness of the deposit as generated by a convection-style motion, may lie behind the existence of some degree of universality in pattern-formation.

As it is understood from laboratory experience [Aranson and Tsimring, 2009], pattern-formation mechanisms within a granular medium can arise from injection of energy through vibrations, either through the interaction between the roughness of a surface and the grains of a high-speed flow or through vibrations transmitted to a granular layer resting on a plate. At field scale we have injection of energy in the landslide during emplacement through the

interaction between the moving mass and the roughness of the surface over which it slides and also through ground vibrations generated by the event itself.

I conceive particle vibrations as the fundamental way through which energy is supplied to the landslide-system. I conceptualize the occurrence of a folding-type mechanism and a convection-type mechanism as a continuum that is dependent on both the lithologies involved and the velocity (i.e., energy) at play: a mechanical instability would emerge generating a convection-style of motion when conditions of certain lithologies, velocity and stresses brecciate the sliding mass to the point that it behaves in the manner of a granular flow. In other cases, such as the El Magnifico landslide, the mechanical instability does not emerge but instead pattern-forming vibration propagates within the sliding mass.

5.5 Conclusions.

For the first time in a terrestrial long runout landslide, I report the occurrence of a scaling relationship between the wavelength of longitudinal ridges and the thickness of the deposit, in agreement with previous results in ice-free laboratory experiments on rapid granular flows and in a martian long runout landslide. The finding of this scaling relationship in the El Magnifico landslide, in the Atacama region where ice was not present at the time of the landslide emplacement, further supports the idea that ice is not a necessary condition for the development of longitudinal ridges. Indeed, the recurrence of the same scaling relationship between the wavelength of the ridges and the thickness of the slide strongly suggests the existence of a scale-independent mechanism that takes place during the emplacement of these high-speed events.

I have used the terrestrial case of the El Magnifico landslide in order to ground truth the convection-style mechanism proposed for the martian Coprates Labes landslide. The observations of the internal structures of the El Magnifico landslide cannot rule out a convection-style mechanism but are also not conclusive in its support. I speculate on an alternative vibration-

assisted mechanism that would be able to produce the same scaling relationship between the wavelength of the ridges and the thickness of the deposit (this scaling relationship is therefore independent of the type of mechanism), to generate the superficial pattern of longitudinal ridges (as a result of vibrations) and to generate the internal structures observed (i.e., interaction with no chaotic mixing between different lithologies and the presence of megablocks exhibiting preserved bedding planes). The internal structures are associated with fluctuation of stress, which are qualitatively similar to results from numerical modelling of rapid granular slides as reported in Campbell *et al.* [1995] and [Johnson *et al.*, 2016a], which were suggested, to some degree, to be associated with acoustic fluidization.

This proposed alternative mechanism remains speculative and calls for more observations of the internal structures of longitudinal ridges, as well as 3D numerical simulations and experiments on unconfined rapid granular landslides to provide a further level of comparison for field-based observations and insights on the importance of the three-dimensional effects of the mechanisms proposed for the formation of longitudinal ridges in long runout landslides.

6 Case study III – The Moon: the Tsiolkovskiy crater landslide, far side, and the Light Mantle landslide, near side.

Part of this chapter has been submitted for peer-review as: "*Magnarini, G., Mitchell, T.M., Grindrod, P., Schmitt, H. H., and Petro, N. E. – Scaling relationship between the wavelength of longitudinal ridges and the thickness of long runout landslides on the Moon.*"

6.1 Introduction.

On the Moon, mass wasting processes are mainly reported on the inner steep slopes of impact craters [Kokelaar *et al.*, 2017]. These events involve dry granular material, from regolith to boulder sized, and occur in vacuum in the absence of liquid water. These features can reach runout lengths of about 3 km. It is only recently that these landslides have been studied in morphological detail, as high-resolution images acquired by the Chandrayaan-1 Terrain Mapping Camera (TMC, 5 m spatial resolution; [Kumar and Chowdhury, 2005]) and the Lunar Reconnaissance Orbiter Narrow Angle Camera (LROC NAC, 0.5 m spatial resolution; Robinson *et al.* [2010]) has become available [Kokelaar *et al.*, 2017; Schmitt *et al.*, 2017; Boyce *et al.*, 2020].

However, since the early orbital observations of the Moon from the Lunar Orbiter mission and during the Apollo programme, two unusually long lunar

landslides have been also observed: the Light Mantle avalanche in the Taurus-Littrow Valley, on the near side [El-Baz, 1972] and the Tsiolkovskiy crater landslide, on the far side [Guest and Murray, 1969; El-Baz, 1972] (Figure 6-1). Initially, both were thought to be ejecta deposits [Howard, 1973; Lucchitta, 1977; Morse *et al.*, 2018], but it is currently commonly accepted that these two landforms are landslides [Schmitt *et al.*, 2017; Boyce *et al.*, 2020]. The Light Mantle avalanche and the Tsiolkovskiy crater landslides are the only two long runout landslides known on the Moon. Long runout landslides are landslides that are distinguished for their hypermobility (conventionally expressed by the H/L ratio << 0.6, where H is the height drop and L describes the horizontal travel length of the slide deposits, both parameters measured from the highest point of the source area to the furthest point of the deposit), but the physics behind such behaviour is still poorly understood. The existence of these features on the Moon is intriguing, as the origin of the reduction of friction required to explain the hypermobility remains unknown on a dry, airless body. For the Light Mantle avalanche, Schmitt *et al.* [2017] suggest that the release of solar wind volatiles may have fluidized the landslide in a way comparable to long runout pyroclastic flows.

Although the Tsiolkovskiy and the Light Mantle landslides have different morphological features, which could be due to differences in their formation processes, including different preparatory and triggering factors, and modality of transport, both landslide deposits are marked by a longitudinal linear pattern that results from the existence of longitudinal ridges and troughs. On the surface of the Light Mantle Avalanche, such morphological structures are subtle and extend from the base of the slope to about half the length of the deposit [e.g., El-Baz, 1972; Wolfe *et al.*, 1981; Schmitt *et al.*, 2017]. On the other hand, the surface of the Tsiolkovskiy crater landslide shows prominent longitudinal ridges and furrows that stretch for almost the entire extent of the deposit [e.g., Guest and Murray, 1969; El-Baz, 1972; Boyce *et al.*, 2020]. These distinctive longitudinal structures are common in large-scale mass movements across the Solar System [Howard, 1973; Lucchitta, 1979; Schmidt *et al.*, 2017; Boyce *et al.*, 2020].

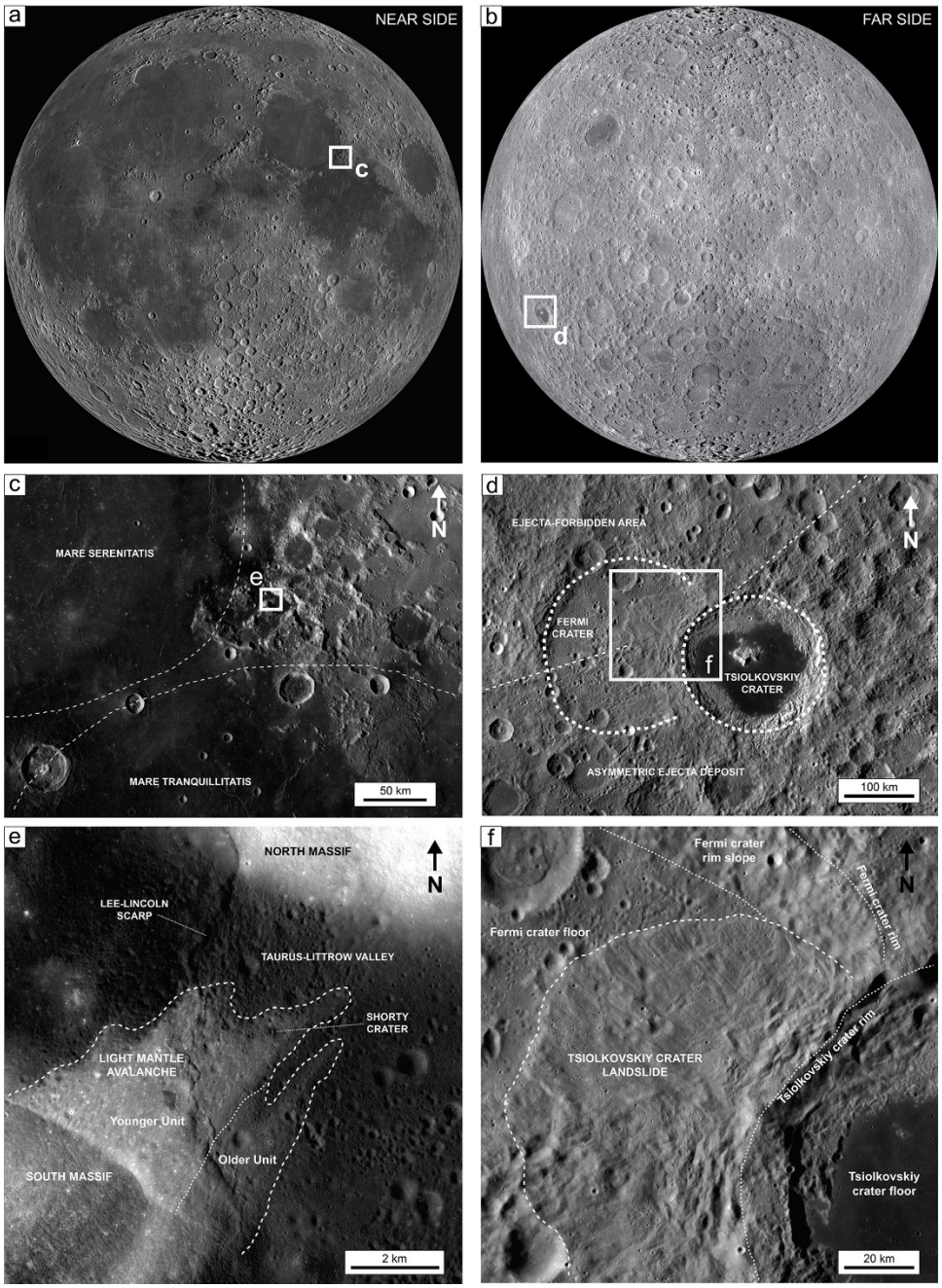

Figure 6-1 – Regional context for the Tsiolkovskiy crater landslide and the Light Mantle landslide areas of study. Location of the Light Mantle Avalanche is indicated in (c) and (e) in Taurus-Littrow Valley, on the near side of the Moon (a), and the location of the Tsiolkovskiy crater landslide is shown in (d) and (f), on the far side of the Moon (b). (c) Location of Taurus-Littrow Valley, landing site of the Apollo 17 mission in 1972; the region is located between Mare Serenitatis, to the west, and Mare Tranquillitatis, to the south; the mountains that surround the valley are part of an uplifted crater rim; the effect of dilation stress that followed Serenitatis or Imbrium-Crisium impact events is thought to be responsible for the opening of the valley. (e) The Light Mantle avalanche in Taurus-Littrow Valley, which originated from the South Massif; current interpretation identifies a younger and older deposit forming the Light Mantle avalanche; the SW-dipping Lee-Lincoln thrust fault cuts across the landslide deposit. (d) Location of the Tsiolkovskiy crater landslide; the landslide developed from the outward collapse of the NW part of the Tsiokovskiy crater rim; the SW part of the deposit overlaps the Tsiolkovskiy ejecta deposit and the West and North part of the deposit are emplaced on the Fermi crater floor. (f) Details of the Tsiolkovskiy crater landslide; longitudinal ridges mark the north part of the deposit, they become less prominent in the west part of the deposit, and they are absent in the SW part of the deposit; the north part of the deposit is bounded by the Fermi crater rim.

However, their origin and their relationship with the emplacement of long runout landslides have been a matter of considerable discussion, in particular whether they are environmental conditions, such as the presence of slippery basal ice or clay minerals [Dufresne and Davies, 2009; De Blasio, 2011], or linked to mechanical instabilities within the rapid moving flow [Borzsonyi *et al.*, 2009; Magnarini *et al.*, 2019].

Ice-free laboratory experiments on rapid granular flows [Forterre and Pouliquen, 2001; Borzsonyi *et al.*, 2009] and studies of the martian Coprates Labes landslide (Chapter 4) and the terrestrial El Magnifico landslide (Chapter 5) have showed that the wavelength of the ridges is consistently 2 to 3 times the thickness of the landslide deposit. In light of the debate about the formation mechanism of longitudinal ridges and the possible influence of an icy basal surface, the presence of longitudinal ridges in lunar landslides offers an ideal site to further investigate the recurrence of the scaling relationship between the wavelength of the ridges and the thickness of the landslide deposit on a planetary body that is considered to be broadly ice-free throughout its geological time. Here I use high resolution imagery and topographic datasets to conduct morphometric analysis of the Tsiolkovskiy crater landslide and the Light Mantle landslide.

6.2 Study Regions.

6.2.1 The Tsiolkovskiy crater landslide.

The Tsiolkovskiy crater is an easily recognizable structure on the far side of the Moon (Figure 6-1b, d, f), for it is filled with dark basaltic material in contrast with extensive distribution of anorthositic megaregolith and paucity of mare deposits that are typical of the far side [e.g., Pieters and Tompkins, 1999]. A range of ages have been assigned to the Tsiolkovskiy impact, yet all studies agree that the event occurred in the Imbrium Era (3.2-3.8 Gya) [e.g., Tyrie, 1988; Pasckert *et al.*, 2015; Boyce *et al.*, 2020]. The Tsiolkovskiy impact partially overlapped the older Fermi crater (Figure 6-2a).

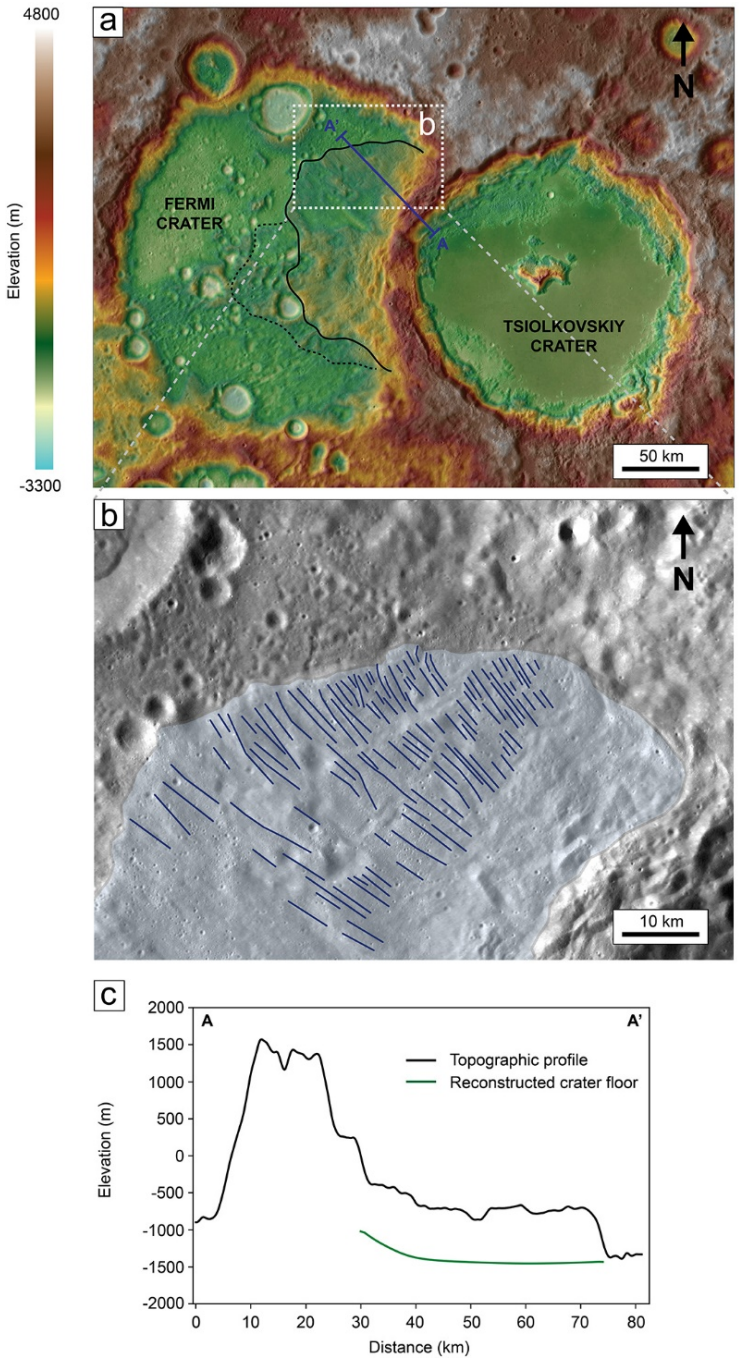

Figure 6-2 - The Tsiolkovskiy crater landslide. a) LROC WAC-derived elevation map overlapping WAC images; black line marks the edge of the landslide deposit; dashed black line marks a possible older landslide deposit and the blue line marks the location of the topographic profile shown in c). b) close-up view of the north part of the landslide deposit (coloured in light blue), where longitudinal ridges (dark blue lines) that characterise the deposit are more prominent. c) Longitudinal topographic profile of the crater rim and of the landslide deposit (black line); the green line represents the reconstructed surface of the Fermi crater over which the Tsiolkovskiy landslide was emplaced.

Being an oblique impact, it produced an asymmetric ejecta deposit, leaving an ejecta-forbidden area on the west-northwest side, which partially coincides

with the Fermi crater floor [Guest and Murray, 1969]. Within this area, Guest and Murray [1969] identified a unit that is morphologically different from the ejecta blanket and likely reflects difference in the mechanism of emplacement. The hypothesis is that this ejecta flow unit developed at the foot of the crater rim slump as a density current simultaneously with formation of the rim. Morse *et al.* [2018] do not consider this unit separately, mapping it as part of the ejecta blanket deposits. Conversely, Wu *et al.* [1972], Masursky *et al.* [1978] and Boyce *et al.* [2020] interpret the unit as a giant landslide. Access to high resolution images acquired by Lunar Reconnaissance Orbiter's LROC allowed Boyce *et al.* [2020] to identify at least 3 morphologically different units that make up the landslide deposit, which formed as a single event 3.55 ± 0.1 Ga [Boyce *et al.*, 2020], following the collapse of the northwest rim of Tsiolkovskiy crater.

The Tsiolkovskiy crater landslide has morphological and morphometric aspects that are strikingly similar to giant martian long runout landslides. The Tsiolkovskiy landslide extends for about 50 km (L) on the broadly flat floor of the Fermi crater and has a vertical drop of about 3 km (H) (Figure 6-2c). These values give an H/L ratio of ~ 0.06, a value that shows the high mobility of the landslide. Its thickness is estimated to be several hundred metres in the proximal areas close to the crater rim that progressively reduces to about 100 m in the distal areas [e.g., Guest and Murray, 1969; Wu *et al.*, 1972; Boyce *et al.*, 2020]. Although the development of a giant landslide outwards from a crater appears to be a unique case on the Moon, similar development has been observed for some cases on Ceres [Schmidt *et al.*, 2017] and they appear to be common on Mars.

The landslide deposit is marked by longitudinal ridges that stretch for almost the entire length of the deposit in the direction of the flow (Figure 6-2b), in a comparable fashion to those observed in martian long runout landslides (e.g., Lucchitta [1979] and Chapter 4). The longitudinal ridges are most prominent in the north part of the landslide deposit, whereas in the other parts of the landslide deposit ridges are less obvious or apparently absent. The longitudinal ridges of the Tsiolkovskiy crater landslide appear not to diverge significantly from each other and they do not bend outward in a fan-shape, as

do the longitudinal ridges of the martian Coprates Labes landslide (Chapter 4). This may be due to the fact that the Tsiolkovskiy crater landslide is laterally confined to the east by the internal rim slope of the Fermi crater (Figure 6-1f).

The fact that this section of the landslide deposit exhibits longitudinal ridges suggests that the lateral spreading of the deposit is not the primary mechanism for the formation of these morphologies, as proposed by De Blasio [2011]. In addition, Boyce *et al.* [2020] remark that the presence of longitudinal ridges on the Moon, a planetary body that has been ice-free throughout its geological history, clearly suggests that the presence of ice is not required to develop these morphologies.

6.2.2 The Light Mantle landslide.

The Light Mantle avalanche in Taurus-Littrow Valley (Figure 6-1a, c, e) was one of the primary geological targets of the Apollo 17 mission. The Taurus-Littrow Valley is interpreted as originating from the effects of dilation stress following either the Serenitatis impact event [Head, 1979], or Imbrium or Crisium basin-forming events ([Spudis *et al.*, 2011; Fassett *et al.*, 2012]). The mountains that bound the valley form part of the uplifted basin rim.

The Light Mantle avalanche developed from the NE-facing slope of the South Massif (Figure 6-3a), and although a clearly identifiable source area is lacking, the avalanche consists of material similar to the anorthositic impact-breccia-derived regolith on the slope of the South Massif [Schmitt, 1973; Wolfe *et al.*, 1981]. The avalanche covers an area of 20 km^2 [Howard, 1973; Schmitt *et al.*, 2017]. Howard [1973] estimated an average thickness of 10 m, which gives a volume of 0.2 km^3. More recent considerations on impact craters and mobilized material provide a minimum volume estimation of 0.06 km^3 [Schmitt *et al.*, 2017]. The avalanche travelled a total horizontal distance (L) of about 10 km, of which 5 km is along the sub-horizontal valley floor, and has a vertical drop (H) of about 2.2 km (Figure 6-3b). Given the high mobility that has characterized the emplacement of the Light Mantle avalanche deposit (H/L ratio is 0.22), and following Apollo 17 field work activity in the Taurus-Littrow Valley and subsequent sample analysis, gas fluidization due

to release of solar wind volatiles by agitation has been speculated to be the principal mechanism generating the long runout, although acoustic fluidization could be an alternative mechanism [Schmitt *et al.*, 2017].

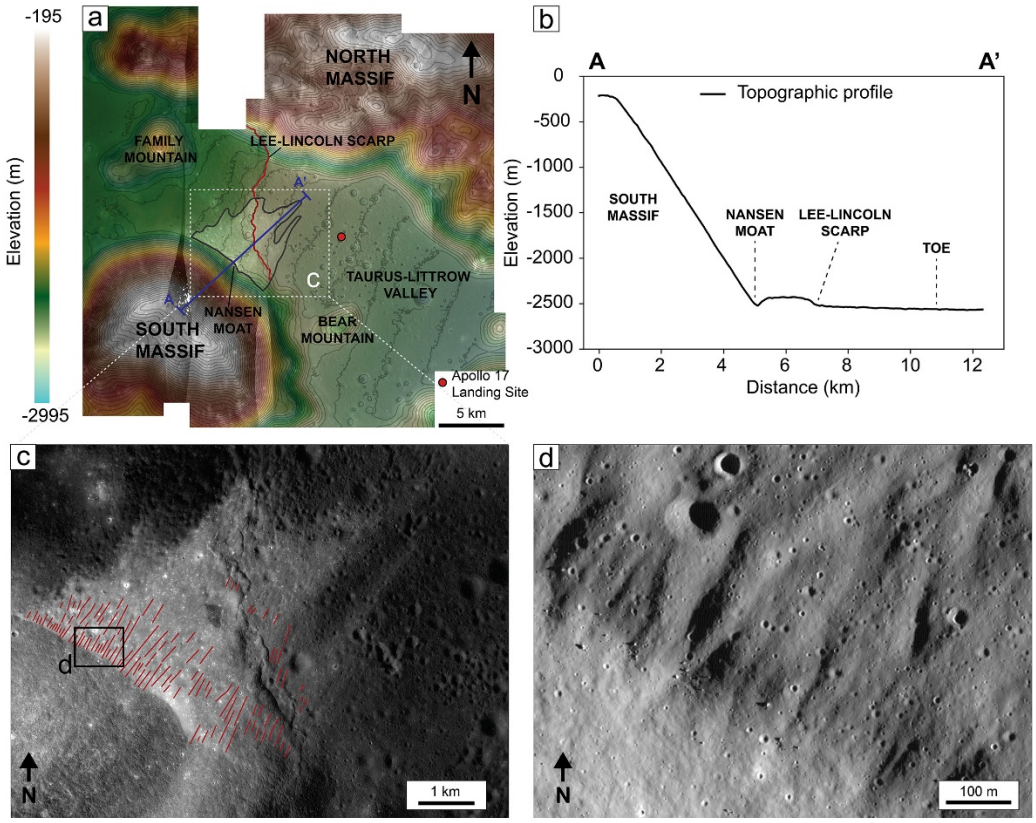

Figure 6-3 - The Light Mantle landslide. a) LROC NAC-derived elevation map of Taurus-Littrow Valley, where the Apollo 17 landed in 1972 (red dot); the DEM overlaps NAC-derived orthoimages; 50 m contour lines; the black line marks the Light Mantle Avalanche deposit; the red line traces the Lee-Lincoln scarp, which is thought to represent the superficial expression of a SW-dipping, shallow thrust fault that runs through the North Massif and the Taurus-Littrow Valley, including the Light Mantle Avalanche; the continuation of the scarp to the south becomes less obvious and its superficial evidence is not clear; the blue line marks the position of the profile in b). b) Longitudinal topographic profile of the South Massif and of the landslide deposit. c) close-up view of the Light Mantle Avalanche and of the base of the South Massif; longitudinal ridges that characterise the landslide deposit are mapped in red. d) Details of the LROC NAC image M1276388423 (Courtesy of Noah Petro): longitudinal ridges are clearly visible.

Originally thought to represent a single event, the Light Mantle avalanche is probably formed of two distinct units [Schmitt *et al.*, 2017; Iqbal *et al.*, 2019]. Schmitt *et al.* [2017] showed that the two units have different ages: 70-110 Myr for the youngest deposit, and possibly twice this age for the oldest deposit. As the origin of the Light Mantle avalanche was attributed to the

secondary impacts related to the Tycho impact event [Howard, 1973; Lucchitta, 1977], the presence of two units has important implications in regard to determining the triggering factors, ruling out the Tycho event as the trigger mechanism of either unit of the Light Mantle Avalanche [Schmitt *et al.*, 2017; Van Der Bogert *et al.*, 2019].

The Light Mantle avalanche is cut by the Lee-Lincoln thrust fault (Figure 6-3a), which extends across the Taurus-Littrow Valley, from the North Massif to the South Massif with an approximate N-S trend [Schmitt, 1973; Scott, 1973; Watters *et al.*, 2010]. Morphologically, the Lee-Lincoln thrust fault is expressed as a lobate scarp and it formed as a result of continued thermal contraction of a cooling Moon [Watters *et al.*, 2010]. As other lunar lobate scarps, the Lee-Lincoln thrust fault appears to be a young tectonic structure [e.g., Binder and Gunga, 1985; Watters *et al.*, 2010], with a suggested bracket age of about 70-110 Ma for its occurrence or reactivation [Schmitt *et al.*, 2017; Van Der Bogert *et al.*, 2019]. This suggested age derives from crater-size frequency distribution measurements [Van Der Bogert *et al.*, 2012; Van Der Bogert *et al.*, 2019], minimum exposure ages of boulders at the base of the South Massif, and considerations on its spatial association with the Nansen Moat and its burial by the Light Mantle avalanche [Schmitt *et al.*, 2017]. In regard to the avalanche triggering mechanism, the apparent contemporaneity of the youngest Light Mantle avalanche unit and the activity of the Lee-Lincoln thrust fault points (based on crater-size frequency distribution dating method [Van Der Bogert *et al.*, 2012; Van Der Bogert *et al.*, 2019]) to the faulting activity as a plausible alternative explanation to the secondary impacts derived from the Tycho impact event: either through displacement of the valley floor from the South Massif, causing slope destabilization following the removal of support at the base of the slope [Schmitt *et al.*, 2017]; or through seismic shaking.

Apart from being characterized by high albedo material that makes its identification unequivocal on the darker valley floor from image data (Figure 6-3c), the two units of the Light Mantle avalanche do not have raised edges that clearly define their morphological existence. As a matter of fact, Apollo 17 astronauts Harrison Schmitt and Gene Cernan, while driving towards

Station 2, were not able to tell where the contact between the valley floor and the avalanche material was, as the change in albedo appeared subtle from the ground (EVA-2, 142:04:27; 142:05:31 [Apollo Lunar Surface Journal] – It should be read as: Extra Vehicular Activity-Day number since the beginning of activities on the lunar surface, time elapsed since launch in hours:minutes:seconds). However, the astronauts recognised that they were on the deposit as the material into which craters had penetrated was different and their rims and walls brighter (EVA-2, 142:04:10; 142:05:31; 142:05:42; 142:09:14 [Apollo Lunar Surface Journal]). Dispersion of the original contact between the avalanche material and the darker floor material over at least 70 Myr of regolith formation has resulted in this obscuration.

The youngest avalanche deposit exhibits longitudinal ridges that extend from the base of the South Massif for about half the length of the deposit [Howard, 1973] (Figure 6-3c-d). A few longitudinal ridges are also visible on the older unit of the avalanche deposit (Figure 6-3c). As noted by Schmitt *et al.* [2017], the presence of such structures may represent a record of the flow dynamics of the avalanche.

6.3 Data and Methods.

6.3.1 Satellite image data and stereo-derived topography data.

To study the Tsiolkovskiy crater landslide, I used the LROC WAC global digital elevation model (100 m/px resolution) available at the NASA Planetary Data System. I used two LROC NAC stereo-derived digital elevation models (DEMs) (4 m/px resolution) and orthoimages (1 m/px resolution), generated using the USGS Integrated Software for Imagers and Spectrometers (ISIS) and the BAE Systems commercial photogrammetry suite SOCET SET, and standard methods and procedures [e.g., Henriksen *et al.*, 2017]. The data were vertically controlled using LOLA elevation data. The estimated horizontal precision of these DEMs is to be the same as the spatial resolution (i.e. 4 m), and the vertical precision (assuming 1/5 pixel misregistration) to be ~0.5 m [Henriksen *et al.*, 2017]. These products (Table 3-1; Table 6-1) were

used to conduct detailed morphological mapping and detailed morphometric analysis of part of the Tsiolkovskiy crater landslide deposit.

To obtain the regional topography of the Taurus-Littrow Valley, I used LROC NAC-derived digital elevation models (5 m/px resolution; vertical precision ~0.5 m) and orthoimages (1.2 m/px resolution) available at the NASA Planetary Data System [Henriksen *et al.*, 2017]. To conduct morphological mapping and morphometric analysis of the Light Mantle Avalanche deposit I used digital elevation model (1.5 m/px resolution) and orthoimage (50 cm/px resolution) products provided by Haase *et al.* [2019], and LROC NAC low sun-angle image M1276388423R (Table 6-1).

Table 6-1 - List of imagery datasets used to conduct norphometric analysis of the Tsiolkosvkiy crater landslide and the Light Mantle landslide.

Target	Camera	Product Type	Resolution (m/px)	Image Pair	Source
Tsiolkovskiy crater landslide	LROC WAC	DEM	100		NASA PDS
	LROC NAC	DEM	4	M1174585981LE/RE M1174578873LE/RE	This work
		ORTHO	1		
	LROC NAC	DEM	4	M1214606049LE/RE M1214613084LE/RE	This work
		ORTHO	1		
Light Mantle avalanche	LROC NAC	DEM	1.5		[Haase *et al.*, 2019]
		ORTHO	0.5		
	LROC NAC	DEM	5		NASA PDS
		ORTHO	1.2		

6.3.2 Morphological characterization and thickness estimation.

In ArcGIS, I mapped longitudinal ridges on the Tsiolkovskiy and Light Mantle landslide deposits (Figure 6-2b and Figure 6-3b).

At the Tsiolkovskiy crater landslide, longitudinal ridges were mapped using WAC images and the two NAC-derived orthoimages that I made. Three

transverse profiles (P1, P2, and P3 in Figure 6-7) were traced in the areas covered by the NAC-derived orthoimages, where the ridge morphologies are most prominent and, along them, the distance between adjacent ridge crests were measured. Other three transverse profiles (P4, P5, and P6 in Figure 6-8) were traced over the WAC-derived DEM so to cover almost the entire extent of the deposit that exhibits most prominently the longitudinal ridges. In this way, the morphometric analysis is not limited to a small fraction of the deposit covered by high-resolution topographic data, as using few data points may not be ideal to make extrapolation to the entire deposit. As the NAC-derived and the WAC-derived DEMs have different resolution (4 m/px and 100 m/px resolution, respectively; see Table 6-1), I first checked that the thickness estimated with the WAC-DEM is comparable with the thickness derived from the NAC-DEM, as I assumed the latter more accurate. To do so, I estimated the thickness along the profile P1, P2, and P3 using the WAC-DEM and compared with the thickness obtained with the NAC-DEM. The difference between the NAC-derived and the WAC-derived thickness is negligible (Figure 6-4), thus allowing to conduct the morphometric analysis using both the NAC-derive DEM and the WAC-derived DEM.

In order to estimate the thickness of the Tsiolkovskiy crater landslide, I built the topography of the crater floor underneath the deposit by interpolating topographic contours of the area around the landslides obtained from the WAC DEM (Figure 6-5) and applied the methods, including Python scripts and error estimation, used by Magnarini *et al.* [2019].

The estimated thickness is derived using the reconstructed crater floor underneath the deposit and the NAC-derived DEM I made (for the profiles P1, P2, and P3), and the WAC-derived DEM (for the profiles P4, P5, and P6). These newly created surface only approximate the real original topography of the crater floor and, therefore, the final estimation of the thickness carries uncertainties.

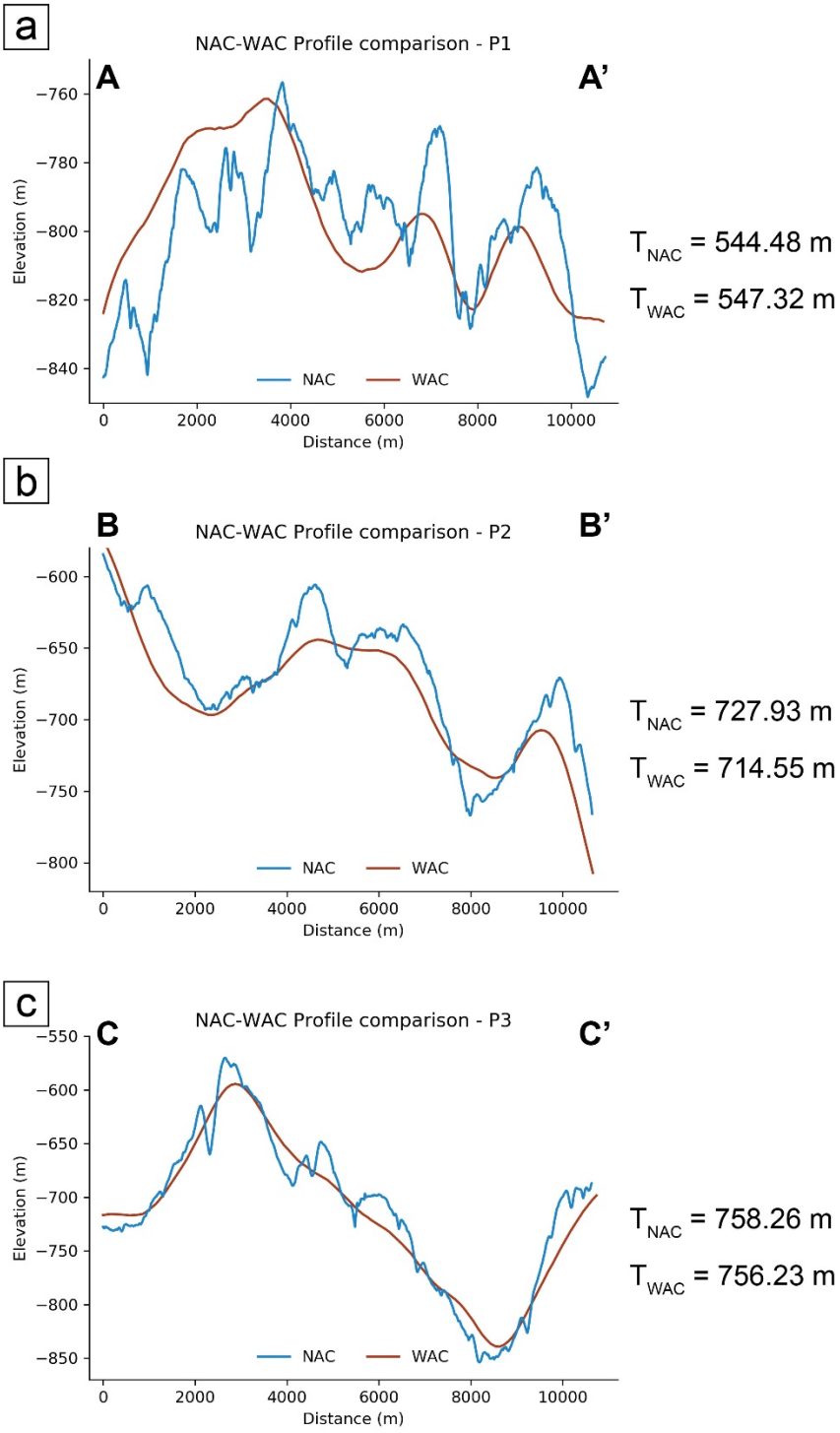

Figure 6-4 – Comparison between the landslide thickness derived with the NAC-derived DEM and the WAC-derived DEM.

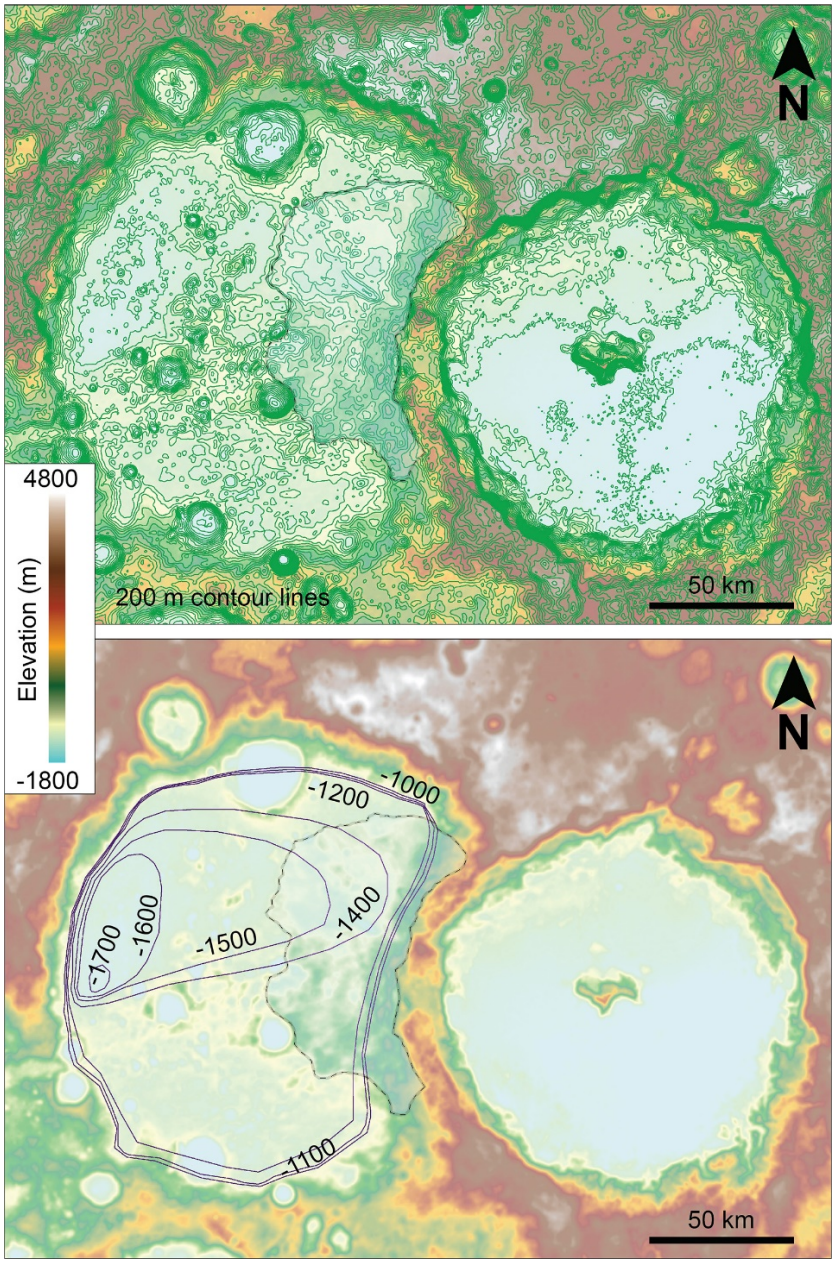

Figure 6-5 – Reconstruction of the Fermi crater floor underneath the Tsiolkovskiy landslide deposit. Top panel shows 200 m contour lines extracted from the WAC DEM. Bottom panel shows the contour lines I have traced to reconstruct the crater floor underneath the landslide deposit (here shown with dashed black line and low-opacity-grey colour. The reconstructed crater floor takes in consideration the presence of the ejecta deposit in the southern zone of the Fermi crater and the 'forbidden' ejecta zone in the northern part.

At the Light Mantle landslide deposit, longitudinal ridges were mapped using the NAC-derived orthophotos generated by the NASA PDS and by Haase *et al.* [2019], and NAC image M1276388423. Two transverse profiles were traced on the deposit (P7 and P8 in Figure 6-9a) and the distance between adjacent ridge crests were measured.

6.3.3 Landslide deposit thickness error estimation.

I traced two profiles on the crater floor (yellow profiles), adjacent to the landslide edge and parallel to the profiles traced for the morphometric analysis (Figure 6-6). This set of transects (yellow lines), and their linear fits (burgundy lines), are compared to a mirror set of transects traced within the landslide deposit (blue lines) so as to: 1) assess the plausibility of the overall elevations of our reconstructed basal surface, and 2) to provide an error estimation of the average thickness that we provide in the manuscript.

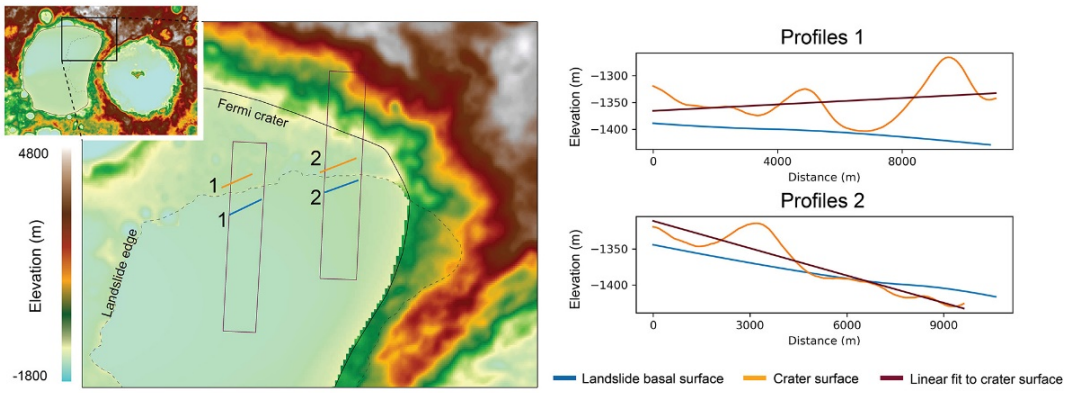

Figure 6-6 – Validation of the reconstructed surface underneath the Tsiolkovskiy landslide deposit. Left panels show the LROC WAC DEM of the of the Fermi crater and Tsiolkovskiy crater region and the reconstructed DEM of the Fermi crater floor underneath the landslide deposit as inferred by interpolation of the LROC DEM contour lines adjacent the deposit; we keep same scale for both DEMs (max 4800 m; min -1800 m) so that colour coded visualization provides a first order of qualitative comparison between the real topography adjacent the landslide deposit and the reconstructed topography underneath the landslide deposit. The plots on the right show the comparison of mirror transects (blue and yellow lines 1-2).

1) I expect the natural topography of the inner region of an impact crater to gently decrease in elevation moving away from the crater walls, towards the central areas of a crater. Therefore, I consider the elevation of the reconstructed topography underneath the landslide deposit plausible.

2) I expect a random natural roughness of the crater floor at various scales. Therefore, I assign a confidence bracket to the reconstructed topography underneath the landslide deposit (blue lines) that corresponds to the calculated standard deviation of the elevation of the real topography profiles (yellow lines). The standard deviation for the yellow line 1 is assigned as confidence bracket to the profile P3 in the manuscript; the standard deviation

for the yellow line 2 is assigned as confidence bracket to the profiles P1 and P2 in the manuscript.

6.4 Results.

In this section, I present the results from the morphometric analysis of the longitudinal ridges that I have obtained following the approach used in Chapter 4.

6.4.1 Morphometric analysis of the Tsiolkovskiy crater landslide.

I conducted the morphometric analysis along the six transverse profiles that were traced on the two LROC NAC DEMs and orthoimages produced for this study (Figure 6-7a) and on the WAC-derived DEM (Figure 6-8a). At each profile, I measured the distance between the ridges and obtained an average spacing, which was considered representative of the wavelength of the ridges (S in Table 6-2).

Table 6-2 – Results of the morphometric analysis of longitudinal ridges of the Tsiolkovskiy crater landslide. The error of the thickness value is derived as the standard deviation of the elevation variation of the profiles (yellow lines) adjacent to landslide edge and parallel to the profiles traced for the morphometric analysis (Figure 6-6). The spacing error corresponds to one standard deviation of the ridge spacing distribution.

	Profile Length (m)	Number of Ridges	S (m)	T (m)	S/T ratio
Tsiolkovskiy Landslide					
P1	10587	7	1082 ± 316	571 ± 36	1.89 ± 0.30
P2	11585	8	1466 ± 540	717 ± 36	2.04 ± 0.37
P3	10442	9	1334 ± 460	702 ± 36	1.90 ± 0.35
P4	33878	24	1473 ± 740	653 ± 36	2.25 ± 0.50
P5	30851	23	1402 ± 802	578 ± 36	2.42 ± 0.58
P6	34018	25	1417 ± 766	635 ± 36	2.32 ± 0.54

Using the LROC WAC DEM and the interpolation-derived basal surface, I also calculated the average thickness of the deposit corresponding to each profile (T in Table 6-2, Figure 6-7c, d, e, Figure 6-8c, d, e). For each profile, I calculated the ratio between the average spacing between the ridges and the average thickness of the landslide deposit (S/T ratio in Table 6-2).

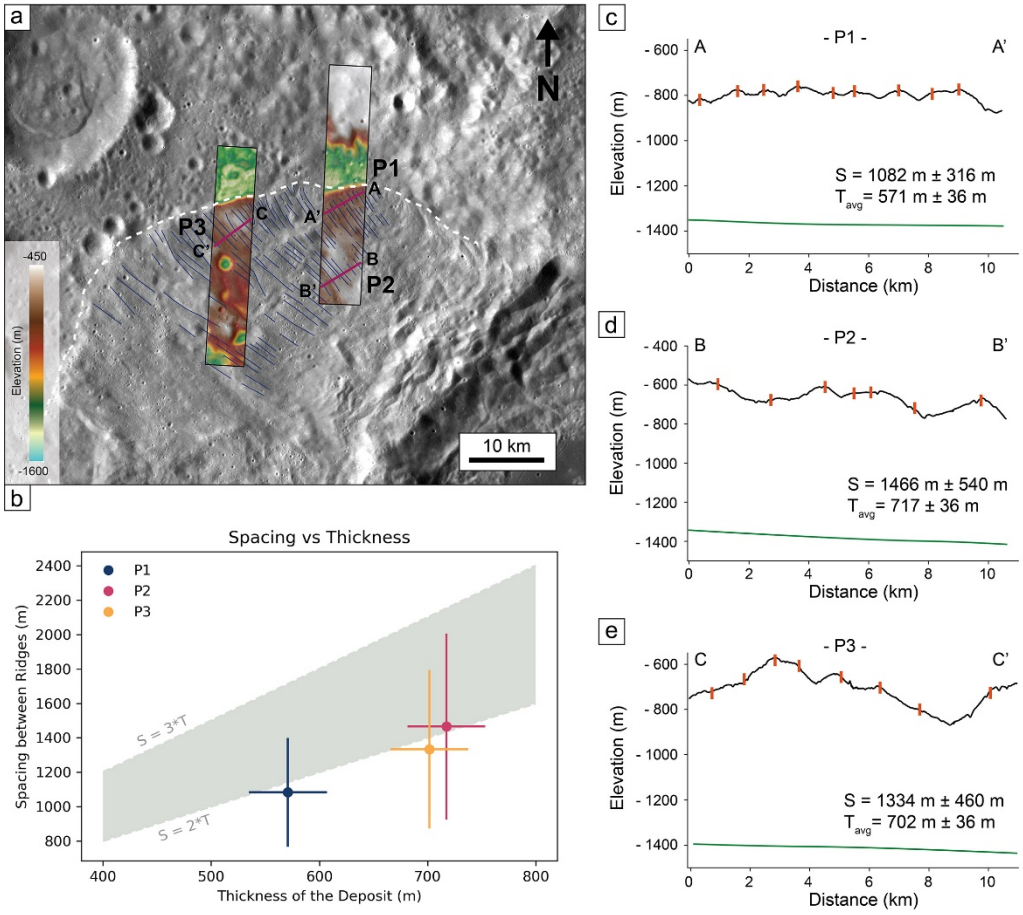

Figure 6-7 – Morphometric analysis of longitudinal ridges at the Tsiolkovskiy crater landslide. a) LROC NAC-derived digital elevation models over LROC WAC base image; longitudinal ridges are mapped with blue lines; fuchsia lines are the transversal profiles (P1-A/A', P2-B/B', P3-C/C') along which the morphometric analysis of the ridges was conducted and the thickness of the landslide deposit was estimated. b) Plot showing the S/T ratio calculated at the three profiles; the grey area represents the scaling relationship between the spacing between longitudinal ridges and the thickness of the landslide deposit found in ice-free laboratory experiments on rapid granular flows; the error bars correspond to the error values provided in Table 6-2. c-d-e) Transversal profiles at P1, P2, P3, respectively; black lines are the landslide deposit topographic profiles, orange ticks show the location of longitudinal ridges as mapped in (a), green lines show the landslide basal surface and correspond to the reconstructed Fermi crater floor surface.

Figure 6-7b shows the S/T ratio values found at the three profiles traced in the area covered by the NAC-derived DEM. Profile 3 show an S/T ratio of 2.04 that falls within the range of the scaling relationship between the two parameters found in laboratory experiments on rapid granular flows, which is represented as the grey area in Figure 6-7b. Profile 1 and Profile 2 have S/T ratio value of 1.9 and 1.89, respectively, slightly below the minimum value of the range of the scaling relationship.

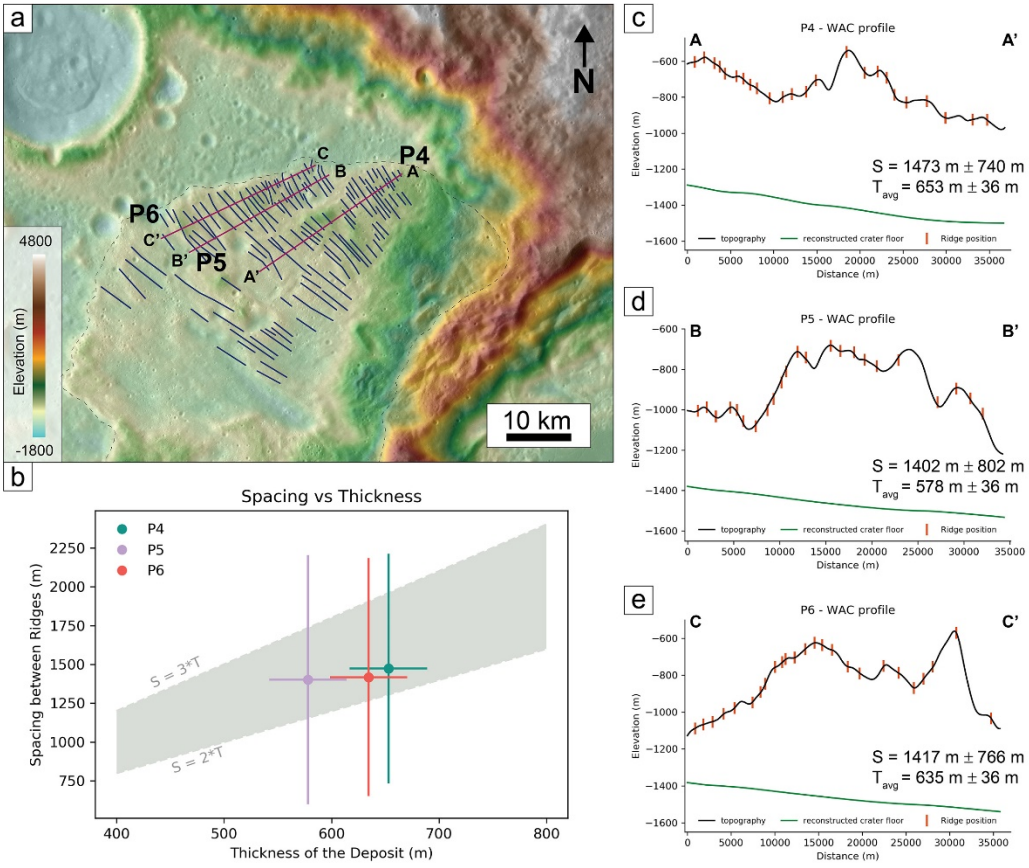

Figure 6-8 – Morphometric analysis of longitudinal ridges at the Tsiolkovskiy crater landslide using WAC-derived DEM. a) LROC WAC-derived digital elevation models over LROC WAC base image; longitudinal ridges are mapped with blue lines; fuchsia lines are the transversal profiles (P4-A/A', P5-B/B', P6-C/C') along which the morphometric analysis of the ridges was conducted and the thickness of the landslide deposit was estimated. b) Plot showing the S/T ratio calculated at the three profiles; the grey area represents the scaling relationship between the spacing between longitudinal ridges and the thickness of the landslide deposit found in ice-free laboratory experiments on rapid granular flows; the error bars correspond to the error values provided in Table 6-2. c-d-e) Transversal profiles at P4, P5, P6, respectively; black lines are the landslide deposit topographic profiles, orange ticks show the location of longitudinal ridges as mapped in (a), green lines show the landslide basal surface and correspond to the reconstructed Fermi crater floor surface.

Figure 6-8b shows the S/T ratio values found at the three profiles traced using the WAC-derived DEM. The S/T ratio values obtained with the WAC-derived DEM fall within the range of the scaling relationship between the two parameters found in laboratory experiments on rapid granular flows, which is represented as the grey area: Profile 4 shows an S/T ratio of 2.25, Profile 5 shows an S/T ratio of 2.42, and Profile 6 shows an S/T ratio of 2.32.

6.4.2 Morphometric analysis of the Light Mantle landslide deposit.

I conducted the morphometric analysis along the two transverse profiles that were traced on the LROC DEM produced by Haase *et al.* [2019] (Figure 6-9a). At each profile, I measured the distance between the ridges and obtained an average spacing, which was considered representative of the wavelength of the ridges (Figure 6-9c-d; S in Table 6-3).

Table 6-3 – Results of the morphometric analysis of longitudinal ridges of the Light Mantle landslide. In grey: minimum and maximum thickness of the Light Mantle avalanche derived by using the scaling relationship between the wavelength of the longitudinal ridges (S) and the thickness of the deposit (T), given that S is known.

	Profile Length (m)	Number of Ridges	S (m)	T (m)		S/T ratio
Light Mantle Avalanche				**T_{min} (m)**	**T_{max} (m)**	
P7	2735	36	73	*24.3*	*36.5*	*2 -> 3*
P8	2180	17	124	*41.3*	*62*	*2 -> 3*

As the Light Mantle Avalanche does not show a deposit that unequivocally stands out on the surface of the Taurus-Littrow Valley and the presence of the Lee-Lincoln fault further complicates the geomorphology of the area, it was not possible to estimate the thickness of the landslide deposit using the interpolation method as done for the Tsiolkovskiy crater landslide. The absence of a thickness estimate of the landslide deposit corresponding to the

transverse profiles means the S/T ratio for the Light Mantle Avalanche cannot be derived. However, assuming that the expected range of the S/T ratio is also valid for the Light Mantle Avalanche, I use the ratio to provide an estimation of the thickness of the landslide deposit, given that we have a value of S (Figure 6-9b; Table 6-3).

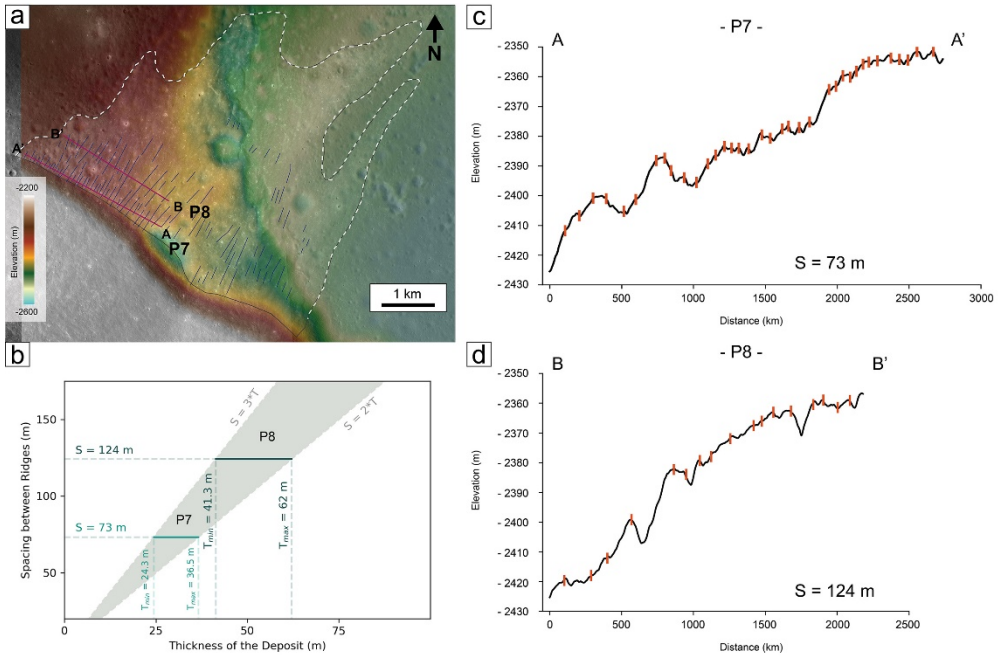

Figure 6-9 – Morphometric analysis of longitudinal ridges at the Light Mantle landslide. a) LROC NAC-derived digital elevation model [Haase *et al.*, 2019] over LROC NAC base image mosaic; longitudinal ridges are mapped with blue lines; fuchsia lines are the transversal profiles (P7-D/D', P8-E/E') along which the morphometric analysis of the ridges was conducted; dotted white line represent the edge of the Light Mantle deposit; continuous black lines with rounded head indicate locations at which an estimation of the thickness of the deposit (T) is provided in the literature. b) Plot showing the scaling relationship between the spacing between longitudinal ridges and the thickness of the landslide deposit found in ice-free laboratory experiments on rapid granular flows (grey area); we used the scaling relationship to infer a minimum and a maximum value of the landslide deposit, given that we have an average spacing between the ridges; aquamarine lines and values refer to P7 and dark green lines and values refer to P8. c-d) Transversal profiles at P7 and P8, respectively; black lines are the landslide deposit topographic profiles, orange ticks show the location of longitudinal ridges as mapped in (a).

6.5 Discussion.

In this section I will first comment on the finding of the scaling relationship between the wavelength of longitudinal ridges and the thickness of the deposit at the Tsiolkovskiy crater landslide and its significance in respect to

the idea that the presence of ice is not a necessary condition for the formation of longitudinal ridges. Secondly, I will suggest that the scaling relationship can be used to estimate the thickness of landslides and I will apply this method to the Light Mantle landslide. Assuming the validity of the existence of such scaling relationship, this can become a useful tool in cases where the thickness of deposit cannot be calculated, for instance due to lack of digital elevation models.

6.5.1 Scaling relationship between the wavelength of longitudinal ridges and the thickness of the landslide deposit.

The results of the morphometric analysis conducted for the Tsiolkovskiy crater landslide show the existence of a scaling relationship between the thickness (T) of the Tsiolkovskiy crater landslide deposit and the wavelength (S) of the longitudinal ridges (S = 2*T). The value of the ratio (~2) is in agreement with values reported in the literature: ice-free laboratory experiments on rapid granular flows demonstrated that the wavelength of the ridges is within 2 to 3 times the value of the thickness of the flow [Forterre and Pouliquen, 2001; Borzsonyi *et al.*, 2009]; at field scale, the same scaling relationship has been found for the Coprates Labes long runout landslide, in Valles Marineris, Mars (Chapter 4) and the El Magnifico long runout landslide, in Chile, Earth (Chapter 5).

The morphological similarity between the longitudinal ridges that characterise the deposit of martian long runout landslides and the longitudinal features of the deposit of terrestrial landslides emplaced on glaciers has been noted for a long time [e.g., Lucchitta, 1978a; 1979]. The existence of these morphologies in martian landslides has been suggested to represent evidence for the presence of ice at the time of landslide emplacement. According to Dufresne and Davies [2009] and De Blasio [2011], the presence of a basal icy surface would explain both the hypermobility of long runout landslide, by providing a low friction sliding surface, and the formation of longitudinal ridges, by tensile deformation of the sliding mass due to spreading over a slippery surface.

However, ice-free laboratory experiments on rapid granular flows by Forterre and Pouliquen [2001] showed that the development of longitudinal structures derives from a mechanical instability within the flow that is generated by the interplay of a rough surface and the high velocity of the flow, demonstrating that ice is not a necessary condition for the development of such longitudinal morphologies. In the light of the morphometric results and observations of the martian Coprates Labes landslide being in agreement with the aforementioned finding in ice-free laboratory experiments on rapid granular flows, in Chapter 4 I concluded that the presence of longitudinal ridges on the deposit of martian long runout landslides should not be used as evidence for the presence of ice on Mars at the time of their emplacement. The presence of longitudinal ridges at the Tsiolkovskiy crater landslide on the Moon should be on its own an argument against the idea that ice is required to develop such structures [Boyce *et al.*, 2020], as it is well established that the Moon has been free from such large-scale ice throughout its geological history. Indeed, the finding of the scaling relationship between the wavelength of the longitudinal ridges and the thickness of the landslide deposit at the Tsiolkovskiy crater landslide provides support to the idea that ice is not a necessary condition for the development of longitudinal ridges in long runout landslides. Moreover, this conclusion is also further reinforced by the finding of the same scaling relationship at the terrestrial El Magnifico landslide, in the north region of the Atacama Desert, Chile, where ice was also not involved (Chapter 5).

6.5.2 Estimated deposit thickness based on expected scaling with the wavelength of longitudinal ridges.

Given the validity of the scaling relationship between the wavelength of longitudinal ridges and the thickness of landslide deposits, the ratio between these two parameters can be applied to infer the thickness of the deposits where its calculation is not otherwise possible using typical methods in planetary geomorphology (e.g., estimation based on the elevation of the deposit rim above the valley floor; interpolation of the valley floor topography

to reconstruct the surface underneath the deposit). This is the case of the Light Mantle landslide in Taurus-Littrow Valley, as its deposit does not have edges that stand out topographically over the valley floor and the presence of the Lee-Lincoln scarp cutting through the deposit complicates the geological relationship between different units.

An estimated average thickness of 10 m was initially given by Howard [1973]. Based on considerations on impact craters and mobilized material, Schmitt *et al.* [2017] provide thickness estimation at different locations of the landslide deposit: at least 3 m in the NW portion (the furthest part, where Shorty crater is located), at least 6-10 m in the SE portion, and less than 16 m at the base of the South Massif.

I have calculated the average wavelength of longitudinal ridges (S) along two different transverse profiles (Figure 6-9, P7 and P8), and I derived a minimum (T_{min}) and a maximum (T_{max}) thickness of the landslide deposit at these two locations by applying the scaling relationship between the two parameters (i.e., T_{min} = S/3 and T_{max} = S/2; Figure 6-9, shaded cells in Table 6-2). The profile P7 is located at the base of the South Massif and so the range of thickness we obtained at P7 (24.41 m - 36.61 m) can be compared with the estimated thickness at the base of the South Massif provided by Schmitt *et al.* [2017] (<16 m). The profile P8 is located less than 1 km further along the direction of the flow and no previous estimation of the thickness at this area has been given; the range of thickness we obtained at P8 (41.37 m – 62.06 m) is almost double the value obtained at the base of the South Massif (Figure 6-10).

The thickness of unconfined landslide deposits is usually expected to decrease with distance. In order to account for the increase of thickness, two possible explanations can be invoked: a) the existence of a topographically depressed area prior to the landslide event that is now entirely filled with landslide debris and/or b) the scouring potential of the high speed landslide impacting on the valley floor, causing removal of valley floor material, then entrained into the landslide debris.

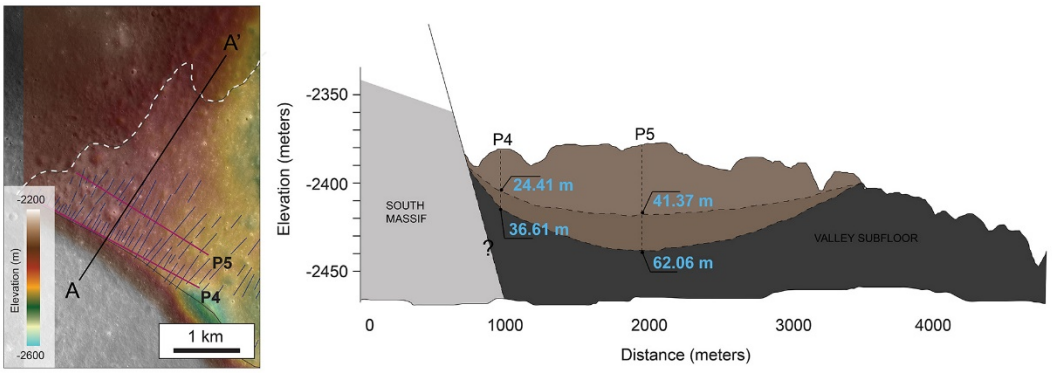

Figure 6-10 – Thickness estimation of the Light Mantle landslide using the expected scaling relationship between the wavelength of longitudinal ridges and the thickness of the deposit. Left panel is a cropped image from Figure 6-9a that shows mapped longitudinal ridges (blue lines), the two profiles along which the distance between the ridges was measured (fuchsia lines); dotted white line shows the edge of the landslide deposit; the black line shows the location of the profile A-A', along which the section shown in the right panel was created. The cross section of the landslide deposit in the right panel shows the estimated range of the thickness of deposit (text in light blue) in correspondence of the two profiles; the minimum and maximum estimated depth of basal surfaces of the deposit are represented by dotted black lines, obtained by interpolating the depth points; light brown shows the deposit which basal surface corresponds to the minimum estimated thickness and darker brown shows the deposit which basal surface corresponds to the maximum estimated thickness.

However, using the morphometry of longitudinal ridges to infer the thickness of the deposit must include considerations about the modification of surface topography due to space weathering, impact cratering, and seismic shaking. These processes contribute, to different degrees, to the re-distribution of surface material and possibly causing the obliteration of the original morphology. The activity of lunar lobate scarps can alter the aspect of crater rim (i.e., morphological freshness), thus causing seismic resetting of crater size-frequency distribution [Van Der Bogert *et al.*, 2012; Van Der Bogert *et al.*, 2018]. The morphological freshness of craters present on the deposit of the Light Mantle landslide could have been modified by the seismic shaking generated by the activity of the Lee-Lincoln scarp, which runs through the Taurus-Littrow Valley and the deposit of the Light Mantle landslide [Van Der Bogert *et al.*, 2019]. Watters *et al.* [2019] suggest that the Lee-Lincoln thrust fault may be still active. Therefore Taurus-Littrow valley may represent an important site where recent and active geological processes on the Moon can be studied. If seismic shaking has affected the aspect of the craters on the Light Mantle landslide, we should expect that it would also modify the morphology of longitudinal ridges. For instance, seismic shaking could cause

re-distribution of material downslope, from the top of ridges to the bottom of troughs. This material re-distribution can cause the attenuation of the morphology and even the total removal of topographic evidence of longitudinal ridges, both situations resulting in the underestimation of the actual number of longitudinal ridges formed during the emplacement of the landslide. Consequently, the underestimation of the number of longitudinal ridges would result in the overestimation of the distance between the ridges (i.e., wavelength of the ridges), thus in the overestimation of the thickness of the deposit. Therefore, caution is necessary in the use of the scaling relationship between the wavelength of longitudinal ridges and the thickness of landslide deposit in order to derive the thickness, especially in the case of relatively small-scale longitudinal ridges (such as longitudinal ridges of the Light Mantle landslide compared to the longitudinal ridges of the Tsiolkovskiy crater landslide), which are more easily and quickly obliterated.

6.6 Conclusions.

I report on the occurrence of a scaling relationship between the wavelength of longitudinal ridges and the thickness of the Tsiolkovskiy crater landslide deposit. I found that the wavelength of the longitudinal ridges is ~2 times the thickness of the deposit at three different locations of the deposit. This value is consistent with previous findings in experimental work on rapid granular flows and field-scale long runout landslides on Mars and on Earth. The significance of the existence of such scaling relationship across scales, planetary bodies, and lithologies is important in the light of the debate around the formation mechanism of longitudinal ridges in long runout landslides. Its recurrence clearly suggests that the presence of longitudinal ridges cannot be used to infer environmental conditions or lithology involved during the emplacement of long runout landslides. I suggest that similar morphometric analysis should be conducted for longitudinal ridges that characterise double layer ejecta of martian impact craters in order to investigate whether a scaling relationship between the wavelength of the ridges and the ejecta thickness

also exists for similar morphologies formed during seemingly different geological process. This may further elucidate the relationship between longitudinal ridge morphology and high-energy/high-speed events.

7 Discussion.

In the Introduction section of this thesis I identified four questions important to the debate about the formation mechanism of long runout landslides on planetary bodies:

a) to what extent is the role of fluids important for the emplacement of these catastrophic events?

b) to what extent does slope lithology and material present on valley floors play a role in facilitating the runout?

c) to what extent the tectonic and structural context predisposes slope failures to evolve into long runout landslides?

d) is there a universal explanation or instead different mechanisms that are able to produce the same end result?

Although complete answers have not been found, I identified three key points as outcome of my doctoral studies that contribute to addressing these questions and to further advancing the discussion on the formation mechanisms of long runout landslides.

The first key point (Section 7.1) is the existence of a scaling relationship between the wavelength of longitudinal ridges and the thickness of long runout landslide deposits that has emerged from the morphometric analysis conducted for three of my long runout landslide case studies, the Coprates Labes landslide (Mars), the El Magnifico landslide (Earth), and the Tsiolkovskiy crater landslide (the Moon). I will discuss its importance in supporting the idea that ice is not a necessary condition for the development of longitudinal ridges in long runout landslides. Therefore, the first key point partially contribute to addressing the question about the role of valley floor

material during the emplacement of long runout landslides and to further stimulate discussion about the existence of either a universal or different mechanisms.

The second key point (Section 7.2) derives from the first key point, that of the existence of the scaling relationship between the wavelength of the ridges and the thickness of the deposit. I will argue that the lateral spreading of the landslide deposit is not the fundamental mechanism for the development of longitudinal ridges. I will discuss the effect of lateral confinement on the thickness of long runout landslide deposits and on the behaviour of longitudinal ridges, which are linked by the scaling relationship discussed. Elements of this discussion have been inspired by a conversation with Professor Jay Melosh, who asked me whether longitudinal ridges in laterally confined long runout landslide would be expected to be diverging as they are in unconfined long runout landslides. The arguments presented in regard of this key point have emerged from the morphometric analysis conducted for the Coprates Labes and the Tsiolkovskiy crater landslides, from the observation of the longitudinal ridges behaviour at these two sites, and from the observation of the longitudinal ridges behaviour and considerations of thickness deposit of two other selected martian long runout landslides.

The third key point (Section 7.3) is a discussion on a new framework under which the understanding of the formation mechanism of long runout landslides should be approached; this discussion draws upon the extensive literature on long runout landslides, on frictional weakening in fault mechanics, on the similarity of weakening of shear zones in landslide and earthquake mechanics, on the geomorphology of long runout landslide deposits; this is merged with the arguments in regard of the formation mechanism of longitudinal ridges during landslide emplacement put forward in the study of the Coprates Labes and the El Magnifico landslide.

7.1 The existence of a scaling relationship between the wavelength of longitudinal ridges and the thickness of long runout landslide deposits.

From the morphometric analysis I conducted for the Coprates Labes landslide (Mars), the El Magnifico landslide (Earth), and the Tsiolkovskiy crater landslide (the Moon) it emerges that the wavelength of longitudinal ridges in long runout landslides scales with the thickness of the landslide deposit. The recurrence of the same scaling relationship between the wavelength of the longitudinal ridges and the thickness of the landslide deposit on three different planetary bodies suggests that the mechanism involved in the formation of longitudinal ridges is independent of environmental conditions (Figure 7-1).

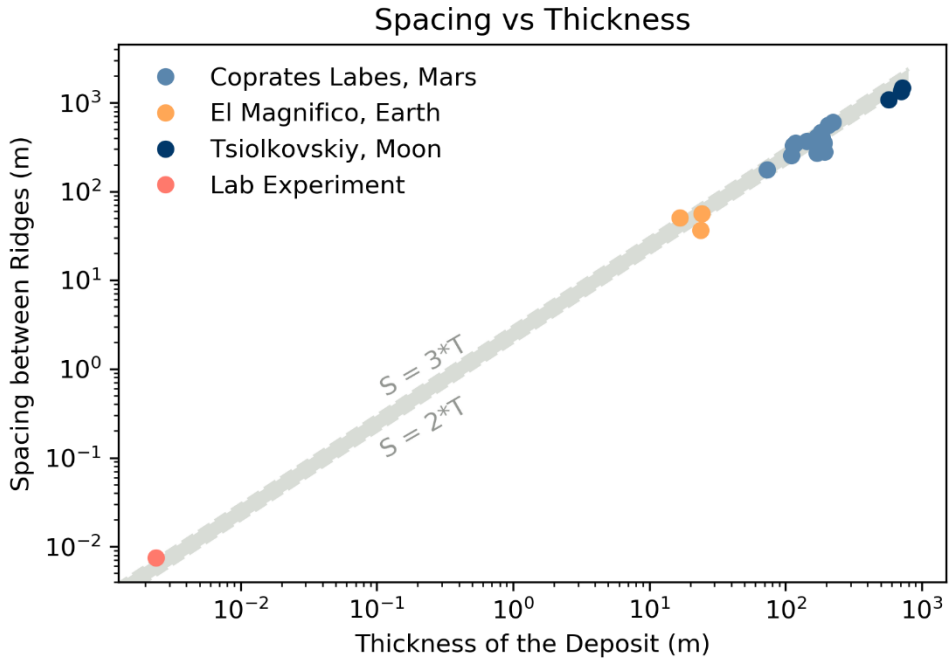

Figure 7-1 – The spacing between longitudinal ridges in long runout landslides is consistently 2 to 3 times the thickness of the deposit. Plot showing the scaling relationship between the spacing between longitudinal ridges and the thickness of the landslide deposit is in agreement with the results from ice-free laboratory experiments on rapid granular flows (grey area); the data comes from the morphometric analysis conducted for the Coprates Labes, in Valles Marineris on Mars (light blue dots; Chapter 4), the El Magnifico landslide, in the northern Atacama region on Earth (yellow dots; Chapter 5), and the Tsiolkovskiy crater landslide, at the far side of the Moon (dark blue dots; Chapter 6).

Environmental conditions and the nature of the substrate over which the slides moved have been considered important factors for explaining both the

hypermobility of long runout landslides and the development of their associated longitudinal ridges. The morphological similarity of longitudinal ridges in martian long runout landslides and terrestrial landslides emplaced on glaciers has been often used to suggest the correlation of longitudinal ridges with the presence of an icy basal surface on Mars at the time of landslide emplacement [e.g., Lucchitta, 1978a; 1979]. However, Lucchitta [1979] concludes that the most important condition for the formation of longitudinal ridges is the availability of large potential energy that results in high speed. Secondarily, their formation can be also favoured by low frictional resistance during motion. Although acknowledging the similarity of the martian morphologies with those of terrestrial landslides on glaciers [e.g., Shreve, 1966; Marangunic and Bull, 1968] and therefore considering the importance of ice, Lucchitta [1979] also questions the morphological similarity of longitudinal ridges in martian long runout landslides with those observed in impact crater ejecta, in the lunar Tsiolkovskiy crater landslide, and in some pyroclastic flows and ponders about its meaning for a mechanism that seems to operate in such diverse deposits.

Two studies attempt to explain the occurrence of longitudinal ridges in long runout landslides. Dufresne and Davies [2009] and De Blasio [2011] conclude that one of the most important conditions for the formation of longitudinal ridges is the presence of a substrate that provides a low basal friction. Types of substrates are identified with those that can provide strong lubrication and a soft surface [De Blasio, 2011], which create a mechanical contrast with the sliding mass constituted of stronger and more competent, fragmented high friction material [Dufresne and Davies, 2009]. On the base of such characteristics, favourable substrates are identified with ice, permafrost, water (or loose saturated material), or evaporites. These studies also acknowledge the high velocity nature of the events and the inertial effect that a lubricant basal surface would have on the high-speed sliding mass, favouring both longitudinal stretching and lateral spreading and therefore causing its tensional deformation. Such deformation generates the longitudinal structures observed on the surface of long runout landslide

deposits by necking. However, there are arguments that undermine the plausibility of these models.

The first argument against a mechanism dependent upon environmental conditions is the diversity of settings, both geological and climatic, in which long runout landslides exhibiting longitudinal ridges are found. In particular, scepticism about the necessity of an icy surface in order to develop longitudinal ridges is expressed by Boyce *et al.* [2020], who based their argument simply on the fact that longitudinal ridges appear in the Tsiolkovskiy crater landslide on the Moon, which does not show any evidence of former presence of surficial masses of ice or water. The presence of longitudinal ridges in the El Magnifico landslide, which occurred at a time when hyperarid conditions where set in the Atacama region, also argues against the requirement for a basal surface of ice.

The second argument comes from the study of the time of occurrence of long runout landslides present in Valles Marineris, which has been estimated spanning from 3.6 Gya to 100 Ma [Quantin *et al.*, 2004b] and younger cases possibly exist [Hager and Schedl, 2017]. According to these results, it appears that long runout landslides have been recurring throughout much of the martian history, suggesting that the formation mechanism of long runout landslides and their longitudinal ridges is persistent in time. Therefore, mechanisms that rely on specific environment or lithology are not supported by these observations. Mars is thought to have gone through global climatic changes that transformed the planet from having extensive fluvial processes, lacustrine systems, and possibly an ocean early in its history to having more episodic surficial water activity, with ephemeral water standing bodies and localized valley network, to having even drier conditions with water playing a minor role in shaping the surface of the planet [Carr and Head, 2010]. In addition, Valles Marineris is located a few degrees south of the martian equator. Although, glacial processes appear to have shaped mid- and high-latitude terrains [e.g., Fastook and Head, 2014; Butcher *et al.*, 2017] and obliquity forces may have caused global glaciations up to recent time [Laskar *et al.*, 2004], and diagnostic features of glacial and paraglacial processes in Valles Marineris have been proposed and described [e.g., Mège and

Bourgeois, 2011; Gourronc *et al.*, 2014; Makowska *et al.*, 2016], evidence for extensive and continuous glaciations at martian equatorial latitudes still remains contentious [e.g., Kissick and Carbonneau, 2019].

Final arguments are provided from observations of details of long runout landslide deposits at some locations in Valles Marineris on Mars. Several landslide deposits exhibiting longitudinal ridges are found overlapping each other at different sites. The overlapping does not only occur with landslides that developed from adjacent slopes of the same valley cliff (Figure 7-2) but also with landslides that developed from opposite valley cliffs. In the latter scenario, landslides run up the distal part of other landslide deposits, astonishingly blanketing them and preserving the longitudinal pattern (Figure 7-3).

With the assumption that the overlapping landslide deposits have similar compositional, physical, and mechanical properties – as they develop from the same slope or opposite slopes that are assumed to have same bulk composition, it is likely that the presence of lower older deposits serving as basal surface for the overrunning younger deposits invalidates the necessity for a lubricant basal surface and a mechanical properties contrast between the basal surface and the sliding mass in order to develop longitudinal ridges.

One cannot exclude that deposition of clay-bearing sediments, the formation of ice, or the rising of a standing body of water has not occurred in between the emplacement of the individual landslides, thus providing a low basal friction for the next landsliding event. However, it should be expected that some of these processes would modify the surface aspect of landslide deposits and leave some degree of evidence of their past existence. In fact, in Coprates Chasma, there is evidence for a number of landslide deposits being buried by sediments and now partially exhumed (Figure 7-4).

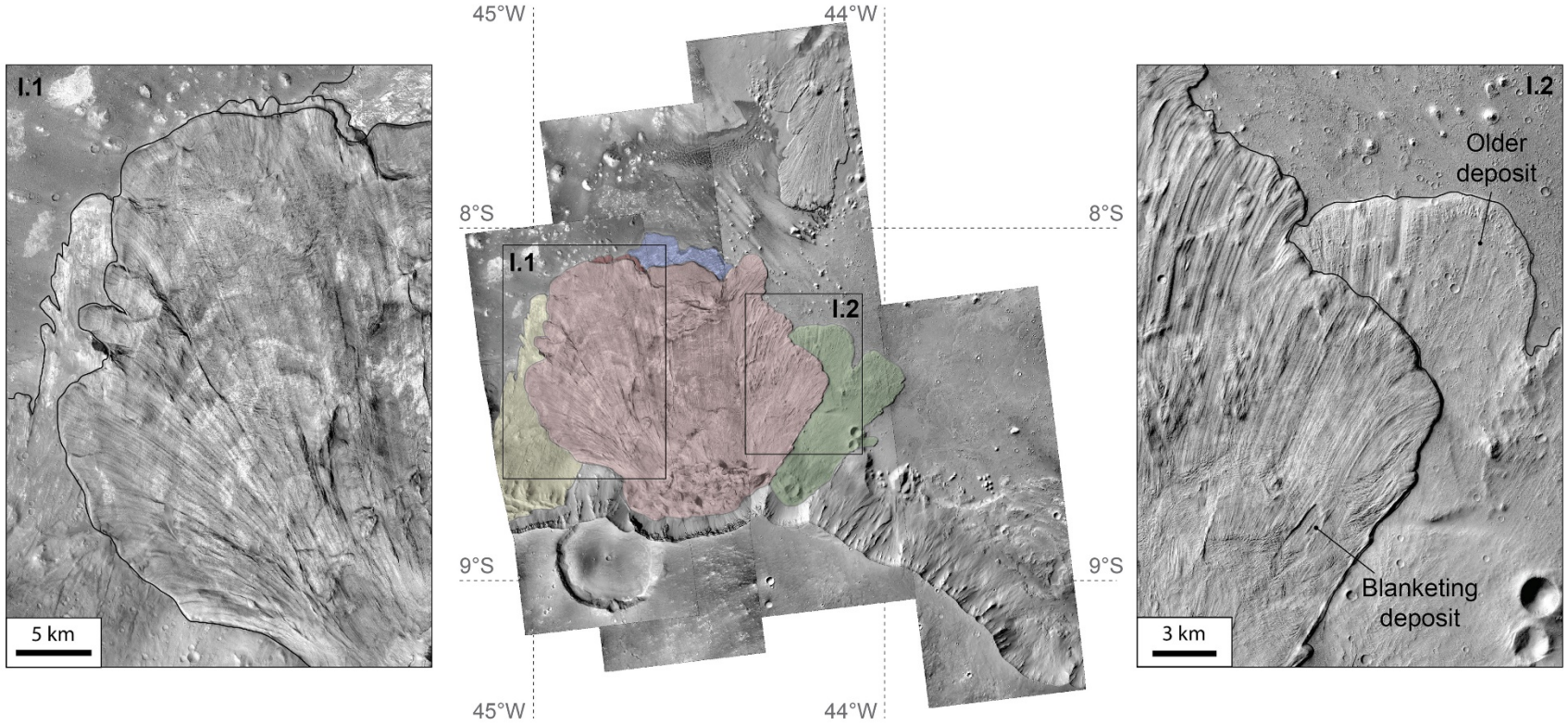

Figure 7-2 – Examples of martian overlapping long runout landslides that originated from adjacent slopes. The landslides are located in Ganges Chasma. At least three landslide deposits can be identified: a top-most deposit (red), corresponding to the youngest of the cluster; two overridden deposits (yellow and green), for which is not possible to tell which one is the oldest, based on overlapping relationships. A forth deposit (violet) is evident, however it is not clear whether this is an older landslide deposit or another deposit not formed by landsliding process. I.1 and I.2 are insets showing details of the overlapping relationships between landslide deposits: the longitudinal pattern of ridges characterizes both overridden and overriding deposits.

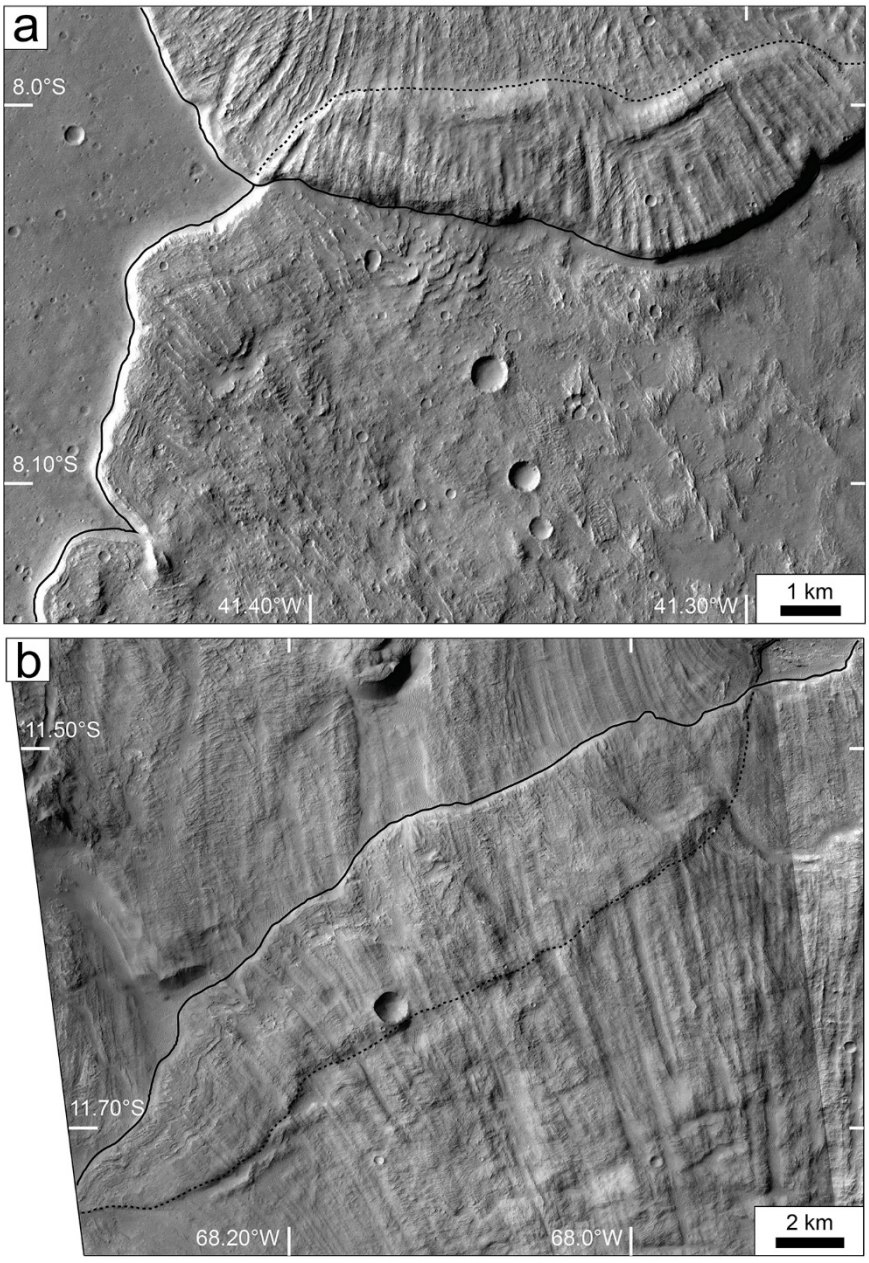

Figure 7-3 – Details of martian overlapping long runout landslides that originated from opposite slopes. a) Overlapping landslides in Ganges Chasma: the landslide at the top of the figure, the younger, runs up another landslide deposit, the older, whose covered edge is marked with a dashed black line; longitudinal ridges characterize the younger deposit and their pattern remains unperturbed despite the landslide superimposing another deposit. b) Overlapping landslides in Coprates Chasma: the landslide at the bottom of the figure, the Coprates Labes landslide studied in Chapter 4, runs up another landslide deposit, whose covered edge is marked with a dashed black line; longitudinal ridges that characterize the Coprates Labes landslide and their pattern remain visible on the overriding distal part of the deposit.

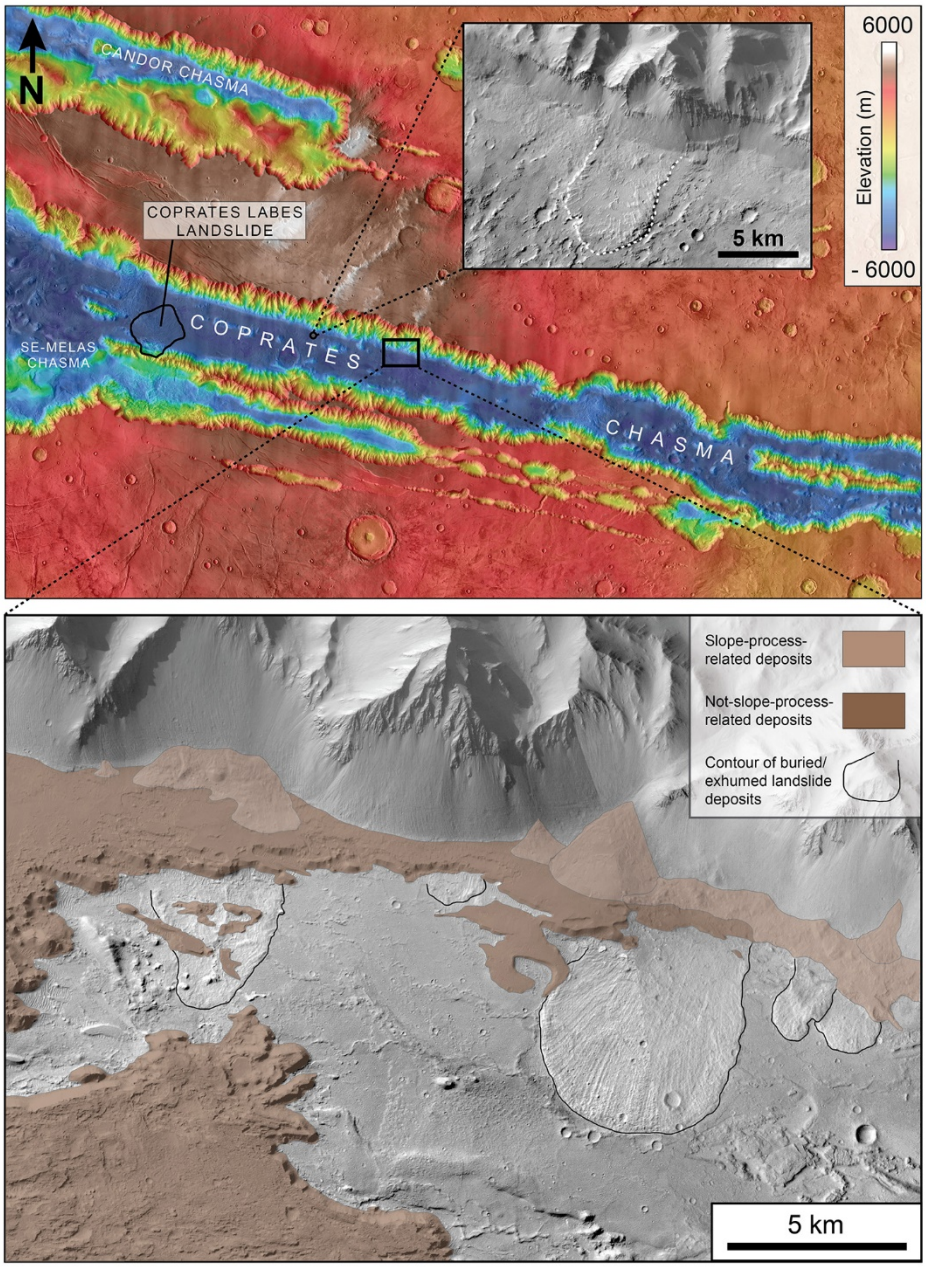

Figure 7-4 – Buried and exhumed landslide deposits in Coprates Chasma. Evidence of partially buried and partially exhumed long runout landslide deposits suggests a complex geological history in which diverse processes have been at play in Coprates Chasma. Landslide deposits can be used as stratigraphic markers in order to constrain the timing of sedimentological processes and tectonic activity.

The scaling relationship between the wavelength of longitudinal ridges and the thickness of landslide deposits that I have found for my three case studies on three different planetary bodies is in agreement with previous ice-free experimental laboratory work on and numerical simulation of rapid granular flows [Forterre and Pouliquen, 2001; 2002; Borzsonyi *et al.*, 2009]. In addition

to further support the idea that ice is not a necessary condition for the development of longitudinal ridges, the agreement between laboratory-scale and field-scale results suggests the existence of a mechanism that is also scale-independent. The experimental work on rapid granular flows has recognized high speed, along with the surface roughness, as a critical factor for the onset of the flow instability that generates the longitudinal pattern. Indeed, all the case studies of long runout landslides found in the literature report on the high speeds that have characterized the emplacement of these catastrophic events [e.g., Goren *et al.*, 2010; Roberts and Evans, 2013; Mazzanti *et al.*, 2016; Magnarini *et al.*, 2019].

Additional support of the hypothesis that high speed is the determining factor for the development of longitudinal ridges is provided by the existence of longitudinal ridges in martian double layer ejecta (DLE) deposits, whose morphology and behaviour is closely related to the longitudinal ridges in long runout landslides [e.g., Boyce *et al.*, 2014; Wulf and Kenkmann, 2015] (Figure 7-5).

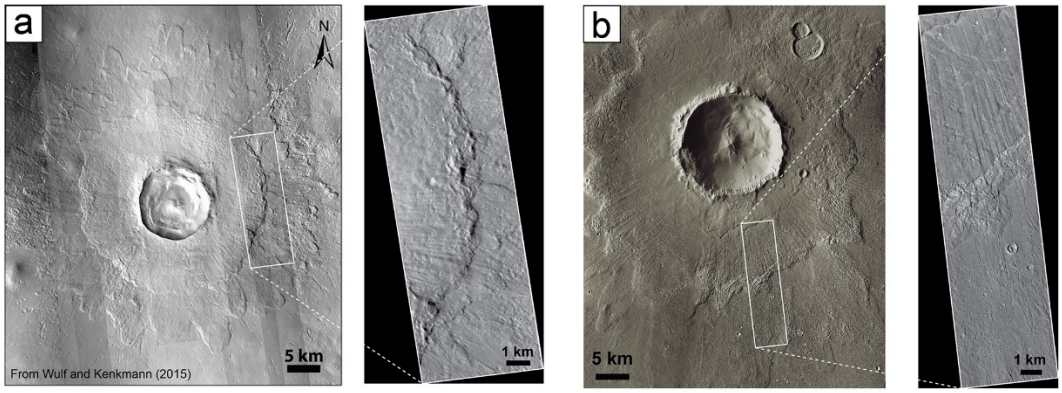

Figure 7-5 – Martian double layer ejecta craters exhibiting longitudinal ridges morphologically similar to longitudinal ridges in long runout landslides. a) Steinheim crater (54.6°N 169.38 W); CTX mosaic from Wulf and Kenkmann [2015] and HiRISE image ESP_027647_2350. b) Bacolor crater (33°N 118.6°E); the left panel shows a view that combines images taken during the period from September 2002 and October 2005 by the THEMIS instrument on board the Mars Odyssey mission (PIA13664; NASA/JPL-Caltech/ASU) and HiRISE image PSP_007462_2130.

High velocity is the common denominator at play during the emplacement of long runout landslides and of impact crater ejecta, in which the high velocity

in the latter is provided to the system by the explosive release of energy during the impact of a bolide with the surface. Future morphometric analysis of longitudinal ridges and grooves of double layer ejecta deposits is required in order to find out whether the same scaling relationship reported in long runout landslide also occurs in these different type of deposits.

Although I was not able to pinpoint the type of mechanism responsible for the formation of longitudinal ridges, the evidence I collected and have discussed suggests that it is likely linked to the high-energy/high-speed nature of long runout landslide emplacement events. As will be discussed in Section 7.3, I conclude that the high speed that characterizes the emplacement in the sub-horizontal sector of the runout are not generated at this stage by a mechanism favoured by specific environmental conditions, instead they are inherited from the initial collapse phase. However, it has to be noticed that in the El Magnifico landslide longitudinal ridges only appear in the terminal part of deposit, which is the zone where velocities are expected to reduce as the landslide comes to a halt. This is in contradiction with the suggested mechanism that relies on high velocity. Nevertheless, it is interesting that the scaling relationship between the longitudinal ridges and the thickness of the deposit is maintained. In Section 7.3 I will discuss the possibility of the existence of two end-member mechanisms able to generate similar morphological pattern.

The occurrence of a scaling relationship between the wavelength of longitudinal ridges and the thickness of the sliding mass, the fact that is found at different scales, the lack of robust evidence in support of the importance of environmental conditions in the development of longitudinal ridges, and the fact that high-speed is a consistent factor across different geological processes that generate longitudinal ridges suggest that the mechanism involved is intrinsic to the catastrophic nature of the long runout landslides emplacement.

7.2 The effect of lateral confinement on the thickness of the landslide deposits and on the behaviour of longitudinal ridges.

It has been suggested that the lateral spreading of landslides emplaced at high speed on a lubricating surface causes the sliding masses to split in a pattern of longitudinal ridges and furrows, following analogous extensional deformation that forms boudinage [Dufresne and Davies, 2009; De Blasio, 2011]. However, there is evidence of development of longitudinal ridges also in instances of laterally confined long runout landslides. One case is the Tsiolkovskiy crater landslide, which, as described in Chapter 6, has well developed longitudinal ridges and appears to have its northeast lateral edge constrained by the inner slope of the Fermi crater rim (Figure 6-1f). I also identified two martian long runout landslides characterized by remarkable longitudinal ridges that were confined at the time of their emplacement: a landslide in Tithonium Chasma that is laterally confined by high relief (Figure 7-6a); and a landslide in Ophir Chasma that was obstructed and diverted by interior layered deposit (ILDs) mounds ([Grindrod and Warner, 2014], Figure 7-6b).

Therefore, it can be concluded that lateral spreading is not the reason why longitudinal ridges form. In fact, longitudinal ridges are observed forming in laboratory rapid granular flows moving down an inclined plane with side walls [Forterre and Pouliquen, 2001], which supports the idea that the formation mechanism of longitudinal ridges is not linked to tensional stress applied to the sliding mass.

Although the lateral confinement of long runout landslides does not preclude the development of longitudinal ridges, it does affect their behaviour. In unconfined landslides, ridges are observed drifting away from each other while new smaller ridges appear in between (Figure 4-14); on the other hand, in laterally confined landslides, ridges remain fairly parallel. In addition, the confined/unconfined status of a landslide does affect the thickness of its deposit. In unconfined landslides, the deposit thickness gradually decreases with the distance and the most distal parts all appear to roughly have the

same thickness, tens of meters [Melosh, 1983]. Instead, laterally confined landslides show more constant thickness throughout their length, in the range of hundreds of meters (for instance, the Tsiolkovskiy crater landslide, Section 6.4.1).

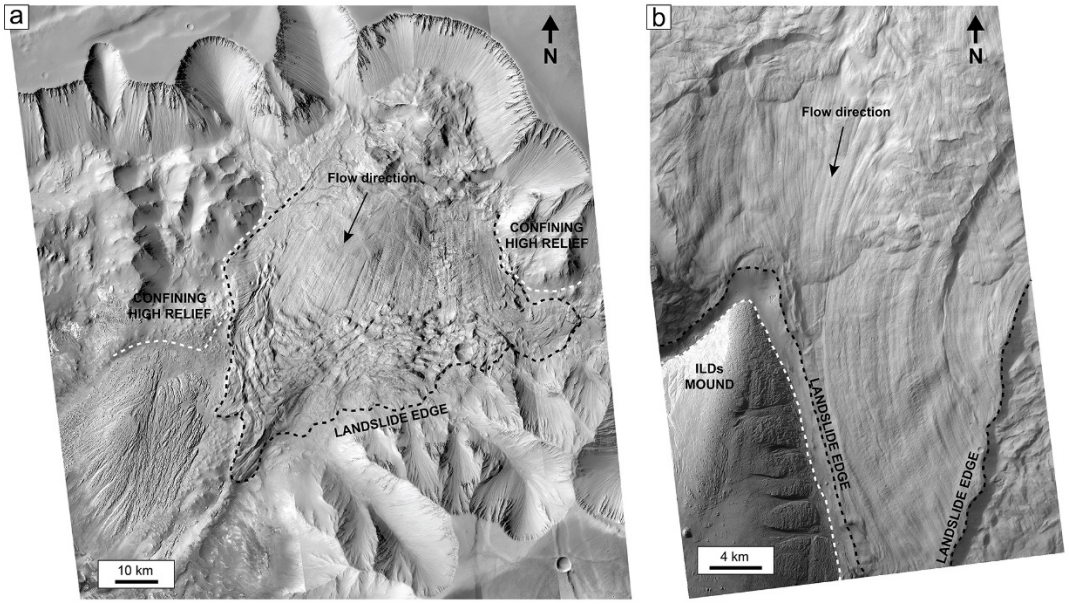

Figure 7-6 – Examples of laterally confined landslides on Mars. a) The long runout landslide in Tithonium Chasma, Mars, is laterally confined by high relief; the part of the landslide deposit confined shows parallel longitudinal ridges; the corrugated terminal part is made by compressional ridges that are generated due to frontal confinement of the landslide (MRO CTX image mosaic: D04_028673_1752, P17_007707_1751, F16_042031_1744, J03_045987_1756). b) The long runout landslide in Ophir Chasma, Mars, was confined and diverted by interior layered deposits (IDLs) at the time of emplacement and they have now retreated due to erosion; the diverted lobe bends and consequently so do the longitudinal ridges, which nevertheless remain parallel due to the lateral confinement (MRO CTX-derived orthoimage: P22_009750_1765 – B01_009895_1764; modified after Grindrod and Warner [2014]).

Following these observations, it can be concluded that the spreading of long runout landslides does not cause the development of longitudinal ridges, but it does cause the landslide deposits to become thinner and the ridges to diverge from one another. As the ridges diverge due to spreading of the unconfined sliding mass, the distance between the ridges increases. However, given the existence of the scaling relationship between the wavelength of longitudinal ridges and the thickness of the landslide deposit, as the slide gets thinner due to the spreading, the distance between the ridges has to decrease. This situation is solved with the appearance of new ridges

in between diverging ridges, so that the distance between ridges actually reduces (Figure 7-7). In the case of unconfined landslides, the thickness of the deposit does not vary significantly, thus accordingly the distance between the ridges does not change considerably, explaining why the longitudinal ridges remain fairly parallel.

It can be concluded that the thickness of landslides dictates the behaviour of the longitudinal ridges. This reinforces the idea that whatever is the mechanism involved in the origin of longitudinal ridges, it is a mechanism that is environmentally-independent, thickness-dependent, and likely to be intrinsic to the high-velocity nature of long runout landslides.

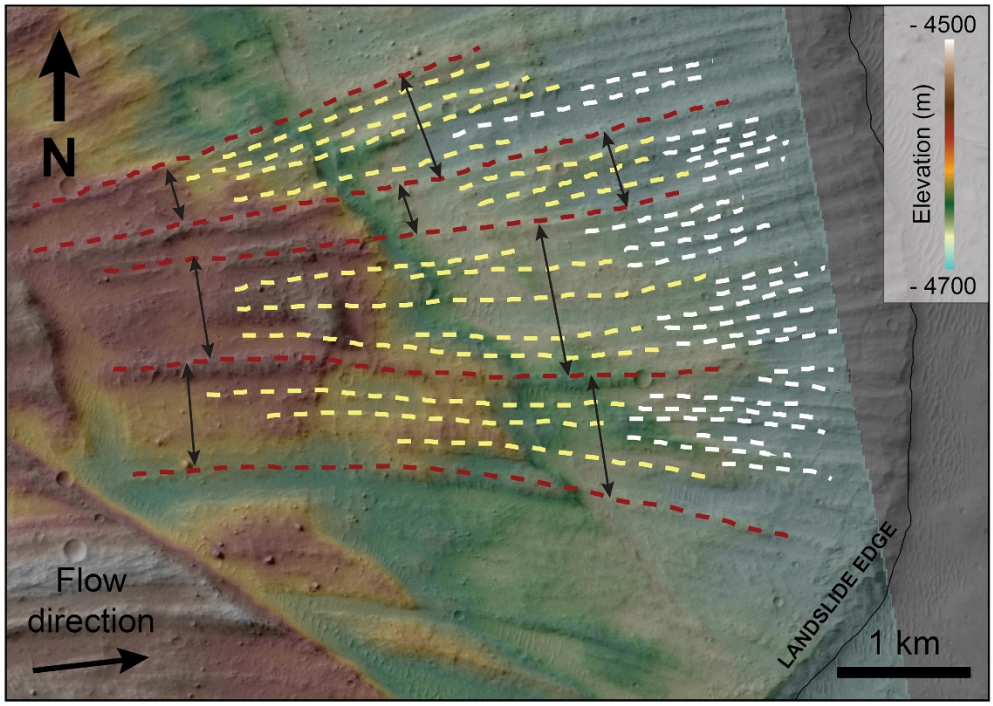

Figure 7-7 – Conservation of the scaling relationship between the spacing between the ridges and the thickness of the landslide deposit. As the thickness of the landslide deposit decreases because of the spreading, existing ridges diverge (red). Given the existence of the scaling relationship between the spacing between the ridges and the thickness of the deposit, new ridges appear (yellow and then white) between diverging ridges so that the spacing between them is reduced.

7.3 Understanding long runout landslides: converging fault mechanics, granular flow physics and geomorphology.

The remarkable ability of long runout landslides to move for several kilometres with high velocities on almost horizontal surfaces has concerned geologists for more than a century. A number of studies have focused on mechanisms that would allow the dramatic reduction of friction required to explain the behaviour of these catastrophic events along the sub-horizontal sector of their runout. A number of other studies have instead focused on the mechanisms that could generate the high velocities in the early stages of the landslide event, soon after the slope collapse, which cannot be characterised by the simple transformation of potential energy to kinetic energy. This division highlights the fact that long runout landslides, as a system, consist of two distinct sectors along which different mechanisms take place. It is my opinion that there is the need to update the framework within which long runout landslides are studied, bringing into focus the causality between the mechanisms operating at the two sectors. In the following sections I will propose and describe a new framework and discuss how my observations have motivated its definition, with a focus on the formation mechanism of longitudinal ridges and the landslide stress field during emplacement.

7.3.1 The long runout landslide system.

The scarp-to-toe system of a long runout landslide can be divided into: 1) a steep slope sector, where the slope collapse occurs, and 2) a sub-horizontal sector of the runout, where the deposit extends over the valley floor, displaying the characteristic hypermobility of such type of events. These two sectors are connected via an abrupt change in slope (Figure 7-8a). The zone where the change in slope occurs is crucial, as this is where the landslide mass moving as a coherent, rigid body mass transforms into a mass moving as a coherent, yet fragmented mass, and momentum is transferred from one state to the other. The change in the physical state of the deposit can be identified in the field (Figure 7-8).

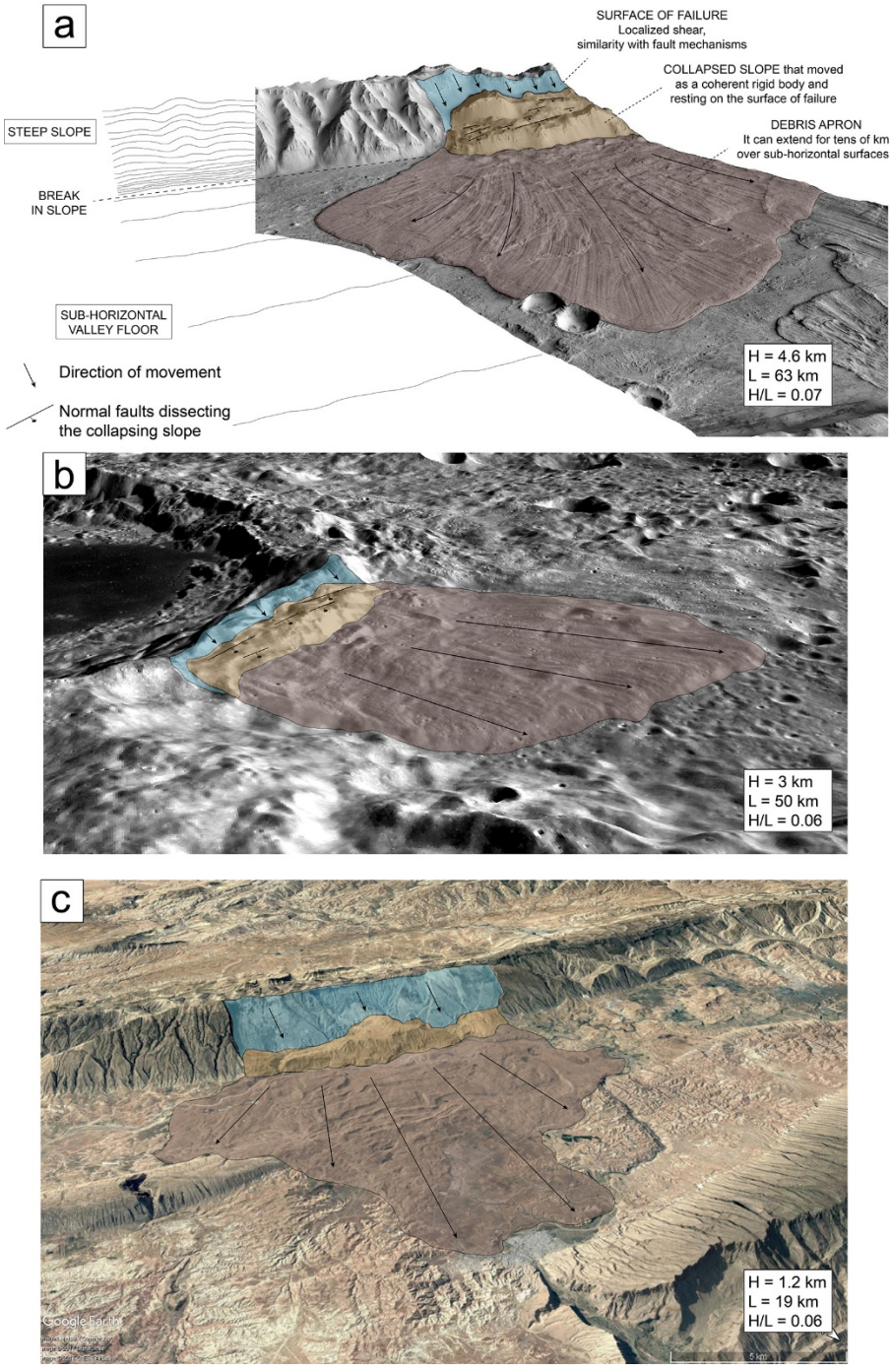

Figure 7-8 – Schematic representation of a long runout landslide system. a) Two sectors are identified, which correspond to a steep slope, where the slope collapse occurs, and a sub-horizontal floor (these sectors are visualized contour lines to the left-hand side of the panel), where the deposit extends for several kilometres, showing its characteristic hypermobility; the two sectors are separated by a sudden break in slope (the landslide example is the martian Coprates Labes; oblique view; CTX-derived orthoimages overlapping CTX-derived digital elevation model; Vertica exaggeration 1.5x). b) The lunar Tsiolkovski crater landslide; with the colours used following the scheme presented in a) (WAC-derived digital elevation models overlain by WAC imagery; oblique view; vertical exaggeration 1.5x). c) The Iranian Saidmarreh landslide; colours are used following the scheme presented in a) (oblique view of Google Earth imagery).

The part of the landslide deposit that does not evacuate the source area (i.e., it does not pass the break in slope zone and it is found resting on the surface of failure) appears as relatively intact sections or blocks of the original slope. This is observed regardless of the nature of the failure plane. Failure planes may correspond to cataclinal bedding planes or metamorphic foliation (i.e., surfaces dipping with same or shallower angles and towards the same direction of the slope), in which displacement may occur along one or a number of bedding/foliation planes (e.g., the Vajont landslide, the Saidmarreh landslide (Figure 7-8c), the Elm landslide). Failure planes may also correspond to faults or reactivated surfaces of failure, commonly dipping at higher angles than the slope, in which the collapsed slope is fragmented in blocks that are displaced by normal faulting to accommodate its rotation along the surface of failure, in a similar fashion to the toreva blocks in classic rotational slides (e.g., Coprates Labes landslide, Figure 7-8a; Tsiolkovskiy crater landslide Figure 7-8b).

Scrutiny of the scarp zones and failure planes of the Coprates Labes landslide, the El Magnifico landslide and the Tsiolkovskiy crater landslide, and details about the source area of other known long runout landslides available from the literature suggest that failure planes are deep-seated and localized along already existing weaker surfaces. These surfaces can correspond to sedimentary contacts (e.g., the El Magnifico landslide; the Saidmarreh landslide; the Vaiont landslide), metamorphic foliation (e.g., the Elm landslide), reactivated failure planes (e.g., the Oso landslide), and likely faults or large-scale fractures or weak layers at the base of a slope that becomes gravitationally unsupported (e.g., landslides in Valles Marineris; the lunar Tsiolkovskiy crater landslide). These are well known settings that commonly favour landsliding, yet in these specific cases are capable of generating catastrophic events such as long runout landslides. In fact, the tragic Vaiont landslide (Italy, 1963) has demonstrated that a catastrophic acceleration leading to velocities higher than expected from classical friction models can be achieved early during the initial phase of landslide motion along the slope failure plane [Habib, 1975; Hendron and Patton, 1987]. One of the key factors of the initial phase attributed to the development of catastrophic slope failures

is the localization of the deformation that leads to the nucleation of a thin slip zone [Viesca and Rice, 2012], along which the collapsing slope moves as a rigid body: acceleration is initially driven by gravity and it is rapidly promoted by a series of velocity-weakening mechanisms that lead to strength loss. Work by Habib [1975], Voight and Faust [1982] and Vardoulakis [2000] highlighted frictional heating as leading to slip-weakening mechanisms during the initial phase of catastrophic landslides, picturing a scenario that is similar to what is described in the mechanics of faulting [e.g., Rice, 2006]. These surfaces of rupture can be considered as superfaults, that is faults that are capable of undergoing very large displacements, even kilometres, during a single-slip event because they are not pinned at their ends [Spray, 1997].

The high velocity at which the failed slope moves continues to characterize the debris that moves over the sub-horizontal sector of the runout. The velocities of some long runout landslides have been derived with different indirect methods (see Section 2.1.2) and they all appear to fall within the range of several tens of meter per second [e.g., Goren *et al.*, 2010; Roberts and Evans, 2013; Mazzanti *et al.*, 2016; Magnarini *et al.*, 2019]. I conclude that the high velocity that characterizes the emplacement in the sub-horizontal sector of the runout is not generated at this stage but it is instead inherited from the initial collapse phase. Yet, a mechanism must exist that allows the high velocity to be maintained, and maybe further incremented, for tens of kilometres along a sub-horizontal surface. The concept of inheritance from the collapse phase to the runout phase is important because it prompts the idea that the formation mechanism of long runout landslides involves a series of mechanisms that are linked one to another, as a chain of events throughout the two phases. Under this perspective, the break in slope, at which the sliding mass undergoes a radical transformation of its physical state (as discussed earlier), becomes a fundamental point in the system. Understanding this transformation and the transfer of energy from one phase to another will help in constraining the mechanisms that are involved in the sub-horizontal sector of the runout, which can only be partially unlocked through morphological analysis of the landslide deposit. Two works have noted the relevance of the abrupt change of slope in the analysis of their

models: Campbell *et al.* [1995] report that “it is somewhat interesting, but not very surprising, to see that the largest stresses are encountered at the beginning of the circular arc when the ground surface forces the landslide to change direction”; similarly, Goren and Aharonov [2007] describe that “upon reaching the end of the slope, as the slide continues sliding on the plane, the shear stress increases immediately, leading to a jump in pore pressure”.

In addition to being characterized by high velocity and hypermobility, the part of the landslide debris that moves over a sub-horizontal surface, during the second phase of the long runout landslide-system, also exhibits morphological features that are distinctive to such catastrophic mass-wasting process (Section 2.1.3; Section 2.1.4). The landslide deposits appear as if they moved and were emplaced as a coherent mass, with distinct edges, steeply standing out several meters above the surrounding terrain and, in some instances, marked by longitudinal ridges for almost the entire extent of the deposit. In Chapter 4, I conclude that longitudinal ridges are structures that reflect the high-speed nature of the emplacement of long runout landslides. As longitudinal ridges do appear already in the proximal sector of the landslide deposit (e.g., the Coprates Labes landslide and the Tsiolkovskiy crater landslide in this thesis), this suggests that high velocity was present at the early stage of the runout phase, supporting the idea that the runout phase along the sub-horizontal surface inherits the high velocity that develops from the catastrophic acceleration during the first phase of the slope collapse.

7.3.2 Evidence for the existence of heterogeneous stress distribution and stress fluctuation within long runout landslide deposits.

As it is understood from laboratory experience (for a summary see Aranson and Tsimring [2009]), pattern-formation mechanisms within a granular medium can arise from injection of energy through vibrations, either through the interaction between the roughness of a surface and the grains of a high-speed flow or through vibrations transmitted to a granular layer resting on a plate. During the emplacement of natural long runout landslides, injection of energy occurs, first of all, through ground vibrations generated by the event

itself and, secondly, through vibrations generated by the interaction between the moving mass and the roughness of the surface over which it moves. As discussed earlier, the break in slope zone is where the highest stresses are modelled, following the downslope movement of the collapsed slope at very high speeds. Here, the high stresses are released to the slide in form of acoustic energy. I suggest that the break in slope represents the fundamental point at which high amount of energy is injected into the sub-horizontal phase of the long runout landslide system in form of vibrations.

The propagation of vibrations within a sliding mass is expected to result in stress fluctuation. In fact, large fluctuation of stresses are reported in computer simulations by Campbell *et al.* [1995] and Johnson *et al.* [2016a], and they are considered the hallmark of the acoustic fluidization hypothesis [Melosh, 1979]. As explained in Melosh [1979], one of the characteristics that acoustic fluidization would be able to explain is the preservation of stratigraphy, as turbulent flow does not occur and rocks in the landslide never lose contact with each other. In Chapter 5, I show evidence of lack of turbulent mixing between different lithological units, which appear to be separated by well-defined boundaries (Figure 5-10). What is also interesting from those observations is that the well-defined contacts appear to be both sub-horizontal and sub-vertical (Figure 5-13), with a possible interdigitating relationship (Figure 5-12), suggesting a complex level of interaction during the emplacement of the landslide, thus excluding shearing limited to a basal layer, or simple laminar flow-style longitudinal stretching of a shearing mass. Further evidence of such level of interaction between different units is provided by another long runout landslide deposit - ‘North cluster’ following Crosta *et al.* [2017] denomination -, few kilometres north of the El Magnifico landslide (Figure 7-9). An interdigitating relationship between lithological units, wavy contacts between them and the wavy appearance of some units suggest that the sliding mass went through some sort of plastic deformation that may have been facilitated by vibrations. A beautiful example of layers with a wavy aspect is observed in a long transversal outcrop of the El Magnifico landslide, which does not exist anymore, but shown in Mather *et al.* [2014] and Crosta *et al.* [2017] (Figure 7-10).

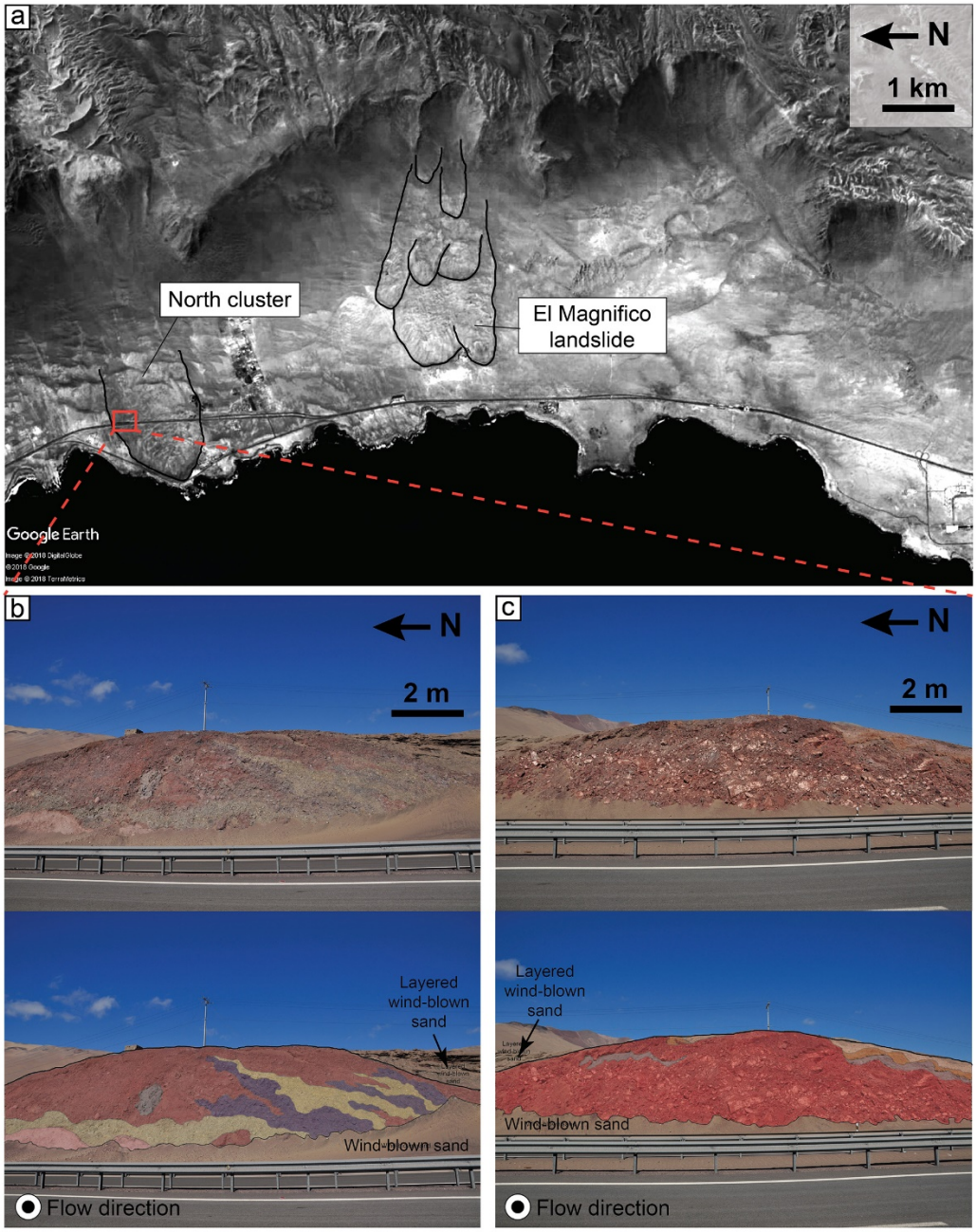

Figure 7-9 – Outcrops of the North cluster landslide, Chile. a) Location of the North cluster landslide, few kilometres north from the El Magnifico landslide. b) and c) Photographs of the outcrops and below a schematic representation of the structures observed (colours represent different sections of the deposit identified in the photographs); in b) in particular, interdigitating units clearly show wavy shapes; instead, in c) a wavy boundary between different lithological units is visible to the top-right section of the outcrop.

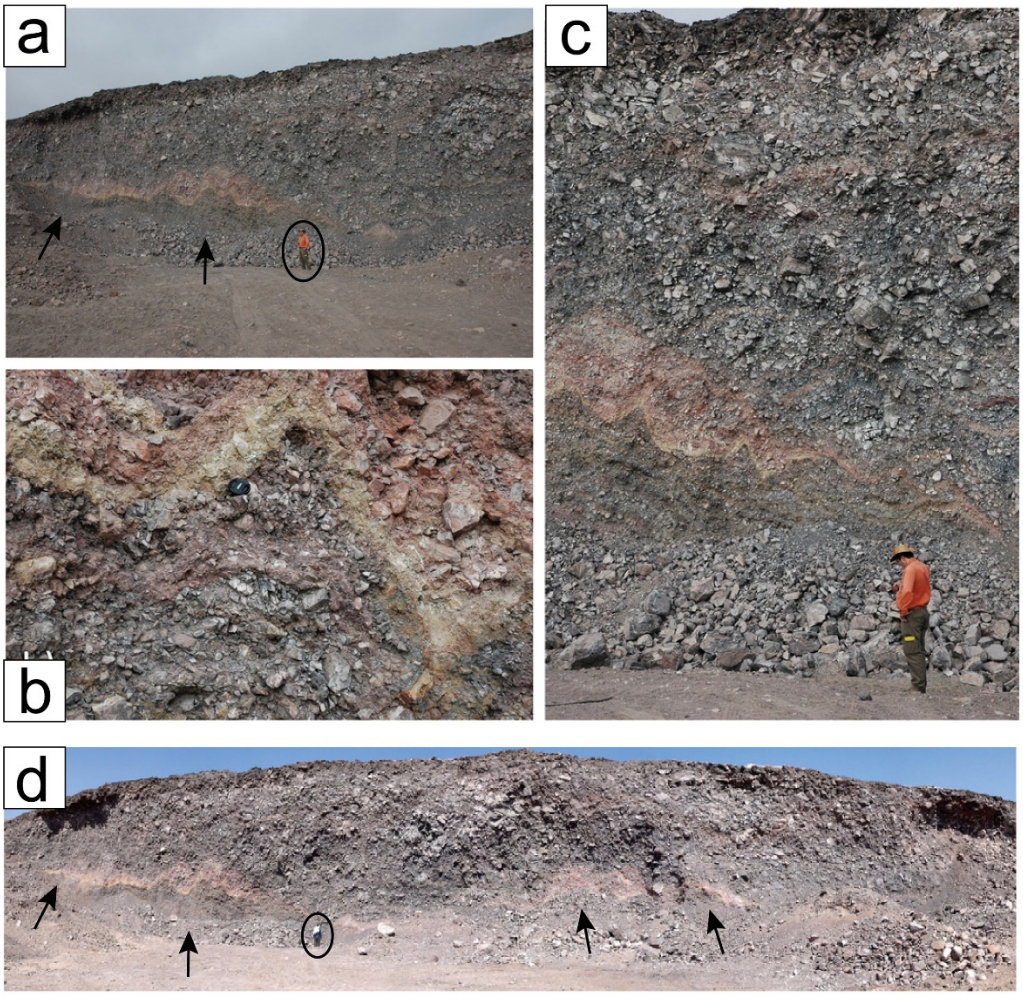

Figure 7-10 – Old outcrop at the El Magnifico landslide quarry. Internal structures at a section of the El Magnifico landslide deposit. This section does not exists any longer, as the quarry activity has destroyed it. It was likely several tens of meter to the west of the existing current section that I studied for this thesis. Thus, this section represented a more distal section than the current one. The black arrows are pointing to a layer within the grey breccia that is constituted of red, yellow, green sublayers. The coloured layer shows evidence of deformation, with folding in some locations. Black ellipses show person for scale. These photos are modified from Crosta *et al.* [2017] (a, b, and c) and from Mather *et al.* [2014] (d).

Heterogeneous stress distribution and stress fluctuation have been discussed by Dufresne *et al.* [2016], in their analysis of facies and sub-facies of rock avalanche deposits. In the field, evidence for heterogeneous stress distribution is provided by the presence of 'megablocks' within the sliding mass, not just at the proximal areas of a deposit, as observed by Dufresne *et al.* [2016], but also at the most distal areas of a deposit, as I reported in the El Magnifico landslide (Figure 5-14, Figure 5-15, Figure 5-16). The

preservation of such large portions of the original slope-forming material throughout the entire runout of a catastrophic landslide is remarkable. These structures exhibit different degrees of deformation, from bed thickness reduction and fracturing normal to bedding planes, to as far as resembling cataclastic rock in some zones near their edges. I was also able to observe very similar megablocks in an ancient landslide deposit in Kyrgyzstan (Figure 7-11).

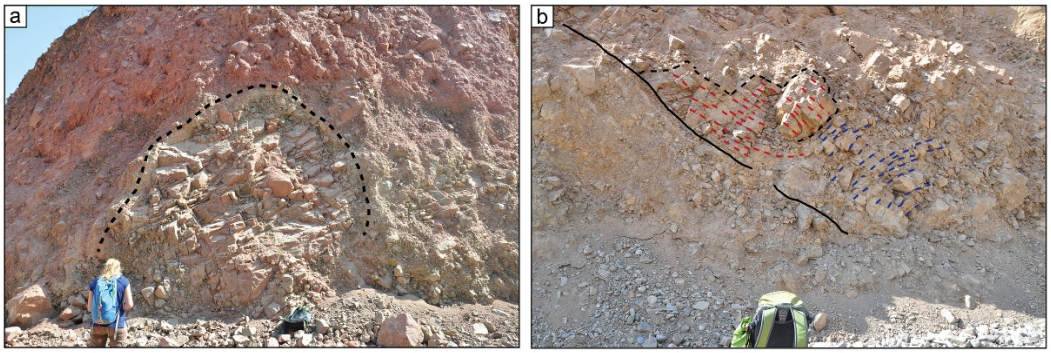

Figure 7-11 – Megablocks in an ancient long runout landslide deposit in Kyrgyzstan. a) The megablock is encircled by the black dashed line and closely resembles the megablock observed in outcrop 3 at the El Magnifico landslide; note the reduction of grain size towards its edges. b) Original bedding planes preserved in a fractured block; at the centre of the image, right above the backpack, the fractured block seems to fold (concave up); note the orientation of the long axis of the fractured blocks; in fact, at the upper part of the photo and above the black line, long axes are oriented diagonally top-left/bottom-right (red lines) and, in the lower area of the outcrop, they are diagonally oriented top-right/bottom-left (blue lines); the black continuous line separate a zone of fractured blocks preserving bedding discontinuity (to the right) from the breccia-type part of the deposit.

7.3.3 Friction-weakening mechanisms operating during the emplacement of long runout landslides.

Landslides that show long runout come with disparate physical characteristics due to the fact that they occur in different lithological and structural contexts – which include different planetary bodies -, they are affected by different degree of confinement, and they develop within a continuum from completely saturated debris flows to dry rock avalanches [Legros, 2002]. As discussed in Section 2.4, a variety of mechanisms have been proposed to explain the reduction of friction in long runout landslides, some focusing on an overall

internal reduction of friction, others on a localized basal reduction of friction. Each of these mechanisms is able to satisfactorily describe one or more case studies. It is logical to consider that a universal explanation is not needed [Johnson *et al.*, 2016c]. I would further extend the idea suggesting that also more than one mechanism may be expected to be acting along the sub-horizontal sector during the same event. Certainly, one can expect that the basal layer of all giant landslides undergoes tremendous stress due to the high-velocity interaction with the basal surface, which would generate a gouge, in a similar way a gouge is produced within a fault core. In fact, all the observed basal layers of large landslides show shear bands [e.g., Dufresne *et al.*, 2016], heavily shattered matrix, which can includes micro-breccias and convoluted bands of diamictic landslide material [e.g., Weidinger *et al.*, 2014]. I myself observed sheared material at the base of the Ornok landslide in Kyrgyzstan (Figure 7-12a, b). The gouge derives from mylonitized purple and green claystones and it appears now as an undulated basal layer of the Orlok landslides (Figure 7-12c, d, e, f).

Works such Goren *et al.* [2010] and Mitchell *et al.* [2015] have demonstrated that shear heating-triggered weakening mechanisms operate at the base of catastrophic landslides. However, it is not given to know whether other weakening mechanisms also take part and it is possible that basal friction weakening mechanisms may operate in synergy with other mechanisms of reduction of friction expected operating internally to the slide bulk mass [Johnson *et al.*, 2016c]. Thus, mechanisms of reduction of basal friction and mechanisms of reduction of internal friction should not be considered mutually exclusive. For example, I note that acoustic waves should be always present during the emplacement of long runout landslides, as a simple consequence of the release of a high amount of energy that characterizes such catastrophic events. In addition, the basal layer of a voluminous landslide may also undergo tremendous basal stress due to the high-velocity interaction with the basal floor. Both mechanisms may contribute to the overall reduction of friction.

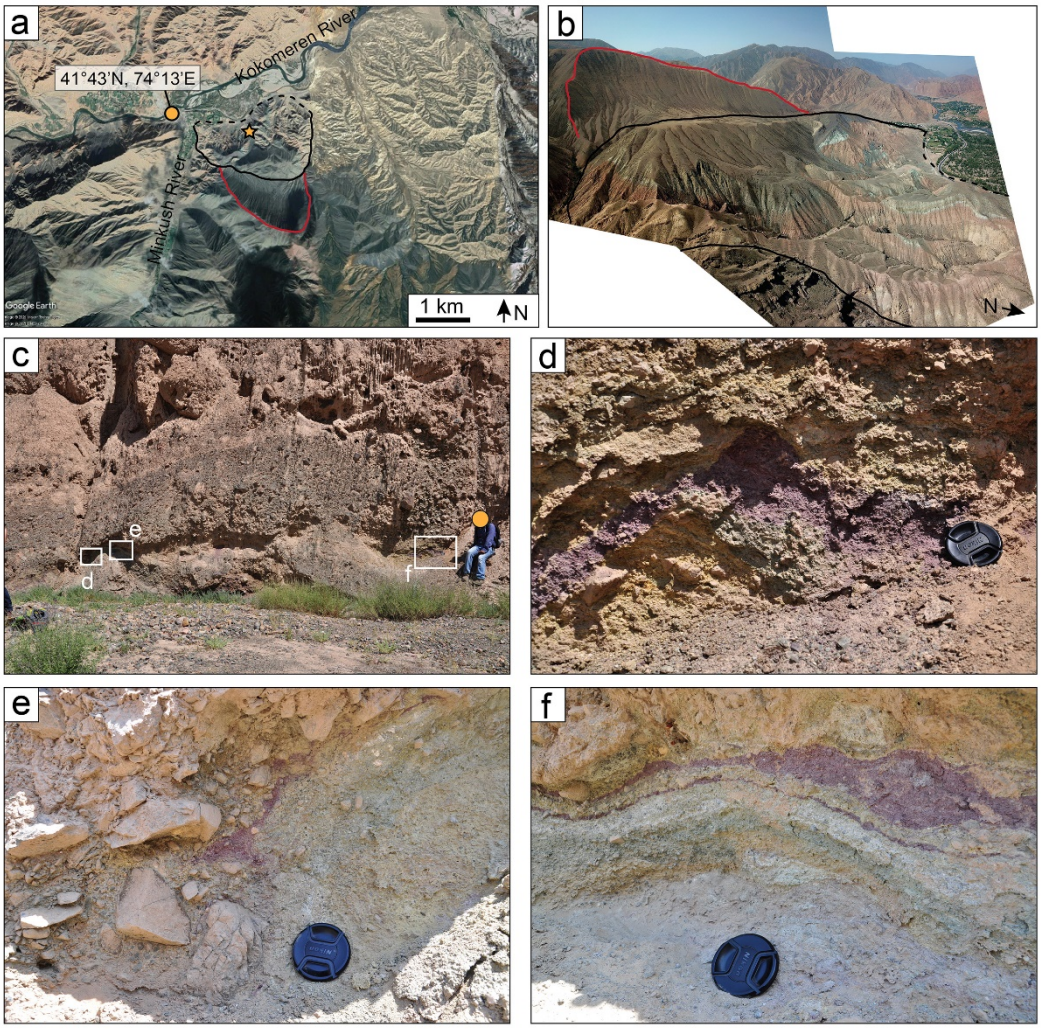

Figure 7-12 – Basal layer of the Ornok landslide, Kyrgyzstan. a) Location of the Ornok landslide; red line identifies the head scarp; black line identifies the landslide deposit and the dashed black line shows the eroded termination of the deposit; yellow star shows the location of the outcrops in c, d, e, and f; yellow dot shows the coordinates of the confluence of the Minkush River with the Kokomeren River. b) Drone mosaic shows an oblique view of the head scarp (red line) and deposit (black line) of the Ornok landslide. c) The basal layer exhibits a clear undulated shape; the basal contact is covered by alluvial deposit. d), e) and f) show details of the basal gouge that consists of differently coloured layers, which derive from comminution and deformation of mylonitized claystone rocks.

Melosh [1979] and Melosh [1983] explain that large enough acoustic energy density would be able to fluidize a landslide. Numerical modelling by Collins and Melosh [2003] and Johnson *et al.* [2016a] have shown that acoustic fluidization is able to explain the hypermobility of long runout landslides and successfully reproduced many field observations. It is known that acoustic energy applied to granular materials or fluids is able to change their rheological properties. It is possible that high amount of energy released at the break in slope would generate a large amount of acoustic energy and

change the rheology of the landslide. The landslide would be characterized by non-Newtonian rheology, showing behaviour of shear thinning (i.e., apparent viscosity decreases with increasing stress), also called pseudoplasticity. Such a scenario may represent the frictional weakening rheology proposed by Lucas *et al.* [2014], whose simulations were able to accurately reproduce the landslide deposits of a number of terrestrial and extraterrestrial long runout landslides.

It is not my intention to propose a universal mechanism for the reduction of friction in long runout landslides. As I state above, more than one mechanism may be operating during the emplacement of long runout landslides and contributing to the reduction of friction that characterizes such catastrophic events. My focus is to propose a plausible mechanism that could generate the superficial pattern of longitudinal ridges, to produce the scaling relationship between the wavelength of the ridges and the thickness of the deposit, and to generate the internal structures observed (i.e., interaction with no chaotic mixing between different lithologies and the presence of megablocks exhibiting preserved bedding planes). Such mechanism is initiated by vibrations within the slide during its motion. Such vibrations may be responsible of the change in rheology that seems to characterize long runout landslides [Melosh, 1979; Harrison and Grimm, 2003; Lucas *et al.*, 2014]. In fact, the presence of vibrations and the distinct rheology are indicated by evidence of stress fluctuation and a type of deformation by which the brittle landslide moves as a low viscosity material – similarly to a cataclastic flow along faults where at clast level the deformation is brittle but the bulk deformation is a ductile flow. Acoustic energy may well also be responsible for fluidization of the slide, however other mechanisms that simultaneously reduce basal friction cannot be excluded.

8 Conclusions and future work.

This chapter summarizes the outcomes of this thesis. Directions for future work are also presented. These recommendations represent follow-ons of projects that have been already started, parallel to the doctorate work, and new ideas that have originated from the doctorate work.

8.1 Main conclusions.

(1) For the first time in long runout landslides, I report in this thesis on the occurrence of a scaling relationship between the wavelength of longitudinal ridges and the thickness of a landslide deposit. The results of the morphometric analysis that I conducted for 3 case studies (the Coprates Labes landslide on Mars (Chapter 4); the El Magnifico landslide on Earth (Chapter 5); the Tsiolkovskiy crater landslide on the Moon (Chapter 6)), show that the wavelength of the longitudinal ridges is consistently 2 to 3 times the thickness of the deposit. This value is consistent with previous findings in experimental work on rapid granular flows. The significance of the existence of such scaling relationship across different length scales, planetary bodies, and lithologies is important in the light of the debate around the formation mechanism of longitudinal ridges in long runout landslides. Its recurrence clearly suggests a scale- and environment-independent mechanism and that the presence of longitudinal ridges cannot be used to infer environmental conditions or lithology involved during the emplacement of long runout landslides.

(2) In Chapter 4, I propose that the pattern of longitudinal ridges observed in the martian Coprates Labes landslide are imparted by high-speed mechanisms similar to that described in laboratory rapid granular flows, in

which the onset of a mechanical instability within the flow generates helicoidal vortices parallel to the direction of flow. Such mechanism would be expected to give rise to internal structures of the deposit that would reflect a convection-style motion. However, as I discuss in Chapter 5, the observed organization of the internal structures of the El Magnifico landslide does not necessarily support a convective-style motion. As a convection-style mechanism cannot be ruled out nor it can be unequivocally supported, I speculate on an alternative vibration-assisted mechanism that would be able to generate the superficial pattern of longitudinal ridges, to produce the same scaling relationship between the wavelength of the ridges and the thickness of the deposit, and to generate the internal structures observed. The source of the vibration is the release of a high amount of energy that characterizes catastrophic events, such as long runout landslides. Acoustic waves are always expected to be propagating during landslide motion, therefore explaining widespread evidence of heterogeneous stress distribution and stress fluctuation in long runout landslide deposits.

(3) In Chapter 7, I highlight that longitudinal ridges are not exclusive features of unconfined long runout landslides and that they also characterize laterally confined long runout landslides. Therefore, the development of longitudinal ridges in long runout landslides does not depend on the lateral spreading of the sliding mass. However, I point out the role of the lateral spreading in causing the thinning of the slide and the divergence of longitudinal ridges. As the thickness of the slide (T) and the distance between the ridges (S) are governed by the scaling relationship S = 2-3 *T, new ridges appear in between the diverging ridges and so reducing the spacing between them while the landslide deposit thickness decreases (Figure 4-12, Figure 7-7).

8.2 Future work.

In this section four lines for future work are proposed. The first project idea (“Morphometric analysis of longitudinal ridges that characterize supraglacial, volcanic and submarine landslides, and martian double layered ejecta”) originates directly from the results of the morphometric analysis of this

doctoral work and aims to extend the analysis of longitudinal ridges that are present on other landforms. The second research project idea ("Investigating the effect of surface roughness in the formation of longitudinal ridges") aims to better understand the role of surface roughness at field scale given evidence of its fundamental importance at laboratory scale. The third research project ("Friction experiments on anorthosite-bearing rocks and implications for mechanism of long runout landslides on the Moon") is a side project that I have started in parallel to the doctoral work; I here present preliminary results of this ongoing project. The fourth project idea ("Constraining the timing of geological processes in Coprates Chasma using landslide deposits as stratigraphic markers") stems from observations made of long runout landslide in Valles Marineris and their relationship with sedimentary material.

8.2.1 Morphometric analysis of longitudinal ridges that characterize supraglacial, volcanic and submarine landslides, and martian double layered ejecta.

The main conclusion of this thesis is the recurrence of a scaling relationship between the wavelength of longitudinal ridges and the thickness of the deposit for three case studies of long runout landslides (on Mars, Chapter 4; on Earth, Chapter 5; on the Moon, Chapter 6). Given the occurrence of longitudinal ridges in terrestrial landslides emplaced on glaciers and in martian double layered ejecta, two questions instinctively emerge: 1) does the scaling relationship found in this thesis also apply to the wavelength of ridges and thickness of supraglacial landslides and impact crater ejecta? Would such a finding point towards a universal (for these landforms) formation mechanism; 2) or does a different scaling relationship exist for these other landforms? If the latter is true, it would be interesting to check whether each landform has a discriminative scaling relationship.

This project will involve applying the same methods applied to the case studies of this thesis. This should lead to collecting more data points that include landslides developed in different environments (supraglacial,

volcanic, submarine, dry or saturated, extraterrestrial) and with different characteristics (confined of unconfined), and on martian double layered ejecta. The plotting of a larger sample sets of landforms exhibiting longitudinal ridges will help visualizing the existence of one scaling relationship, different scaling relationships, or perhaps a much broader random scatter of points which will argue against the existence of any scaling relationship in natural landforms at all.

8.2.2 Investigating the effect of surface roughness in the formation of longitudinal ridges.

The morphometric analysis of longitudinal ridges in three long runout landslides (on Mars, Chapter 4; on Earth, Chapter 5; on the Moon, Chapter 6) conducted for this thesis has provided first field evidence of the occurrence of the same scaling relationship between the wavelength of the longitudinal ridges and the thickness of the landslide deposit (see discussion in Chapter 7.1). The results support the possibility that longitudinal ridges develop from an instability that emerges from the physics of fast-flowing dry grains [Forterre and Pouliquen, 2001; Borzsonyi *et al.*, 2009].

As surface roughness has been recognized as important condition for the onset of the mechanical instability within rapid granular flows [Forterre and Pouliquen, 2001; 2002], investigation and quantification of the effects of surface roughness on the formation of longitudinal ridges at laboratory-scale in rapid granular flows is important in order to assess its significance at field-scale in natural long runout landslides. Keeping in mind the arguments raised by Campbell *et al.* [1995]; Johnson *et al.* [2016a] against the applicability of the kinetic theory of rapid granular flows to long runout landslides, particular attention should be paid to the possibility that surface roughness, which causes the particle collisions at the laboratory scale, can be interpreted as a source of vibrational energy at field scale. This means that surface roughness would remain an important source of fluctuating motion of the grains at the base of mechanical instability, but, rather than generating collisions between the particles, it generates acoustic waves. In such a scenario, longitudinal

ridges in long runout landslides would not form from via a convection-style motion, as proposed by Magnarini *et al.* [2019] but rather from a vibrated-assisted deformation-style mode (as discussed in Chapter 5.4.3 and Chapter 7.3.2).

In order to investigate the role of surface roughness and stress fluctuations in the onset of instabilities that lead to the formation of longitudinal ridges in long runout landslides, I identify two major objectives, which will be pursued by combining laboratory-scale analogue modelling and state-of-the-art photogrammetry techniques (Figure 8-1).

Analogue modelling - Experimental work using granular material along an inclined plane. The novelty in the technique lies in using 3D printed surfaces that have different degrees of roughness. Compared to the traditional method of gluing particles over the surface, 3D printed surfaces will be easily interchangeable on the surface setting and will allow reliable reproducibility of the experiments.

Photogrammetry – In order to conduct detailed morphometric analysis of the wavelength of ridges and flow thickness, stereo-image pairs will be obtained so as to make digital elevation models of the surface, as done in remote sensing studies.

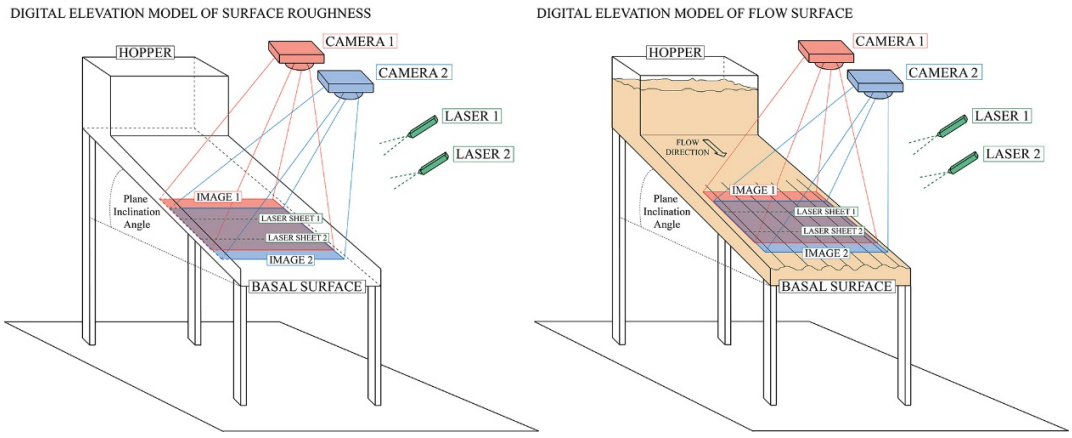

Figure 8-1 – Experimental setting to investigate the effect of surface roughness in the formation of longitudinal ridges. A continuous recycling system will be used, not a fixed volume hopper.

8.2.3 Friction experiments on anorthosite-bearing rocks and implications for mechanism of long runout landslides on the Moon.

Evidence for the presence of a long runout landslide at the Apollo 17 landing site (Light Mantle landslide, Chapter 6) has important implications for the mechanisms of reduction of friction on planetary bodies in the absence of an atmosphere and water availability. Dry granular fluidization involving interaction between regolith particles has been considered the most likely process during emplacement of the Apollo 17 landslide [Howard, 1973], as well as for other lunar mass-wasting landforms discovered in recent years thanks to new high-resolution imagery [Senthil Kumar *et al.*, 2013; Kokelaar *et al.*, 2017]. Following field work activity in Taurus-Littrow Valley and sample analysis, astronaut geologist Harrison H. Schmitt has speculated that gas fluidization is the principal mechanism involved in the emplacement of the Apollo 17 landslide [Schmitt *et al.*, 2017]. Fluidization of lunar regolith could be a consequence of solar wind volatiles release by agitation of the granular material during the flow. Contribution to the fluidization of the landslide could also derive from some other friction-weakening mechanisms. However, both hypotheses are lacking theoretical and experimental support.

In recent years, experimental work has been used to investigate emplacement mechanisms of long runout landslides [Mitchell *et al.*, 2015; Hu *et al.*, 2018], inspired by the experimental work conducted in the field of fault mechanics. Rotary shear apparatuses have been designed to achieve large slip rates and displacements typical of earthquakes and they have shown that a dramatic drop of friction occurs at seismic velocities (>0.1 ms^{-1}), independent of the rock type and independent of the weakening mechanism involved [e.g., Di Toro *et al.*, 2004; Di Toro *et al.*, 2011 and references within; Violay *et al.*, 2014].

High-speed friction experiments using the rotary shear apparatus SHIVA (Slow to HIgh-Velocity rotary shear Apparatus) at the Istituto Nazionale di Geofisica e Vulcanologia (INGV) in Rome, Italy [Di Toro *et al.*, 2010], have been performed to study the role of thermal decomposition of carbonates

during the emplacement of the catastrophic Heart Mountain landslide, Wyoming, USA [Mitchell *et al.*, 2015], for which only theoretical calculations were available [Goren *et al.*, 2010]. The microstructures obtained during these experiments compared favourably with the theoretical calculations and field-scale observations.

Following the success of experimental work by Mitchell *et al.* [2015], friction experiments with rotary-shear apparatus SHIVA (Figure 8-2) can be performed in order to determine the viability dynamic weakening mechanisms in anorthosites-bearing rocks that could explain the exceptional runout of the Light Mantle landslide and the Tsiolkovskiy Crater landslide. Here, I present the preliminary work that has been done and the initial results.

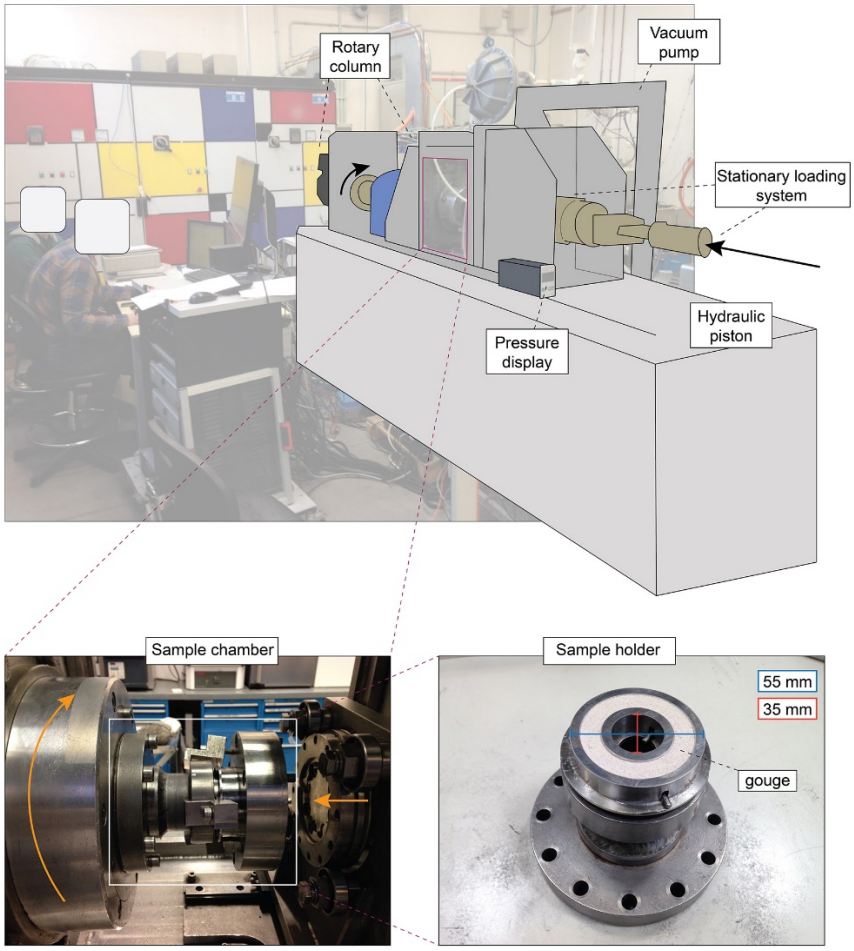

Figure 8-2 – Rotary-shear apparatus SHIVA. Top figure shows a schematic of the rotary-shear apparatus at the INGV in Rome. The bottom annotated images show the sample chamber and the sample holder.

I used Proterozoic anorthosites of the Scandinavian Shield, provided by the European Space Agency Sample Analogue Curation Facility (ESA SAFC). These Proterozoic anorthosites are used as analogue of the lunar highlands (Figure 8-3a). I visited the INGV laboratory in Rome in 2019 and I was assisted by Early Career Researcher Stefano Aretusini. Powders were prepared by crushing and sieving (< 250 μm, Figure 8-3b) the anorthosites-bearing rock, using the facility at the Universita' La Sapienza di Roma and helped by Pier Carlo Giacomel. Cores were prepared at the INGV (Figure 8-3c).

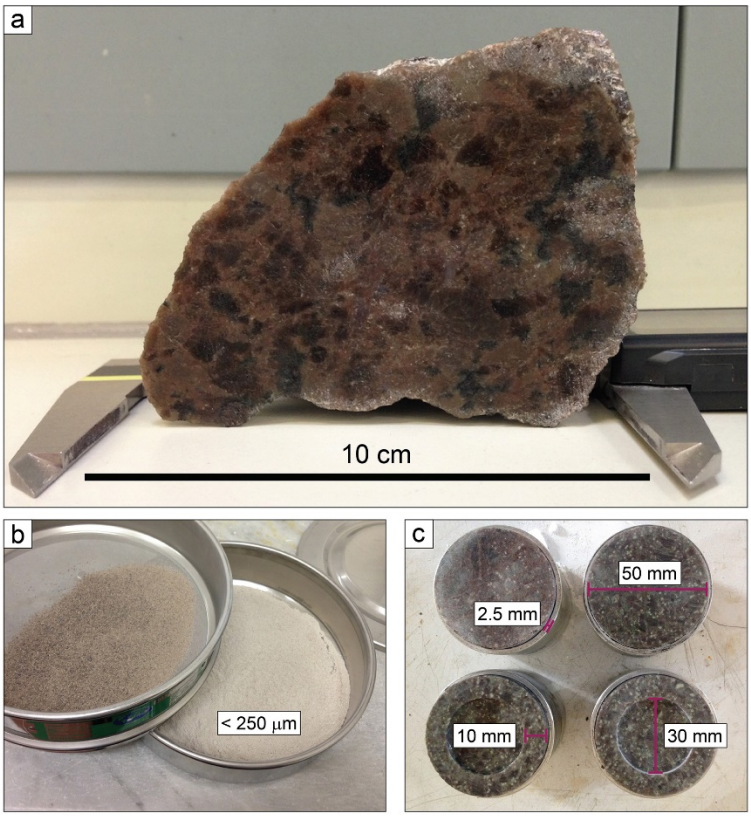

Figure 8-3 – Anothosite-bearing lunar rock analogue. a) Example of the anorthosite-bearing rock provided by the European Space Agency Sample Analogue Curation Facility (ESA SAFC). From this rock, I have obtained gouges (b) and cores (c) to conduct friction experiments.

Powder samples were sheared simulating the landslide runout with a single slip pulse at constant slip rate of 1 m s^{-1} for up to 5 m displacement with a constant acceleration of 0.8 m s^{-2}. Experiments were performed at a constant normal stresses of 2 MPa, 5 MPa and 10 MPa, and both at room humidity

and in high vacuum (< $5e^{-4}$ mbar) to simulate the absence of a lunar atmosphere (Table 8-1; Figure 8-4). The experimental parameters were chosen so to simulate sliding conditions of material along a surface inclined with an angle of 30° (slightly steeper than the current slope of the South Massif at Taurus-Littrow valley, where the Light Mantle avalanche developed) with an acceleration of 1.6 m s^{-2}, which corresponds to the lunar gravity acceleration (i.e., g_{Moon} * sin(30°) = 0.8 m s^{-2}); the normal stresses applied would correspond to different thickness of a slide constituted of material with a density of 2500 kg m^{-3} (anorthosite density varies between 2200 kg m^{-3} and 2600 kg m^{-3}), moving with lunar gravity acceleration (2MPa = 500 m; 5MPa = 1250 m; 10 MPa = 2500 m).

Table 8-1 - List of experiments conducted on anorthosite-bearing gouges. The asterisk marks successful experiment.

Experiment Code	Sample Weight (g)	Acceleration (ms^{-2})	Peak Velocity (ms^{-1})	Slip (m)	Normal Stress (MPa)	Pressure (mbar)
s1668*	6	0.8	1	5	2	High Vacuum
s1669*	6.15	0.8	1	5	5	High Vacuum
s1669_2	3	0.8	1	0.5	17.5	Room Humidity
s1670*	6.08	0.8	1	2	10	High Vacuum
s1671*	6.06	0.8	1	5	5	Room Humidity
s1672	6.04	0.8	1	5	2	Room Humidity
s1673*	6.06	0.8	1	2	10	Room Humidity
s1674*	6.08	0.8	1	5	2	Room Humidity

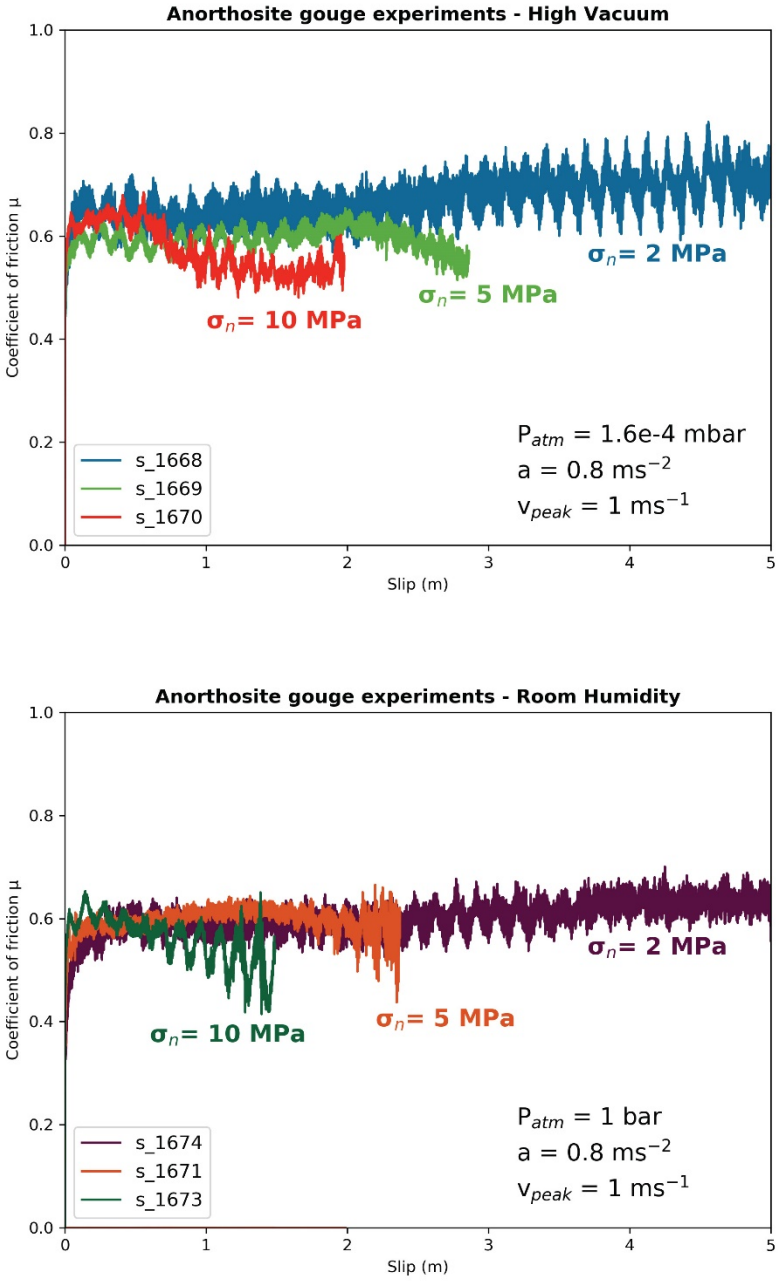

Figure 8-4 – Results of the experiments on gouges.

XRD analysis of the sample gouges (original gouge and post-experiment gouges) have been conducted by Professor Ian Wood in the Department of Earth Science at University College London (Figure 8-5).

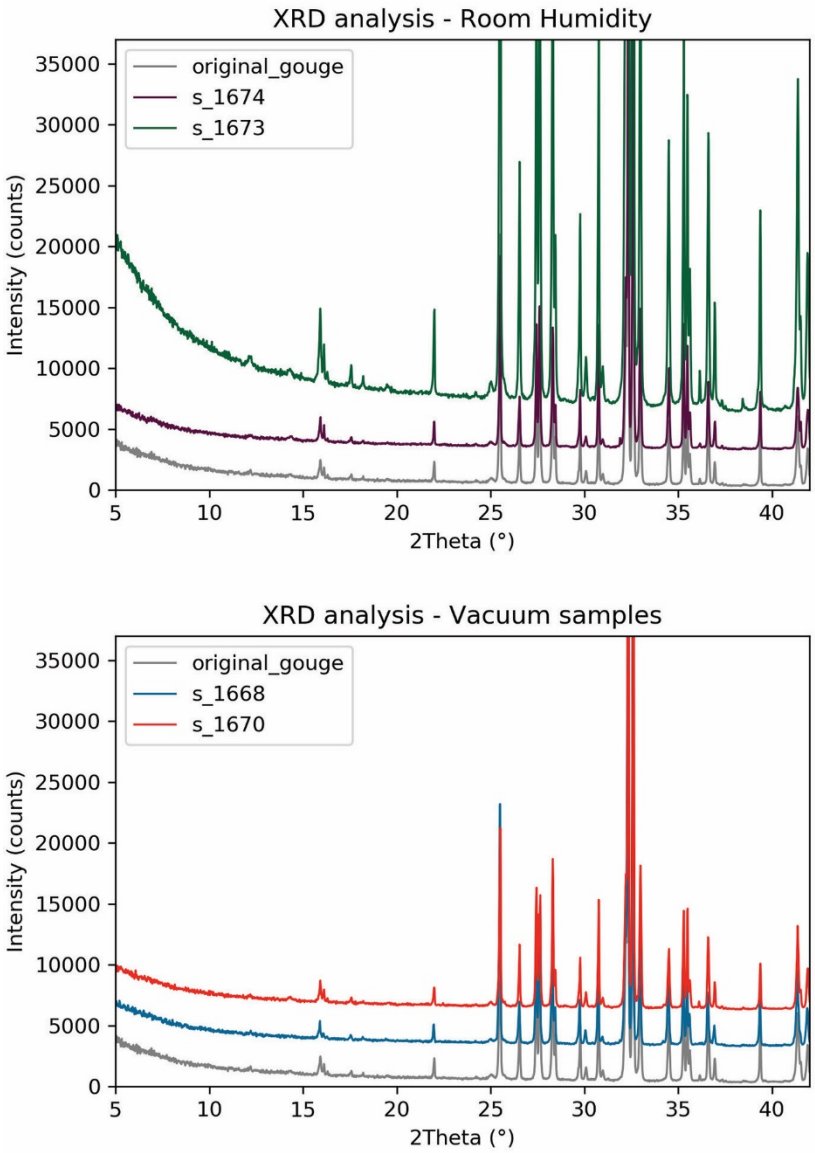

Figure 8-5 – Results of the XRD analysis on gouge samples.

These preliminary data show no significant weakening of the anorthosite-bearing material. A reduction in friction of 0.1-0.2 occurs at the highest normal stress experiments, both at room humidity and vacuum conditions. XRD analysis shows no evidence of any new phases. Microstructure analysis will be conducted of the thin section of the sheared gouges. These preliminary results show that the material is strong and no dynamic weakening is seen at conditions where it is seen for many other rock compositions [e.g., Di Toro *et al.*, 2011 and references within]. Perhaps the material favours other

weakening mechanisms. Further experiments on gouges and cores at higher normal stresses will be conducted to search for evidence of weakening.

8.2.4 Constraining the timing of geological processes in Coprates Chasma using landslide deposits as stratigraphic markers.

Coprates Chasma, in the Valles Marineris subequatorial canyon system on Mars, is the region where the Coprates Labes landslide case study (Chapter 4) is located. To the west, it is connected with Melas Chasma, a region that shows evidence of fluvial and lacustrine activity [e.g., Williams and Weitz, 2014; Davis *et al.*, 2018]. To the east, it is connected to the chaotic terrains and the Chryse outflow channels system, which are thought to have been carved by catastrophic floods that may have originated from Valles Marineris [Warner *et al.*, 2013]. It has been suggested that Coprates Chasma may have hosted a standing body of water [e.g., Lucchitta, 2010; Andrews-Hanna, 2012b]. Therefore, Coprates Chasma represents an interesting region in which studying water provenance, the relation that the chasmata has with adjacent regions which record aqueous activity, and whether it has ever been a conduit for the fluids discharged into the outflow channels (Figure 8-6).

Coprates Chasma shows geomorphological evidence for diverse geological processes throughout its history – e.g., tectonic and sedimentary terraces [e.g., Andrews-Hanna, 2012a]; dykes [Brustel *et al.*, 2017] and mud volcanoes [Okubo, 2016; Brož *et al.*, 2017]; layered deposits [e.g., Catling *et al.*, 2006; Noel *et al.*, 2015; Weitz *et al.*, 2015] and alluvial fans [Grindrod *et al.*, 2012]; and sand dunes [Boazman *et al.*, 2021]. Tens of landslide deposits are present in Coprates Chasma, of which some have been partially buried by sediments and others have been exhumed (Figure 7-4; Figure 8-6c). Landslide deposits can be used as stratigraphic markers in order to constrain the timing of other geomorphological elements and related geological processes. Core tasks in this project will be dating landslide deposits, updating the current ages provided in Quantin *et al.* [2004b], geological and geomorphological mapping of structures and landforms using high resolution digital elevation models, analysis of spectral data from CRISM instrument to

search for indications of hydrous minerals, as done by Watkins *et al.* [2015; 2020].

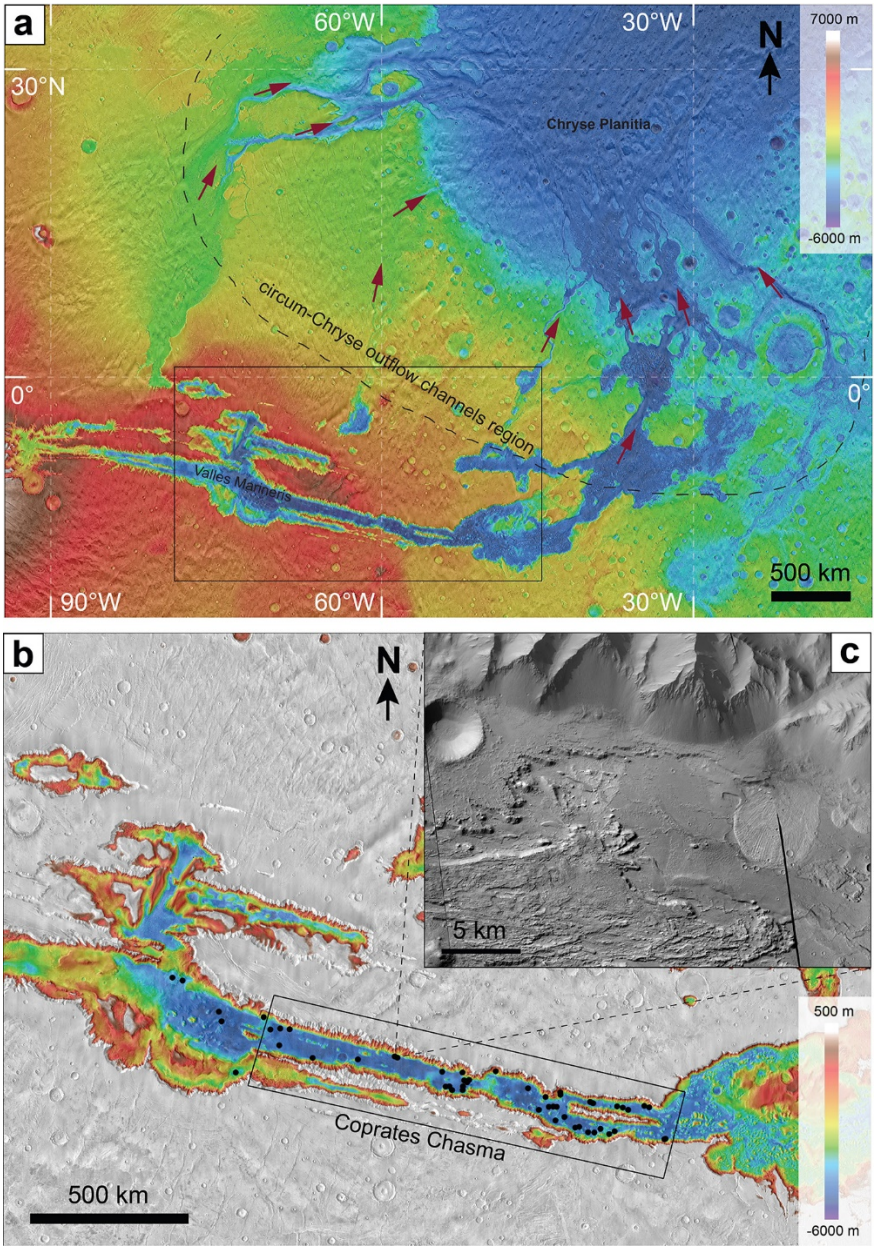

Figure 8-6 – Regional context of Valles Marineris and the circum-Chryse outflow channels. a) and b) Regional context in which Coprates Chasma are located; MOLA Global elevation data over THEMIS-VIS (Visual Imager) image mosaic; black dots in (b) mark the locations of long runout landslides in Melas Chasma and in Coprates Chasma. c) CTX images showing buried and exhumed long runout landslides in Coprates Chasma (see also Figure 7-4).

Appendix I – List of long runout landslides in the Solar System.

Appendix Table 1 - List of long runout landslides in the Solar System for which measurements of their vertical drop (H), horizontal runout (L), and volume are found in the literature. These data are used to create the plot in Figure 2-4 that shows the increase in mobility of long runout landslides with increasing volume.

Planetary Body	H	L	H/L ratio	Volume (km^3)	Reference
Earth	1.22	9	0.135	0.28	The Blackhawk landslide [Shreve, 1968a]
	1.9	7.6	0.25	0.38	San Martinez Grande landslide [Bock, 1977]
	1.21	19	0.064	44	The Saidmarreh landslide [Harrison and Falcon, 1938; Watson and Wright, 1969; Roberts and Evans, 2013]
	0.18	1	0.18	0.006	The Oso landslide [Iverson *et al.*, 2015]
	0.6	2.4	0.25	0.01	The Elm landslide [Buss and Heim, 1881; Heim, 1882]
	0.75	2.7	0.27	0.036	The Frank landslide [Cruden and Hungr, 1986; Jones, 1993]
	0.8	4	0.2	0.08	The El Magnifico landslide [Mather *et al.*, 2014; Crosta *et al.*, 2017]
	0.6	5	0.12	0.03	The Sherman glacier landslide [Shreve, 1966; Marangunic and Bull, 1968]
	0.2	1.6	0.2	0.03	Sale Mountain landslide [Zhang *et al.*, 2002]
Mars	7		0.059	17880	[Mcewen, 1989]
	7		0.1	4880	
	8.4		0.102	4183	
	6.8		0.072	4047	
	7.2		0.095	3267	
	8		0.125	2960	
	6.8		0.108	2761	
	8.2		0.13	1282	

Planetary Body	H	L	H/L ratio	Volume (km^3)	Reference
	5.4		0.096	833	
	3.6		0.08	688	
	4.4		0.142	668	
	7.6		0.141	655	
	5.4		0.15	321	
	2.8		0.085	157	
	3.6		0.124	32	
	4		0.2	29	
	2		0.111	14	
	1.2		0.15	11	
	6.4		0.305	5.5	
	6.2		0.31	5.3	
	6.2		0.326	4.3	
	5		0.313	3.3	
	6.2		0.365	1.4	
	2.2		0.314	0.9	
	2.2		0.367	0.3	
	4.2		0.56	0.1	
	6.9	12.4	0.554	550.79	[Quantin *et al.*, 2004a]
	6.4	25.3	0.254	155.51	
	6.4	22.7	0.283	100.49	
	8.5	83	0.103	397.25	
	8	66.3	0.12	9081.83	
	7.9	62.74	0.126	1646.10	
	6.1	51.38	0.118	2420.79	
	6.7	12.7	0.529	391.07	
	9.3	69.01	0.135	637.77	
	8	61.2	0.13	1583.46	
	8	48	0.166	910.12	
	5.6	53.54	0.105	698.72	
	5.5	38.5	0.142	851.59	
	5	63.83	0.078	1003.39	
	4	29.95	0.133	316.23	
	5.2	32.47	0.16	179.2	
	2.5	20	0.124	15.98	
	6.2	24.5	0.2	63.5	[Brunetti *et al.*, 2014]
	6.2	25.1	0.2	210.3	
	5.5	22.5	0.2	72.2	
	0.6	1.8	0.3	0.1	
	4.3	14.2	0.3	77.1	

Planetary Body	H	L	H/L ratio	Volume (km^3)	Reference
	4.3	19.2	0.2	4.6	
	5.5	21.4	0.3	217.1	
	1	4.4	0.2	0.8	
	1.8	5.5	0.3	0.6	
	3.2	10.8	0.3	17.4	
	4.6	20.1	52.4	0.2	
	2.5	14.1	0.2	1.6	
	5.6		0.14	833	[Lucas *et al.*, 2014]
	4.4		0.15	1500	
	4.4		0.08	730	
	5.8		0.12	2600	
	3.29		0.1	530	
	0.5		0.13	19	
	0.75		0.14	9.95	
	0.32		0.4	0.165	
	0.4		0.07	31.9	
Ceres			0.297	1.9	[Chilton *et al.*, 2019]
			0.159	97.5	
			0.258	13.01	
			0.415	4.1	
			0.245	11.2	
			0.305	0.6	
			0.194	29.8	
			0.189	67.2	
			0.13	19.8	
			0.172	2.8	
			0.207	1.2	
			0.094	6.1	
			0.289	0.7	
			0.147	3.61	
			0.305	4.2	
			0.204	13.3	
			0.228	22.1	
			0.314	2.11	
			0.228	69.07	
			0.124	173.82	
			0.234	7.37	
			0.086	25.46	
			0.188	4.3	
			0.208	5	

Planetary Body	H	L	H/L ratio	Volume (km^3)	Reference
Iapetus	9.5	80	0.119	1600	[Singer *et al.*, 2012]
	8	60	0.133	3000	
	7-9	55-75	0.119	12400	
	6	50	0.123	24000	[Lucas *et al.*, 2014]
Io	6	71	0.085	25000	[Lucas *et al.*, 2014]

Appendix II – List of Ground Control Points used at the El Magnifico landslide.

Appendix Table 2 - List of Ground Control Points (GCPs) used to georeference drone-derived digital elevation models. Locations of GCPs are shown in Figure 5-4.

Name ID	Latitude	Longitude	Grid Zone	Easting	Northing	Altitude (m)
GCP1	20º 27' 10.3260" S	70º 08' 41.7315" W	19K	380575	7737986	66.068
GCP2	20º 27' 11.1127" S	70º 08' 45.7404" W	19K	380459	7737961	71.386
GCP3	20º 27' 17.7846" S	70º 08' 54.9696" W	19K	380193	7737754	69.481
GCP4	20º 27' 27.5261" S	70º 09' 02.3238" W	19K	379982	7737453	78.366
GCP5	20º 27' 30.0692" S	70º 09' 01.4109" W	19K	380009	7737375	78.146
GCP6	20º 27' 41.1022" S	70º 08' 50.5184" W	19K	380327	7737038	51.862
GCP7	20º 27' 45.5253" S	70º 09' 00.4217" W	19K	380041	7736900	77.414
GCP8	20º 27' 30.6623" S	70º 08' 45.4713" W	19K	380471	7737360	57.792
GCP9	20º 27' 18.5647" S	70º 08' 40.2396" W	19K	380620	7737733	55.155
GCP10	20º 27' 48.5090" S	70º 08' 42.0145" W	19K	380575	7736812	59.44
GCP11	20º 27' 28.1983" S	70º 08' 34.3751" W	19K	380792	7737438	54.788
GCP12	20º 27' 37.0776" S	70º 08' 34.4063" W	19K	380793	7737165	60.352
GCP13	20º 27' 13.0662" S	70º 08' 30.6051" W	19K	380898	7737904	58.748
GCP14	20º 27' 14.7146" S	70º 08' 27.2353" W	19K	380996	7737854	60.634
GCP15	20º 27' 24.9899" S	70º 08' 27.6563" W	19K	380986	7737538	57.608
GCP16	20º 27' 28.4871" S	70º 08' 25.0593" W	19K	381062	7737431	58.11
GCP17	20º 27' 38.9129" S	70º 08' 22.3753" W	19K	381142	7737111	102.349
GCP18	20º 27' 15.2138" S	70º 08' 10.6052" W	19K	381478	7737842	92.502
GCP19	20º 27' 48.4800" S	70º 06' 51.3338" W	19K	383782	7736835	804.74
GCP20	20º 27' 35.3179" S	70º 06' 49.6513" W	19K	383828	7737240	795.492
GCP21	20º 27' 30.0692" S	70º 09' 01.4109" W	19K	380575	7737986	66.068

Appendix III – More drone-derived digital elevation models of the El Magnifico landslide.

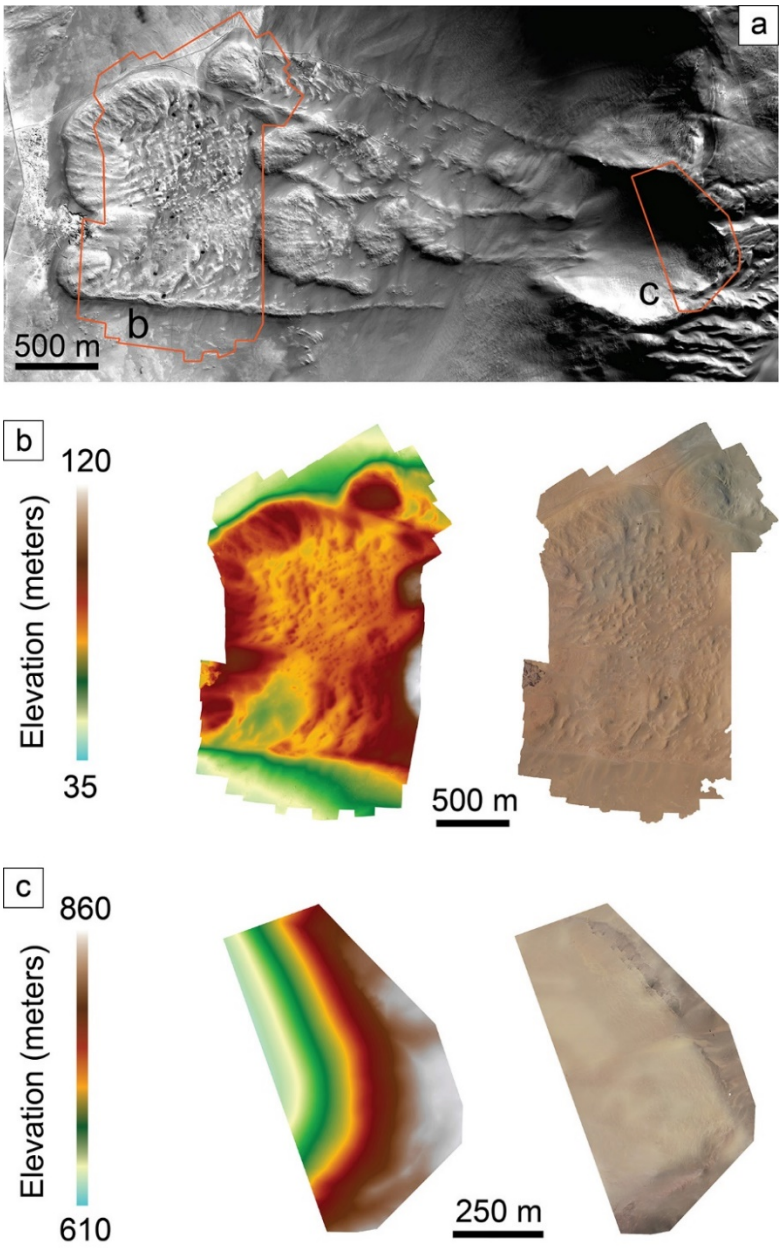

Appendix Figure 1 – Drone-derived digital elevation models of parts of the El Magnifico landslide not used for the morphometric analysis of longitudinal ridges. a) Coloured polygons mark the areas covered by the two drone-derived digital elevation models. b) Drone-derived digital elevation model of the hummocky region of the lobe 1 and 2. c) Drone-derived digital elevation model of part of the head scarp.

Appendix IV – Python scripts to automate morphometric analysis.

Here I attach the Python scripts I wrote in order to automate some tasks of the morphometric analysis of longitudinal ridges.

Script n°1: This calculates the spacing of the ridges, the thickness of the landslide deposit, and their ratio, along a topographic profile. Figure 3-4 shows the passage of Part 1 of this script.

```
"""This script consists of 3 parts: first it calculates the
average thickness, second it calculates the average spacing,
and third it calculates the S/T ratio."""


# ----------------------1st PART----------------------------#

import numpy as np

# Importing Deposit Profile and Floor Profile form text
files. These text files are generated in ArcGIS. Elevation
data are exported as text files.
# Calculate the average thickness along a profile.
# Remember to cancel out the header (if present) otherwise
there will be a conflict for the number of columns.

Floor = np.genfromtxt("File_directory\File_name.txt", dtype =
None)
deposit = np.genfromtxt("File_directory\File_name.txt ",
dtype = None)


# Calculate the length of the deposit profile. There is a
discrepancy between the points of both profiles because of
resolution.
```

```
d = len(deposit)
f = len(floor)


# Create an empty array that it will be filled with "new"
topographic values so to match the points with the shorter
array of the floor.

avg_topo = []


# Loop with 2 counters to deal with two arrays with different
length.
# When the deposit element > floor element take the average
of the two points, closest before and closest after.
# Be careful to INDEX. Some .txt files have 3 column, others
only 2. This creates conflict in the loop and gives wrong
result (check the exported topography data text file!!!).
c = 0

for i in range(d):
    if deposit[i][0] > floor[c][0]:
        h = (deposit[i][1] + deposit[i-1][1])/2
        avg_topo.append(h)
        c += 1
        if c == f:
            break


# Calculate the thickness relative to each point (between
avg_topo and floor).

avg_h = 0
h_points = []

for i in range(len(avg_topo)):
    avg_h += avg_topo[i] - floor[i][1]
    h_points.append(avg_topo[i] - floor[i][1])

avg_thickness = avg_h/len(avg_topo)

print(avg_thickness)



# ---------------------2nd PART-----------------------------#

"""Script that creates a point shapefile where the ridges
intersect the profile. It calculates the spacing between the
ridges as measured along the profile. It gives the average
spacing."""

# Import system modules

import arcpy
from arcpy import env
```

```
# Set environment settings

env.workspace = "Workspace_directory"


# Intersecting
inFeatures = ["ProfileD", "Ridges"] #--> Name of input
shapefiles #
output_Intersect = "Enter_Name_of_output_shapefile"
arcpy.Intersect_analysis(["ProfileD.shp", "Ridges.shp"],
output_Intersect, "", "", "point")


# Counting
count = arcpy.GetCount_management("Intersect_ProfileD.shp")

# Split the profile line where ridges intersect
arcpy.SplitLineAtPoint_management("ProfileD.shp",
"Intersect_ProfileD.shp", "splitline_ProfileD.shp", "1000
Meters")


# Creates new field "Length"
arcpy.AddField_management("splitline_ProfileD.shp", "Length",
"DOUBLE")


# Calculate the length of the line --> This part failed to
work! So I had to manually measure the distance between
ridges.
arcpy.CalculateField_management("splitline_ProfileD.shp",
"Length", "!shape.length@meters!", "PYTHON_9.3")


# Get the length value from the "Length" field and add it to
the LineLength list.
lineLength = []
searchField = arcpy.SearchCursor("splitline_ProfileD.shp")
for row in searchField:
    lineLength.append(row.getValue("Length"))


# Sum the spacing between the ridges and calculate the
average.
total_length = 0

for i in range(1, len(lineLength)):
    total_length += lineLength[i]

avg_spacing = total_length/len(lineLength)

print(avg_spacing)
```

```
# Creates text file that has ID, spacing, and cumulative
spacing that will be use in the script that generates the
plots.
# Remember to manually add the elevation values to the file.
They are extracted from the ArcGIS project.

text = open("File_Directory\File_Name.txt", "w") #--> It
creates a new text file with the name given here.

for s in range(len(lineLength)-2):
    text.write( str(s) + " " + str(lineLength[s+2]) + " \n")

text.close()



# -----------------3rd PART----------------------------------#

ST_ratio = avg_spacing/avg_thickness

print(ST_ratio)
```

Appendix V – Published paper.

nature COMMUNICATIONS

ARTICLE

https://doi.org/10.1038/s41467-019-12734-0 OPEN

Longitudinal ridges imparted by high-speed granular flow mechanisms in martian landslides

Giulia Magnarini [1]*, Thomas M. Mitchell [1], Peter M. Grindrod [2], Liran Goren [3] & Harrison H. Schmitt[4]

The presence of longitudinal ridges documented in long runout landslides across our solar system is commonly associated with the existence of a basal layer of ice. However, their development, the link between their occurrence and the emplacement mechanisms of long runout landslides, and the necessity of a basal ice layer remain poorly understood. Here, we analyse the morphometry of longitudinal ridges of a martian landslide and show that the wavelength of the ridges is 2–3 times the average thickness of the landslide deposit, a unique scaling relationship previously reported in ice-free rapid granular flow experiments. We recognize en-echelon features that we interpret as kinematic indicators, congruent with experimentally-measured transverse velocity gradient. We suggest that longitudinal ridges should not be considered as unequivocal evidence for presence of ice, rather as inevitable features of rapid granular sliding material, that originate from a mechanical instability once a kinematic threshold is surpassed.

[1] Department of Earth Sciences, University College London, London, UK. [2] Natural History Museum, London, UK. [3] Department of Geological and Environmental Sciences, Ben Gurion University of Negev, Beer-Sheva, Israel. [4] Department of Engineering Physics, University of Wisconsin Madison, Madison, WI, USA. *email: giulia.magnarini.14@ucl.ac.uk

Distinctive longitudinal raised ridges are common in large-scale mass movements across the surfaces of planetary bodies, but their formation mechanism is poorly understood. These longitudinal ridges have been identified in impact ejecta on every planetary surface with sufficient image resolution[1], but are best documented in long-runout landslides[2–4]. The emplacement dynamics of long-runout landslides is a subject of ongoing debate[2,5–9], and various mechanisms have been proposed for the reduction of basal friction, which appears to be a condition necessary for controlling the ability of long-runout landslides to travel even more than ten times their vertical drop over nearly flat surfaces[2,5,8,10].

Longitudinal ridges and furrows are seen ubiquitously on the surface of long-runout landslides on Mars. On Earth, such features are commonly found in landslides emplaced on glaciers, amongst which is the iconic Sherman Glacier landslide[11]. Consequently, their morphological similarity to those observed in martian landslides has been used as an analogy to infer the presence of an icy substrate at the time of landslide emplacement[12,13] on Mars. It has been proposed that presence of ice on the surface reduces the frictional coefficient, permitting the splitting of the deposit as a consequence of either lateral spreading[13] or the dominant role of inertia over lateral spreading forces[12], leading to the formation of ridges and troughs perpendicular to the spreading direction. The presence of ice is also suggested to explain the development of longitudinal grooves in martian double-layered ejecta craters[14], which also show morphological similarity to the longitudinal ridges associated with landslides, although other mechanisms are not excluded[1,15]. However, longitudinal ridges have been observed also in landslides on the Moon[16–18], which is considered to be free of ice throughout its geological history.

Borzsonyi et al.[19] suggested the possibility that longitudinal ridges and furrows of large planetary rock avalanches may be related to fluid-like instabilities forming convection cells that result in longitudinal stripes parallel to the flow direction. This was based on previous experimental and theoretical work[20,21] demonstrating turbulent flow processes that are well known to occur in fluid mechanics. The experimental work and stability analysis on rapid granular flows conducted by Forterre and Pouliquen[20,21] showed for the first time the spontaneous formation of longitudinal vortices that manifest as superficial longitudinal ridges and furrows, which initiation depends on the velocity of the flow, roughness of the basal surface, and the consequent strong shear at the base of the flow. Importantly, Forterre and Pouliquen[20] demonstrated a clear morphological scaling relationship in that the wavelength of the ridges scales with the thickness of the flow by a factor of ~2–3 and that the pattern drifts in the transverse direction. Further experiments and numerical modelling by Borzsonyi et al.[19] confirmed that the longitudinal pattern naturally arises from mechanical instabilities within rapid granular flows. While demonstrated experimentally, such scaling relationship have yet to be demonstrated in any planetary landslide.

Here, we use state-of-the-art Mars Reconnaissance Orbiter imagery (CTX[22] and HiRISE[23] cameras) in order to analyse a giant martian landslide with some of the best defined longitudinal ridges (Fig. 1) for comparison with the longitudinal morphologies obtained during granular experimental slides, so to investigate the possibility that the same instability may be responsible for the longitudinal ridges and furrows of large planetary rock avalanches, as suggested by Borzsonyi et al.[19]. We find similar scaling relationship between the wavelength of longitudinal ridges and the thickness of the deposit as seen in the martian landslide and in experiments of self-forming ice-free ridges. We infer that the emplacement velocity of the martian landslide could have been as high as tens to hundreds of m/s. On the basis of these results, we suggest that longitudinal ridges that characterise long-runout terrestrial and planetary landslides may be the expression of an instability that emerges within the flowing mass, as observed in laboratory experiments on rapid granular flows[20].

Results

Ridges morphometry with distance and with deposit thickness. We identified longitudinal ridges on the surface of the landslide deposit. We chose the two areas with the best exposed ridges to conduct our analysis (Fig. 1c, d) and traced profiles transversal to the flow direction to study how ridges evolve with distance. We measured the spacing between the ridges and calculated their density (number of ridges/profile length) in each profile (see the Methods section). Within both areas, from the proximal to distal edge, we found that ridges diverge while their number increases and their amplitude and wavelength decrease (Fig. 2a). At each profile, we also assessed the average spacing between the ridges (S) and the local average thickness of the deposit (T) and calculated the S/T ratio, as done by Forterre and Pouliquen[20] (Supplementary Tables 1 and 2). The central area (Fig. 1c and blue in Fig. 2) shows an almost constant S/T ratio, between 2.55 and 2.99. The east area (Fig. 1d and yellow in Fig. 2) shows lower values, yet, still with small variability that ranges between 1.44 and 2.4.

Our results suggest a scaling relationship between the wavelength of ridges and the average thickness of the landslide deposit. We compare the S/T ratio obtained from our morphometric analysis with the results obtained by Forterre and Pouliquen[20]. In particular, the values of the S/T ratio obtained in the central area (Fig. 2b) are in agreement with the value of ~2–3 found by Forterre and Pouliquen[21]. In the east area (Fig. 2b), profiles P3, P4 and P5 show S/T ratio below 2, which is a consequence of a localised increase in the deposit thickness (Supplementary Table 2). We observed the appearance of new ridges between diverging ridges (Fig. 3a–d), confirming that the number of ridges increases with distance, as found from the morphometric analysis (Supplementary Tables 2 and 3). This is also consistent with the observations of Forterre and Pouliquen[21] of transversal vortex drifting accompanied by annihilation and creation of ridges. Divergence of ridges is also observed in martian double-layered ejecta craters[1,24].

Kinematic indicator features and flow structure models. We also identified s-shaped en-echelon features superposed on longitudinal ridges that we interpret as kinetic indicators (Fig. 3e–h). Laboratory experiments have shown the existence of a velocity gradient between ridges and furrows: for very rapid flows (dilute regime), furrows move faster than ridges[19,20], whereas for less rapid flows (dense regime), the ridges are the faster-flowing region[19]. In both regimes, the faster-flowing regions are denser, i.e., their solid fraction is greater than the slower-flowing features. As a consequence, when the flow ceases, inversion of topography is expected in the dilute regime. Here, the ridges, being less dense, are expected to deflate and sink. The ridges become furrows, and the fast-flowing dense furrows become ridges. The en-echelon features that we report in Fig. 3 pointing at faster-flowing ridges is therefore consistent with both the dense regime and with the dilute regime after topography inversion (Fig. 4).

Discussion

A self-lubrication mechanism for long-runout landslides has been proposed by Campbell[25] suggesting that a dilute layer of highly

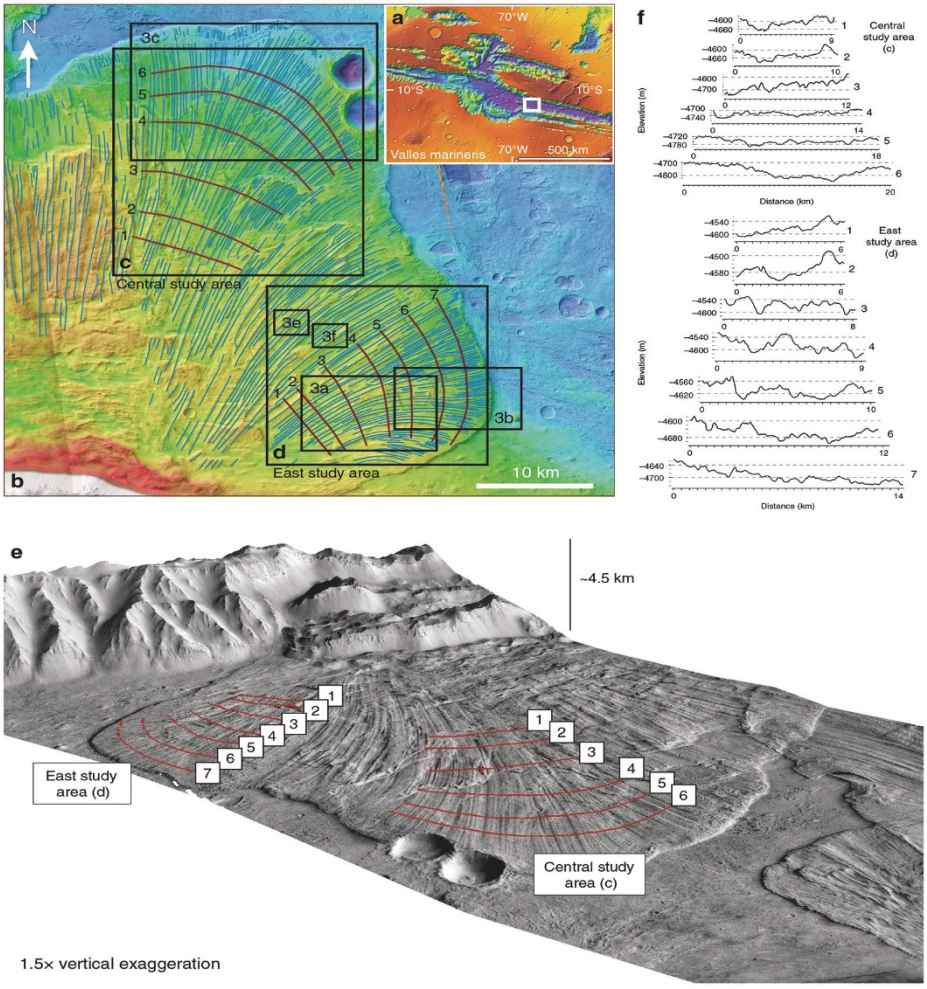

Fig. 1 Area of the study. **a** Valles Marineris, Mars, showing the location of the landslide that we study here in Coprates Chasma (white box). **b** CTX Stereo-derived DEMs. **c**, **d** Study areas within which morphological and morphometric characterisation is conducted; burgundy lines: topographic profiles, numbered from proximal to distal edge of the landslide deposit; blue lines: longitudinal ridges. (3a), (3b), (3c), (3e), (3f): locations of close-up images shown in Fig. 3. **e** Oblique view of the landslide object of the study. Red lines represent topographic profiles, numbered from proximal to distal area (following flow direction). **f** Topographic profiles of the landslide deposit of the east and central areas of the study

agitated particles at the bottom of the flow can explain the apparent low coefficient of friction in long-runout landslides and that such a layer should form naturally in rapid granular flows. As the formation of longitudinal vortices also seems to be a natural development of rapid granular flows that involves a low-density layer at the bottom of the flow[19–21], it is not unreasonable to suggest that longitudinal ridges and furrows are inevitable features that originate from a mechanical instability once certain threshold conditions within a flow moving over a rough surface are passed.

The mechanism responsible for the formation of longitudinal vortices proposed by Forterre & Pouliquen[20] relies on the inversion of the density profile, with denser granular packing closer to the top of the slide, and on a continuous energy supply to the system, in the form of shear forces, so to maintain the collisional regime and, therefore, to prevent the granular temperature to decay rapidly due to the inelastic nature of particle collisions[25]. The instability derives from the inversion of density profile, due to an increase of granular temperature[26,27] at the base of the flow by collision and shear between particles and the rough

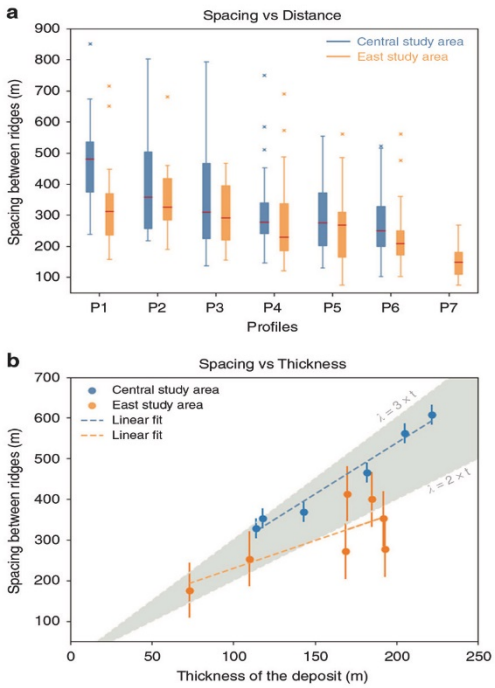

Fig. 2 Variation of the spacing between longitudinal ridges with the distance and with the thickness of the deposit. Panel **a** shows how the spacing between longitudinal ridges varies with distance (from the proximal to distal areas of the deposit); boxes represent the 'interquartile range', red segments within boxes show the median value, whiskers above and below boxes show the locations of the maximum and minimum, symbols 'x' represent values above three times the interquartile range. Panel **b** shows the relationship between the spacing of the ridges and the thickness of the deposit; the grey band shows the experimentally predicted range for the scaling relationship between the spacing between the ridges and the thickness of the deposit[20]

substrate. Such particle interactions may well contribute to acoustic fluidisation[28] processes within the landslide that would lead to the dynamic reduction of viscosity and explain the long-runout distance. Several other dynamic weakening mechanisms have also been proposed to explain long run-outs, such as flash heating[3], frictional melting[29], and thermal decomposition[30–33] (and subsequent thermal pressurisation). Such mechanisms rely on the generation of heat at the base of the landslide, which would contribute to the energy supply at the base of the system.

From the results of our morphometric analysis of longitudinal ridges in a giant martian landslide appears the similarity of the scaling relationship between the wavelength of longitudinal ridges and the thickness of the landslide seen in nature and in experiments of self-forming ice-free ridges. Moreover, scaling analysis of the martian landslide studied here indicates that its emplacement velocity could have been as high as tens to hundreds of m/s (see the Methods section). It follows that longitudinal ridges that characterise long-runout terrestrial and planetary landslides may be the expression of an instability that emerges within the flowing mass once a velocity threshold is surpassed, as observed in laboratory experiments on rapid granular flows[20]. Although not ruling out the presence of ice and other mineralogical facies as a key factor, our results suggest that the origin of longitudinal ridges does not necessarily depend on the presence of an icy substrate.

Our results and observations represent the first field evidence of experimental and numerical studies that show the spontaneous development of longitudinal ridges in ice-free rapid granular flows, and support the existence of a convincing fundamental process responsible for the origin of such morphologies, challenging existing analogies to terrestrial landslides on ice that have been proposed to explain their widespread occurrence throughout the Solar System. If indeed the scaling relations that we identify indicate that the martian landslide that we study developed longitudinal ridges through an instability that emerges from the physics of fast-flowing dry grains, then we should expect such morphological features throughout the Solar System, regardless of the availability of other lubrication mechanism, such as ice layers.

Methods

Satellite image data and stereo-derived topography data. Morphological mapping of the martian landslide object of this study (Coprates Chasma, 67.75W-11.80S) was conducted using Mars Reconnaissance Orbiter imagery (CTX[22] and HiRISE[23] cameras) provided by the NASA Planetary Data System. This study has made use of the USGS Integrated Software for Imagers and Spectrometers (ISIS)[34] package to pre-process CTX stereo-pair images (Supplementary Table 3). The processed CTX images were imported in SOCET SET commercial suite from BAE Systems to obtain digital elevation models and ortho-rectified images using well-validated previous methods[34]. These image products were post-processed with ISIS to create final images that could be used in ArcGIS.

Morphological characterisation methods. In ArcGIS, longitudinal ridges are traced in correspondence of the crest. Two sets of transversal topographic profiles were traced (Fig. 1c, d) so that the most external ridges (at the left and right end) were always the same ones in every profile. Distances between ridges were measured manually with the ruler tool. The number of ridges and their density along each profile were obtained using a custom Python script (see the Code availability section). In order to assess the average thickness of the landslide deposit in the correspondence of every profile, we built the topography of the valley floor underneath the deposit by interpolating topographic contours of Valles Marineris floor around the landslide (Supplementary Figs. 1 and 2). Because the CTX-derived DEM and the newly built DEM representing the valley floor have different resolution, the number of elevation points available is different, therefore preventing a direct correlation and thickness assessment point by point. We overcame this aspect by taking elevation points of the valley floor and the correspondent closest elevation points (one before and one after) of the landslide deposit. We then averaged the elevation between these two points and calculated the thickness. The thickness values obtained per each point of the valley floor were finally averaged. We automated these steps by means of a custom Python script (see the Code availability section).

Landslide deposit thickness error estimation. We traced profiles transversal and longitudinal to the valley floor, adjacent to the central and east areas of the study (Supplementary Fig. 3). This set of transects (yellow lines), in the specific their linear fits (burgundy lines), is compared with a mirror set of transects traced in the correspondence of the landslide deposit (blue lines) so to assess the plausibility of the overall elevations of our reconstructed bottom surface, and to provide an error estimation of the average thickness that we provide in the paper.

As the floor of Valles Marineris gently dips towards east (in the figure, from left to right), the higher elevations of the blue lines 1 and 2 are plausible. However, we are also expecting a random natural roughness of the valley floor at various scales so that also blue lines 3 and 4 appear plausible, as their maximum offset (blue line 3) is ~80 m, which is within a reasonable magnitude of topographic variation (as seen in profile 1, Supplementary Fig. 3).

We use these profiles to evaluate the errors on the deposit thickness, and we do so by accounting for the standard deviation of the elevation in the topographic profiles (Supplementary Table 4). To do so, we use the topographic profiles that we traced in the valley floor, adjacent to the central and east areas of study (yellow lines). As the topographic profiles that we traced for the morphometric analysis are parallel to neither transversal nor longitudinal direction, we determine the final error taking into account the propagation of error along these two axes (Eq. (1)), that is combining standard deviation for yellow lines 1 and 2 to obtain the error in

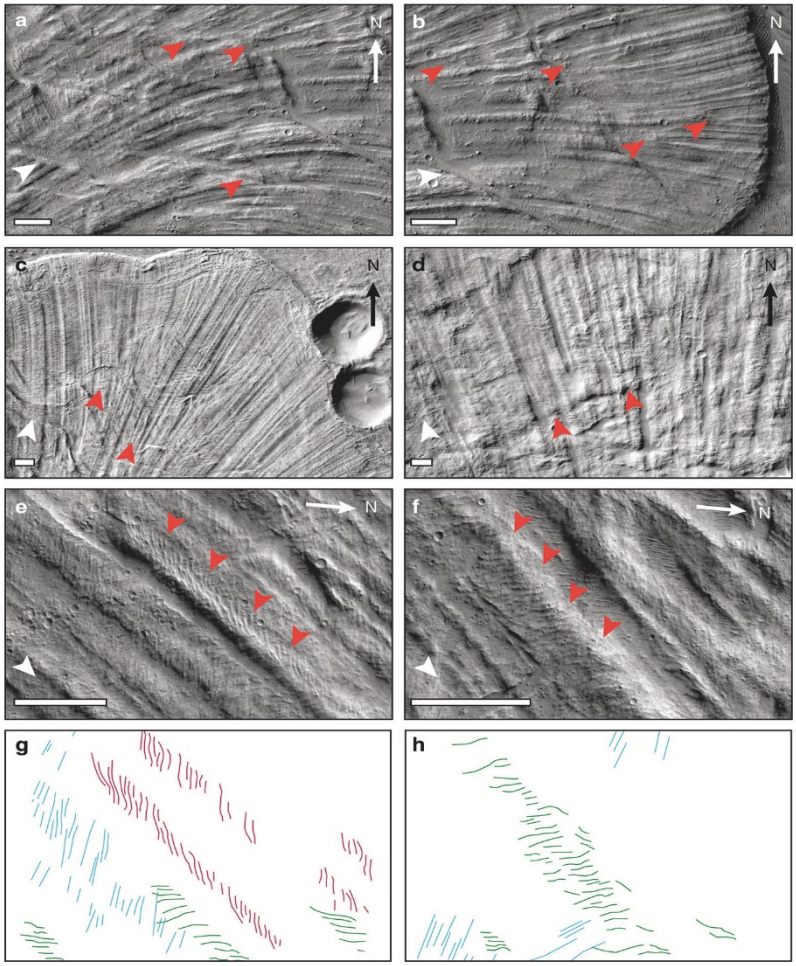

Fig. 3 Close-up images showing the behaviour of longitudinal ridges and superposed en-echelon features. **a**–**d** appearance of new, smaller ridges between diverging ridges, as indicated by orange arrowheads; this behaviour may represent field evidence for laboratory observations made by Forterre and Pouliquen[20], who reported of a complex non-linear evolution that includes transversal drift and creation of longitudinal streaks in rapid granular flows. **e**, **f** s-shaped en-echelon features superposed on longitudinal ridges; these features may represent kinematic indicators, providing evidence of a velocity gradient between ridges and furrows. **g**, **h** Digitalised en-echelon features observed on ridges in (**e**) and (**f**), respectively; red and green colour represent s-shaped features with a rough east-west and north–south orientation, respectively; cyan colour represents other linear features that are not considered in this study. Image (3a), (3b) and (3c) locations are shown in Fig. 1b; location of (3d) is westward to Fig. 1b. White arrowheads indicate flow direction. Scale bar is 1 km

the central area of study (c) and yellow lines 3 and 4 for the error in the east area of study (d), represented as error bars in Fig. 2b of the main text:

$$\sigma_k = \sqrt{\sigma_i^2 + \sigma_j^2} \quad (1)$$

Velocity estimation. The experimental work of Börzsönyi et al.[19] identified a range of scaled downstream surface velocity.

The flow velocity u is scaled with $\sqrt{g * d}$, where g is the gravitational acceleration and d is the grain size, providing the normalised downstream surface velocity $\tilde{u}^S$:

$$\tilde{u}^S = \frac{u^S}{\sqrt{g * d}} \quad (2)$$

From the data in Fig. 3 of Börzsönyi et al.[19], we consider $\tilde{u}^S = 40$, as this is a value for which the longitudinal ridges develop. We use the gravitational acceleration for Mars, 3.71 m/s^2, and the largest grain sizes recognisable on the

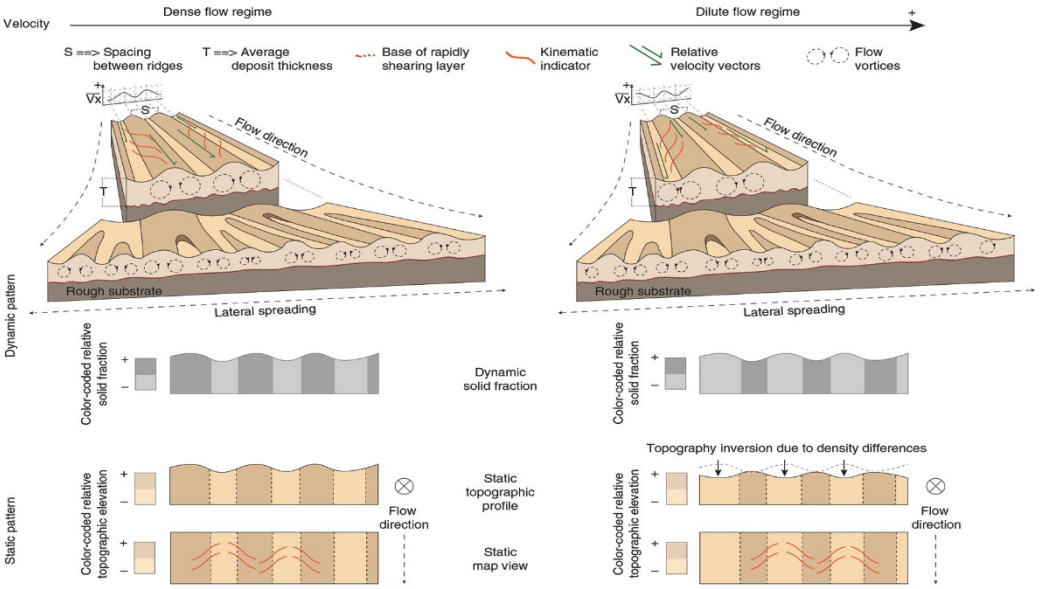

Fig. 4 Flow structure models. Illustration of the two possible flow structure scenarios as inferred from the orientation of the en-echelon features observed superposing longitudinal ridges and interpreted as evidence of a velocity gradient between ridges and furrows. The current static pattern that we observe matches two dynamic patterns, a dense regime flow structure and a dilute flow regime structure followed by inversion of the topography as the flow stops and the ridges deflate

surface deposit of the martian landslide, $d = 1–20$ m (Supplementary Fig. 4), using HiRISE images (resolution 25 cm/px). We infer that the velocity of the martian landslide could range between 77 m/s and 345 m/s. Note that our estimation of the grain size may be biased towards higher values by resolution limitation and by a possible grain size segregation effect that brings larger grains closer to the surface. As such, we are aware that the range provided may exaggerate the most effective grain size and, therefore, the inferred velocity may be overestimated.

Data availability

Imagery dataset used to generate DEMs and Orthophotos analysed in this study are available through the NASA PDS website http://pds-geosciences.wustl.edu/missions/mro/default.htm. We also provide the CTX and HiRISE image files and stereo-derived CTX DEMs and Orthophotos used in this study through data repository figshare https://doi.org/10.5522/04/9759266. All results generated during the morphometric analysis conducted in this study are included in this published article and its Supplementary Information.

Code availability

Code used to generate some of the dataset analysed in this study is available from the corresponding author upon request.

Received: 4 February 2019; Accepted: 19 September 2019;
Published online: 24 October 2019

References

1. Boyce, J. M. & Mouginis-Mark, P. J. Martian craters viewed by the Thermal Emission Imaging System instrument: double-layered ejecta craters. *J. Geophys. Res.* 111, https://doi.org/10.1029/2005JE002638 (2006).
2. Legros, F. The mobility of long-runout landslides. *Eng. Geol.* **63**, 301–331 (2002).
3. Singer, N. K., McKinnon, W. B., Schenk, P. M. & Moore, J. M. Massive ice avalanches on Iapetus mobilized by friction reduction during flash heating. *Nat. Geosci.* **5**, 574–578 (2012).
4. Schmidt, B. E. et al. Geomorphological evidence for ground ice on dwarf planet Ceres. *Nat. Geosci.* **10**, 338–343 (2017).
5. Collins, G. S. & Melosh, H. J. Acoustic fluidization and the extraordinary mobility of sturzstroms. *J. Geophys. Res.* **108**, 2473 (2003).
6. Goren, L. & Aharonov, E. Long runout landslides: the role of frictional heating and hydraulic diffusivity. *Geophys. Res. Lett.* **34**, L07301 (2007).
7. Pudasaini, S. P. & Miller, S. A. The hypermobility of huge landslides and avalanches. *Eng. Geol.* **157**, 124–132 (2013).
8. Lucas, A., Mangeney, A. & Ampuero, J. P. Frictional velocity-weakening in landslides on Earth and on other planetary bodies. *Nat. Commun.* **5**, 3417 (2014).
9. Johnson, B. C., Campbell C. S. & Melosh H. J. The reduction of friction in long runout landslides as an emergent phenomenon. *J. Geophys. Res. Earth Surf.* **121**, https://doi.org/10.1002/2015JF003751 (2016).
10. Watkins, J. A., Ehlmann, B. L. & Yin, A. Long-runout landslides and the long-lasting effects of early water activity on Mars. *Geology* **43**, 107–110 (2015).
11. Marangunic, C. & Bull, C. The landslide on the Sherman Glacier. *The Great Alaska Earthquake of 1964, Hydrology. Natl Acad. Sci. Publ.* **1603**, 383–394 (1968).
12. Dufresne, A. & Davies, T. R. Longitudinal ridges in mass movement deposits. *Geomorphology* **105**, 171–181 (2009).
13. De Blasio, F. V. Landslides in Valles Marineris (Mars): a possible role of basal lubrication by sub-surface ice. *Planet Space Sci.* **59**, 1384–1392 (2011).
14. Weiss, D. K. & Head, J. W. Formation of double-layered ejecta craters on Mars: a glacial substrate model. *J. Geophys. Res.* **40**, 3819–3824 (2013).
15. Quintana, S. N. & Schultz, P. H. The formation of crater-related blast wind streaks on Mars. *LPSC* **XLV**, 1971 (2014).
16. Guest, J. E. & Murray, J. B. Nature and origin of Tsiolkovsky crater, lunar farside. *Planet Space Sci.* **17**, 121–141 (1969).
17. Boyce, J. M., Mouginis-Mark, P. & Robinson, M. An LROC update: the Tsiolkovsky landslide. *LPSC* **XLVII**, 2471 (2016).

18. Schmitt, H. H. et al. Revisiting the field geology of Taurus-Littrow. *Icarus*, https://doi.org/10.1016/j.icarus.2016.11.042 (2017).
19. Börzsönyi, T., Ecke, R. E. & McElwaine, J. N. Patterns in flowing sand: understanding the physics of granular flow. *Phys. Rev. Lett.* **103**, https://doi.org/10.1103/PhysRevLett.103.178302 (2009).
20. Forterre, Y. & Pouliquen, O. Longitudinal vortices in granular flows. *Phys. Rev. Lett.* **86**, 5886–5889 (2001).
21. Forterre, Y. & Pouliquen, O. Stability analysis of rapid granular flows: formation of longitudinal vortices. *J. Fluid Mech.* **46**, 361–387 (2002).
22. Malin, M. C. et al. Context camera investigation on board the Mars reconnaissance orbiter. *J. Geophys. Res.* **112**, https://doi.org/10.1029/2006JE002808 (2007).
23. McEwen, A. S. et al. Mars reconnaissance orbiter's high resolution imaging science experiment (HiRISE). *J. Geophys. Res.* **112**, https://doi.org/10.1029/2005JE002605 (2007).
24. Pietrek, A., Weis, J., Hergarten, S., Wulf, G. & Kenkmann, T. Morphometric analysis and comparison of martian landslides and layered deposits of impact crater ejecta blankets. *LPSC* **XLVII**, 2250 (2016).
25. Campbell, C. S. Self-lubrication for long runout landslides. *J. Geol.* **97**, 653–665 (1989).
26. Campbell, C. S. & Brennen, C. E. Chute flows of granular material: some computer simulations. *J. Appl. Mech.* **52**, 172–178 (1985).
27. Campbell, C. S. Rapid granular flows. *Annu. Rev. Fluid Mech.* **22**, 57–92 (1990).
28. Melosh, H. J. Acoustic fluidization: a new geologic process? *J. Geophys. Res.* **84**, https://doi.org/10.1029/JB084iB13p07513 (1979).
29. Masch, L., Wenk, H. R. & Preuss, E. Electron microscopy study of hyalomylonites–evidence for frictional melting in landslides. *Tectonophysics* **115**, 131–160 (1985).
30. Voight, B. & Faust, C. Frictional heat and strength loss in some rapid landslides. *Geotechnique* **32**, 43–54 (1982).
31. Vardoulakis, I. Dynamic thermos-poro-mechanical analysis of catastrophic landlsides. *Geotechnique* **52**, 157–171 (2002).
32. Goren, L., Aharanov, E. & Anders, M. H. The long runout of the Heart Mountain landslide: heating, pressurization, and carbonate decomposition. *J. Geophys. Res.* **115**, https://doi.org/10.1029/2009JB007113 (2010).
33. Mitchell, T. M. et al. Catastrophic emplacement of giant landslides aided by thermal decomposition: heart mountain, Wyoming. *Earth Planet Sci. Lett.* **411**, 199–207 (2015).
34. Kirk, R. L. et al. Ultra-high-resolution topographic mapping of Mars with MRO HiRISE stereo images: meter-scale slopes of candidate Phoenix landing sites. *J. Geophys. Res.* **113**, E00A24 (2008).

Acknowledgements
G.M. and T.M.M. acknowledge Science and Technology Facilities Council (STFC) funding ST/N504476/1.

Author contributions
G.M. & T.M.M. came up with the concept. P.M.G., L.G. and H.H.S. contributed to the paper writing led by G.M.

Competing interests
The authors declare no competing interests.

Additional information
Supplementary information is available for this paper at https://doi.org/10.1038/s41467-019-12734-0.

Correspondence and requests for materials should be addressed to G.M.

Peer review information *Nature Communications* thanks Jay Melosh and other, anonymous, reviewers for their contribution to the peer review of this work. Peer reviewer reports are available.

Reprints and permission information is available at http://www.nature.com/reprints

Publisher's note Springer Nature remains neutral with regard to jurisdictional claims in published maps and institutional affiliations.

References

Abele, G. (1974), Bergsturze in den Alpen, *Wiss. Alpenvereinshefte*, *25*, 1-230.

Aharonov, E., and M. H. Anders (2006), Hot water: A solution to the Heart Mountain detachment problem?, *Geology*, *34*(3), 165-168.

Allmendinger, R. W., and G. González (2010), Invited review paper: Neogene to Quaternary tectonics of the coastal Cordillera, northern Chile, *Tectonophysics*, *495*(1), 93-110, doi:https://doi.org/10.1016/j.tecto.2009.04.019.

Alonso, E. E., and N. M. Pinyol (2010), Criteria for rapid sliding I. A review of Vaiont case, *Eng Geol*, *114*(3), 198-210, doi:https://doi.org/10.1016/j.enggeo.2010.04.018.

Anders, M. H., B. W. Fouke, A. L. Zerkle, E. Tavarnelli, W. Alvarez, and G. E. Harlow (2010), The Role of Calcining and Basal Fluidization in the Long Runout of Carbonate Slides: An Example from the Heart Mountain Slide Block, Wyoming and Montana, U.S.A, *The Journal of Geology*, *118*(6), 577-599, doi:10.1086/656383.

Anderson, J. A., S. C. Sides, D. L. Soltesz, T. L. Sucharski, and K. J. Becker (2004), Modernization of the Integrated Software for Imagers and Spectrometers, in *LPSC XXXV*, edited, The Woodlands, Houston, TX.

Andrews-Hanna, J. C. (2012a), The formation of Valles Marineris: 1. Tectonic architecture and the relative roles of extension and subsidence, *Journal of Geophysical Research: Planets*, *117*(E3), doi:https://doi.org/10.1029/2011JE003953.

Andrews-Hanna, J. C. (2012b), The formation of Valles Marineris: 3. Trough formation through super-isostasy, stress, sedimentation, and subsidence, *Journal of Geophysical Research: Planets*, *117*(E6), doi:https://doi.org/10.1029/2012JE004059.

Andrews-Hanna, J. C., and K. W. Lewis (2011), Early Mars hydrology: 2. Hydrological evolution in the Noachian and Hesperian epochs, *Journal of Geophysical Research: Planets*, *116*(E2), doi:https://doi.org/10.1029/2010JE003709.

Apollo Lunar Surface Journal, https://www.hq.nasa.gov/alsj/, edited.

Apollo Lunar Surface Journal https://www.hq.nasa.gov/alsj/.

Aranson, I. S., and L. Tsimring (2009), *Granular patterns /by Igor S. Aranson, Lev TSimring*, Oxford : Oxford University Press, Oxford.

Balme, M. R., A. S. Bargery, C. J. Gallagher, and S. Gupta (2011), Martian Geomorphology, *GSL Special Publications*, *356*.

Becerra, P., S. Conway, N. Thomas, and H. Team (2020), Avalanches of the martian north polar cap, in *EGU General Assembly*, edited, Online, doi:https://doi.org/10.5194/egusphere-egu2020-22331.

Beddingfield, C. B., et al. (2019), Landslides on Charon, *Icarus*, doi:https://doi.org/10.1016/j.icarus.2019.07.017.

Beutner, E. C., and G. P. Gerbi (2005), Catastrophic emplacement of the Heart Mountain block side, Wyoming and Montana, USA, *Geological Society of America Bulletin*, *117*, 724-735.

Binder, A. B., and H.-C. Gunga (1985), Young thrust-fault scarps in the highlands: evidence for an initially totally molten moon, *Icarus*, *63*(3), 421-441, doi:https://doi.org/10.1016/0019-1035(85)90055-7.

Blasius, K. R., J. A. Cutts, J. E. Guest, and H. Masursky (1977), Geology of the Valles Marineris: First analysis of imaging from the Viking 1 Orbiter Primary Mission, *Journal of Geophysical Research (1896-1977)*, *82*(28), 4067-4091, doi:10.1029/JS082i028p04067.

Boazman, S. J., J. M. Davis, P. M. Grindrod, M. R. Balme, P. Vermeesch, and T. Baird (2021), Measuring Ripple and Dune Migration in Coprates Chasma, Valles Marineris: A Source to Sink Aeolian System on Mars?, *Journal of Geophysical Research: Planets*, *126*(3), e2020JE006608, doi:https://doi.org/10.1029/2020JE006608.

Bock, C. G. (1977), Martinez Mountain rock avalanche, in *Landslides*, edited by D. R. Coates, Geological Society of America.

Borzsonyi, T., R. E. Ecke, and J. N. McElwaine (2009), Patterns in Flowing Sand: Understanding the Physics of Granular Flow, *Phys Rev Lett*, *103*(17), doi:10.1103/PhysRevLett.103.178302.

Boyce, J. M., and P. J. Mouginis-Mark (2006), Martian craters viewed by the Thermal Emission Imaging System instrument: Double-layered ejecta craters, *J Geophys Res-Planet*, *111*(E10), doi:10.1029/2005je002638.

Boyce, J. M., P. J. Mouginis-Mark, and M. Robinson (2016), An LROC update: the Tsiolkovsky crater landslide, in *47th Lunar and Planetary Science Conference*, edited, The Woodlands, TX.

Boyce, J. M., P. J. Mouginis-Mark, and M. Robinson (2020), The Tsiolkovskiy crater landslide, the moon: An LROC view, *Icarus*, *337*, 113464, doi:https://doi.org/10.1016/j.icarus.2019.113464.

Boyce, J. M., P. J. Mouginis-Mark, and L. L. Tornabene (2014), The morphometry of grooves on the inner layer of martian DLE craters suggests that they were produced by either high-speed granular flow or explosion surge, in *Lunar and Planetary Science Conference*, edited, The Woodlands, Texas.

Brantut, N., R. Han, T. Shimamoto, N. Findling, and A. Schubnel (2011a), Fast slip with inhibited temperature rise due to mineral dehydration: Evidence from experiments on gypsum, *Geology*, *39*(1), 59-62, doi:10.1130/g31424.1.

Brantut, N., A. Schubnel, J. N. Rouzaud, F. Brunet, and T. Shimamoto (2008), High-velocity frictional properties of a clay-bearing fault gouge and implications for earthquake mechanics, *J Geophys Res-Sol Ea*, *113*(B10), doi:10.1029/2007jb005551.

Brantut, N., J. Sulem, and A. Schubnel (2011b), Effect of dehydration reactions on earthquake nucleation: Stable sliding, slow transients, and unstable slip, *J Geophys Res-Sol Ea*, *116*, doi:Artn B05304

10.1029/2010jb007876.

Brož, P., E. Hauber, J. J. Wray, and G. Michael (2017), Amazonian volcanism inside Valles Marineris on Mars, *Earth and Planetary Science Letters*, *473*, 122-130, doi:https://doi.org/10.1016/j.epsl.2017.06.003.

Brunetti, M. T., F. Guzzetti, M. Cardinali, F. Fiorucci, M. Santangelo, P. Mancinelli, G. Komatsu, and L. Borselli (2014), Analysis of a new geomorphological inventory of landslides in Valles Marineris, Mars, *Earth Planet Sc Lett*, *405*, 156-168, doi:10.1016/j.epsl.2014.08.025.

Brunetti, M. T., Z. Xiao, G. Komatsu, S. Peruccacci, and F. Guzzetti (2015), Large rock slides in impact craters on the Moon and Mercury, *Icarus*, *260*, 289-300, doi:https://doi.org/10.1016/j.icarus.2015.07.014.

Brustel, C., J. Flahaut, E. Hauber, F. Fueten, C. Quantin, R. Stesky, and G. R. Davies (2017), Valles Marineris tectonic and volcanic history inferred from dikes in eastern Coprates Chasma, *Journal of Geophysical Research: Planets*, *122*(6), 1353-1371, doi:https://doi.org/10.1002/2016JE005231.

Buss, E., and A. Heim (1881), Der Bergsturz von Elm den 1. September 1881. Denkschrift, *Zurich, Switzerland: Wurster*.

Butcher, F. E. G., M. R. Balme, C. Gallagher, N. S. Arnold, S. J. Conway, A. Hagermann, and S. R. Lewis (2017), Recent Basal Melting of a Mid-Latitude Glacier on Mars, *J Geophys Res-Planet*, *122*(12), 2445-2468, doi:10.1002/2017je005434.

Byerlee, J. (1978), Friction of rocks, *pure and applied geophysics*, *116*(4), 615-626, doi:10.1007/BF00876528.

Campbell, C. S. (1989), Self-Lubrication for Long Runout Landslides, *J Geol*, *97*(6), 653-665, doi:10.1086/629350.

Campbell, C. S. (1990), Rapid Granular Flows, *Annu Rev Fluid Mech*, *22*, 57-92, doi:10.1146/annurev.fl.22.010190.000421.

Campbell, C. S., and C. E. Brennen (1985), Chute Flows of Granular Material - Some Computer-Simulations, *J Appl Mech-T Asme*, *52*(1), 172-178, doi:Doi 10.1115/1.3168990.

Campbell, C. S., P. W. Cleary, and M. Hopkins (1995), Large-scale landslide simulations: Global deformation, velocities and basal friction, *Journal of Geophysical Research: Solid Earth*, *100*(B5), 8267-8283, doi:doi:10.1029/94JB00937.

Carr, M. H., and J. W. Head (2010), Geologic history of Mars, *Earth Planet Sc Lett*, *294*(3), 185-203, doi:https://doi.org/10.1016/j.epsl.2009.06.042.

Catling, D. C., S. E. Wood, C. Leovy, D. R. Montgomery, H. M. Greenberg, C. R. Glein, and J. M. Moore (2006), Light-toned layered deposits in Juventae Chasma, Mars, *Icarus*, *181*(1), 26-51, doi:https://doi.org/10.1016/j.icarus.2005.10.020.

Charriere, M., F. Humair, C. Froese, M. Jaboyedoff, A. Pedrazzini, and C. Longchamp (2016), From the source area to the deposit: Collapse, fragmentation, and propagation of the Frank Slide, *Geological Society of America Bulletin*, *128*(1-2), 332-352, doi:10.1130/B31243.1.

Chilton, H. T., et al. (2019), Landslides on Ceres: Inferences Into Ice Content and Layering in the Upper Crust, *Journal of Geophysical Research: Planets*, *124*(6), 1512-1524, doi:10.1029/2018je005634.

Chuang, F. C., and R. Greeley (2000), Large mass movements on Callisto, *Journal of Geophysical Research: Planets*, *105*(E8), 20227-20244, doi:10.1029/2000je001249.

Cleary, P. W., and C. S. Campbell (1993), Self-lubrication for long runout landslides: Examination by computer simulation, *J Geophys Res*, *108*(B10), 2473, doi:10.1029/2003JB002465.

Clifford, S. M., J. Lasue, E. Heggy, J. Boisson, P. McGovern, and M. D. Max (2010), Depth of the Martian cryosphere: Revised estimates and implications for the existence and detection of subpermafrost groundwater, *Journal of Geophysical Research: Planets*, *115*(E7), doi:https://doi.org/10.1029/2009JE003462.

Collins, G. S., and H. J. Melosh (2003), Acoustic fluidization and the extraordinary mobility of sturzstroms, *J Geophys Res-Sol Ea*, *108*(B10), doi:10.1029/2003jb002465.

Conway, S. J., and M. R. Balme (2014), Decameter thick remnant glacial ice deposits on Mars, *Geophys Res Lett*, *41*(15), 5402-5409, doi:10.1002/2014gl060314.

Conway, S. J., M. R. Balme, M. A. Kreslavsky, J. B. Murray, and M. C. Towner (2015), The comparison of topographic long profiles of gullies on Earth to gullies on Mars: A signal of water on Mars, *Icarus*, *253*, 189-204, doi:10.1016/j.icarus.2015.03.009.

Conway, S. J., A. Decaulne, M. R. Balme, J. B. Murray, and M. C. Towner (2010), A new approach to estimating hazard posed by debris flows in the Westfjords of Iceland, *Geomorphology*, *114*(4), 556-572, doi:10.1016/j.geomorph.2009.08.015.

Craddock, J. P., J. Geary, and D. H. Malone (2012), Vertical injectites of detachment carbonate ultracataclasite at White Mountain, Heart Mountain detachment, Wyoming, *Geology*, *40*(5), 463-466, doi:10.1130/g32734.1.

Crosta, G. B., F. V. De Blasio, and P. Frattini (2018a), Global Scale Analysis of Martian Landslide Mobility and Paleoenvironmental Clues, *Journal*

of Geophysical Research: Planets, *123*(4), 872-891, doi:10.1002/2017je005398.

Crosta, G. B., P. Frattini, and E. Valbuzzi (2013), A new inventory of Martian landslides, *LPI Contributions*, *1719*, Abstract 2283.

Crosta, G. B., P. Frattini, E. Valbuzzi, and F. V. De Blasio (2018b), Introducing a New Inventory of Large Martian Landslides, *Earth and Space Science*, *5*(4), 89-119, doi:10.1002/2017EA000324.

Crosta, G. B., R. L. Hermanns, J. Dehls, S. Lari, and S. Sepulveda (2017), Rock avalanches clusters along the northern Chile coastal scarp, *Geomorphology*, *289*, 27-43, doi:10.1016/j.geomorph.2016.11.024.

Cruden, D. M., and O. Hungr (1986), The Debris of the Frank Slide and Theories of Rockslide Avalanche Mobility, *Can J Earth Sci*, *23*(3), 425-432, doi:10.1139/e86-044.

Davies, T. R. (1982), Spreading of Rock Avalanche Debris by Mechanical Fluidization, *Rock Mechanics*, *15*(1), 9-24, doi:10.1007/Bf01239474.

Davies, T. R., and M. J. McSaveney (2002), Dynamic simulation of the motion of fragmenting rock avalanches, *Can Geotech J*, *39*(4), 789-798, doi:10.1139/T02-035.

Davies, T. R., and M. J. McSaveney (2009), The role of rock fragmentation in the motion of large landslides, *Eng Geol*, *109*(1), 67-79, doi:10.1016/j.enggeo.2008.11.004.

Davies, T. R., and M. J. McSaveney (2012), Mobility of long-runout rock avalanches, in *Landslides: Types, Mechanisms and Modeling*, edited by D. Stead and J. J. Clague, pp. 50-58, Cambridge University Press, Cambridge, doi:10.1017/CBO9780511740367.006.

Davies, T. R., and M. J. McSaveney (2016), Comment on “The Reduction of Friction in Long-Runout Landslides as an Emergent Phenomenon” by Brandon C. Johnson, Charles S. Campbell, and H. Jay Melosh, *Journal of Geophysical Research: Earth Surface*, *121*(10), 1718-1720, doi:10.1002/2016jf003954.

Davis, J. M., P. M. Grindrod, P. Fawdon, R. M. E. Williams, S. Gupta, and M. Balme (2018), Episodic and Declining Fluvial Processes in Southwest Melas Chasma, Valles Marineris, Mars, *J Geophys Res-Planet*, *123*(10), 2527-2549, doi:10.1029/2018je005710.

De Blasio, F. V. (2011), Landslides in Valles Marineris (Mars): A possible role of basal lubrication by sub-surface ice, *Planet Space Sci*, *59*(13), 1384-1392, doi:10.1016/j.pss.2011.04.015.

De Blasio, F. V. (2014), Friction and dynamics of rock avalanches travelling on glaciers, *Geomorphology*, *213*, 88-98, doi:10.1016/j.geomorph.2014.01.001.

De Blasio, F. V., and A. Elverhøi (2008), A model for frictional melt production beneath large rock avalanches, *Journal of Geophysical Research: Earth Surface*, *113*(F2), doi:10.1029/2007JF000867.

Di Toro, G., D. L. Goldsby, and T. E. Tullis (2004), Friction falls towards zero in quartz rock as slip velocity approaches seismic rates, *Nature*, *427*, 436, doi:10.1038/nature02249.

Di Toro, G., R. Han, T. Hirose, N. De Paola, S. Nielsen, K. Mizoguchi, F. Ferri, M. Cocco, and T. Shimamoto (2011), Fault lubrication during earthquakes, *Nature*, *471*, 494, doi:10.1038/nature09838.

Di Toro, G., T. Hirose, S. Nielsen, G. Pennacchioni, and T. Shimamoto (2006), Natural and Experimental Evidence of Melt Lubrication of Faults During Earthquakes, *Science*, *311*(5761), 647-649, doi:10.1126/science.1121012.

Di Toro, G., et al. (2010), From field geology to earthquake simulation: A new state-of-the-art tool to investigate rock friction during seismic cycle (SHIVA), *Rendiconto Lincei. Scienze Fisiche e Naturali*, *21*, 95-114, doi:10.1007/s12210-010-0097-x.

Douglass, J., R. I. Dorn, and B. Gootee (2005), A large landslide on the urban fringe of metropolitan Phoenix, Arizona, *Geomorphology*, *65*(3), 321-336, doi:https://doi.org/10.1016/j.geomorph.2004.09.022.

Dufresne, A., A. Bosmeier, and C. Prager (2016), Sedimentology of rock avalanche deposits - Case study and review, *Earth-Sci Rev*, *163*, 234-259, doi:10.1016/j.earscirev.2016.10.002.

Dufresne, A., and T. R. Davies (2009), Longitudinal ridges in mass movement deposits, *Geomorphology*, *105*(3-4), 171-181, doi:10.1016/j.geomorph.2008.09.009.

Dufresne, A., G. J. Wolken, C. Hibert, E. K. Bessette-Kirton, J. A. Coe, M. Geertsema, and G. Ekström (2019), The 2016 Lamplugh rock avalanche, Alaska: deposit structures and emplacement dynamics, *Landslides*, doi:10.1007/s10346-019-01225-4.

Dundas, C. M., S. Diniega, and A. S. McEwen (2015), Long-term monitoring of martian gully formation and evolution with MRO/HiRISE, *Icarus*, *251*, 244-263, doi:https://doi.org/10.1016/j.icarus.2014.05.013.

El-Baz, F. (1972), New geological findings in Apollo 15 lunar orbital photography, paper presented at Lunar Sci Conf.

EO Portal https://directory.eoportal.org/web/eoportal/satellite-missions/p/pleiades, edited.

Erismann, T. H. (1979), Mechanisms of large landslides, *Rock mechanics*, *12*(1), 15-46, doi:10.1007/bf01241087.

Erismann, T. H., and G. Abele (2001), *Dynamics of rockslides and rockfalls*, 316 pp., Springer, Berlin.

Erismann, T. H., H. Heuberger, and E. Preuss (1977), Fused Rock of Kofels (Tyrol) - Frictionite Generated by a Landslide, *Tscher Miner Petrog*, *24*(1-2), 67-119, doi:10.1007/Bf01081746.

European Space Agency (2012), ESA SP-13322/2 Sentinel 2*Rep.*, ESA Publications.

Fassett, C. I., J. W. Head, S. J. Kadish, E. Mazarico, G. A. Neumann, D. E. Smith, and M. T. Zuber (2012), Lunar impact basins: Stratigraphy, sequence and ages from superposed impact crater populations measured from Lunar Orbiter Laser Altimeter (LOLA) data, *Journal of Geophysical Research E: Planets*, *117*(2), doi:10.1029/2011JE003951.

Fastook, J. L., and J. W. Head (2014), Amazonian mid- to high-latitude glaciation on Mars: Supply-limited ice sources, ice accumulation patterns, and concentric crater fill glacial flow and ice sequestration, *Planet Space Sci*, *91*, 60-76, doi:https://doi.org/10.1016/j.pss.2013.12.002.

Fauque, L., and M. R. Strecker (1988), Large Rock Avalanche Deposits (Sturzstrome, Sturzstroms) at Sierra Aconquija, Northern Sierras Pampeanas, Argentina, *Eclogae Geol Helv*, *81*(3), 579-592.

Fondriest, M., J. Mecklenburgh, F. X. Passelegue, G. Artioli, F. Nestola, E. Spagnuolo, and G. Di Toro (2019), Pseudotachylytes alteration and their loss from the geological record, in *EGU*, edited, Vienna.

Forterre, Y., and O. Pouliquen (2001), Longitudinal vortices in granular flows, *Phys Rev Lett*, *86*(26), 5886-5889, doi:10.1103/PhysRevLett.86.5886.

Forterre, Y., and O. Pouliquen (2002), Stability analysis of rapid granular chute flows: formation of longitudinal vortices, *J Fluid Mech*, *467*, 361-387, doi:10.1017/S0022112002001581.

Forterre, Y., and O. Pouliquen (2011), Granular Flows, *Prog Math Phys*, *61*, 77-109.

Gassen, W. V., and D. M. Cruden (1989), Momentum transfer and friction in the debris of rock avalanches, *Can Geotech J*, *26*(4), 623-628, doi:10.1139/t89-075.

Germanovich, L. N., S. Kim, and A. M. Puzrin (2016), Dynamic growth of slip surfaces in catastrophic landslides, *Proceedings of the Royal Society A: Mathematical, Physical and Engineering Sciences*, *472*(2185), 20150758, doi:doi:10.1098/rspa.2015.0758.

Goguel, J. (1978), Scale-dependent rockslide mechanisms, *in Voight, B., ed. Rockslides and avalanches*, *1*, 693-705.

Goldsby, D. L., and T. E. Tullis (2002), Low frictional strength of quartz rocks at subseismic slip rates, *29*(17), 25-21-25-24, doi:10.1029/2002GL015240.

Goldsby, D. L., and T. E. Tullis (2011), Flash Heating Leads to Low Frictional Strength of Crustal Rocks at Earthquake Slip Rates, *Science*, *334*(6053), 216-218, doi:10.1126/science.1207902.

Goren, L., and E. Aharonov (2007), Long runout landslides: The role of frictional heating and hydraulic diffusivity, *Geophys Res Lett*, *34*(7), doi:10.1029/2006gl028895.

Goren, L., E. Aharonov, and M. H. Anders (2010), The long runout of the Heart Mountain landslide: Heating, pressurization, and carbonate

decomposition, *J Geophys Res-Sol Ea*, *115*, doi:10.1029/2009jb007113.

Gourronc, M., O. Bourgeois, D. Mège, S. Pochat, B. Bultel, M. Massé, L. Le Deit, S. Le Mouélic, and D. Mercier (2014), One million cubic kilometers of fossil ice in Valles Marineris: Relicts of a 3.5Gy old glacial landsystem along the Martian equator, *Geomorphology*, *204*, 235-255, doi:https://doi.org/10.1016/j.geomorph.2013.08.009.

Grindrod, P. M., and N. H. Warner (2014), Erosion rate and previous extent of interior layered deposits on Mars revealed by obstructed landslides, *Geology*, *42*(9), 795-798, doi:10.1130/g35790.1.

Grindrod, P. M., M. West, N. H. Warner, and S. Gupta (2012), Formation of an Hesperian-aged sedimentary basin containing phyllosilicates in Coprates Catena, Mars, *Icarus*, *218*(1), 178-195, doi:https://doi.org/10.1016/j.icarus.2011.11.027.

Guest, J. E., and J. B. Murray (1969), Nature and Origin of Tsiolkovsky Crater Lunar Farside, *Planet Space Sci*, *17*(1), 121-&, doi:Doi 10.1016/0032-0633(69)90128-7.

Haase, I., M. Wählisch, P. Gläser, J. Oberst, and M. S. Robinson (2019), Coordinates and Maps of the Apollo 17 Landing Site, *Earth and Space Science*, *6*(1), 59-95, doi:10.1029/2018ea000408.

Habib, P. (1975), Production of gaseous pore pressure during rock slides, *Rock mechanics*, *7*(4), 193-197, doi:10.1007/bf01246865.

Hager, A., and A. D. Schedl (2017), Classification and ages of landslides within Valles Marineris, in *LPSC XLVIII*, edited.

Harrison, K. P., and R. E. Grimm (2003), Rheological constraints on martian landslides, *Icarus*, *163*(2), 347-362, doi:10.1016/S0019-1035(03)00045-9.

Harrison, V. J., and N. L. Falcon (1938), An ancient landslip at Saidmarreh in southwestern Iran, *J Geol*, *46*(3), 296-309, doi:10.1086/624654.

Head, J. W. (1979), Serenitatis multi-ringed basin: Regional geology and basin ring interpretation, *The moon and the planets*, *21*(4), 439-462, doi:10.1007/BF00897836.

Head, J. W., J. F. Mustard, M. A. Kreslavsky, R. E. Milliken, and D. R. Marchant (2003), Recent ice ages on Mars, *Nature*, *426*(6968), 797-802, doi:10.1038/nature02114.

Heim, A. (1882), Der Bergstruz von Elm, *Zeits, deutscen geol Gesellsch.*, *34*, 74-115.

Heim, A. (1932), Der Bergsturz und Menschenleben, *Fretz und Wasmuth Verlag, Zurich*, 218 pp.

Helgason, J. K., Þ. Sæmundssson, V. Drouin, T. Jóhannesson, H. Grímsdóttir, M. H. Jónsson, and S. S. Gylfadóttir (2019), The Hítardalur landslide in West Iceland in July 2018, paper presented at Geophysical Research Abstracts.

Hendron, A. J., and F. D. Patton (1987), The vaiont slide — A geotechnical analysis based on new geologic observations of the failure surface, *Eng Geol*, *24*(1), 475-491, doi:https://doi.org/10.1016/0013-7952(87)90080-9.

Henriksen, M. R., et al. (2017), Extracting accurate and precise topography from LROC narrow angle camera stereo observations, *Icarus*, *283*, 122-137, doi:https://doi.org/10.1016/j.icarus.2016.05.012.

Highland, L. M., and P. Bobrowsky (2008), *The landslide handbook - A guide to understanding landslides*, 129 pp., U.S. Geological Survey, Reston, Virginia.

Holsapple, K. A. (2013), Modeling granular material flows: The angle of repose, fluidization and the cliff collapse problem, *Planet Space Sci*, *82-83*, 11-26, doi:https://doi.org/10.1016/j.pss.2013.03.001.

Howard, K. A. (1973), Avalanche Mode of Motion - Implications from Lunar Examples, *Science*, *180*(4090), 1052-1055, doi:10.1126/science.180.4090.1052.

Hsü, K. (1975), Catastrophic debris stream (Sturzstroms) generated by rockfalls, *Geological Society of America Bulletin*, *86*(1), doi:10.1130/0016-7606(1975)86<129:CDSSGB>2.0.CO;2.

Hsü, K. (1978), Chapter 1 - Albert Heim: Observations on Landslides and Relevance to Modern Interpretations, in *Developments in Geotechnical Engineering*, edited by B. Voight, pp. 71-93, Elsevier, doi:https://doi.org/10.1016/B978-0-444-41507-3.50009-X.

Hu, W., R. Q. Huang, M. McSaveney, X. H. Zhang, L. Yao, and T. Shimamoto (2018), Mineral changes quantify frictional heating during a large low-friction landslide, *Geology*, *46*(3), 223-226, doi:10.1130/G39662.1.

Hungr, O. (1981), Dynamics of rock avalanches and other types of slope movements, *PhD Thesis*.

Hungr, O., and S. G. Evans (2004), Entrainment of debris in rock avalanches: An analysis of a long run-out mechanism, *Geological Society of America Bulletin*, *116*(9-10), 1240-1252, doi:10.1130/B25362.1.

Hutchinson, J. N., and R. K. Bhandari (1971), Undrained Loading, A Fundamental Mechanism of Mudflows and other Mass Movements, *21*(4), 353-358, doi:10.1680/geot.1971.21.4.353.

Ibanez, J. P., and Y. H. Hatzor (2018), Rapid sliding and friction degradation: Lessons from the catastrophic Vajont landslide, *Eng Geol*, *244*, 96-106, doi:10.1016/j.enggeo.2018.07.029.

Iqbal, W., H. Hiesinger, and C. H. van der Bogert (2019), New geological maps and crater size-frequency distribution measurements of the Apollo 17 landing site, in *50th Lunar and Planetary Science Conference*, edited, The Woodlands, TX.

Iverson, R. M., et al. (2015), Landslide mobility and hazards: implications of the 2014 Oso disaster, *Earth Planet Sc Lett*, *412*, 197-208, doi:10.1016/j.epsl.2014.12.020.

James, M. R., and S. Robson (2012), Straightforward reconstruction of 3D surfaces and topography with a camera: Accuracy and geoscience application, *Journal of Geophysical Research: Earth Surface*, *117*(F3), doi:doi:10.1029/2011JF002289.

James, M. R., S. Robson, and M. W. Smith (2017), 3-D uncertainty-based topographic change detection with structure-from-motion photogrammetry: precision maps for ground control and directly georeferenced surveys, *Earth Surface Processes and Landforms*, *42*(12), 1769-1788, doi:doi:10.1002/esp.4125.

Jaumann, R., et al. (2007), The high-resolution stereo camera (HRSC) experiment on Mars Express: Instrument aspects and experiment conduct from interplanetary cruise through the nominal mission, *Planet Space Sci*, *55*(7), 928-952, doi:https://doi.org/10.1016/j.pss.2006.12.003.

Johnson, B. (1978), Chapter 14 - Blackhawk Landslide, California, U.S.A, in *Developments in Geotechnical Engineering*, edited by B. Voight, pp. 481-504, Elsevier, doi:https://doi.org/10.1016/B978-0-444-41507-3.50022-2.

Johnson, B. C., and C. S. Campbell (2017), Drop Height and Volume Control the Mobility of Long-Runout Landslides on the Earth and Mars, *Geophys Res Lett*, *44*(24), 12,091-012,097, doi:doi:10.1002/2017GL076113.

Johnson, B. C., C. S. Campbell, and H. J. Melosh (2016a), The reduction of friction in long runout landslides as an emergent phenomenon, *J Geophys Res-Earth*, *121*(5), 881-889, doi:10.1002/2015jf003751.

Johnson, B. C., C. S. Campbell, and H. J. Melosh (2016b), Reply to comment by Davies and McSaveney on "The reduction of friction in long runout landslides as an emergent phenomenon", *J Geophys Res-Earth*, *121*(10), doi:10.1002/2016jf003993.

Johnson, B. C., C. S. Campbell, and H. J. Melosh (2016c), Reply to comment by Iverson on "The reduction of friction in long runout landslides as an emergent phenomenon", *J Geophys Res-Earth*, *121*(11), 2243-2246, doi:10.1002/2016jf004093.

Johnson, B. C., and M. M. Sori (2020), Landslide Morphology and Mobility on Ceres Controlled by Topography, *Journal of Geophysical Research: Planets*, *125*(12), e2020JE006640, doi:https://doi.org/10.1029/2020JE006640.

Jones, P. B. (1993), Structural Geology of the Modern Frank Slide and Ancient Bluff Mountain Slide, Crowsnest, Alberta, *B Can Petrol Geol*, *41*(2), 232-243.

Jouannic, G., et al. (2019), Morphological characterization of landforms produced by springtime seasonal activity on Russell Crater megadune, Mars, *Geological Society, London, Special Publications*, *467*(1), 115-144, doi:10.1144/sp467.16.

Kent, P. E. (1966), The Transport Mechanism in Catastrophic Rock Falls, *The Journal of Geology*, *74*(1), 79-83, doi:10.1086/627142.

Kirk, R. L., et al. (2008), Ultrahigh resolution topographic mapping of Mars with MRO HiRISE stereo images: Meter-scale slopes of candidate Phoenix landing sites, *Journal of Geophysical Research: Planets*, *113*(E3), doi:10.1029/2007je003000.

Kirkpatrick, J. D., and C. D. Rowe (2013), Disappearing ink: How pseudotachylytes are lost from the rock record, *J Struct Geol*, *52*, 183-198, doi:10.1016/j.jsg.2013.03.003.

Kissick, L. E., and P. E. Carbonneau (2019), The case against vast glaciation in Valles Marineris, Mars, *Icarus*, *321*, 803-823, doi:https://doi.org/10.1016/j.icarus.2018.12.021.

Kite, E. S., T. I. Michaels, S. Rafkin, M. Manga, and W. E. Dietrich (2011), Localized precipitation and runoff on Mars, *Journal of Geophysical Research: Planets*, *116*(E7), doi:https://doi.org/10.1029/2010JE003783.

Kokelaar, B. P., R. S. Bahia, K. H. Joy, S. Viroulet, and J. M. N. T. Gray (2017), Granular avalanches on the Moon: Mass-wasting conditions, processes, and features, *J Geophys Res-Planet*, *122*(9), 1893-1925, doi:10.1002/2017je005320.

Krohn, K., et al. (2014), Mass movement on Vesta at steep scarps and crater rims, *Icarus*, *244*, 120-132, doi:https://doi.org/10.1016/j.icarus.2014.03.013.

Krumdieck, A. (1984), On the mechanics of large landslides, paper presented at 4th International Symposium on Landslides, University of Toronto Press, Toronto, September 1.

Kumar, A. K., and A. R. Chowdhury (2005), Terrain mapping camera for Chandrayaan-1, *Journal of earth system science*, *114*(6), 717-720.

Lajeunesse, E., C. Quantin, P. Allemand, and C. Delacourt (2006), New insights on the runout of large landslides in the Valles-Marineris canyons, Mars, *Geophys Res Lett*, *33*(4), doi:10.1029/2005gl025168.

Laskar, J., A. C. M. Correia, M. Gastineau, F. Joutel, B. Levrard, and P. Robutel (2004), Long term evolution and chaotic diffusion of the insolation quantities of Mars, *Icarus*, *170*(2), 343-364, doi:https://doi.org/10.1016/j.icarus.2004.04.005.

Legros, F. (2002), The mobility of long-runout landslides, *Eng Geol*, *63*(3-4), 301-331, doi:10.1016/S0013-7952(01)00090-4.

Legros, F., J. M. Cantagrel, and B. Devouard (2000), Pseudotachylyte (Frictionite) at the Base of the Arequipa Volcanic Landslide Deposit (Peru): Implications for Emplacement Mechanisms, *The Journal of Geology*, *108*(5), 601-611, doi:10.1086/314421.

Lucas, A., and A. Mangeney (2007), Mobility and topographic effects for large Valles Marineris landslides on Mars, *Geophys Res Lett*, *34*(10), doi:10.1029/2007gl029835.

Lucas, A., A. Mangeney, and J. P. Ampuero (2014), Frictional velocity-weakening in landslides on Earth and on other planetary bodies, *Nature Communications*, *5*, doi:10.1038/ncomms4417.

Lucas, A., A. Mangeney, D. Mege, and F. Bouchut (2011), Influence of the scar geometry on landslide dynamics and deposits: Application to Martian landslides, *J Geophys Res-Planet*, *116*, doi:10.1029/2011je003803.

Lucchitta, B. K. (1977), Crater clusters and light mantle at the Apollo 17 site; A result of secondary impact from Tycho, *Icarus*, *30*(1), 80-96, doi:https://doi.org/10.1016/0019-1035(77)90123-3.

Lucchitta, B. K. (1978a), Large Landslide on Mars, *Geological Society of America Bulletin*, *89*(11), 1601-1609, doi:10.1130/0016-7606(1978)89<1601:Allom>2.0.Co;2.

Lucchitta, B. K. (1978b), Morphology of Chasma Walls, Mars, *J Res Us Geol Surv*, *6*(5), 651-662.

Lucchitta, B. K. (1979), Landslides in Valles Marineris, Mars, *J Geophys Res*, *84*, 8097-8113, doi:DOI 10.1029/JB084iB14p08097.

Lucchitta, B. K. (1987), Valles Marineris, Mars - Wet Debris Flows and Ground Ice, *Icarus*, *72*(2), 411-429, doi:10.1016/0019-1035(87)90183-7.

Lucchitta, B. K. (2010), Lakes in Valles Marineris, in *Lakes on Mars*, edited by N. A. Cabrol and E. A. Grin, pp. 111-161, Elsevier, Amsterdam, doi:10.1016/B978-0-444-52854-4.00005-2.

Lucieer, A., S. M. d. Jong, and D. Turner (2014), Mapping landslide displacements using Structure from Motion (SfM) and image correlation of multi-temporal UAV photography, *Progress in Physical Geography: Earth and Environment*, *38*(1), 97-116, doi:10.1177/0309133313515293.

Magnarini, G., T. M. Mitchell, P. M. Grindrod, L. Goren, and H. H. Schmitt (2019), Longitudinal ridges imparted by high-speed granular flow mechanisms in martian landslides, *Nature Communications*, *10*(1), 4711, doi:10.1038/s41467-019-12734-0.

Main-Knorn, M., B. Pflug, J. Louis, v. Debaecker, U. Müller-Wilm, and F. Gascon (2017), Sen2Cor for Sentinel-2, *Image and Signal Processing for Remote Sensing XXIII*, *Proc. SPIE 10427*.

Makowska, M., D. Mège, F. Gueydan, and J. Chéry (2016), Mechanical conditions and modes of paraglacial deep-seated gravitational spreading in Valles Marineris, Mars, *Geomorphology*, *268*, 246-252, doi:https://doi.org/10.1016/j.geomorph.2016.06.011.

Malin, M. C. (1992), Mass Movements on Venus - Preliminary-Results from Magellan Cycle-1 Observations, *J Geophys Res-Planet*, *97*(E10), 16337-16352, doi:10.1029/92je01343.

Malin, M. C., et al. (2007), Context Camera Investigation on board the Mars Reconnaissance Orbiter, *J Geophys Res-Planet*, *112*(E5), doi:10.1029/2006je002808.

Marangunic, C., and C. Bull (1968), The landslide on the Sherman Glacier. The Great Alaska Earthquake of 1964, Hydrology., *National Academy of Science Publication*, *1603*, 383-394.

Marangunic, C. B., C. (1968), The landslide on the Sherman Glacier. The Great Alaska Earthquake of 1964, Hydrology., *National Academy of Science Publication*, *1603*, 383-394.

Masch, L., H. R. Wenk, and E. Preuss (1985), Electron-Microscopy Study of Hyalomylonites - Evidence for Frictional Melting in Landslides, *Tectonophysics*, *115*(1-2), 131-160, doi:10.1016/0040-1951(85)90103-9.

Masursky, H., et al. (1978), Apollo over the Moon: A view from orbit, *Report Rep. NASA SP-362*, Washington, D.C.

Mather, A. E., A. J. Hartley, and J. S. Griffiths (2014), The giant coastal landslides of Northern Chile: Tectonic and climate interactions on a classic convergent plate margin, *Earth Planet Sc Lett*, *388*, 249-256, doi:10.1016/j.epsl.2013.10.019.

Mazzanti, P., F. V. De Blasio, C. Di Bastiano, and F. Bozzano (2016), Inferring the high velocity of landslides in Valles Marineris on Mars from morphological analysis, *Earth Planets Space*, *68*(1), doi:10.1186/s40623-015-0369-x.

McEwen, A. S. (1989), Mobility of Large Rock Avalanches - Evidence from Valles Marineris, Mars, *Geology*, *17*(12), 1111-1114, doi:10.1130/0091-7613(1989)017<1111:Molrae>2.3.Co;2.

McEwen, A. S., et al. (2007), Mars Reconnaissance Orbiter's High Resolution Imaging Science Experiment (HiRISE), *J Geophys Res-Planet*, *112*(E5), doi:10.1029/2005je002605.

McKinnon, M. (2010), Landslide runout: statistical analysis of physical characteristics and model parameters, *MSc Thesis*.

McSaveney, M. J. (1978), Sherman Glacier Rock Avalanche, Alaska, U.S.A, in *Developments in Geotechnical Engineering*, edited by B. Voight, pp. 197-258, Elsevier, doi:10.1016/B978-0-444-41507-3.50014-3.

Mège, D., and O. Bourgeois (2011), Equatorial glaciations on Mars revealed by gravitational collapse of Valles Marineris wallslopes, *Earth Planet Sc Lett*, *310*(3), 182-191, doi:https://doi.org/10.1016/j.epsl.2011.08.030.

Melosh, H. J. (1979), Acoustic Fluidization - New Geologic Process, *J Geophys Res*, *84*(Nb13), 7513-7520, doi:10.1029/JB084iB13p07513.

Melosh, H. J. (1983), Acoustic Fluidization, *Am Sci*, *71*(2), 158-165.

Mitchell, T. M., S. A. F. Smith, M. H. Anders, G. Di Toro, S. Nielsen, A. Cavallo, and A. D. Beard (2015), Catastrophic emplacement of giant

landslides aided by thermal decomposition: Heart Mountain, Wyoming, *Earth Planet Sc Lett*, *411*, 199-207, doi:10.1016/j.epsl.2014.10.051.

Morse, Z. R., G. R. Osinski, and L. L. Tornabene (2018), Morphological mapping and analysis of Tsiolkovsky crater ejecta, in *49th Lunar and Planetary Science Conference*, edited, The Woodlands, TX.

Neukum, G., R. Jaumann, and H. E. Team (2004), HRSC: the high resolution stereo camera of Mars Express, *ESA Special Publications*, *1240*, 1-19.

Noel, A., J. L. Bishop, M. Al-Samir, C. Gross, J. Flahaut, P. C. McGuire, C. M. Weitz, F. Seelos, and S. Murchie (2015), Mineralogy, morphology and stratigraphy of the light-toned interior layered deposits at Juventae Chasma, *Icarus*, *251*, 315-331, doi:https://doi.org/10.1016/j.icarus.2014.09.033.

Novoa, A. T. (1970), Carta Geologica de Chile: Cuagrangulos Iquique y Caleta Molle: Provincia de Tarapaca., Instituto de Investigaciones Geologicas (Chile). Carta Geologica N. 21 y 22.

Okubo, C. H. (2010), Structural geology of Amazonian-aged layered sedimentary deposits in southwest Candor Chasma, Mars, *Icarus*, *207*(1), 210-225, doi:https://doi.org/10.1016/j.icarus.2009.11.012.

Okubo, C. H. (2016), Morphologic evidence of subsurface sediment mobilization and mud volcanism in Candor and Coprates Chasmata, Valles Marineris, Mars, *Icarus*, *269*, 23-37, doi:https://doi.org/10.1016/j.icarus.2015.12.051.

Okura, Y., H. Kitahara, T. Sammori, and A. Kawanami (2000), The effects of rockfall volume on runout distance, *Eng Geol*, *58*(2), 109-124, doi:10.1016/S0013-7952(00)00049-1.

Paguican, E. M. R., B. V. de Vries, and A. M. F. Lagmay (2014), Hummocks: how they form and how they evolve in rockslide-debris avalanches, *Landslides*, *11*(1), 67-80, doi:10.1007/s10346-012-0368-y.

Pasckert, J. H., H. Hiesinger, and C. H. van der Bogert (2015), Small-scale lunar farside volcanism, *Icarus*, *257*, 336-354, doi:https://doi.org/10.1016/j.icarus.2015.04.040.

Persson, B. N. J. (2000), *Sliding friction physical principles and applications*, Springer-Verlag, Berlin.

Pieters, C. M., and S. Tompkins (1999), Tsiolkovsky crater: A window into crustal processes on the lunar farside, *J Geophys Res-Planet*, *104*(E9), 21935-21949, doi:Doi 10.1029/1998je001010.

Pinyol, N. M., and E. E. Alonso (2010), Criteria for rapid sliding II.: Thermo-hydro-mechanical and scale effects in Vaiont case, *Eng Geol*, *114*(3), 211-227, doi:https://doi.org/10.1016/j.enggeo.2010.04.017.

Preuss, E. (1971), Uber den Bimsstein von Kofels, Tirol, *Fortschr. Mineral.*, *49*(1), 70.

Pudasaini, S. P., and S. A. Miller (2013), The hypermobility of huge landslides and avalanches, *Eng Geol*, *157*, 124-132, doi:10.1016/j.enggeo.2013.01.012.

Quantin, C., P. Allemand, and C. Delacourt (2004a), Morphology and geometry of Valles Marineris landslides, *Planet Space Sci*, *52*(11), 1011-1022, doi:10.1016/j.pss.2004.07.016.

Quantin, C., P. Allemand, N. Mangold, and C. Delacourt (2004b), Ages of Valles Marineris (Mars) landslides and implications for canyon history, *Icarus*, *172*(2), 555-572, doi:10.1016/j.icarus.2004.06.013.

Quintana, S. N., and P. H. Schultz (2014), The formation of crater-related blast wind streaks on Mars, *Lunar and Planetary Science Conference XLV*, Abstract 1971.

Rice, J. R. (1999), Flash heating at asperity contacts and rate-dependent friction, *Eos Trans. AGU*, *80*(46), F471.

Rice, J. R. (2006), Heating and weakening of faults during earthquake slip, *Journal of Geophysical Research: Solid Earth*, *111*(B5), doi:10.1029/2005JB004006.

Rice, J. R. (2017), Heating, weakening and shear localization in earthquake rupture, *Philosophical Transactions of the Royal Society A: Mathematical, Physical and Engineering Sciences*, *375*(2103), 20160015, doi:doi:10.1098/rsta.2016.0015.

Roberts, N. J., and S. G. Evans (2013), The gigantic Seymareh (Saidmarreh) rock avalanche, Zagros Fold-Thrust Belt, Iran, *J Geol Soc London*, *170*(4), 685-700, doi:10.1144/jgs2012-090.

Robinson, M. S., et al. (2010), Lunar Reconnaissance Orbiter Camera (LROC) Instrument Overview, *Space Science Reviews*, *150*(1), 81-124, doi:10.1007/s11214-010-9634-2.

Roche, O., M. Attali, A. Mangeney, and A. Lucas (2011), On the run-out distance of geophysical gravitational flows: Insight from fluidized granular collapse experiments, *Earth Planet Sc Lett*, *311*(3-4), 375-385, doi:10.1016/j.epsl.2011.09.023.

Rowe, C. D., and W. A. Griffith (2015), Do faults preserve a record of seismic slip: A second opinion, *J Struct Geol*, *78*, 1-26, doi:https://doi.org/10.1016/j.jsg.2015.06.006.

Salese, F., M. Pondrelli, A. Neeseman, G. Schmidt, and G. G. Ori (2019), Geological Evidence of Planet-Wide Groundwater System on Mars, *Journal of Geophysical Research: Planets*, *124*(2), 374-395, doi:https://doi.org/10.1029/2018JE005802.

Sassa, K. (1988), Special lecture-Geotechnical model for the motion of landslides, *Proceedings, 5th International Symposium on Landslides*, *1*, 37-56.

Scheidegger, A. E. (1973), On the prediction of the reach and velocity of catastrophic landslides, *Rock Mechanics*, *5*(4), 231-236, doi:10.1007/BF01301796.

Schmidt, B. E., et al. (2017), Geomorphological evidence for ground ice on dwarf planet Ceres, *Nat Geosci*, *10*(5), 338-343, doi:10.1038/Ngeo2936.

Schmitt, H. H. (1973), Apollo 17 Report on the Valley of Taurus-Littrow, *A geological investigation of the valley visited on the last Apollo mission to the moon*, *182*(4113), 681-690, doi:10.1126/science.182.4113.681.

Schmitt, H. H., N. E. Petro, R. A. Wells, M. S. Robinson, B. P. Weiss, and C. M. Mercer (2017), Revisiting the field geology of Taurus-Littrow, *Icarus*, *298*, 2-33, doi:10.1016/j.icarus.2016.11.042.

Scott, D. F. (1973), Small structures of the Taurus-Littrow region*Rep. SP330*, 31-25 pp, NASA.

Scott, D. H., B. K. Lucchitta, and M. H. Carr (1972), Geologic maps of the Taurus-Littrow region of the Moon Apollo 17 pre-mission maps, *Report Rep. 800*.

Sejourne, A., et al. (2019), Grid Mapping the Northern Plains of Mars: Using Morphotype and Distribution of Ice-Related Landforms to Understand Multiple Ice-Rich Deposits in Utopia Planitia, *J Geophys Res-Planet*, *124*(2), 483-503, doi:10.1029/2018je005665.

Senthil Kumar, P., V. Keerthi, A. Senthil Kumar, J. Mustard, B. Gopala Krishna, Amitabh, L. R. Ostrach, D. A. Kring, A. S. Kiran Kumar, and J. N. Goswami (2013), Gullies and landslides on the Moon: Evidence for dry-granular flows, *Journal of Geophysical Research: Planets*, *118*(2), 206-223, doi:doi:10.1002/jgre.20043.

Shaller, P. J. (1991), Analysis and implications of large Martian and terrestrial landslides, *PhD Thesis*.

Sharp, R. P. (1973a), Mars: Troughed terrain, *Journal of Geophysical Research (1896-1977)*, *78*(20), 4063-4072, doi:10.1029/JB078i020p04063.

Sharp, R. P. (1973b), Mars: Troughed terrain, *J Geophys Res*, *78*(20), 4063-4072, doi:10.1029/JB078i020p04063.

Sharpe, C. F. S. (1938), *Landslides and related phenomena*, Columbia University Press, New York.

Shea, T., and B. van Wyk de Vries (2008), Structural analysis and analogue modelling of the kinematics and dynamics of large-scale rock avalanches, *Geosphere*, *4*, 657-686.

Shingareva, T. V., and R. O. Kuzmin (2001), Mass-wasting processes on the surface of Phobos, *Solar Syst Res+*, *35*(6), 431-443, doi:10.1023/A:1013082711274.

Shreve, R. L. (1959), Geology and mechanics of the Blackhawk landslide, Lucerne Valley, California, *PhD Thesis*, doi:10.22002/D1.709.

Shreve, R. L. (1966), Sherman Landslide Alaska, *Science*, *154*(3757), 1639-&, doi:DOI 10.1126/science.154.3757.1639.

Shreve, R. L. (1968a), The Blackhawk Landslide, in *The Blackhawk Landslide*, edited by R. L. Shreve, Geological Society of America.

Shreve, R. L. (1968b), Leakage and Fluidization in Air-Layer Lubricated Avalanches, *Geological Society of America Bulletin*, *79*(5), 653-&, doi:10.1130/0016-7606(1968)79[653:Lafial]2.0.Co;2.

Sibson, R. H. (1973), Interactions between Temperature and Pore-Fluid Pressure during Earthquake Faulting and a Mechanism for Partial or Total Stress Relief, *Nature Physical Science*, *243*, 66, doi:10.1038/physci243066a0.

Sibson, R. H. (1975), Generation of Pseudotachylyte by Ancient Seismic Faulting, *Geophysical Journal of the Royal Astronomical Society*, *43*(3), 775-794, doi:10.1111/j.1365-246X.1975.tb06195.x.

Singer, K. N., W. B. McKinnon, P. M. Schenk, and J. M. Moore (2012), Massive ice avalanches on Iapetus mobilized by friction reduction during flash heating, *Nat Geosci*, *5*(8), 574-578, doi:10.1038/Ngeo1526.

Slatcher, N., M. R. James, S. Calvari, G. Ganci, and J. Browning (2015), Quantifying Effusion Rates at Active Volcanoes through Integrated Time-Lapse Laser Scanning and Photography, *Remote Sensing*, *7*(11), 14967.

Smith, D. E., et al. (2001), Mars Orbiter Laser Altimeter: Experiment summary after the first year of global mapping of Mars, *J Geophys Res-Planet*, *106*(E10), 23689-23722, doi:Doi 10.1029/2000je001364.

Smith, D. E., et al. (2010), The Lunar Orbiter Laser Altimeter Investigation on the Lunar Reconnaissance Orbiter Mission, *Space Science Reviews*, *150*(1), 209-241, doi:10.1007/s11214-009-9512-y.

Sobiesiak, M. S., B. Kneller, G. I. Alsop, and J. P. Milana (2018), Styles of basal interaction beneath mass transport deposits, *Marine and Petroleum Geology*, *98*, 629-639, doi:https://doi.org/10.1016/j.marpetgeo.2018.08.028.

Spray, J. G. (1997), Superfaults, *Geology*, *25*(7), 579-582.

Spudis, P. D., D. E. Wilhelms, and M. S. Robinson (2011), The Sculptured Hills of the Taurus Highlands: Implications for the relative age of Serenitatis, basin chronologies and the cratering history of the Moon, *Journal of Geophysical Research: Planets*, *116*(E12), doi:https://doi.org/10.1029/2011JE003903.

Staron, L., and E. Lajeunesse (2009), Understanding how volume affects the mobility of dry debris flows, *Geophys Res Lett*, *36*, doi:10.1029/2009gl038229.

Straub, S. (1996), Self-organization in the rapid flow of granular material: evidence for a major flow mechanism, *Geologische Rundschau*, *85*(1), 85-91, doi:10.1007/bf00192064.

Straub, S. (1997), Predictability of long runout landslide motion: implications from granular flow mechanics, *Geologische Rundschau*, *86*(2), 415-425, doi:10.1007/s005310050150.

Strom, A., and K. Abdrakhmatov (2018), Chapter 11 - Structure and Grain-Size Composition of Large-Scale Bedrock Landslide Deposits, in *Rockslides and Rock Avalanches of Central Asia*, edited by A. Strom and K. Abdrakhmatov, pp. 349-364, Elsevier, doi:https://doi.org/10.1016/B978-0-12-803204-6.00011-9.

Stucky de Quay, G. (2014), Landslides in Valles Marineris, Mars: Combining global database statistics and a digital terrain model to assess the role of ice during emplacement, University College London (UCL).

Terzaghi, K. (1943), Stability of Slopes, in *Theoretical Soil Mechanics*, edited, pp. 144-181, doi:https://doi.org/10.1002/9780470172766.ch9.

Torson, J. M., and K. J. Becker (1997), ISIS - A Software Architecture for Processing Planetary Images, in *LPSC XXVIII*, edited, The Woodlands, Houston, TX.

Tusima, K. (2010), Estimation friction coefficient of stone and mechanism of curl, *Proceedings of cold region technology conference*, *26*, 422-427.

Tyrie, A. (1988), A description of the crater Tsiolkovsky on the lunar far side, *Earth, Moon, and Planets*, *42*(3), 265-275, doi:10.1007/bf00058490.

van der Bogert, C. H., J. D. Clark, H. Hiesinger, M. E. Banks, T. R. Watters, and M. S. Robinson (2018), How old are lunar lobate scarps? 1. Seismic resetting of crater size-frequency distributions, *Icarus*, *306*, 225-242, doi:https://doi.org/10.1016/j.icarus.2018.01.019.

van der Bogert, C. H., H. Hiesinger, M. E. Banks, T. R. Watters, and M. S. Robinson (2012), Derivation of absolute model ages for lunar lobate scarps, in *43rd Lunar and Planetary Science Conference*, edited, The Woodlands, TX.

van der Bogert, C. H., H. Hiesinger, W. Iqbal, J. D. Clark, M. S. Robinson, B. L. Joliff, T. M. Hahn Jr., T. R. Watters, and M. E. Banks (2019), Timing of recent events near the Apollo 17 landing site, in *50th Lunar and Planetary Science Conference*, edited, The Woodlands, TX.

Vardoulakis, I. (2000), Catastrophic landslides due to frictional heating of the failure plane, *Mech Cohes-Frict Mat*, *5*(6), 443-467, doi:10.1002/1099-1484(200008)5:6<443::Aid-Cfm104>3.0.Co;2-W.

Vardoulakis, I. (2002), Dynamic thermo-poro-mechanical analysis of catastrophic landslides, *Geotechnique*, *52*(3), 157-171, doi:10.1680/geot.52.3.157.41012.

Viesca, R. C., and J. R. Rice (2012), Nucleation of slip-weakening rupture instability in landslides by localized increase of pore pressure, *Journal of Geophysical Research: Solid Earth*, *117*(B3), doi:10.1029/2011jb008866.

Violay, M., S. Nielsen, B. Gibert, E. Spagnuolo, A. Cavallo, P. Azais, S. Vinciguerra, and G. Di Toro (2014), Effect of water on the frictional behavior of cohesive rocks during earthquakes, *Geology*, *42*(1), 27-30, doi:10.1130/g34916.1.

Voight, B., and C. Faust (1982), Frictional Heat and Strength Loss in Some Rapid Landslides, *Geotechnique*, *32*(1), 43-54, doi:10.1680/geot.1982.32.1.43.

Voight, B., R. J. Janda, H. Glicken, and P. M. Douglass (1983), Nature and mechanics of the Mount St Helens rockslide-avalanche of 18 May 1980, *Geotechnique*, *33*(3), 243-273, doi:10.1680/geot.1983.33.3.243.

Voight, B., and J. Sousa (1994), Lessons from Ontake-san: a comparative analysis of debris avalanche dynamics, *Eng Geol*, *38*, 261-297.

Walker, S., and A. Pietrzak (2015), Remote measurement methods for 3-D modeling purposes using BAE Systems' Software, *vol. 64*(No 1).

Warner, N. H., M. Sowe, S. Gupta, A. Dumke, and K. Goddard (2013), Fill and spill of giant lakes in the eastern Valles Marineris region of Mars, *Geology*, *41*(6), 675-678, doi:10.1130/g34172.1.

Watkins, J. A., B. L. Ehlmann, and A. Yin (2015), Long-runout landslides and the long-lasting effects of early water activity on Mars, *Geology*, *43*(2), 107-110, doi:10.1130/G36215.1.

Watkins, J. A., B. L. Ehlmann, and A. Yin (2020), Spatiotemporal evolution, mineralogical composition, and transport mechanisms of long-runout landslides in Valles Marineris, Mars, *Icarus*, *350*, 113836, doi:https://doi.org/10.1016/j.icarus.2020.113836.

Watson, R. A., and H. E. Wright (1969), The Saidmarreh Landslide, Iran, *Geological Society of America Special Papers*, *123*, doi:10.1130/SPE123-p115.

Watters, T. R., et al. (2010), Evidence of Recent Thrust Faulting on the Moon Revealed by the Lunar Reconnaissance Orbiter Camera, *Science*, *329*(5994), 936-940, doi:10.1126/science.1189590.

Watters, T. R., R. C. Weber, G. C. Collins, I. J. Howley, N. C. Schmerr, and C. L. Johnson (2019), Shallow seismic activity and young thrust faults on the Moon, *Nature Geoscience*, *12*(6), 411-417, doi:10.1038/s41561-019-0362-2.

Weidinger, J. T., and O. Korup (2009), Frictionite as evidence for a large Late Quaternary rockslide near Kanchenjunga, Sikkim Himalayas, India — Implications for extreme events in mountain relief destruction, *Geomorphology*, *103*(1), 57-65, doi:https://doi.org/10.1016/j.geomorph.2007.10.021.

Weidinger, J. T., O. Korup, H. Munack, U. Altenberger, S. A. Dunning, G. Tippelt, and W. Lottermoser (2014), Giant rockslides from the inside, *Earth Planet Sc Lett*, *389*, 62-73, doi:https://doi.org/10.1016/j.epsl.2013.12.017.

Weiss, D. K., and J. W. Head (2013), Formation of double-layered ejecta craters on Mars: A glacial substrate model, *Geophys Res Lett*, *40*(15), 3819-3824, doi:10.1002/grl.50778.

Weitz, C. M., E. Noe Dobrea, and J. J. Wray (2015), Mixtures of clays and sulfates within deposits in western Melas Chasma, Mars, *Icarus*, *251*, 291-314, doi:https://doi.org/10.1016/j.icarus.2014.04.009.

Williams Jr, R. S., and W. D. Carter (1976), ERTS-1, a new window on our planet, *Report Rep. 929*.

Williams, R. M. E., and C. M. Weitz (2014), Reconstructing the aqueous history within the southwestern Melas basin, Mars: Clues from stratigraphic and morphometric analyses of fans, *Icarus*, *242*, 19-37, doi:https://doi.org/10.1016/j.icarus.2014.06.030.

Wolfe, E. W., N. G. Bailey, B. K. Lucchitta, W. R. Muehlberger, D. H. Scott, R. L. Sutton, H. G. Wilshire, R. M. Batson, K. B. Larson, and R. L. Tyner (1981), The geologic investigation of the Taurus-Littrow Valley; Apollo 17 landing site, with a section on Apollo 17 lunar surface photography, *Report Rep. 1080*.

Wu, S. C., F. J. Schafer, R. Jordan, G. M. Nakata, and J. L. Derick (1972), Apollo 15: Preliminary Science Report SP-289*Rep.*, 25-36 pp, NASA.

Wulf, G., and T. Kenkmann (2015), High-resolution studies of double-layered ejecta craters: Morphology, inherent structure, and a phenomenological formation model, *Meteoritics & Planetary Science*, *50*(2), 173-203, doi:https://doi.org/10.1111/maps.12416.

Zhang, Z.-Y., S.-M. Chen, L.-J. Tao, S. G. Evans, and J. V. Degraff (2002), 1983 Sale Mountain landslide, Gansu Province, China, in *Catastrophic Landslides*, edited, p. 0, Geological Society of America, doi:10.1130/REG15-p149.

Zuber, M. T., D. E. Smith, S. C. Solomon, D. O. Muhleman, J. W. Head, J. B. Garvin, J. B. Abshire, and J. L. Bufton (1992), The Mars Observer laser altimeter investigation, *Journal of Geophysical Research: Planets*, *97*(E5), 7781-7797, doi:10.1029/92je00341.